THE UNIVERSITY OF CHICAGO

ADSORPTION, DIFFUSION, AND REACTION IN CONDENSED FILMS: NERVE AGENT SIMULANTS, EXTRATERRESTRIAL ICES, AND OLEFIN OXIDATION

A DISSERTATION SUBMITTED TO
THE FACULTY OF THE DIVISION OF THE PHYSICAL SCIENCES
IN CANDIDACY FOR THE DEGREE OF
DOCTOR OF PHILOSOPHY

DEPARTMENT OF CHEMISTRY

BY
REBECCA THOMPSON

CHICAGO, ILLINOIS
MARCH 2020

The unpredictable and the predetermined unfold together to make everything the way it is. It's how nature creates itself, on every scale, the snowflake and the snowstorm. It makes me so happy. To be at the beginning again, knowing almost nothing. People were talking about the end of physics. Relativity and quantum looked as if they were going to clean out the whole problem between them. A theory of everything. But they only explained the very big and the very small. The universe, the elementary particles. The ordinary-sized stuff which is our lives, the things people write poetry about – clouds – daffodils – waterfalls – and what happens in a cup of coffee when the cream goes in – these things are full of mystery, as mysterious to us as the heavens were to the Greeks. We're better at predicting events at the edge of the galaxy or inside the nucleus of an atom than whether it'll rain on auntie's garden party three Sundays from now... The future is disorder. A door like this has cracked open five or six times since we got up on our hind legs. It's the best possible time to be alive, when almost everything you thought you knew is wrong.
- Tom Stoppard, *Arcadia*

I do love the shapes of things, you know. I love them even before they mean something.
- Anna Ziegler, *Photograph 51*

Table of Contents

List of Figures

List of Tables

Acknowledgments

Thank you to Russ Kohnken, Mark Vondracek, Mark Marshall, and Helen Leung, for teaching with passion and inspiring me to pursue a scientific career.

Thank you to Vera, Melinda, John, Maria, and Tanya, for keeping the lights on, the paychecks and reimbursements signed, and making order out of administrative disorder.

Thank you to my committee members, Sarah and Andrei, for taking an interest in me and my science, and for being wonderful mentors in the department.

Thank you to the Sibener group (Sibener-ites, Sibe-nerds): Wenxin, Zack, Bryan, Grant, Kevin, Jon, Jeff, Darren, Jacob, Rachael, Ross, Sarah B., Tim, Michelle, Julia, Ali, Caleb, and Sarah W. Truly the brightest and best looking group around – I'm glad we never take ourselves too seriously.

Thank you to Kevin Gibson, for always taking the time out of your day to help me work through even the dumbest of issues, and for teaching me how to better appreciate a good beer.

Thank you to Kevin Nihill. Your cynicism and wit is matched only by your sweetness, phenomenal teaching ability, and love for David Foster Wallace.

Thank you to Grant, the epitome of patience. You are the reason I didn't drop out immediately on viewing our monstrous instrument, and I loved bonding over cooking, loud music, and good TV.

Thank you to Michelle, for putting up with my quirks and tackling the 50^{th} diffusion pump repair in good spirits. I love our boba adventures and afternoon walks, and I don't know what I'd do without you to compare online shopping carts with.

Thank you to Clara, my first and best friend from graduate school, for showing me how to be more thoughtful with my time, and teaching me the power of local organizing.

Thank you to my advisor, Steve Sibener, for your "mentoring moments", your unfailing kindness and encouragement, and for showing me how to really think like an experimentalist.

Thank you to Clare, Jordan, Lisa, and Megan. You made Chicago feel like home, opened me up to new experiences, and together we cooked some of the best meals I've ever had.

Thank you to Andrea, Susannah, Kristin, and Becca. Never shy about a deep conversation or an exhaustive food tour, you've always known and loved me for exactly who I am.

Thank you to Grandma Dean, for our shared love of organization, for making me chocolate cake even though you can't eat it, and for teaching me that we are lost if we don't understand our history.

Thank you to Grandpa Don, for loving me even though I turned out to be terrible at bowling, and for insisting that we do the things in life that make us most happy.

Thank you to Grandma Mary-Anne, for teaching me how to teach, for your generosity and empathy, and for never *ever* letting me win at cards.

Thank you to Grandpa Gordon, for teaching me that there is nothing more important than family, theater, and finding a quiet place to read good books.

Thank you to Sarah, for being fiercely competitive *and* fiercely kind, for living loudly *and* being an amazing listener. In the 26 years that we've known each other, I don't think we've ever truly had a fight. Thank you for being the easier daughter to manage, and for always being on my team.

Thank you to my mom, for teaching me the value of making lists, the necessity of honoring one's commitments, and the beauty in succeeding not because it was easy, but because you worked really, really hard.

Thank you to my dad, for teaching me how to talk confidently about books I haven't read, and for modeling a selfless kindness that draws everyone into your orbit.

Thank you to Ali, for more backrubs than any one woman deserves. Thank you for always making me laugh, believing in my intelligence and ability, and for being the best cat dad to Algie and Sly.

Abstract

This thesis describes a diverse set of experiments that probe the interfacial dynamics of complex molecular thin films. Topics include the oxidative and thermal destruction of chemical warfare agents, sticking of small molecules on and in extraterrestrial ices, heterogeneous catalysis in a high-pressure reactor, and oxidation of an important industrial alkene. While the systems of study differ dramatically, all projects focus on uncovering the precise mechanisms of reactivity in condensed films in which diffusion, stable reactive intermediates, and film structure play a crucial role in the observed chemistry. In the oxidative destruction of chemical warfare agent simulants, we find that despite rapid initial reactivity, the build up of a dense product overlayer on the simulant film hinders full destruction of thicker films. Oxygen plays a similarly vital role in the destruction of these compounds under high-temperature, atmospheric pressure conditions.

Even initial adsorption can be critically influenced by film structure, as is the case for methane adsorption on water ice. Our work on this system, which has direct relevance to astrophysical environments, demonstrates that high energy methane sticks more readily to porous amorphous ice films than to either crystalline or non-porous amorphous films, likely due to efficient energy accommodation by the pore structure. Even when a reaction *isn't expected*, the right high-temperature and high-pressure system can be ripe for heterogenous chemistry. In this case, a supersonic molecular beam nozzle acts as a highly efficient reactor for the production of CO and H_2O from a mixture of CO_2 and H_2. Finally, we find that in the oxidation of condensed propene (an important combustion intermediate species), propene film structure can have a profound effect on the diffusion and subsequent reactivity of oxygen. In addition to highlighting the applicability and effectiveness of time-resolved, surface-sensitive spectroscopic techniques, this work clearly demonstrates the many factors that influence complex reactivity in condensed phases. Product distributions and reaction barriers often differ dramatically due to many-body interactions in the film. Even when barriers are low, contact between reactive species may be significantly hindered by low adsorption probabilities, diffusion constraints, and film morphology.

Chapter 1

Introduction

Chemistry in condensed phases is *messy*. Solid films and their gaseous interfaces present unique challenges to conventional analytical techniques; while product identities and energy distributions may be relatively straightforward to identify in a particular gas phase reaction, analogous reactivity in the condensed phase may be starkly different and significantly more difficult to fully characterize. A thin molecular film presents a complex and dynamic reaction environment with a particular energetic landscape. Reaction barriers and product branching ratios are often influenced by the presence of so many close-packed neighboring molecules. Moreover, the solid film itself can impact the reaction in unique ways by allowing or impeding reactant diffusion, presenting complex interfacial morphologies, or changing composition throughout the reaction timescale. Put simply, teasing apart the many competing reaction variables on and in complex molecular films is an exercise in patience, creativity, and hard work.

Though challenging, condensed phase research is essential to a number of fields including astrophysics, national defense, industrial chemical production, and countless others. The reason for this is straightforward: real-world chemistry often (either by design or as a result of atmospheric conditions) takes place on surfaces. Industrial heterogenous catalysis relies on the unique properties of metal surfaces that differ from the bulk. Self-assembled coatings are useful for corrosion protection because they impede the diffusion of damaging oxidative species. Accurately modeling the atmospheric dispersal and lifetimes of many pollutants depends critically on whether they are traveling in condensed or gas phases. Though the chapters in this thesis have different applications and implications, they each detail a system in which the condensed film impacts the reaction dynamics in a critical way that would not be otherwise observed in the gas phase.

In **Chapters 3** and **4**, we explore the fundamental oxidative chemistry of organophosphonate compounds similar in structure to the deadly nerve agents Sarin and Soman (termed "simulants"). This work is directly tied to ongoing efforts within the Defense Threat Reduction Agency to detect and mitigate the impact of these dangerous compounds. Existing work suggests that oxygen plays

a significant role in various remediation techniques, but the essential condensed phase oxidation mechanism is not well established. We use atomic oxygen, O(^{3}P), as a basic oxidant; it rapidly reacts with thin simulant films. The presence of so many neighboring molecules leads to a cascade of secondary reactions and cross-linked product species. It is this easy reaction, however, that ultimately prevents effective oxidation of the complete film. Over time, the product build-up creates a protective crust, blocking oxygen from reacting with the layers buried closest to the substrate.

In **Chapter 5** we extend our study of this simulant system to more practical environmental conditions. This time, we investigate the role of both rapid heating and oxygen, all under realistic atmospheric pressure conditions. Again we find that oxygen plays a significant role in simulant degradation. Suggesting a mechanism unique from the analogous gas phase pyrolysis, we find that atmospheric oxygen is directly incorporated into the incinerated simulant molecule.

The probability for reactive encounter can also influence the observed reaction kinetics in condensed phases. In other words, reactivity is often impossible until a gaseous reactant can adsorb to a film or otherwise embed in the first place. It is precisely this issue that we explore in **Chapter 6**, in which we investigate the role of water ice film morphology in the initial sticking and embedding events for gaseous projectiles with high incident momenta. We find that the sticking probability of methane is highest on porous ice morphologies, regardless of pore size and orientation relative to the substrate. Icy bodies serve as the site for numerous astrophysical and prebiotic reactions; these results suggest that large-scale pores, cracks, fissures, and other morphological deformities in the surface of ice may lead to an increased uptake of gaseous molecules, impacting downstream phenomena such as the outgassing of comets, chemical reactions in the interstellar medium, and thermal and electrical processing of icy dust grains.

Sometimes, the impact of a surface can be so significant that it derails the very experiment you intend to perform. Such is the case with the research detailed in **Chapter 7**. During routine heating of a seeded molecular beam of CO_2 and H_2, we discovered that the stainless steel beam nozzle was acting as an extremely efficient catalyst to convert the seed gases to CO and H_2O. This reverse water-gas shift (RWGS) reaction is the reverse of an important industrial catalytic reaction for the

production of H_2. The results of the subsequent analysis demonstrate that this beam-as-reactor method may present a heretofore unexplored route to efficient, high pressure inline catalysis.

Finally, we highlight yet another way that film structure and morphology can dramatically impact the observed chemistry in a condensed film. In **Chapter 8**, thin films of propene are observed to react readily with atomic oxygen to form propylene oxide and propanal. Propene, a significant intermediate in a number of combustion and industrial processes in it's own right, does not form propylene oxide under gas phase oxidative conditions; efficient production in the condensed phase is significant as market demand for it has increased dramatically in recent years. Importantly, however, we find that propene films deposited at low temperatures are more amorphous and disordered; these films are nearly impervious to oxidation, suggesting that diffusion and reactivity is directly tied to propene ordering within the film.

Chapter 2

Experimental Methods

Vacuum conditions are typically essential for the study of surface chemistry and reaction dynamics in thin films. Because the chamber is pumped clean of background gas, we are assured that the chemistry and kinetics that we measure are uniquely attributable to the desired reaction. As such, with the exception of the experiments detailed in **Chapter 5**, the work described in this thesis was performed in a high volume, ultrahigh vacuum (UHV) chamber equipped with numerous techniques for studying the dynamics of gaseous adsorption on and reactivity in condensed films. The details of the core chamber, supersonic molecular beam, and analytical techniques are described in this chapter; any deviations or unique instrumentation specific to a particular experiment will be detailed in the later chapters.

2.1 Main UHV Chamber

At its cleanest, the commercial UHV chamber (TNB-X, Perkin-Elmer) has a typical base pressure of 10^{-10} Torr, as measured with a Bayard-Alpert nude ion gauge. While this base pressure crept up slightly to 10^{-9} Torr for the ice experiments described in **Chapter 6** due to a larger water background, the remaining experiments also use a cold sample manipulator, which contributes extra cryogenic pumping capacity to the chamber and helps to maintain a base pressure on the order of 10^{-10} Torr. The chamber vacuum is sustained by a 260 L s^{-1} turbomolecular pump (HiPace 300, Pfeiffer Vacuum), backed by a 3 L s^{-1} dry scroll pump (nXDS10i, Edwards Vacuum).

As shown in **Figure 2.1**, The UHV chamber was designed to offer many different analytical techniques and sample configurations *in situ*. The sample substrate used for all experiments performed in this chamber is a square centimeter Au(111) single-crystal. This crystal is mounted on a five-axis manipulator (*x*-, *y*-, and *z*-translation, polar rotation, and precession around a small internal diameter). Additional manipulator detail is provided in **Section 2.4.1**. On the lower deck of the chamber, the crystal can be positioned to allow for concurrent exposure to the molecular

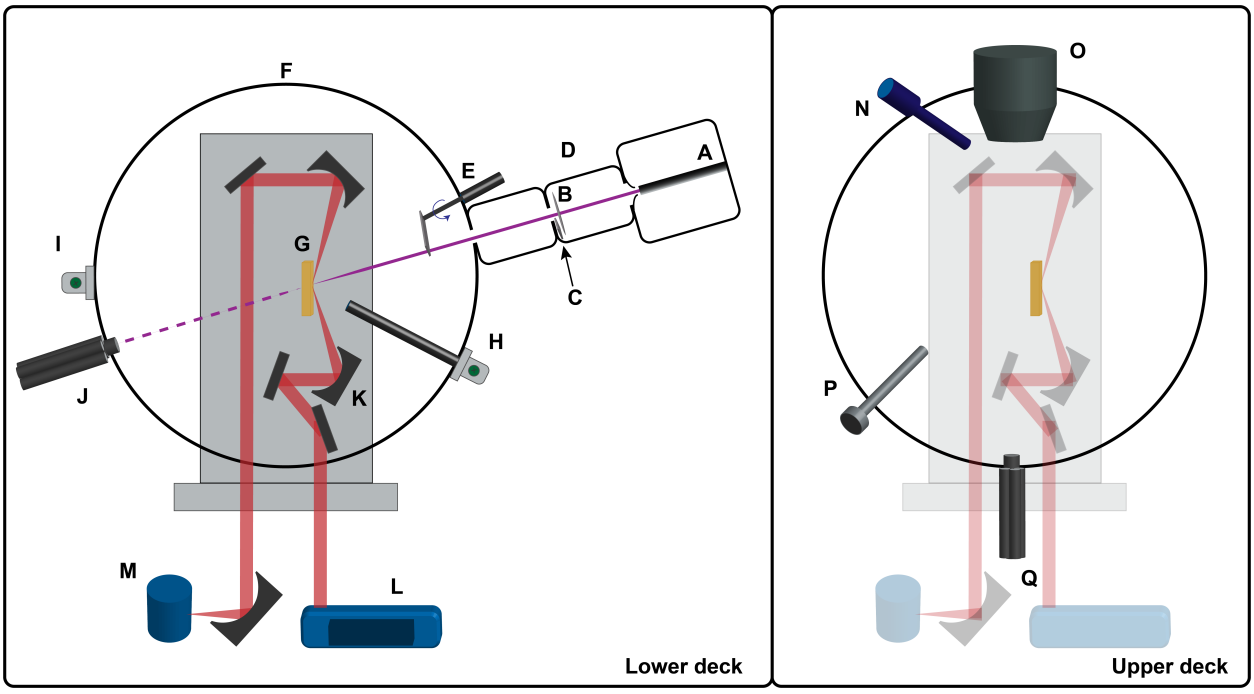

Figure 2.1: **Schematic layout of main chamber**. The instrumentation in the main sample chamber is primarily confined to two vertical levels. The lower level (left) is used for RAIRS and molecular beam exposure. The upper level (right) is used for XPS, sputtering, and mass spectrometry.

A - Molecular beam source
B - Chopper (beam modulation)
C - Flag for timing exposure
D - Differential pumping stages
E - Rotatable flag
F - UHV chamber
G - Au(111) sample
H - Directed doser
I - Leak valve
J - inline QMS
K - RAIRS optics
L - FTIR spectrometer
M - MCT/A detector
N - X-ray source
O - Cylindrical mirror analyzer
P - Ion gun for sputtering
Q - Residual gas analyzer

beam and analysis via reflection-absorption infrared spectroscopy (RAIRS). This is the standard configuration for collecting detailed, time-resolved data about the dynamics at the surface. The same level also contains a quadrupole mass spectrometer (QMS; QMG 112, Balzers) for performing time-of-flight analysis on the molecular beam as well as a leak valve (Varian) and directed doser (MDC). The leak valve is primarily used for admitting Ar into the chamber during sputtering cycles (**Section 2.4.2**), but it also finds use in **Chapter 6** as one of two methods for depositing water ice on the crystal. The second method is via the nearby directed doser. The details of film preparation are discussed in more detail in **Subsection 2.4.3**.

The upper level of the UHV chamber is used for X-ray photoelectron spectroscopy (XPS)

and sample cleaning via Ar^+ ion sputtering. It also contains a second mass spectrometer (RGA 300, Stanford Research Systems) that is used for residual gas monitoring and the King and Wells measurements described in **Subsection 2.2.3**.

2.2 Surface-Sensitive Analytical Techniques

As described in **Section 2.1**, the main UHV chamber contains a variety of instrumentation for analyzing gaseous species in the chamber and directly probing dynamics and composition of thin films. The three techniques used in this thesis and described in the following sections are RAIRS, XPS, and King and Wells. We often use these techniques in concert to provide a full, detailed picture of adsorption and reactivity at the surface.

2.2.1 Reflection-Absorption Infrared Spectroscopy

RAIRS is a technique that leverages the basic principles of vibrational spectroscopy to probe molecules physisorbed to a reflective metal substrate. As with all vibrational spectroscopies, RAIRS can provide detailed information about which chemical species are present on the surface and their respective chemical environments and conformations. In order to circumvent the limits of Beer's law and achieve high sensitivity for thin films down to sub-monolayer coverages, *p*-polarized incident infrared radiation is reflected at a glancing angle from the reflective substrate. As shown in figure **Figure 2.2a**, the electric field vector of the light can be polarized either parallel (*p*) or perpendicular (*s*) to the plane of incidence. Using the Fresnel equations for light reflected from a surface, it can be shown that when *s*-polarization is used, the electric field generated near the surface undergoes a near 180° phase shift, regardless of incident angle. This results in a negligible standing wave at the surface; this standing wave, when present, is what leads to infrared absorption of the molecules on the surface. On the other hand, the phase change for *p*-polarized light is highly angularly dependent.[1,2] This phenomenon, first quantitatively established by Greenler in the 1960's, leads to a maximum standing wave and signal reflectance at high incidence angles,

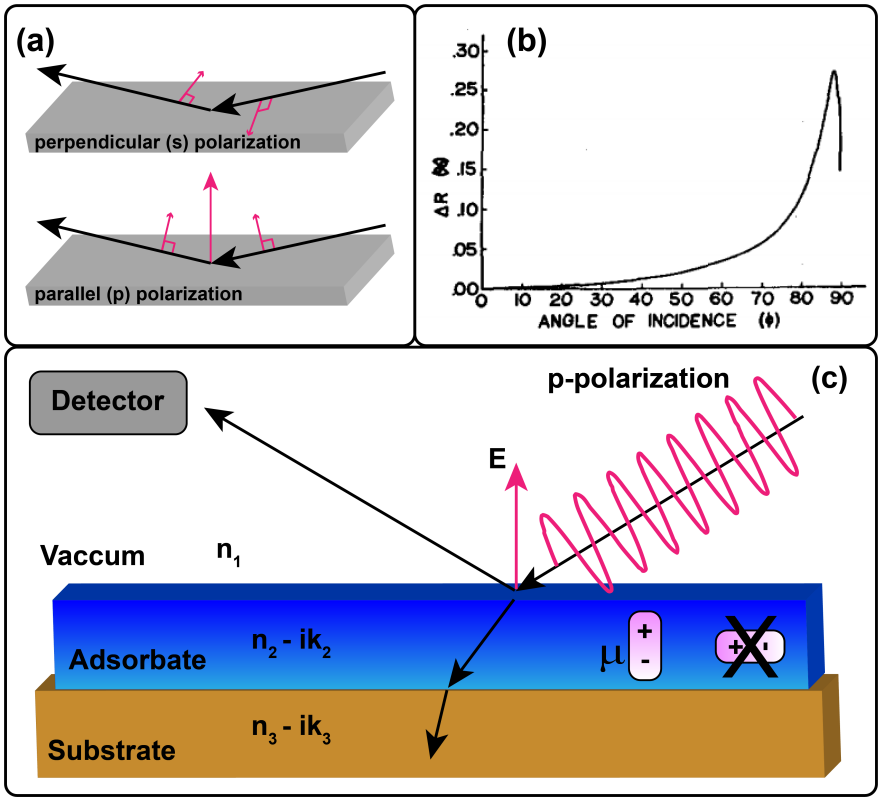

Figure 2.2: **Theoretical description of RAIRS**. (a) Only *p*-polarized light can generate an appreciable standing wave at the surface of a reflective substrate. (b) Maximum reflectance is observed at oblique incidence angles (reproduced from ref. [3]). (c) Dipoles must be oriented perpendicular to the surface in order to be detected via RAIRS.

peaking around 85-89° for most systems (**Figure 2.2b**).[3]

One important consequence of the reflective metal substrate used in RAIRS measurements is the introduction of a new vibrational selection rule. As shown in **Figure 2.2c**, IR-active modes are only detected if the active dipole is perpendicular to the substrate. Because the intensity of absorption is proportional to the square of the dot product between the electric field (E) and the transitional dipole moment μ, dipoles parallel to the surface ($\theta = 90°$) will be virtually undetectable by RAIRS:[4]

$$A \propto E^2 \mu^2 \cos\theta^2 \tag{2.1}$$

This additional selection rule allows for quantitative estimations of structural order in condensed thin films, although care must be taken to account for other optical effects introduced by the exper-

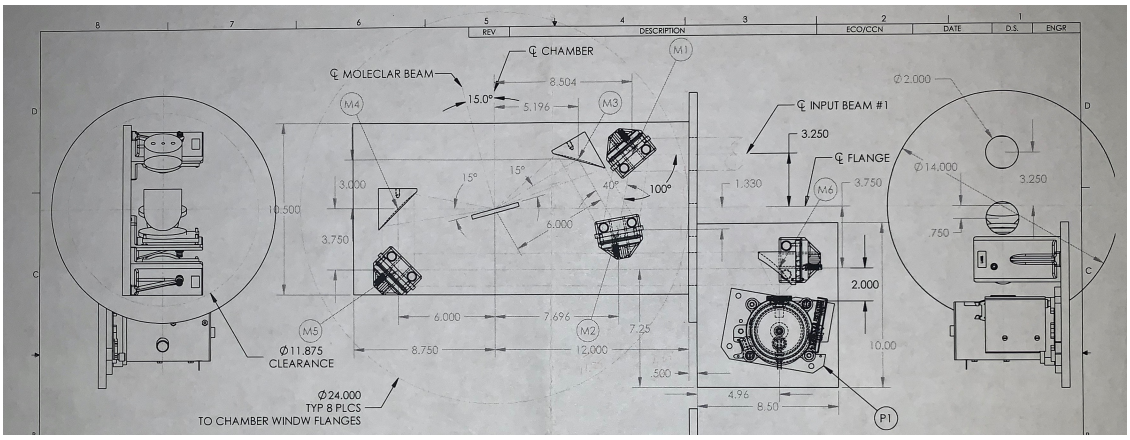

Figure 2.3: **RAIRS optical setup**. After exiting the spectrometer, the IR light is polarized and enters the chamber, glancing off the crystal at an angle of 75°. Signal is collected in an external MCT/A detector.

imental geometry, substrate, and relative surface coverage.

The external RAIRS optical setup in our lab is depicted in **Figure 2.3**. Infrared light from a commercial FTIR spectrometer (Nicolet 6700, Thermo Fisher) passes through a 25 mm ZnSe polarizer (Thermo Fisher) and then into the UHV chamber, in which the optical components are permanently affixed to a metal plate. The beam is focused onto the crystal at angle of 75° via a gold-coated parabolic mirror (Thermo Fisher). After exiting the chamber, the signal is collected in a liquid nitrogen cooled mercury cadmium telluride detector (MCT/A, Thermo Fisher), which affords large signal intensity over the 4000 - 650 cm^{-1} spectral range. For the work described in this thesis, we collect RAIR spectra with a resolution of 4 cm^{-1} that are averaged over 100 - 500 scans.

2.2.2 X-Ray Photoelectron Spectroscopy

In **Chapters 3** and **4**, we use XPS to qualitatively assess the chemical composition of the thin films studied. XPS is a versatile, surface-sensitive technique based on the photoelectric effect; a beam of X-ray photons with a known energy is directed at the surface and core electrons are ejected into vacuum from species present in first 10-20 angstroms of the sample. Because energy must be conserved, the measured kinetic energy (KE_{elec}) of the ejected electrons can be used to directly

calculate their characteristic binding energies (E_B).[5,6] We easily account for the shift in binding energies caused by the unknown work function of the spectrometer (Φ_{spec}) by normalizing all spectra to the assignment of the $4f_{5/2}$ and $4f_{7/2}$ photoemission peaks of gold at 87.63 and 83.95 eV, respectively:[7]

$$KE_{elec} = h\nu - E_B - \Phi_{spec} \tag{2.2}$$

Each element has unique core electron binding energies, so XPS data provides comprehensive elemental analysis of the surface. Chemical bonding and other intermolecular interactions, however, can lead to small perturbations in these binding energies, making XPS a useful technique for probing local chemical environments within thin films.

To perform XPS, we expose the crystal to X-ray photons with an average energy of 1486.6 eV generated by an achromatic Al Kα X-ray source (PHI Model 04-153, Perkin Elmer) positioned 45° from surface normal. The energy of ejected electrons is detected by a double pass cylindrical mirror analyzer (PHI Model 15-255G, Perkin Elmer) approximately 1-2 inches from the crystal surface. We note that X-ray induced damage is commonly observed for physisorbed thin films, so all XPS data reported in this thesis were collected on pristine films that were subsequently discarded or reacted films at the very end of an experiment.

2.2.3 King and Wells

The King and Wells technique is a straightforward method for measuring the sticking probability of an incident projectile onto a surface of interest;[8,9] much of the data in **Chapter 6** is collected in this fashion. Historically, this technique has been used to accurately measure coverage-dependant sticking probabilities and provide detailed information about surface-adsorbate interaction potentials, binding sites, etc.[10] In our experiments, however, we are only concerned with the probability for adsorption of the first few molecules incident on the surface (sticking at zero coverage).

To perform a King and Wells experiment, the out-of-line residual gas analyzer (RGA) is used

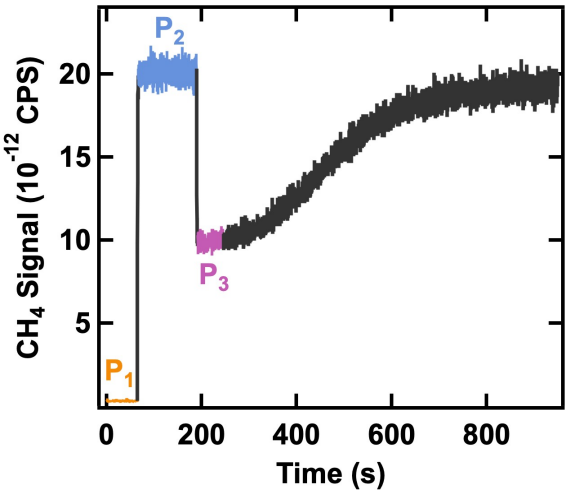

Figure 2.4: **Representative King and Wells data**. CH_4 signal (m/z = 15) monitored with the RGA during a representative King and Wells experiment conducted at a surface temperature of 33.5 K. P_1 (orange) is the background CH_4 signal; P_2 (blue) is the full CH_4 flux with flag blocking the substrate; P_3 (pink) is CH_4 adsorption with flag removed.

to collect signal intensity for the desired mass as a function of time. A representative trial for m/z = 15 (CH_4) is shown in **Figure 2.4**. The experiment begins with monitoring the background signal prior to introducing any CH_4 into the chamber (P_1). Next, the CH_4 beam is introduced into the chamber, but with the rotatable chamber flag in front of the substrate (**Figure 2.1E**), preventing any CH_4 from sticking to the cold sample. This pressure rise is the full indirect CH_4 flux (P_2). Then the flag is rotated out of the way, at which point CH_4 molecules begin sticking to the surface (P_3). The initial sticking probability (S_0) is thus calculated as:

$$S_0 = \frac{P_2 - P_3}{P_2 - P_1} \tag{2.3}$$

Over time, the CH_4 signal rises back up to the blocked value as the available surface sites become filled and no more molecules can adsorb onto the surface. More specific details about this type of measurement in the CH_4/ice system will be discussed in **Chapter 6**.

2.3 Supersonic Molecular Beam

The UHV chamber is connected via a manually operated gate valve to a triply-differentially pumped supersonic molecular beamline. Supersonic molecular beams have been widely used in both gas and condensed phase research to generate collimated, collision-free sources of atoms or molecules with well-defined kinetic energies.[11] Building on earlier beam sources that relied on simple effusion of a high-pressure gas from a small aperture into a region of modest vacuum (the "oven" beam), the supersonic beam construction offer significantly more intense beams with narrower velocity distributions.[12]

Our beamline consists of three chambers, depicted in **Figure 2.5**. First, the beam expands into the vacuum region of the source chamber and passes through the 0.5 mm aperture of a conical skimmer (Gentry) located 7 mm from the beam nozzle exit aperture. With no gas flow, the source chamber has a base pressure of 5×10^{-7} Torr; the vacuum is maintained by an 8000 L s^{-1} diffusion pump (VHS-400, Varian) backed by a 19 L s^{-1} single-stage rotary vane pump (Duo 65 MC, Pfeiffer Vacuum) coupled to a 175 L s^{-1} Roots blower (WKP 500AM, Pfeiffer Vacuum). Next, the skimmer selects for the centerline of the beam, and the gas passes through the first and second differential chambers (1DC and 2DC). The baseline pressures in these chambers are 5×10^{-8} and 5×10^{-9} Torr, respectively. The vacuum is maintained by a 1200 L s^{-1} diffusion pump in the 1DC (VHS-4, Varian) and a 200 L s^{-1} turbomolecular pump (TPU-240, Pfeiffer Vacuum) in the 2DC; the chambers are backed together by a 7 L s^{-1} dual stage rotary vane pump (Duo 20 M, Pfeiffer Vacuum). Finally, the beam passes through a 2.3 mm aperture into the main chamber. This beamline geometry results in a beam spot on the crystal of approximately 2 mm.

2.3.1 Time-of-Flight Analysis

Prior to beginning any experiment involving beam exposure, we characterize the velocity distributions of the pertinent gas species in the expansion using standard time-of-flight (TOF) techniques. The beam can be modulated in a number of patterns by a variable-speed, mechanical chopping

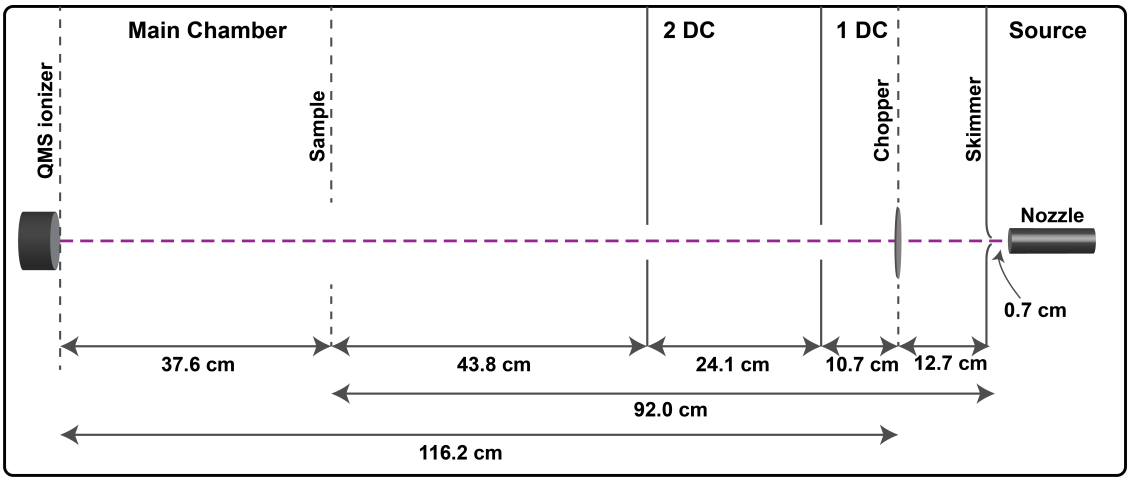

Figure 2.5: **Schematic layout of molecular beamline**. Immediately upon exiting the nozzle, the gaseous expansion passes through a skimmer, two differentially pumped chambers, and into the main UHV chamber. The chopper in the 1DC modulates the beam for time-of-flight analysis.

wheel located in the 1DC (**Figure 2.1B**). In order to rotate the chopper at the desired speed (100 Hz), we use an RC circuit to split the output from a frequency signal generator (651A Test Oscillator, Hewlett-Packard). The two 90° out-of-phase signals are next amplified by a stereo receiver (XGA-3000, Gemini) and delivered to the hysteresis-synchronous motor that drives the chopper. The chopper, in turn, is mounted on a linear motion vacuum feedthrough, allowing us to remove it completely from the line of the beam during experimentation or align one of the three patterns for beam modulation. In this thesis, we use two patterns: the 50% duty-cycle square waveform and the 1% duty-cycle single shot waveform. The latter is used throughout **Chapters 3, 4, 6, 7, and 8** to collect TOF spectra and establish beam velocity and energy distributions.

When the chopper is positioned for 1% duty-cycle modulation, it breaks the beam into packets that are detected 116.2 cm downstream in the QMS detector at the back of the UHV chamber (**Figure 2.1J**). Following initial detection at the QMS, the signal passes through a 90° off-axis secondary electron multiplier (SEM; QMA 120), a pre-amplification stage (VT120, Ortec), and subsequent amplification (Model 771, Phillips Scientific) and discrimination stages (Model 123, LRS), before being counted with a multi-channel analyzer (MCS-PLUS-OPT2, Ortec) in a computer. The timed start of signal counting is triggered when light from an infrared LED passing through the same chopper slit as the beam is detected with a simple photodiode (United Detector

Technologies). There are 4 thin slits on the wheel, which is rotating at 100 Hz, resulting in 0.0025 s separation between packets approaching the detector.

Shown in **Figure 2.6**, the mass spectra (MS) as collected is raw signal intensity as a function of time (from triggering to detection). The first step in converting this to a velocity distribution is to change the time data on the *x*-axis to velocity by dividing the beam flight path distance (*L*, 116.2 cm) by the time. The raw signal must also be converted to counts per second (CPS) using the known values input into the MCA for counting bin size. Next, the signal must be converted from the time to velocity domain using the Jacobian from a standard change of variables (time, *t* to velocity, *v*):

$$n(t)\mathrm{d}t = n\left(\frac{L}{v}\right)\left(-\frac{L}{v^2}\right)\mathrm{d}v \tag{2.4}$$

$$n(v) \propto \frac{n(t)}{v^2} \tag{2.5}$$

We then divide this value by the velocity a third time to account for the inverse proportionality between detector ionization efficiency and velocity. In other words, the detector measures the particle number density (not flux), so the signal intensity varies with incident velocity:

$$n(v) \propto \frac{n(t)}{v^2} = \frac{\left[n_{den}(t)/v^2\right]}{v} = \left[n_{den}(t)/v^3\right] \tag{2.6}$$

After this processing, the data are fit to the theoretical velocity distribution for a supersonic molecular beam (**Equation 2.7**).[12] We note that this analysis does not include deconvolution for the finite width of the chopper slit. In this thesis the width of the slit is negligibly small compared to the measured beam distribution widths, so this is an appropriate omission.

$$n(v) \propto v^3 exp\left[-\frac{(v-v_0)^2}{\alpha^2}\right] \tag{2.7}$$

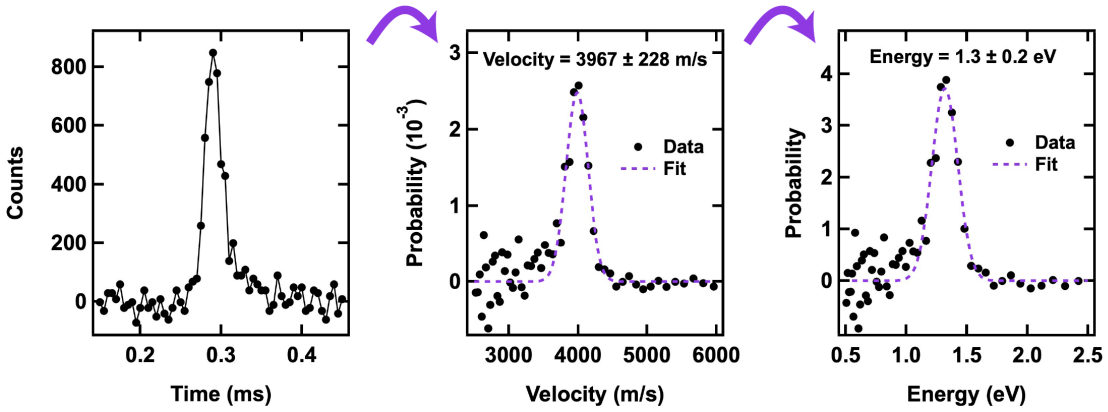

Figure 2.6: **Representative TOF-MS**. Raw signal intensity is converted to the velocity domain, plotted as a function of beam velocity and energy, and fit to the appropriate theoretical probability distribution (see text). This particular distribution (CH_4 seeded in H_2 at 400 K) has an average energy of 1.3 eV and a width of 12%.

2.3.2 Beam Flux Analysis

In addition to beam velocity, we often need to know the absolute flux of gaseous species in the beam to accurately track kinetic processes on the surface during exposure. We cannot, however, establish flux of a seeded (multi-component) beam without prior calibration to a species of interest. We begin this calibration process by measuring the pressure rise in the chamber with a nude Bayard-Albert ion gauge calibrated to N_2 upon introduction of a neat (single-component) beam. Once the pressure has reached a steady value, we assume that molecular flow into and out of the chamber (via pumping) are equivalent. The gas flow rate (Q, throughput) is defined as:[13]

$$Q = \frac{\mathrm{d}(PV)}{\mathrm{d}t} \tag{2.8}$$

At constant pressures, the flow rate can be further simplified and rearranged using ideal gas law relationships. Additionally, the volumetric flow rate ($\frac{\mathrm{d}V}{\mathrm{d}t}$) is synonymous with pumping speed (S), a known value for any commercial pump.

$$Q = P\frac{\mathrm{d}V}{\mathrm{d}t} = \frac{\mathrm{d}N}{\mathrm{d}t}\frac{1}{kT} = P \cdot S \tag{2.9}$$

If we recognize that flux into the chamber (Φ, units of molecules cm^{-2} s^{-1}) is simply the change in number of molecules per unit time per unit area ($\frac{dN}{dt}\frac{1}{A}$), **Equation 2.9** can be rewritten finally as:

$$\Phi = \frac{P \cdot S}{kT \cdot A} \tag{2.10}$$

P is the change in pressure on introduction of the beam and A is the beam spot size on our substrate. **Equation 2.10**, however, still requires two additional corrections to get a quantitative value for Φ. First, P must account for the variable sensitivity of the ion gauge (using the ratio of the ionization cross sections for N_2 and the gas of interest). Second, S must be changed to an "effective pumping speed" that accounts for the conductance (C) of the chamber geometry leading to the pump inlet:

$$\frac{1}{EPS} = \frac{1}{C} + \frac{1}{S} \tag{2.11}$$

Our chamber is connected to the turbomolecular pump via one cylindrical tube, so C (assuming molecular flow conditions) is:[14,15]

$$C\ (\mathrm{L\ s^{-1}}) = 3.81 \left(\frac{T}{m}\right)^{1/2} \left(\frac{D^3}{L}\right)^{1/2} \tag{2.12}$$

In **Equation 2.12**, m is the molar mass of the species of interest, and D and L are the diameter and length of the cylindrical tube, both in cm. Once we establish these values, we calculate the flux using **Equation 2.10** for a range of beam pressures and relate them linearly to either RGA-measured pressure values at the component's parent mass or the integrated area of a TOF curve. An example of this calibration is shown in **Figure 2.7** for a beam of CO_2.

2.3.3 Radio Frequency (RF) Plasma Beam Source

We use two beam sources for the experiments described in this thesis. The first, used in **Chapters 3, 4** and **8**, generates beams of ground state atomic oxygen, $O(^3P)$, which is an effective basic

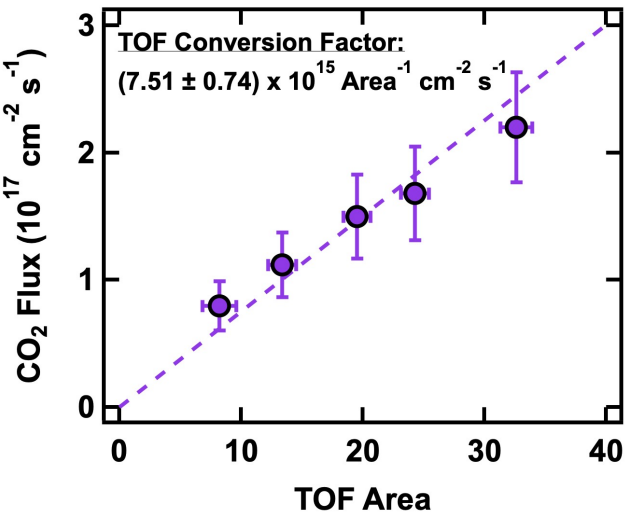

Figure 2.7: **Representative beam flux calibration for a neat CO_2 beam**. The calculated beam flux (see text) is plotted against an experimentally measured quantity like TOF peak area for a particular beam gas. We use this linear relationship to calculate flux for experiments using seeded beams where flux cannot be calculated directly from the pressure rise in the chamber.

oxidant for films of interest. To generate an intense flux of this atomic species, a gas mixture of 5% O_2 in Ne travels through a custom, water-cooled, quartz nozzle.[16] Just before supersonic expansion into the first vacuum chamber, the gas is exposed to an intense radio frequency discharge, which ignites a plasma and leads to O_2 dissociation. We promptly remove other ionic species (O_2^+, O^+, Ne^+) from the beam using a set of 2000 V cm^{-1} deflecting plates located in the 1DC. We select against the production of other possible neutral species in the expansion ($O(^1D_2)$) by using relatively low RF powers and stagnation pressures (100-120 W and $<$100 Torr).[17,18] If small quantities of these species are present, however, they are likely quenched in the beam via collisions with molecular oxygen or Ne. For each experiment, we perform a blank trial using a neat Ne beam; we observe no reactivity, indicating that the only other potential reactive beam component, metastable Ne, is not present. Therefore, the beams used in this thesis contain only O_2, Ne, and the desired reactive $O(^3P)$.

In operation, this beam source can produce discharges containing 30-60% O_2 dissociation. We quantify the extent of dissociation by monitoring the relative QMS signal intensities (square-wave modulation) of O_2 (m/z = 32) and atomic oxygen (m/z = 16) in the beam with the plasma on

and off. This is to account for the fact that signal at m/z = 16 exists even in the absence of the discharge, due to contributions from the dissociative detachment of O_2 in the QMS ionizer. The relative intensities with the plasma off can therefore be represented as:

$$\eta_L = \frac{I_{16}}{I_{32}} = \frac{CQ_{16}[N_{O_2}\sigma_D]}{CQ_{32}[N_{O_2}\sigma_{O_2}]} \tag{2.13}$$

In the equation above, N_{O_2} and N_O are the number densities of O_2 and O, respectively. Q_{O_2} and Q_O are the quadrupole transmission coefficients at those masses, and C is an unknown empirical constant related to our instrument. The two cross-sections refer to the ionization of O_2 (σ_{O_2}, 1.52 $Å^2$) and the dissociative detachment of O_2 (σ_D, 0.88 $Å^2$):[16]

$$O_2 + e^- \xrightarrow{\sigma_D} O^+ + O + 2e^- \tag{2.14}$$

$$O_2 + e^- \xrightarrow{\sigma_{O_2}} O_2^+ + 2e^- \tag{2.15}$$

With the plasma on, atomic oxygen becomes a second source of signal intensity at m/z = 16. A similar equation can then be written for the relative intensities with the plasma on:

$$\eta_H = \frac{I_{16}}{I_{32}} = \frac{CQ_{16}[N_{O_2}\sigma_D] + CQ_{16}[N_O\sigma_O]}{CQ_{32}[N_{O_2}\sigma_{O_2}]} \tag{2.16}$$

A third cross-section is introduced, corresponding to the ionization of O (σ_O, 1.15 $Å^2$):

$$O + e^- \xrightarrow{\sigma_O} O^+ + 2e^- \tag{2.17}$$

Ultimately, our desired quantity is the relative number density between O and O_2; we'll refer to this quantity as R. We solve for this value by dividing **Equation 2.16** by **Equation 2.13** and rearranging:

$$R = \frac{N_{16}}{N_{32}} = \left(\frac{\eta_H}{\eta_L} - 1\right)\left(\frac{\sigma_D}{\sigma_O}\right) \tag{2.18}$$

The percent dissociation is then simply $\frac{R}{R+1}$, and we can use this relationship to convert the measured O_2 flux (following the procedure outlined in **Subsection 2.3.2**) to O(^{3}P) flux.

It is worth noting that this process of calculating a number density ratio between beam species is quite generalizable. We follow the same analysis, albeit with different ionization reactions and cross-sections, in **Chapter 7** to quantify the relative amounts of CO and CO_2 in the beam.

2.3.4 Stainless Steel Beam Source

The second source is a more conventional supersonic source, and we use it in **Chapters 6** and **7** to make intense, high-energy beams of small molecules. The beam nozzle is machined from a $\frac{1}{4}$" VCR gland and the size of the aperture exit from this gland is controlled with Mo or Pt pinholes ranging from 15 - 30 μm (3.04 mm O.D. electron microscope apertures, Ted Pella). To heat the beam, we wrap a tight coil of resistively-heated wire (1 Nc I 10, Thermocoax) around the length of the nozzle. We secure the coil with a sheet of tantalum and copper ties, ensuring even, efficient heating. We monitor and control temperature beam temperature via a Type-K thermocouple spot-welded approximately 0.5 - 1 mm from the aperture. The output of this thermocouple is fed into a feedback loop with a temperature controller (CN76000, Omega) and DC power supply. With this configuration we are routinely able to reach beam temperatures of 1000 - 1100 K.

2.4 Surface Preparation and Temperature Control

For the majority of the work described in this thesis, the substrate is a relatively passive participant in the observed chemistry. When preparing for an experiment, our primary concern is ensuring that the crystal is clean, free of impurities, and that its temperature is easily and evenly controlled. As discussed in **Section 2.1**, all experiments are performed on a single-crystal Au(111) substrate. This surface is not chosen for any particular reactivity. Rather, it is an excellent reflective substrate for RAIRS as well as being oxidation resistant and relatively unreactive under the temperature and atmospheric conditions used. The primary role of the surface, therefore, is as a substrate on which

to deposit multilayer thin films of interest like nerve agent simulants (**Chapters 3** and **4**), water (**Chapter 6**), and propene (**Chapter 8**).

2.4.1 He-Cooled Sample Manipulator

After the conclusion of the work in **Chapter 3**, we replaced our liquid N_2-cooled copper sample manipulator with a custom-designed manipulator and commercial recirculating liquid helium cryostat (204P, Advanced Research Systems). This greatly expanded our cooling capacity; in practice the sample can reach temperatures as low as 19 K, and as high as 800 K (sufficient for sputter/anneal cycles described in **Subsection 2.4.2**). The basic construction of the manipulator is an OFHC copper extension terminating with an OFHC copper sample holder with a sapphire plate for optional electrical isolation. A small cartridge heater sits immediately above the sample, allowing for high-temperature capabilities even while the cryostat is fully cooled. The whole manipulator (excluding a small facet cut out to allow clearance for IR radiation and other surface-sensitive techniques) is also encased in a nickel-plated radiation shield to increase cooling capacity down the length of the manipulator.

Outside of UHV, the cryostat assembly is connected to the chamber via differentially-pumped rotary seal (RNN-400, Thermionics Vacuum Products) to allow for polar rotation of the sample. The cryostat itself is also mounted above a low-vibration interface, which reduces movement at the sample caused by the circulating cryostat (DMX-20B, Advanced Research Systems). When the manipulator system was first installed, we performed a temperature calibration for the permanent sample thermocouple sensor using temperature readouts from a nearby Si diode during cool down. After this calibration we removed the diode from the sample to allow for high temperature experiments. We now monitor temperature in three locations: at the sample (Type-E thermocouple), at the cartridge heater (Pt RTD), and at the second stage of cooling (Si diode). More detail of the configuration, including sites for temperature monitoring, is included in in **Figure 2.8**.

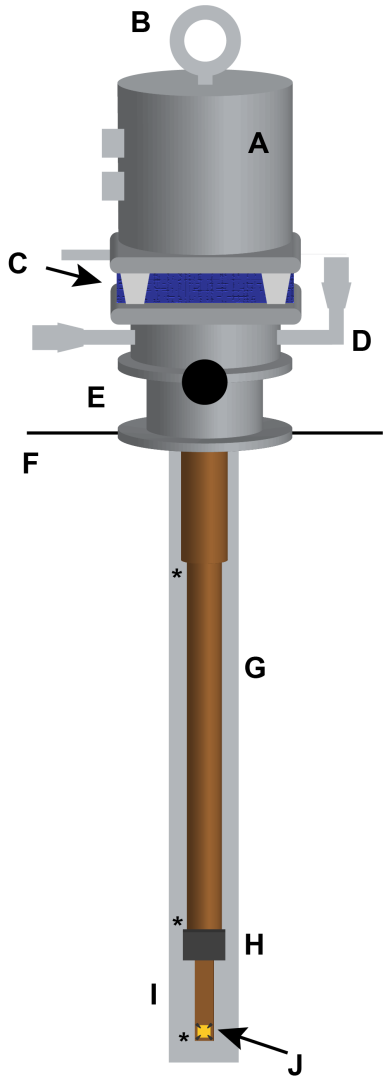

Figure 2.8: **Schematic layout of sample manipulator and cryostat assembly**. Our custom, He-cooled sample manipulator allows for precise temperature control from 19 - 800 K.

A - Cryostat
B - Eyebolt for manipulator removal
C - Vibrational isolation collar
D - Feedthroughs for T sensing and control
E - Extension and polar rotation
F - Entrance to UHV chamber
G - Radiation shield
H - 800 K interface (cartridge heater)
I - Sample holder
J - Au(111) sample (held with BeCu clips)
* - Temperature sensor connections

2.4.2 Surface Preparation

Following the oxidation reactions described in **Chapters 3, 4** and **8**, we routinely clean the Au(111) crystal through a concurrent sputter and anneal cycle to remove any residual impurities and restore the unique $22 \times \sqrt{3}$ herringbone reconstruction.[19] A typical cleaning cycle includes raising the sample temperature to 800 K and bombarding the sample with 1.6 keV Ar^+ ions for 15 minutes.[20] We generate the Ar^+ ions by backfilling the chamber with Ar to a pressure of approximately 5.5×10^{-5} Torr) and directing an ion source (20-045 and 04-161, Perkin Elmer) at the crystal. We then check crystal cleanliness by confirming the absence of carbon or oxygen in high-resolution XPS spectra.

2.4.3 Thin Film Deposition and Characterization

There are multiple ways to deposit a thin film on the Au(111) substrate, each with particular advantages and disadvantages. In **Chapters 4** and **8**, the film of interest is dosed on the crystal via molecular beam. This is the most precise dosing method, because as long as the surface is cold enough (making the sticking coefficient of the gas = 1), the dosed gas will only reside on the crystal. This streamlines kinetic analysis and allows for more robust temperature-programmed desorption experiments. The challenge with beam dosing, however, is that it can be remarkably slow, particularly when using small beam pinhole sizes and low volatility gases. In **Chapter 6**, we needed thick (>200 ML) water ice films in a matter of minutes. To accomplish this, we compromised our chamber cleanliness and switched to dosing via a directed doser, located in the UHV chamber approximately 4 cm from the crystal surface. This process gave us thick, even films in minutes, but had the negative effect of adding more water to chamber, increasing the wait time before beginning experiments and our need to bake the chamber periodically.

We rely on the final dosing method most infrequently because it leaks a tremendous amount of gas into the chamber and can contribute significantly to contamination and higher base pressures. Located in the back of the chamber (behind the crystal), the leak valve used for backfilling Ar

in sputtering cycles (**Subsection 2.4.2**) can easily be repurposed to backfill the chamber with a molecule of interest. We used this method to dose one of the porous ices in **Chapter 6** because it is essential for achieving the desired morphology. More importantly, however, this method is essential for quantifying the deposition rate for molecules that cannot be dosed via the beam. To use RAIR signal intensity as a measure for film thickness, we first calibrate the signal to a controlled dose at a known flux. For example, we know that a monolayer of water is 1.06×10^{15} molecules.[21] Therefore, if we cool the crystal to a temperature at which water sticks and backfill the chamber to a constant background water pressure of 1×10^{-7} Torr, we know that our growth rate is roughly 0.1 layers of water per second.[22–24] We can easily compare this with growth of signal intensity in the RAIR spectra, allowing for easy quantification of future film thicknesses.

Chapter 3

Oxidation, Destruction, and Persistence of Multilayer Dimethyl Methylphosphonate Films during Exposure to O(^{3}P) Atomic Oxygen

We present work detailing the oxidative reactivity of the nerve agent simulant dimethyl methylphosphonate (DMMP) with atomic oxygen using time-resolved *in situ* reflection-absorption infrared spectroscopy (RAIRS) and X-ray photoelectron spectroscopy (XPS). When exposed to a supersonic beam containing O(^{3}P) with average translational energy of 0.12 eV, thermally-annealed DMMP films (less than 50 layers) on single-crystal Au(111) are observed to react *via* hydrogen abstraction, followed by various secondary reactions with resultant hydroxyl and DMMP-derived radicals. This reaction is accompanied by the appearance of hydrogen bonding interactions with the DMMP phosphoryl (P=O) groups on the film surface, and it is also observed to result in both a loss of carbon and an uptake of oxygen by the film. These trends, when considered with the additional thermal stability of reaction products left on the surface, suggest that the mechanism entails reaction with DMMP methyl groups and the formation of various oligomeric and polymeric species; the presence of these products hinders continuous, effective destruction for films thicker than roughly ten layers. This work has specific implications for the implementation of plasma-based and oxidative decontamination methods based upon an improved fundamental understanding of the chemistry of this important class of phosphoryl containing molecules.

3.1 Introduction

The 1993 Chemical Weapons Convention prohibits the creation and stockpiling of chemical weapons, yet these dangerous compounds remain a critical social and environmental threat.[25] Whether decontaminating attack sites or destroying unused chemical weapon stores, there is a great risk to both civilians and military personnel if these agents' surface interactions are not properly understood; any new destruction strategy must, in addition to removing the toxic agent, account for volatile byproducts, secondary contamination, and waste disposal.[26] As such, it is critical to have a comprehensive grasp of the agents' destruction pathways and mechanisms, persistence, and potential redispersal on a myriad of representative environmental and industrial materials.

The surface interactions of nerve agents and their simulants have been investigated thoroughly on a number of surfaces to date, including metals,[27–31] metal oxides,[28,32–43] nanoparticle assemblies,[44–46] and other thin films;[47–50] complementary theoretical analyses have also been published for many of these systems.[51–58] Notably, many of these materials (particularly metal oxides) have demonstrated significant catalytic activity in the decomposition of surface adsorbed dimethyl methylphosphonate (DMMP), a common nerve agent simulant. While effective, active site poisoning often limits the practicality of these methods on a large scale. Furthermore, these oxide materials are often difficult to reactivate once poisoned.[37,38] To overcome these limitations and establish continuous decomposition activity, Mitchell *et. al.* have explored the reaction of DMMP and ozone on alumina-supported iron oxide and manganese oxide. Measurements of the resultant CO and CO_2 production revealed higher catalytic activity in the presence of ozone, due to the formation of reactive atomic oxygen species resulting from ozone's decomposition on the oxide surface.[59,60]

Additional nerve agent decontamination strategies involve exposure to atmospheric pressure plasma sources.[61–65] While many current decontamination methods rely on complete incineration at high temperatures[66–68] or corrosive wet chemicals (i.e., bleach), use of these plasmas provides a nondestructive, environmentally safe alternative that precludes mass storage and long exposure

times.[26,65] Like the aforementioned continuous decomposition studies, the effectiveness of this method is also linked to the presence of both ozone and atomic oxygen in the plasmas.[63] In addition to clarifying the basic mechanisms underlying some of these destruction techniques, the results of this study may also shed light on the known flame-retarding properties of organophosphate compounds.[69,70]

Informed by recent theoretical work on gas-phase reactivity between DMMP and O(^{3}P),[71,72] we present a detailed picture of the oxidative destruction of solid multilayer DMMP films and elucidate the mechanistic role of atomic oxygen in its destruction. Using RAIRS and XPS, we demonstrate that DMMP reacts upon exposure to O(^{3}P) under UHV conditions, and that the reaction likely generates additional reactive species on the surface. Furthermore, we present clear evidence that overall reactivity decays upon continued exposure, and results in formation of additional byproducts possessing greater thermal stability on the surface than the original DMMP. Reactive oxygen species have been shown to be important in the destruction of nerve agents and their simulants in applications ranging from preventative surface treatments to post-contamination remediation. The findings contained herein have direct implications for understanding the fate of dispersed agents subject to naturally occurring oxygen species and better inform development of safe and effective decontamination techniques.[73,74]

3.2 Experimental Section

We performed all of the experiments described in this chapter in the molecular beam scattering instrument described in **Chapter 2**. Our primary analytical techniques were time-resolved RAIRS and XPS.

For each trial, we deposited DMMP on the Au(111) substrate *via* directed doser (**Subsection 2.4.3**). RAIR spectra, fit to Gaussian peaks on cubic baselines, were used to characterize the surface and extent of reactivity. We collected spectra averaged over 300 scans at 4 cm^{-1} resolution, using sputtered/annealed Au(111) as the background reference signal. A representative spectrum of a DMMP film is shown in **Figure 3.1**. The intense P-O-C and P=O modes, highlighted in the

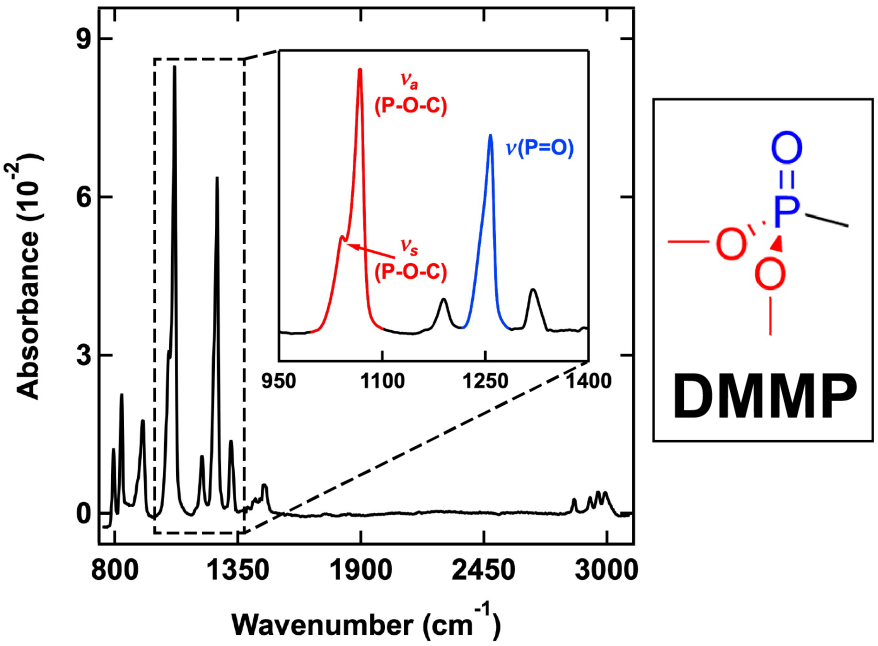

Figure 3.1: **Representative RAIR spectrum of DMMP film**. RAIR spectrum of forty-layer thick DMMP film on single-crystal Au(111). Notable signals discussed throughout text include the P-O-C (red, 1041 and 1066 cm^{-1}) and P=O (blue, 1240-1260 cm^{-1}) stretching modes; these are highlighted in the DMMP molecule and spectrum inset.

figure's inset, are most frequently referenced herein, with observed peak positions and assignments informed by and consistent with the literature.[30,34,35,40,50] For all experiments involving reaction of DMMP with $O(^3P)$, the surface temperature was held at 155 K during dosing, where DMMP desorption is negligible. After dosing, we annealed films at 175 K until they reached the desired thickness.

A series of isothermal desorption experiments allowed us to quantify initial DMMP film thickness *via* RAIRS (**Figure 3.2**). We subjected DMMP films to desorption at surface temperatures ranging from 163-165 K, and tracked the integrated areas of the P-O-C stretching modes as a function of time. Total integrated peak intensity decays linearly at two different rates, corresponding to a difference in multilayer and monolayer desorption rates, respectively.[75] As displayed in each panel of **Figure 3.2**, the spectroscopic signature of the monolayer is determined from the point at which the rate abruptly changes. Using this experimental setup, one layer of DMMP corresponds to a total integrated P-O-C peak intensity of 0.05 absorbance units cm^{-1}. We quantified

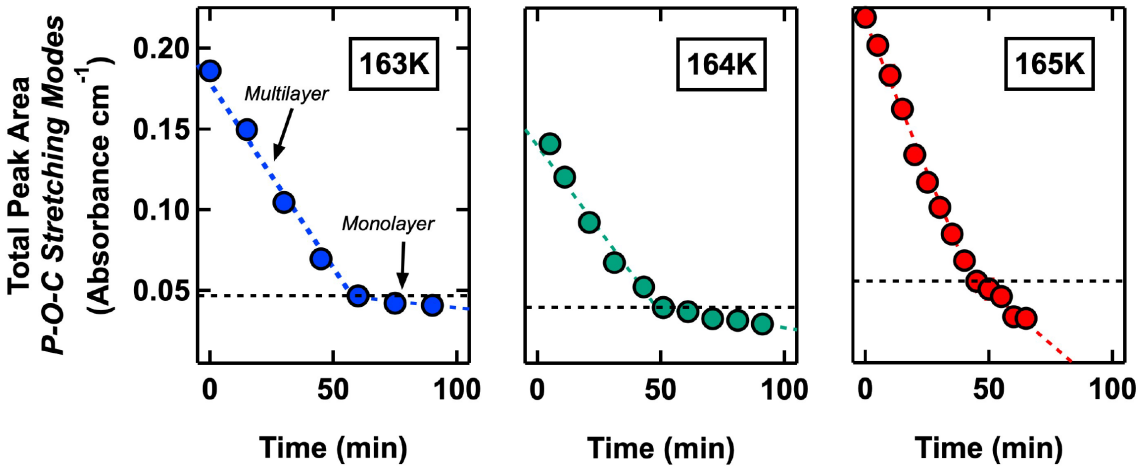

Figure 3.2: **Isothermal desorption of multilayer DMMP**. Isothermal desorption of DMMP films allows for quantification of initial film thicknesses *via* integrated P-O-C signal intensity. The transition from multilayer to monolayer desorption exhibits a marked decrease in desorption rate; the value where this occurs correlates with the infrared intensity of a single layer of DMMP.

initial film thicknesses (reaching 50 layers) with this procedure, observing that peak line shapes remained consistent with continued DMMP exposure.

Following deposition of a film of known thickness, we exposed DMMP films to O(^{3}P) atomic oxygen using the source described in **Subsection 2.3.3**. We similarly determined the O(^{3}P) translational energy and flux following the procedures described in **Subsections 2.3.1** and **2.3.2**. Typical values for the beam impinging at normal incidence were, respectively, 0.12 eV and 5×10^{16} atoms cm^{-2} s^{-1}. Beam energy widths were approximately 0.06 eV.

Our analysis of DMMP reactivity also included collecting XPS spectra of the C(1s), O(1s), and Au(4f) regions. The full XPS system is described in **Subsection 2.2.2**; for these experiments we operated the X-ray source at 10 kV and 20 mA and collected the spectra using 50 eV pass energy and a 0.4 eV step size. We fit the spectral peaks in the same manner as that used in RAIRS analyses.

3.3 Results and Discussion

3.3.1 Spectral Assignment and Film Reactivity

We observe a number of clear spectral changes upon exposing DMMP films to O(^{3}P). **Figure 3.3** depicts, chronologically, changes in the methoxy group signals (1041 and 1066 cm^{-1}) of the film as a function of total O(^{3}P) exposure. While the peak locations, consistent with reported values for the symmetric and antisymmetric P-O-C stretches,[35,47,48] remain unchanged, both peaks are observed to decrease in intensity in **Figure 3.3a**. Given the multilayer character of the films studied, this behavior cannot be attributed to a change in average orientation of these groups, and is instead ascribed to reactive destruction. In contrast, the total integrated intensity of the P=O stretching mode of a given film (≈1200-1270 cm^{-1}) does not exhibit the same behavior. As seen in **Figure 3.3b**, total P=O intensity is left unchanged by extended O(^{3}P) exposure.

To further unpack this behavior, **Figure 3.4a** highlights the individual peaks that comprise the P=O stretching region. P=O peak positions are highly sensitive to coordination environment, whether *via* hydrogen bonding or direct physisorption to surface (Lewis acid) sites.[30,38,43,47,76] While the overall intensity in this region is unchanged during exposure, there are a number of significant changes in the peak shape. Prior to O(^{3}P) exposure, the P=O stretch can be deconvoluted into separate signals at 1249 and 1258 cm^{-1}. These peak locations are consistent with recorded values for DMMP adsorbed on unreactive, nonhydroxylated surfaces.[47–49] Exposure to O(^{3}P) causes the intensity of the 1258 cm^{-1} peak to decrease, replaced by a new signal at 1214 cm^{-1}, highlighted in **Figure 3.4b**. This shift is consistent with DMMP coordination with hydroxylyated metal oxides or other hydroxyl-terminated surfaces, in which the P=O stretch is weakened and red-shifted by the formation of one or two hydrogen bonds.[35,37,47] Further corroborating this assignment is a separate control experiment we performed in which a DMMP monolayer was deposited on a 50- to 60-layer thick amorphous solid water film at 125 K. Detailed in **Figure 3.5**, a comparison of the P=O signals of one DMMP layer deposited on Au(111) versus water ice shows a red shift identical to that observed upon exposure of a multilayer film to O(^{3}P). Finally, this shift

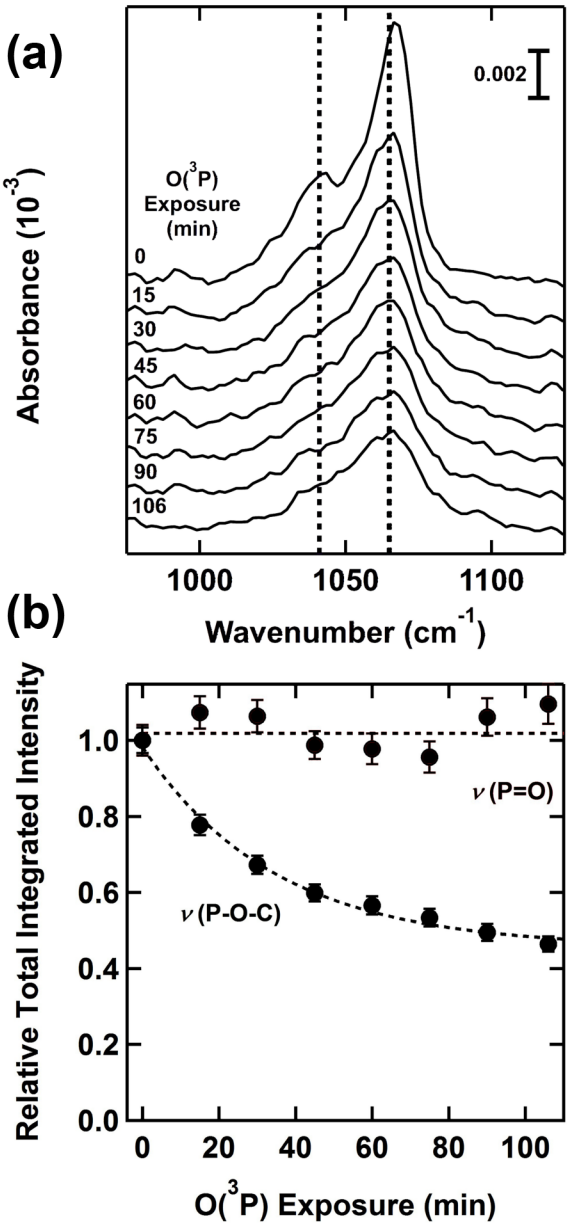

Figure 3.3: **DMMP exposure to O(^{3}P)**. (a) RAIR signal in the P-O-C region of a six-layer thick DMMP film changes during exposure to a molecular beam containing 0.12 eV O(^{3}P) (flux = 2.9 $\times$ 10^{16} cm^{-2} s^{-1}); total intensity decays as a function of O(^{3}P) exposure. (b) Total integrated RAIR peak intensities normalized to their initial values show that, unlike the P-O-C signal intensity, the total P=O intensity is unchanged by O(^{3}P) exposure. Dotted lines are drawn to guide the eye. Error bars, where visible, indicate one standard deviation with respect to the peak fitting.

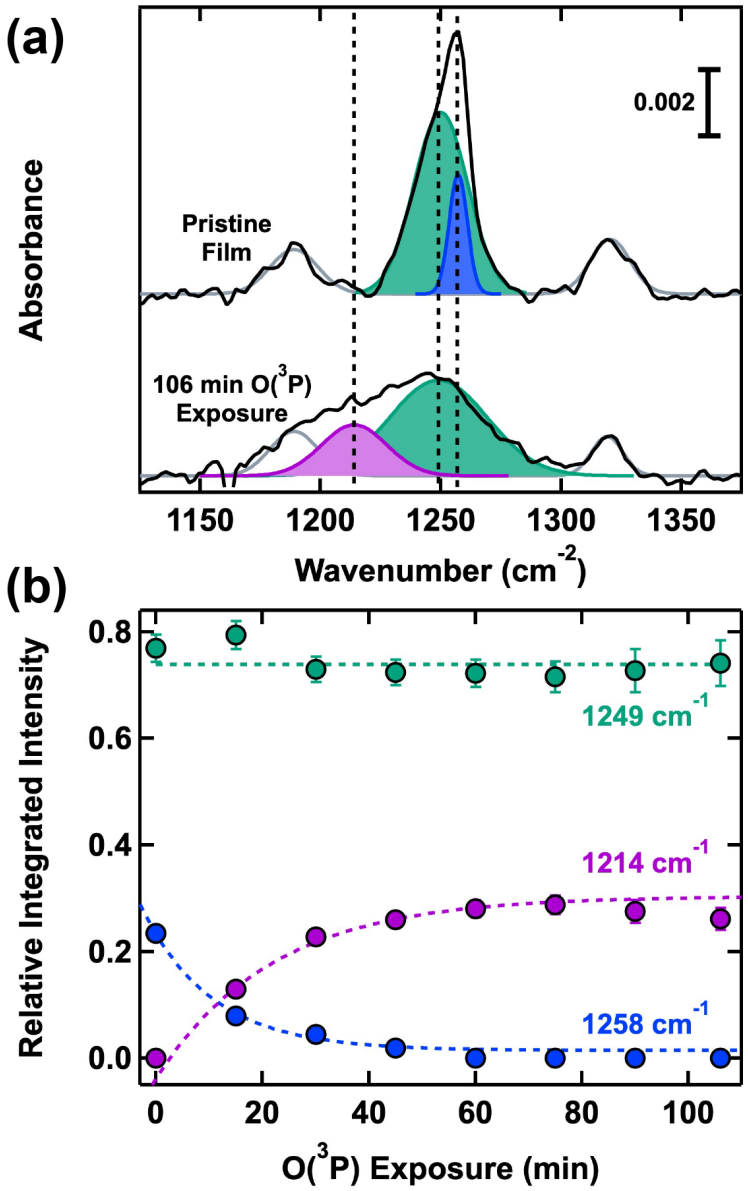

Figure 3.4: **DMMP exposure to O(^{3}P) - P=O region**. (a) We deconvolute P=O signals throughout exposure into contributions from three signals at 1258, 1249, and 1214 cm^{-1}. Individual peaks illustrate the decay of the 1258 cm^{-1} peak (blue) coupled with the emergence of the 1214 cm^{-1} peak (purple) during exposure (O(^{3}P) flux = 2.9 $\times$ 10^{16} cm^{-2} s^{-1}). (b) Corresponding integrated areas of the P=O stretching peaks demonstrate that the 1249 cm^{-1} peak is unaffected by O(^{3}P) exposure, while 1258 and 1214 cm^{-1} peaks exchange intensity. Dotted lines are drawn to guide the eye. Error bars indicate one standard deviation with respect to the peak fitting.

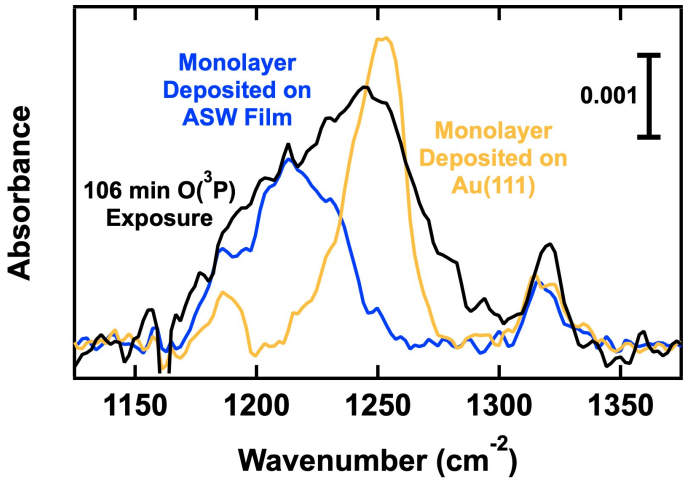

Figure 3.5: **Reacted and pristine DMMP on ice and Au(111)**. Appearance of the 1214 cm^{-1} peak in the spectrum of a six-layer DMMP film exposed to $O(^3P)$ for 106 min (black, 2.9×10^{16} atoms cm^{-2} s^{-1}) is compared to the spectra of a pristine DMMP monolayer deposited on clean Au(111) (gold) and on thick amorphous water ice (blue). This reacted peak's position is consistent with the observed red-shift of the monolayer deposited on water ice, indicative of new hydrogen bonding interactions with the phosphoryl group of DMMP as a result of $O(^3P)$-induced reactivity.

is also consistent with DMMP solvation in the liquid phase.[49,77]

Importantly, $O(^3P)$ exposure only impacts one of the two initial P=O peaks; the 1249 cm^{-1} peak remains essentially unchanged (**Figure 3.4b**) except for some broadening. In order to explain this disparity, it is important to identify the two initial peaks. One possible explanation is conformational; DMMP is reported to have at least two low energy conformers in both the solid and gas phase.[30,56,78–81] Electronic structure calculations predict that the P=O peaks for the two lowest-energy conformers in the gas phase could be as little as 2 cm^{-1} apart.[81] On the other hand, a splitting of 20 cm^{-1} between conformers has been interpreted from FTIR spectra of solid- and liquid-phase DMMP.[79] Our observed splitting of 9 cm^{-1} is within this range, but the lack of agreement complicates definitive assignment. A supplemental explanation may involve the organization of DMMP in the solid film. Other scientists have suggested that spectroscopic signals associated with DMMP aggregates appear between 1240 and 1250 cm^{-1}.[79] A consequence of DMMP aggregates would likely be two general molecular environments. The reactive 1258 cm^{-1} peak could potentially represent molecules at the boundaries of such aggregates, while the 1249 cm^{-1}

peak, mostly unchanging during exposure to O(^{3}P), could correspond to DMMP molecules within the interior of these aggregates. This latter argument is supported by spectroscopically observing DMMP growth, in which the two peak intensities were tracked as DMMP was deposited. The 1258/1249 integrated intensity ratio remains constant from one layer and beyond, eliminating the possibility that the 1258 cm^{-1} peak corresponds simply to DMMP at the vacuum- or substrate-film interfaces.

3.3.2 Product Formation

Partial DMMP film destruction is evinced by the decrease in intensity of the P-O-C stretching modes; this is corroborated by consistent decreases in the C-H stretching mode region below 3000 cm^{-1} upon O(^{3}P) exposure. At the film thicknesses studied, however, the IR intensity for these modes are weak and preclude more detailed spectral analysis. We support the proposed mechanism by citing recent theoretical calculations for collision dynamics between DMMP and O(^{3}P) in the gas phase, the results of which indicate that hydrogen abstraction is the most energetically accessible reaction channel. The calculated upper limit for the gas phase barriers are 0.14 and 0.36 eV for abstraction from the methoxy or methyl groups, respectively.[71,72] These barriers are, however, likely lower in the solid phase due to formation of longer-lived collision complexes in the film. Furthermore, experimental evidence suggests that reactions between O(^{3}P) and organic or hydrocarbon-based films does proceed largely through the abstraction mechanism.[82–84] In the present study, hydrogen abstraction would naturally yield hydroxyl radicals as products:

$$O{=}P(CH_3)(OCH_3)_2 + O(^3P) \longrightarrow O{=}P(CH_3)(OCH_3)(OCH_2)^{\bullet} + {}^{\bullet}OH \tag{3.1}$$

We expect these reactive species will then undergo further reactions within the film. For example:

$$O{=}P(CH_3)(OCH_3)(OCH_2)^{\bullet} \longrightarrow O{=}P(CH_3)(OCH_3)^{\bullet} + OCH_2 \tag{3.2}$$

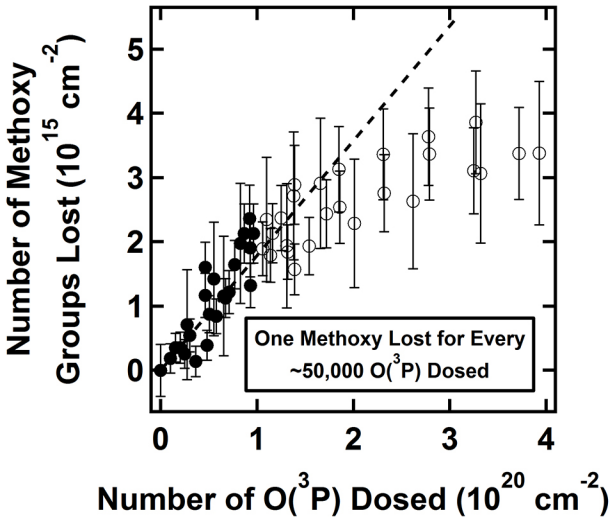

Figure 3.6: **DMMP reaction kinetics - loss of methoxy group on O(^{3}P) exposure**. Aggregated data for all experiments showing methoxy group loss from DMMP as a function of O(^{3}P) exposure. A linear fit to the data early in the exposure (solid circles) shows that one methoxy group reacts for approximately every 50,000 O(^{3}P) dosed onto the surface.

Reaction 3.2, in particular, could help explain the observed methoxy group loss during exposure. **Figure 3.6** contains a plot of all aggregated data collected, arranged to show methoxy group loss as a function of O(^{3}P) exposure. The ordinate axis values estimate that a DMMP monolayer is comprised of 6×10^{14} molecules cm^{-2} *via* its gas phase geometry,[29] and take into account that there are two methoxy groups per DMMP molecule. The observed reactivity does not follow simple first-order, or even half-order kinetics with respect to O(^{3}P) exposure; the observed behavior is likely the product of numerous reactions contributing to the observed spectroscopic changes. We can, however, consider the initial reactivity to get a sense for the initial reaction probability. A linear fit to the data early in the exposure (solid circles in **Figure 3.6**) shows that in the first stages of reaction, a methoxy group is lost for roughly every 50,000 O(^{3}P) dosed onto the surface. If direct reaction occurs, this rather low probability could be a result of low initial sticking probability or only a fraction of the incident O(^{3}P) having sufficient energy to overcome the barrier. Otherwise, after collision and exchange of energy with the film, O(^{3}P) would then have to diffuse both along and through the vacuum-film interface to encounter a methyl group.

Similarly, changes in the P=O region of the spectra during reaction suggest formation of hy-

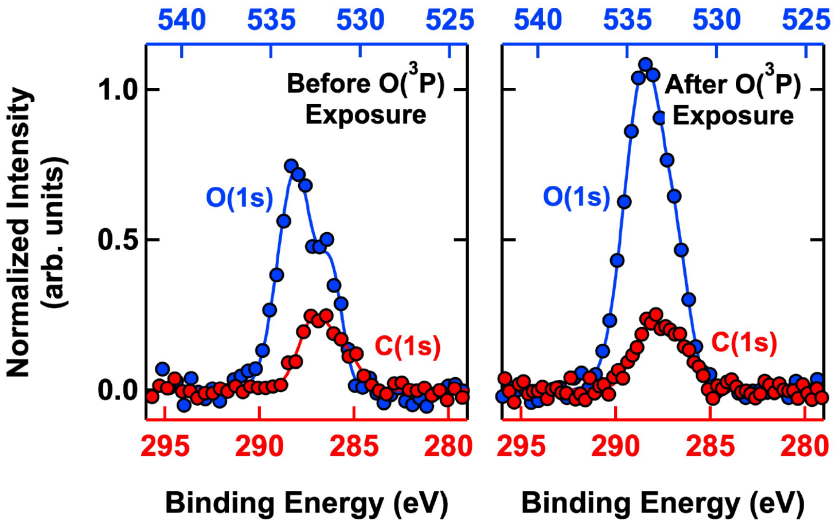

Figure 3.7: **XPS of reacted and pristine DMMP films**. Representative XPS data comparing DMMP films as deposited and after exposure to O(^{3}P) show that the N_O/N_C ratio increases as a result of oxygen uptake by the film. To emphasize this effect, we have scaled the data such that the carbon 1s peak areas are equivalent; this accounts for the fact that some carbon is also lost as gaseous species during reaction.

droxyl species, given that conversion of signal from 1258 cm^{-1} to 1214 cm^{-1} is consistent with "solvation" of phosphoryl oxygens *via* hydrogen bonding.[49,77] It is worth noting that phosphoryl stretching modes of organophosphorus compounds are also influenced by inductive effects from other functional groups attached to the central phosphorus atom.[85] However, all reaction routes considered in the aforementioned theoretical studies—hydrogen abstraction, hydrogen elimination, and methyl elimination—would not result in a redshift of this mode.

XPS data displayed in **Figure 3.7** suggest that in addition to carbon loss, possibly as gaseous CO or CO_2,[60] the reaction results in incorporation of oxygen into the film. Comparison of C(1s) and O(1s) signals between a reacted film and a pristine film, normalized to respective film thicknesses, shows a definitive increase in the relative N_O/N_C ratio at the surface. Reactions with O(^{3}P) and OH radicals would leave radical intermediates that could also react with nondissociated O_2 present in the molecular beam.[86] Thus, there are at least three sources of oxygen resulting from exposure to the beam that are likely contributing to the observed uptake of oxygen in the DMMP film upon beam exposure. These various uptake pathways are further supported by the O(1s) peak shapes before and after O(^{3}P) exposure. On a pristine DMMP film, the O(1s) spectrum is com-

prised of two signals, attributed to the methoxy and phosphoryl oxygens in DMMP. After O(^{3}P) exposure, however, the O(1s) signal is no longer so neatly deconvoluted into distinct oxygen chemical environments.

A slight IR signal increase near 3300 cm^{-1}, indicative of hydroxyl group formation, is observed during exposure to O(^{3}P), but the rate of growth is convoluted with the small amount of background water deposition expected under our conditions (4-8 $\times$ 10^{-11} Torr based on readings from a residual gas analyzer). It is important to note, however, that the observed P=O shift does not take place without exposure to O(^{3}P). DMMP films left in the chamber for periods of time equal to that of an experiment (two hours on average) show no spectroscopic change except for slight growth in the OH region amounting to less than half a layer of water. Moreover, the films remain unchanged when exposed to a pure neon plasma and a mixture of 5% O_2 in helium (no plasma; approximation of O_2 with higher translational energy present in O_2/Ne plasma). We thus conclude that these changes are initiated by reaction of the film with O(^{3}P) and cannot simply be attributed to background water sticking to the vacuum-film interface.

The remaining P-O-C and P=O stretching mode signals of films having an initial thickness fewer than ten layers (e.g. **Figs 3.3 and 3.4**) are clearly broadened with respect to the pristine peaks, indicating disordering. The close spatial proximity of radical intermediates could promote formation of oligomeric or polymeric species on the surface; this has been reported under related circumstances.[62] To test this hypothesis and monitor the thermal stability of the reaction products on the surface *in situ*, we performed isothermal desorption experiments by increasing the surface temperature in a stepwise fashion and collecting RAIR spectra at each temperature. We ramped the surface temperature up from 155 K in 10 K increments at 1 K s^{-1} and held it constant for the duration of an IR scan (roughly three minutes) at each step. We then compared the results to a pristine film subjected to identical treatment, and provided a summary in **Figure 3.8**. From these data we can conclude that *a reacted film's thermal stability on the Au(111) substrate differs dramatically from that of the pristine film*. Whereas the total P-O-C and P=O integrated intensities of the pristine film are effectively zero by the time the surface temperature reaches 195 K, these

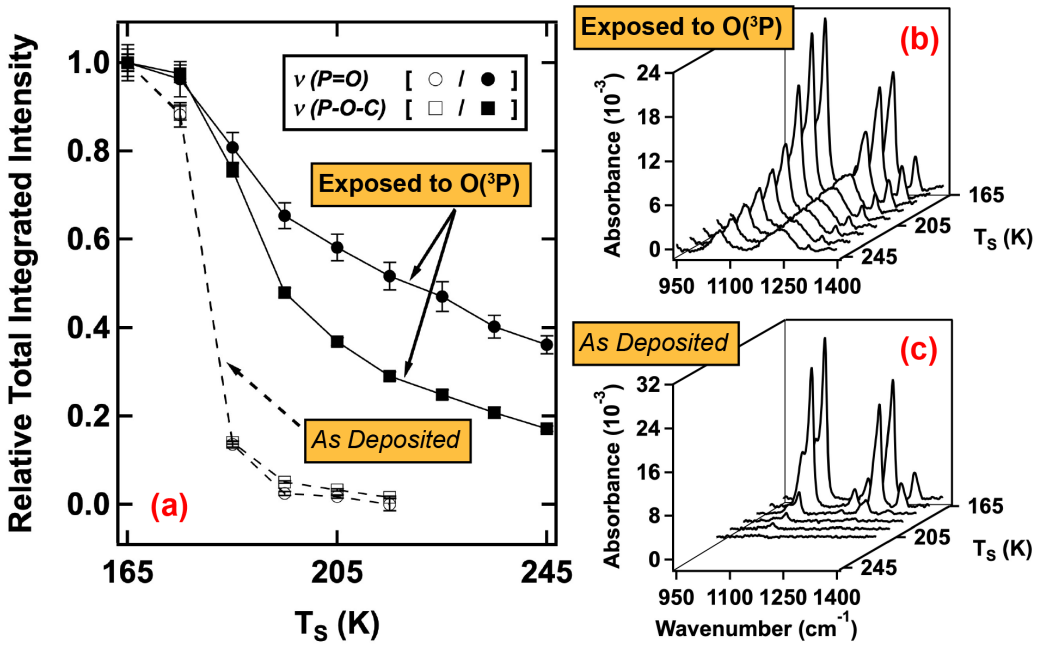

Figure 3.8: **Isothermal desorption of pristine and reacted DMMP films**. (a) Stepped isothermal desorption experiments show that after reaction of a DMMP film with O(^{3}P), a portion of the film exhibits substantially greater thermal stability on the substrate. The P-O-C and P=O modes still exhibit appreciable intensity in spectra of reacted films collected at surfaces temperatures above 195 K as compared to the pristine film as deposited on Au(111). The respective spectra are given in waterfall plots (b) and (c).

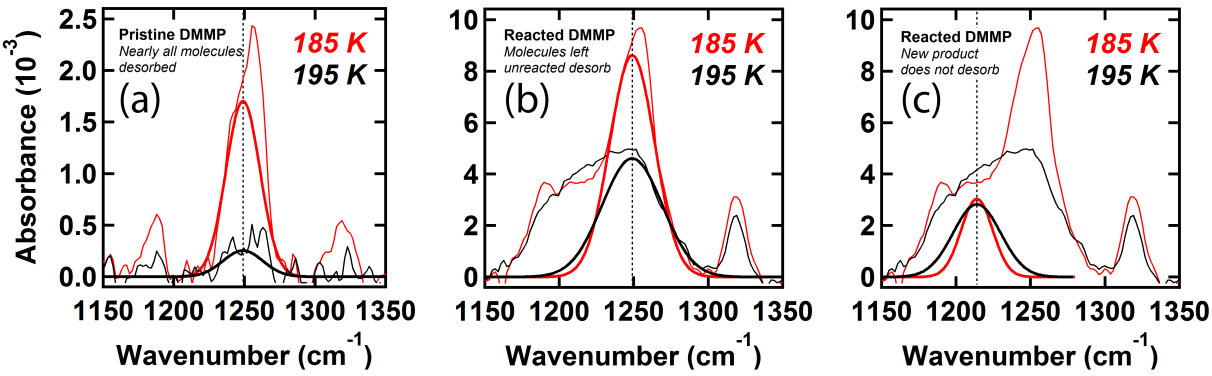

Figure 3.9: **DMMP P=O environment during isothermal desorption**. Behavior of the deconvoluted P=O spectroscopic signals of DMMP during isothermal desorption of films both pristine and exposed to O(^{3}P). The majority of a pristine DMMP film desorbs on the ramp from 185 K to 195 K, as shown in (a). This behavior, shown in (b), is mirrored in a reacted DMMP film, where the non-reacted DMMP is free to desorb, leaving behind the heavier product species, and therefore some intensity at 1249 cm^{-1}. Given that its intensity stays essentially constant during the ramp, the new signal at 1214 cm^{-1} is therefore directly related to formation of the new, more thermally stable product, shown in (c).

peaks are readily observable at 245 K and beyond for the reacted film. Indeed, the most dramatic changes occur during the ramp from 185 K to 195 K for a pristine DMMP film, as emphasized in **Figure 3.9a**. This behavior is mirrored in the reacted DMMP film shown in **Figure 3.9b**, where the non-reacted DMMP molecules freely desorb, leaving behind the product species, and therefore some partial intensity at 1249 cm^{-1}. The new signal at 1214 cm^{-1} stays essentially constant during the ramp (**Figure 3.9c**) and therefore directly corresponds to the presence of the new, more thermally stable polymeric product. Reacted films further show a clear difference in desorption kinetics between the P-O-C and P=O groups (**Figure 3.8a**), and we propose that the combination of increased surface energy and trapped oxygen species induces additional secondary reactions within the film during thermal annealing. These reactions further destroy DMMP methoxy groups, leading to a faster observed rate of decay in those particular infrared signals.

Hydrogen-bonded phosphoryl groups (1214 cm^{-1}), as mentioned previously, are products of the reactions taking place on the surface, and based on the desorption evidence they are likely part of hydroxylated oligomeric species that have significantly greater thermal stability on the surface. In **Figure 3.10**, product formation resulting from reactions of O(^{3}P) with six, twelve,

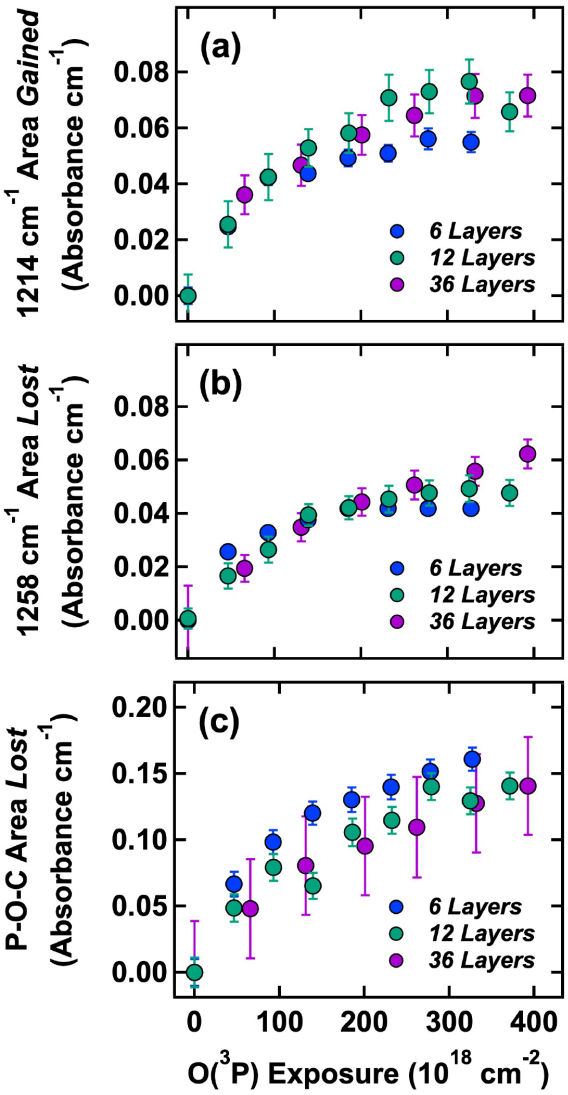

Figure 3.10: **DMMP oxidative reactivity as a function of initial film thickness**. RAIR spectra obtained for six, twelve, and thirty-six layer DMMP films during exposure to $O(^3P)$ suggest that reaction probability decreases as exposure continues, but does not follow half- or first-order kinetics. Panels depict (a) intensity gained in the 1214 cm^{-1} peak, (b) intensity lost from the 1258 cm^{-1} peak, and (c) total intensity lost from the P-O-C stretching modes. Overlap of the data asserts that reactivity is independent of initial film thickness and originates at the vacuum-film interface. Error bars indicate one standard deviation with respect to the peak fitting.

and thirty-six layer DMMP films begins to terminate at similar absolute signal intensities on all films studied. If the reaction begins at the vacuum-film interface and progresses layer-by-layer into the bulk DMMP, this trend suggests a limit to the penetration depth of the reactive species. Given substantial film thickness, a fraction of the DMMP—presumably underneath—is unchanged under our reaction conditions and is left free to desorb from the surface normally upon heating. Coupled with the decay kinetics mentioned previously, reaction energetics presented here seem to preclude the ability for O(^{3}P) to erode thicker DMMP films all the way down to the substrate; we hypothesize that the product overlayer formed hinders continued destruction. It is therefore likely that the effectiveness of surface DMMP decontamination through use of atmospheric plasmas cited in the literature[61–65] is facilitated by thermal desorption or sputtering in addition to reactivity with oxygen species.

3.4 Conclusion

We have characterized the oxidative reactivity of solid multilayer DMMP by O(^{3}P) using time-resolved RAIRS and complementary XPS. Our analysis suggests that destruction is initiated *via* hydrogen abstraction from methyl or methoxy groups. In turn, resultant hydroxyl and DMMP radical intermediates formed subsequently react with surrounding DMMP molecules, and also potentially with additional O_2 present in the beam under our conditions. While XPS confirms that some carbon is lost from the surface, it also shows oxygen incorporation within the film resulting from continued exposure. At 155 K, 0.12 eV O(^{3}P) atoms do not destroy thicker ($\geq$ ten layers) DMMP films all the way down to the substrate on which they are deposited. We propose that the radical side-reactions initiated by O(^{3}P) under our experimental conditions yield hydroxylated oligomeric species whose presence hinders continuous destruction of a significant fraction of thicker DMMP films. Despite this observed resistance, unreacted DMMP can freely desorb from the Au(111) surface upon thermal annealing, leaving the stable products behind.

Chapter 4

Oxidative Destruction of Multilayer Diisopropyl Methylphosphonate Films by O(^{3}P) Atomic Oxygen

In this chapter, we present work detailing the oxidative destruction of the nerve agent simulant diisopropyl methylphosphonate (DIMP) with O(^{3}P) using time-resolved, *in situ* RAIRS and XPS. Thermally annealed DIMP films deposited on Au(111) react upon exposure to a supersonic beam containing O(^{3}P) with average translational energies of 0.12 eV. The reaction is initiated by a hydrogen abstraction from one of three possible sites on DIMP, and then progresses through various secondary reactions with resultant hydroxyl radicals, carbon-centered DIMP-derived radicals, and nondissociated O_2 in the beam. Uptake of oxygen into the film accompanies these reactions, leading to new hydrogen bonding with the DIMP phosphoryl group. The generated products also present greater thermal stability than pristine DIMP, suggesting the formation of a distribution of oligomeric and polymeric products. As reactivity is observed to decrease upon continued O(^{3}P) exposure, this product likely forms a protective layer at the vacuum-film interface, hindering destruction of thicker films. Importantly, the rate of reaction and general reactivity trends are the same between DIMP and the smaller simulant DMMP (**Chapter 3**). The comparable reaction rates of the two molecules coupled with oxygen's inability to erode thick films all the way down to the substrate have specific implications for the development of oxidation-based decontamination strategies for these and other organophosphates in the solid phase. The findings presented in this chapter add significant new fundamental understanding of the oxidative chemistry of such species, knowledge needed in order to develop efficacious nerve agent decontamination strategies and to refine of existing models for the dispersal, adsorption, persistence, and destruction of organophosphates in the environment.

4.1 Introduction

As discussed in **Chapter 3**, understanding the oxidative destruction of organophosphates is increasingly essential for national defense and environmental protection.[87,88] Organophosphonate nerve agents like Soman and Sarin remain a significant threat in modern warfare, despite the multinational treaty aimed at preventing their creation and stockpiling.[25] Additionally, many industries use less toxic organophosphates widely as pesticides and fire-retardant additives.[89,90] Whether combating dangerous exposure to nerve agents, modeling the environmental impact of pest control measures, or exploring the efficacy of flame retardant coatings, it is critical to understand both the atmospheric and condensed phase destruction pathways, persistence, and dispersal of these compounds.[91–93]

In studies of both gas phase and surface adsorbed organophosphate reactivity, it is clear that oxygen plays a crucial role in the effective destruction of these compounds. Under atmospheric conditions, for example, it is widely accepted that reaction with hydroxyl radicals is the dominant loss process for organophosphates.[86,93–96] Scientists have also extensively studied the surface-induced, photocatalytic, or thermal destruction of these compounds on metals,[27,30,31] metal oxides,[32–40] and nanoparticle assemblies.[41,45,46,97] While metal oxides in particular are often successful in decomposing organophosphates through coordination to surface-bound hydroxyl groups, many are limited by the number of active sites and significantly decreased activity upon repeat cycles of adsorption and reaction. Recently, these limitations were partially alleviated by the addition of ozone to the reaction,[59,60] which again highlights the importance of oxygen in the reliable destruction of these compounds. Even in larger-scale decontamination strategies that involve the use of atmospheric pressure plasma sources,[61–65,98] the presence of molecular and atomic oxygen species has been shown to improve overall efficacy.[63,98]

In the current chapter, we present a detailed picture of the oxidative destruction of multilayer diisopropyl methylphosphonate (DIMP) exposed to $O(^3P)$. Again, we chose atomic oxygen in its $O(^3P)$ ground electronic state, as it serves as an aggressive oxidant for simulant destruction

while allowing for incisive experimental and theoretical mechanistic studies. This work is, in part, an extension of the work presented in **Chapter 3** on DMMP.[99] In this chapter, the isopropyl groups in DIMP provide an additional structural similarity with the nerve agent Sarin as well as the possibility of observing alkyl reaction channels unseen in DMMP.[94] The mechanistic conclusions presented here for the oxidative reactions of both simulants are additionally informed by theoretical investigations of the interaction between organophosphates and reactive oxygen species.[71,72,93,100] Through the use of *in situ* RAIRS and XPS, we conclusively demonstrate oxidative destruction between adsorbed DIMP and O(^{3}P) under UHV conditions, and compare that to the analogous reaction with DMMP. For both simulants, an oxygen-enriched, thermally stable product is formed upon exposure to O(^{3}P). Additionally, the overall rate of oxidative destruction is identical between the two molecules, despite the differences in functional groups. As such, the findings contained herein have important implications for the solid phase destruction of organophosphates; future decontamination and environmental modeling techniques will have to take into account the fact that the relative rates, byproducts, and persistence of these compounds may vary greatly between the condensed and gaseous phases.

4.2 Experimental Section

We performed all of the experiments described in this chapter in the molecular beam scattering instrument described in **Chapter 2**. Our primary analytical techniques were time-resolved RAIRS and XPS.

Most of the experimental details described here are identical to those used in **Chapter 3**.[99] One difference, however, is in the method for simulant film deposition. For these experiments, we dosed DIMP on the Au(111) crystal surface through the beam source using 5% O_2 in neon as the carrier gas; all beam lines were pumped out to remove trace DIMP prior to turning on the O(^{3}P) source for reaction. We fit RAIR spectra (averaged over 200 scans at 4 cm^{-1} resolution) to Gaussian peaks with linear baselines; integrated peak areas were used to quantify DIMP film thickness and characterize products and reaction progress during exposure. **Figure 4.1** contains a representative

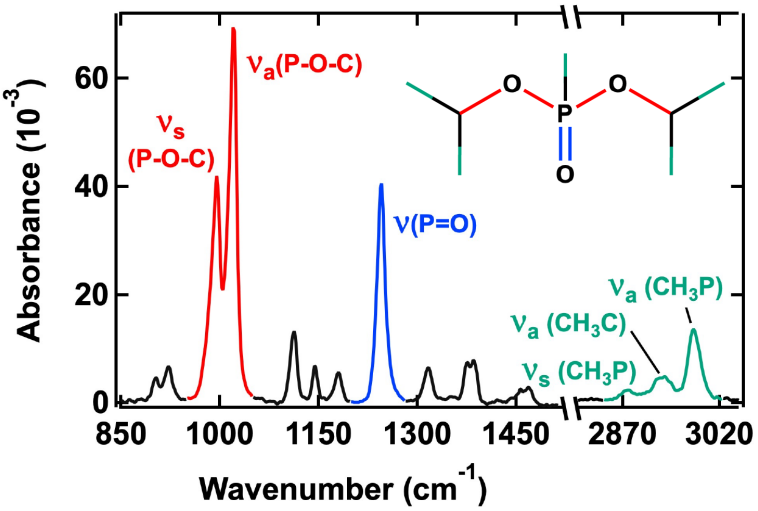

Figure 4.1: **Representative RAIR spectrum of DIMP film**. RAIR spectrum of a 30-layer thick DIMP film deposited on single-crystal Au(111). Signals referred to in the text include the P-O-C (red; 995 and 1020 cm^{-1}), P=O (blue; 1245 cm^{-1}), and C-H (green; 2880, 2931, and 2981 cm^{-1}) stretching modes. All modes are highlighted in the DIMP spectrum and molecule inset.

spectrum of a 27-layer DIMP film, with the three characteristic regions most frequently referenced herein (P-O-C, P=O, and C-H stretches) highlighted in color. The respective peak assignments are consistent with expectations and values previously reported in the literature.[39,101–104]

To prepare films, we dosed DIMP onto the substrate at 165 K, under conditions where desorption is negligible. Immediately following the dosing, we annealed films at 182 K until they reached the desired initial thickness. Analogous to the experiments performed in **Chapter 3**, we correlated RAIR signal with a DIMP film thickness using isothermal desorption experiments within the range 173-175 K. By tracking the integrated area of the P-O-C signals over time, it was possible to distinguish multilayer from monolayer DIMP. As shown in **Figure 4.2**, the rate of desorption changes abruptly upon reaching the monolayer, which allows for the quantitative determination that a monolayer of DIMP corresponds to an average total integrated P-O-C intensity of 0.07 Absorbance units cm^{-1} using our current setup. We used this value to quantify initial DIMP film thicknesses for all trials; peak line shapes remained consistent beyond 30 layers, the maximum thickness referenced in this study.

Following deposition, we exposed DMMP films to $O(^3P)$ atomic oxygen using the source de-

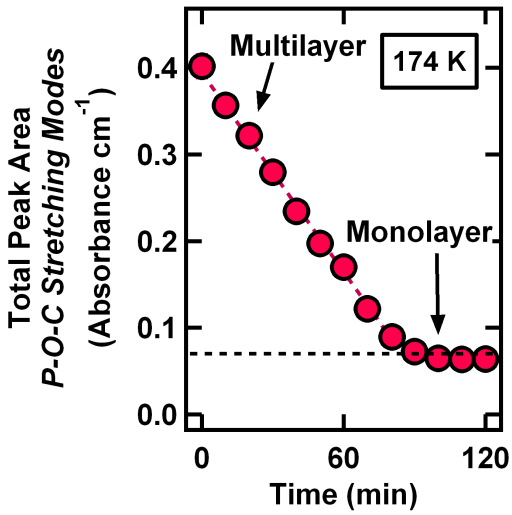

Figure 4.2: **Isothermal desorption of multilayer DIMP**. Isothermal desorption of a DIMP film at 174 K shows a clear distinction between multilayer and monolayer desorption rates, as tracked via integration of P-O-C signals. The value at which the rate changes corresponds to the infrared intensity of a single layer of DIMP.

scribed in **Subsection 2.3.3**. We similarly determined the O(^{3}P) translational energy and flux following the procedures described in **Subsections 2.3.1** and **2.3.2**. Typical values for the beam impinging at normal incidence were, respectively, 0.12 eV and 2×10^{17} atoms cm^{-2} s^{-1}. Beam energy widths were approximately 0.06 eV. We note that while the experimental conditions for O(^{3}P) exposure are the same as in **Chapter 3**, all of the DIMP reactivity experiments discussed herein involved significantly greater total O(^{3}P) exposures. As such, we repeated the DMMP experiments with this increased exposure to better compare the two molecules. This change did not significantly alter any of our previous conclusions; the details of any minor refinements are referenced in **Section 4.3**.

Our analysis of DIMP reactivity also included collecting XPS spectra of the C(1s), O(1s), and Au(4f) regions. The full XPS system is described in **Subsection 2.2.2**; for these experiments we operated the X-ray source at 10 kV and 20 mA and collected the spectra using 50 eV pass energy and a 0.4 eV step size. We fit the spectral peaks in the same manner as that used in RAIRS analyses.

4.3 Results and Discussion

4.3.1 Spectral Evidence of Reaction

As with DMMP, numerous transformations are observed in the RAIR spectra of a DIMP film exposed to O(^{3}P). Changes in four important spectral regions are highlighted in **Figure 4.3** for a 7-layer film. We note here (and discuss further in **Subsection 4.3.2**) that the observed oxidative reactivity is independent of original DIMP film thickness for the O(^{3}P) exposures considered in this study. The original peaks associated with pristine DIMP are clearly observed to decrease in intensity upon exposure. In the P-O-C region (**Figure 4.3a**), it is the 995 and 1020 cm^{-1} signals that decay; these peak locations match reported values for the asymmetric and symmetric P-O-C stretches.[39,101–104] This decay corresponds to reactive destruction of these modes.[99] Concurrent with this destruction, however, new intensity is observed between 1030 and 1100 cm^{-1}. The broadness of this new region makes exact peak fitting difficult, but we routinely established a good fit with peaks at 1041 and 1063 cm^{-1}. These peak locations are also nearly identical to our recorded values for adsorbed DMMP, which suggests that they may correspond to the same asymmetric and symmetric P-O-C stretches in a phosphonate ester with smaller alkyl groups. It has been reported that the P-O-CH_3 peak locations are 40-60 cm^{-1} greater than those associated with P-O-iPr,[85] Alternatively, these signals may be due to the formation of new P-O or P-O-H groups. The locations and broadness of these modes are consistent with reported values for various amorphous or glassy phosphate species.[98,105–108]

The P=O region (**Figure 4.3b**) undergoes a similar transformation on exposure to O(^{3}P). The pristine DIMP film has a single peak at 1245 cm^{-1}, which is consistent with reported values for the P=O stretch in gas and liquid phases or adsorbed on unreactive, nonhydroxylated surfaces.[101–104] With O(^{3}P) exposure, the 1245 cm^{-1} mode decays and is replaced by a new signal at 1216 cm^{-1}. As was reported for DMMP, this red-shifted peak location is the result of the P=O moiety coordinating to surface hydroxyl groups, water, or other hydroxyl-terminated species through hydrogen bonding.[35,53,85,102,109] Therefore, unlike the P-O-C region, the decrease in intensity of the origi-

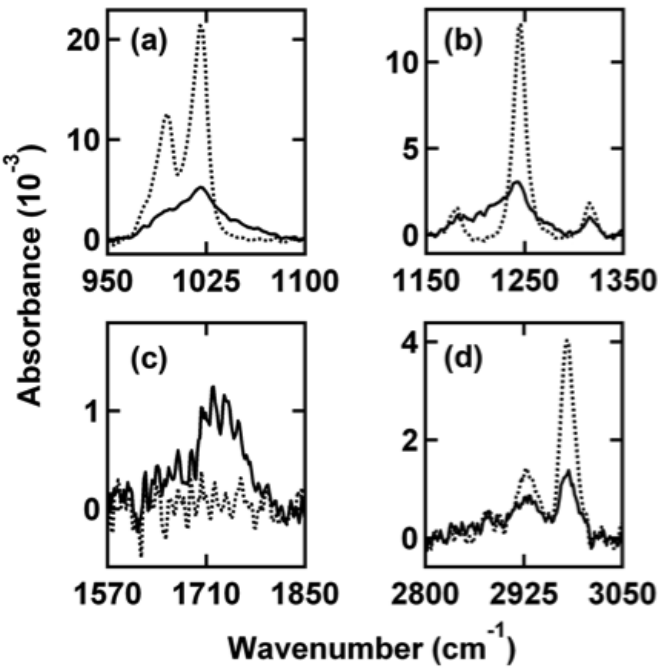

Figure 4.3: **DIMP before and after O(^{3}P) exposure**. RAIR spectra of characteristic regions of a 7-layer DIMP film before (dashed line) and after exposure to O(^{3}P) (solid line; total exposure of 1×10^{21} atoms cm^{-2}). The total signal intensity decreases in the P-O-C (a), P=O (b), and C-H (d) regions, but new signal growth appears in parts a and b. New peaks grow in upon exposure in between 1650 and 1750 cm^{-1} (c). Further explanation of all peak intensity changes and shifts is given in the text.

nal P=O peak does not correlate with reactive destruction of P=O modes. Rather, the reaction of DIMP with O(^{3}P) generates hydrogen bonding sites within the film, resulting in some fraction of the DIMP becoming partially solvated by hydrogen bonds. This is supported by **Figure 4.4**, which shows the absolute areas lost and gained by peaks in the P=O (**Figure 4.4a**) and P-O-C (**Figure 4.4b**) regions. Clearly, the loss of area in the 1245 cm^{-1} signal tracks almost exactly with the area gained in 1216 cm^{-1}. This is unlike the behavior of the P-O-C peaks, for which area growth and loss appear unrelated. Therefore, the P=O region is exhibiting a red shift in the original band.

In the C-H region (**Figure 4.3d**), the three original peak locations are consistent with literature values for asymmetric P-CH_3 (2981 cm^{-1}), asymmetric C-CH_3 (2931 cm^{-1}), and symmetric P-CH_3 stretches (2880 cm^{-1}).[39,102,104] All three peaks decrease in intensity during the reaction but no new peaks or shifts are observed, supporting reactive destruction of DIMP. The fact that all three of these modes are observed to decrease in intensity indicates that the system has enough energy to overcome the barriers for reaction at each of the C-H sites visible in the RAIR spectra (P-CH_3 and C-CH_3). The tertiary C-H stretch of the isopropoxy group is unresolved in our spectra, but theoretical barriers for hydrogen abstraction are comparable for both possible sites on the isopropoxy groups, so the reaction is likely occurring at the tertiary site as well.[71,72,93]

The final change observed in the reacted DIMP RAIR spectra yet to be discussed is the growth of a broad pair of peaks at 1645 and 1724 cm^{-1} (**Figure 4.3c**). A number of prior organophosphate studies have identified carbonyl-containing products or intermediates with similar peak locations, including destructive adsorption on metal oxides,[37,45,97] gas-phase reactions with hydroxyl radicals under atmospheric conditions,[94] and destruction with a radio frequency plasma source.[98] Probable sources of these new C=O bands are addressed in the next section.

4.3.2 Product Formation

Oxidative destruction of both DIMP and DMMP begins with a hydrogen abstraction step leading to formation of a carbon-centered radical. This is supported by a myriad of both theoretical and experimental work concluding that hydrogen abstraction is the most energetically accessible chan-

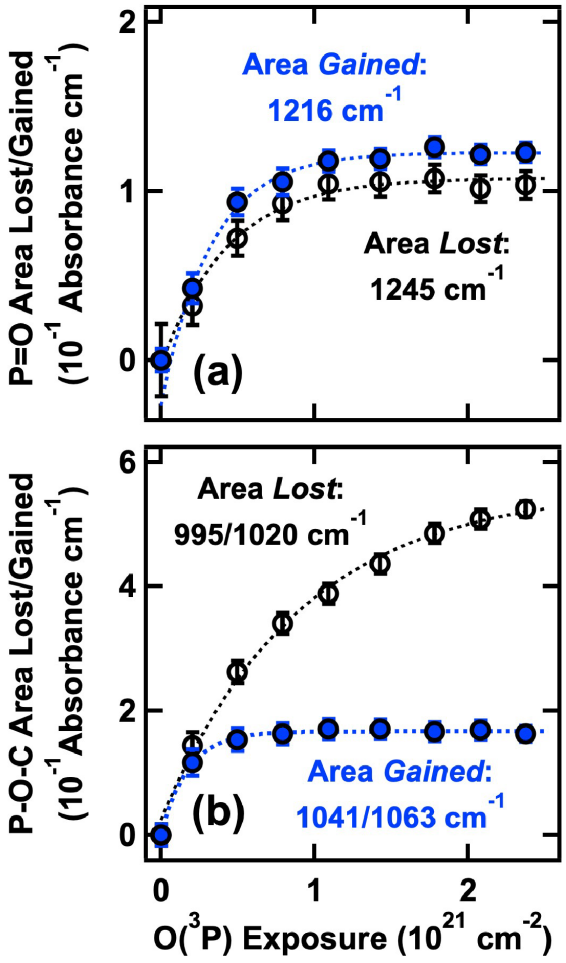

Figure 4.4: **P=O and P-O-C regions during O(^{3}P) exposure**. Changes in integrated peak areas are shown for the P=O (a) and P-O-C regions (b) of a 27-layer DIMP film. The area *lost* from peaks associated with pristine DIMP is shown in black (1245 cm^{-1} for P=O and 995 and 1020 cm^{-1} for P-O-C, while the area *gained* by new peaks is shown in blue (1216 cm^{-1} for P=O and 1041 and 1063 for P-O-C). In the P=O region, intensity shifts away from the original peak due to solvation by new hydrogen bonds. Conversely, in the P-O-C region, the original peaks continue to decay in intensity long after the new peaks have stopped growing in.

nel for these organophosphates. We cite, for example, recent theoretical gas phase calculations for O(^{3}P) and Sarin (nerve gas for which DMMP and DIMP are both simulants), which report that the upper limits for hydrogen abstraction barriers are 0.47, 0.20, and 0.19 eV for abstraction from the methyl, isopropoxy tertiary C-H, and CH_3 sites, respectively.[71,72] While some of these projected barriers are larger than the current study's mean beam energies (accounting for the energy distributions), there are a few reasons why hydrogen abstraction is nevertheless feasible. First, the barriers are likely lower in the solid phase due to formation of longer-lived collision complexes in the film. This assertion is reinforced by experimental evidence indicating that reactions between O(^{3}P) and organic or hydrocarbon-based films proceed largely through such abstraction mechanisms.[82–84] Second, and perhaps more importantly, while the initial abstraction by O(^{3}P) may be energetically-limiting or rate-limiting, once a hydrogen has been abstracted, hydroxyl radicals are produced. These hydroxyl radicals can continue reacting within the film, and the barriers for hydrogen abstraction from DIMP by hydroxyl radicals are significantly lower.[93,110] One theoretical study concluded that abstraction from all three possible sites by hydroxyl radicals is facile under atmospheric conditions, with barriers at or below 2kT for our system.[93] These low-barrier, secondary abstractions help explain why all of the DIMP C-H stretching peaks are observed to decrease concurrently despite the possible disparity in barriers for direct abstraction by O(^{3}P).

Spectral changes in the P=O region, as well as XPS analysis, confirm the continued reaction and retention of oxygen-containing species within the film. In the P=O region, the shift in intensity from 1245 to 1216 cm^{-1} is consistent with the analogous shift observed for DMMP and indicates solvation of the P=O moiety by new hydrogen bonds.[49,77,99] Additionally, the XPS data in **Figure 4.5** verify that even when accounting for the loss of gaseous carbon-containing products such as CO and CO_2,[60] comparison of C(1s) and O(1s) signals between pristine and reacted DIMP films shows a substantial increase in the relative N_O/N_C ratio at the surface.

A number of studies have examined the radical reactions of organophosphates under atmospheric and aqueous conditions, and have proposed relevant pathways that provide a useful mechanistic foundation for this work.[86,93–96,100,111–113] Following the rate-determining hydrogen ab-

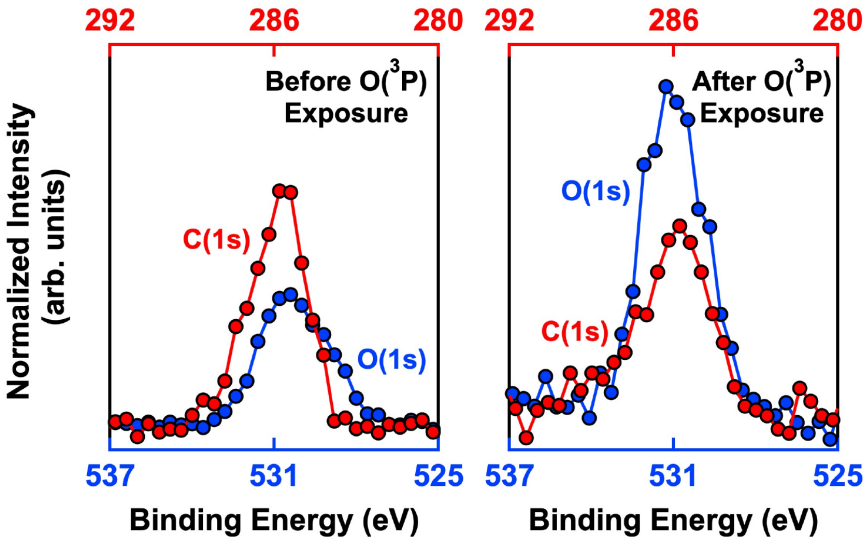

Figure 4.5: **XPS of reacted and pristine DIMP films**. XPS data of 17-layer DIMP films as deposited and after O(^{3}P) exposure demonstrating that the N_O/N_C ratio increases, confirming oxygen is incorporated into the film. We have scaled the data such that the carbon (1s) peak areas are equivalent in both films, which accounts for the fact that some carbon is also lost as gaseous species during reaction.

straction by O(^{3}P) or hydroxyl radical, it is likely that O_2 from the beam adds to the resultant carbon-centered radicals, forming peroxy radicals ($RO_2\cdot$).[93,114–117] These radicals have a number of possible subsequent reaction pathways, including reactions 1 and 2 detailed in **Figure 4.6**.[114,118,119] Reaction 1 presents a clear explanation for the uptake of oxygen in the film that is observed with XPS, since both of the nonradical products have new oxygen-containing functional groups. Additionally, these products account for both the observed increase in hydrogen bonding within the film and the appearance of bands in the C=O stretching region of the RAIR spectra. Reaction 2, on the other hand, is not a termination reaction and therefore presents yet another set of possible reaction pathways, detailed in reactions 3 and 4 in **Figure 4.6**.[120–123]

These latter reactions provide further evidence for carbonyl-containing products, as well as a product with a smaller alkoxy group, possibly accounting for the new bands observed in the P-O-C region of reacted DIMP. Because the initiating hydrogen abstraction step can occur at all three possible sites, there are, of course, a great many more possible reaction pathways than just those discussed here, including combinations and cross-reactions between different radical species.

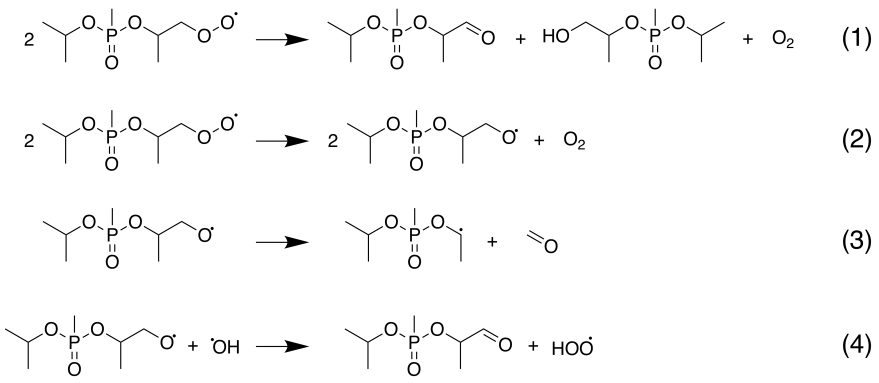

Figure 4.6: **Proposed reaction pathway for DIMP oxidation**. Possible reaction pathways following the hydrogen abstraction from a primary isopropyl carbon in DIMP and subsequent addition of O_2. Reactions include disproportionation (1) to form carbonyl- and hydroxyl-containing products, as well as conversion to alkoxy radical species (2). Alkoxy radicals can undergo unimolecular decomposition (3) or further reaction with hydroxyl radicals in the film (4).

While gas phase barriers, rate constants, and branching ratios have been reported for many of the analogous alkoxy and peroxy radical reactions and decompositions, they are difficult to reliably apply to such a complex solid phase system, whose spectroscopic bands tend only to broaden and convolute. The spectroscopic evidence and mechanisms presented here do, however, largely align with atmospheric studies of DMMP and IMMP (isopropyl methylphosphonate). The products of the reaction between hydroxyl radicals and IMMP, for example, include formaldehyde and acetone as well as the carbonyl-containing phosphonate, $iPrOP(O)(CH_3)OC(O)CH_3$.[94] A distinct P-O-C=O band is unidentifiable in the data presented here, but this mode possibly overlaps with DIMP's P-O-C stretches or may also simply be too small and broad to detect on top of the lower wavenumber DIMP peaks.[85]

Another consequence of the reactions taking place in a solid film is that reaction products and intermediates are in close spatial proximity. Therefore, it can be expected that some of the combination reactions may lead to various cross-linked and higher molecular weight oligomeric and polymeric products (referenced herein as simply "polymeric products"). Polymeric byproducts have been reported during investigations of the decomposition of organophosphates under both gaseous and surface-adsorbed conditions.[62,66] It is often difficult, spectroscopically, to conclusively identify evidence of P-O-P or P-R-P stretching modes, because they either overlap with

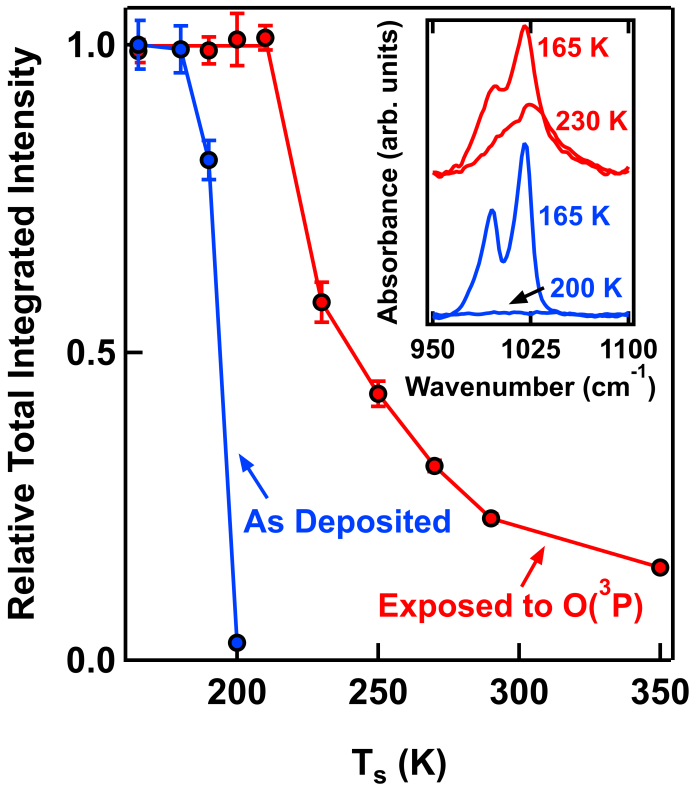

Figure 4.7: **Isothermal desorption of pristine and reacted DIMP films**. Stepped isothermal desorption experiments on pristine (blue) and reacted (red) 17-layer films show that DIMP exposed to O(^{3}P) exhibits much greater thermal stability on the substrate. In the reacted film, the integrated intensity of the P-O-C region (normalized to original film thickness) begins to decrease at a surface temperature approximately 30 K higher than the point at which the pristine film decreases. RAIR spectra in the corresponding region of each of the simulants are displayed in the inset.

other absorption bands or appear as smaller, broader peaks.[85] Instead, we find evidence by monitoring the thermal stability of the film after reaction. After a DIMP film has been exposed to O(^{3}P), we systematically increase the surface temperature from 165 to 350 K at 0.05 K s^{-1} and hold it constant at a series of intermediate temperatures for the duration of a spectrum acquisition. For comparison, a pristine film is subjected to identical treatment. A representative summary of this data for the P-O-C region is given in **Figure 4.7**. Clearly, the thermal stability of a reacted DIMP film is much greater than that of a pristine film. As the RAIR spectra inset shows, unreacted DIMP is fully desorbed by 200 K, whereas a reacted film retains appreciable intensity at 350 K and beyond. Moreover, when the reacted film does begin to desorb, intensity is lost from the original P-O-C peaks first, indicating that unreacted DIMP is eventually freed. This increase in product stability cannot be explained fully with the initial unimolecular and bimolecular reactions given in **Figure 4.6**. Rather, radical intermediates likely react in a series of steps, forming the observed oxygen-containing species of higher molecular weight.

As observed in **Figure 4.7**, the full retention of spectral intensity for an additional 30 K in a reacted film suggests that even the unreacted DIMP possesses some increased thermal stability on the substrate following O(^{3}P) exposure. A possible explanation for this is that the oxidative reaction begins at the vacuum-film interface and progresses layer-by-layer into the film. The subsequent reactions lead to the formation of a thermally stable, polymeric overlayer on top of the remaining unreacted DIMP. Until the surface temperature is high enough to destroy or increase the mobility of this polymeric overlayer, the unreacted DIMP is effectively trapped on the surface. Evidence for this type of "top-down" reactivity is presented in **Figure 4.8**, which shows the absolute area lost from the original P-O-C peaks in a 7, 17, and 27-layer DIMP film as they are exposed to O(^{3}P). Regardless of initial film thickness, the reaction progresses at the same rate. The reaction then begins to slow as either the film is completely eroded or, in the case of thicker films, the O(^{3}P) is simply unable to penetrate and continue reacting in the bulk. This decay, like for DMMP, therefore does not follow simple first or half-order kinetics with respect to O(^{3}P) exposure. *The formation of the polymeric overlayer thus hinders not only desorption of unreacted DIMP but also the destruction*

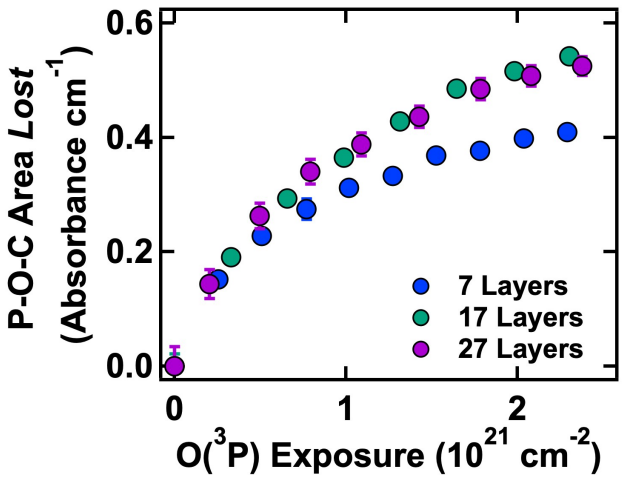

Figure 4.8: **DIMP oxidative reactivity as a function of initial film thickness**. RAIR spectra for 7-, 17-, and 27-layer DIMP films showing that reaction probability decreases with continued $O(^3P)$ exposure. The data shown are the integrated areas lost from the original P-O-C peaks (995 and 1020 cm^{-1}) upon $O(^3P)$ exposure. The overlap of the data confirms that multilayer reactivity is independent of original film thickness and likely initiates at the vacuum-film interface. The earlier turnover of the 7-layer film likely reflects the reaction front beginning to terminate as it approaches the film-substrate interface.

of thicker films all the way down to the substrate. We repeated this experiment with DMMP under the same heating rate conditions for exact comparison. The same trends emerge: a stark increase in thermal stability of the reacted product, and when desorption begins, it is the unreacted simulant that desorbs first.

4.3.3 Comparison of DIMP and DMMP Reactivity

Qualitatively, there are many similarities in the behavior of DIMP and DMMP films exposed to $O(^3P)$. In **Figure 4.9**, the RAIR spectra of both reacted films show: a decrease in intensity of the asymmetric and symmetric P-O-C stretches, a red shift of intensity in the P=O stretch, and a broad growth between 1650 and 1750 cm^{-1} that we attribute to new C=O stretching modes. The only key difference is the growth of two new, bluer peaks at 1041 and 1063 cm^{-1} in the P-O-C region of DIMP. These peaks are attributed to products or intermediates in the oxidative destruction of DIMP and are unobserved in DMMP. As such, total reactivity of the two molecules is compared exclusively via decay of the original P-O-C peaks. Such a comparison is shown in **Figure 4.10**.

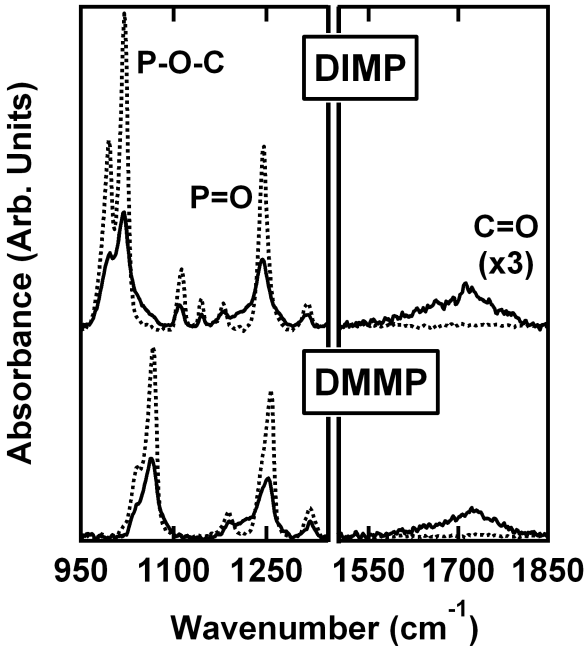

Figure 4.9: **Spectral changes in DIMP and DMMP films during oxidation**. We observe analogous changes in the RAIR spectra of pristine (dashed) and reacted (solid) 17-layer DIMP and 12-layer DMMP films. C-H modes are not included here due to their low intensity in DMMP spectra.

Once the P-O-C peak decay is scaled to the integrated intensity of the monolayer (**Figure 4.2**), the reactivity of DIMP and DMMP are clearly identical.

Many of the reaction channels presented here for DIMP are possible for DMMP as well. Differences may, however, be expected in the overall reaction rates for the two molecules, due in part to differences in both initial hydrogen abstraction rates and preference for tertiary hydrogen abstraction in the gas phase.[94,114,117] However, the barriers for all possible hydrogen abstractions in DIMP and DMMP are comparable in magnitude, especially when considering abstractions by generated hydroxyl radicals.[71,72,93,110] The replicable decay observed in the C-H peaks of both molecules upon O(^{3}P) exposure attests to the fact that these barriers are indeed accessible by the system. Furthermore, once radicals have begun forming, the close spatial proximity of radical species in the film will likely contribute to a high rate of secondary reactions.[124,125] The multitude of channels available, as well as the accessibility of initial abstractions, leads to the comparable observed overall rates of reaction for DIMP and DMMP in this study.

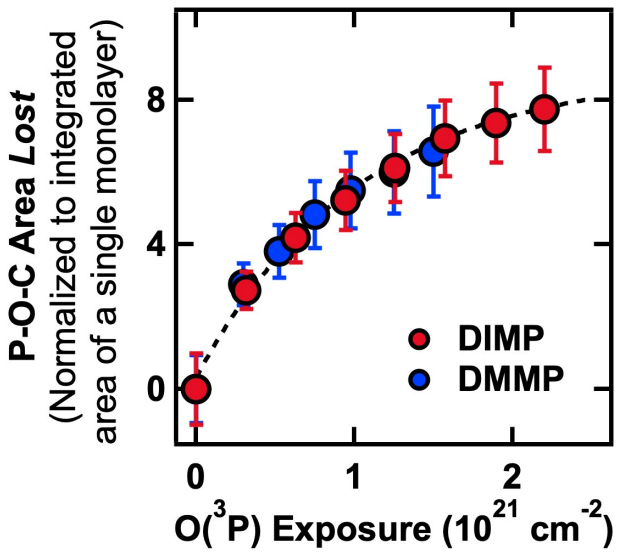

Figure 4.10: **Comparison of DIMP and DMMP oxidation rates**. The integrated area lost from the two original P-O-C peaks of both molecules (995 and 1020 cm^{-1} for DIMP, 1041 and 1066 cm^{-1} for DMMP), scaled to respective monolayer areas. The scaled reaction rates for the two simulants are indistinguishable.

4.4 Conclusion

We have characterized the oxidative destruction of solid multilayer DIMP by $O(^3P)$ using time-resolved RAIRS and XPS. The reaction begins with hydrogen abstraction from one of three possible sites on the DIMP molecule by an incident $O(^3P)$ or hydroxyl radical intermediate. The resultant carbon-centered radicals go on to either unimolecularly decompose or further react with nondissociated O_2 in the beam or a neighboring radical in the film. The overall destruction per unit dose decays upon continued $O(^3P)$ exposure, independent of film thickness. The products formed during reaction possess greater thermal stability on the substrate than unreacted DIMP, which leads to the conclusion that at 165 K, 0.12 eV $O(^3P)$ erodes the top layers of a DIMP film, forming an oxygen-containing product overlayer that hinders the continued reaction of DIMP fully down to the substrate. Interestingly, the reactions of $O(^3P)$ and both DIMP and DMMP progress at the same overall rate and lead to similarly persistent polymeric products. This is in contrast to gas phase analyses that find faster rates of oxidation for DIMP.

These findings aid our understanding of condensed phase organophosphate destruction. For

example, protection of unreacted compounds afforded by a polymeric overlayer could explain why organophosphates coating inert particles in the atmosphere have longer lifetimes than their gas phase counterparts.[96] Additionally, the clear importance of organophosphate reactions with hydroxyl radicals observed here serves to reinforce our understanding of these compounds' known flame retarding properties.[126]

Extension of this work could examine the oxidative destruction of these compounds on a variety of representative environmental surfaces, both reactive and inert; reactive surfaces may include metal oxides like silica or titania, while inert surfaces may include some organic thin films, water ice, or biopolymers. This will aid in developing nerve agent decontamination strategies and refining existing models for the dispersal, persistence, and destruction of organophosphates in the environment.

Chapter 5

Rapid Laser-Induced Temperature Jump Decomposition of the Nerve Agent Simulant Diisopropyl Methylphosphonate under Atmospheric Conditions

In our third study of nerve agent destruction, we present work detailing the destruction of DIMP via rapid laser heating under atmospheric conditions. Following Nd:YAG laser ablation of liquid DIMP deposited on a graphite substrate, both parent and product fragments are transmitted via capillary from an atmospheric chamber to a vacuum chamber containing a high-resolution mass spectrometer. This allows for real time measurements of product distributions under a variety of temperature and atmospheric conditions. *Ex situ* Fourier transform infrared (FTIR) spectroscopy analysis of the same chamber contents provides complementary information about product identities and fragmentation pathways. Results demonstrate that product distributions depend on heating rate, surface temperature, and atmospheric oxygen content. In the destruction of DIMP, the relative production of alkene products depends significantly on laser power; smaller products are relatively more abundant at higher ablation temperatures. We also show that in the absence of atmospheric oxygen, the concentration of oxygenated products decreases sharply relative to alkene and alkane products. This suggests that under high-temperature conditions, atmospheric oxygen is incorporated directly into the products of the fragmented simulant. This project extends significantly our understanding of the fundamental chemistry of these dangerous compounds under atmospheric and rapidly changing thermal conditions. The results have critical implications for the development of effective chemical warfare agent decontamination and destruction strategies.

5.1 Introduction

Due to the threat chemical warfare agents (CWAs) pose to the global community, there is considerable interest in detecting, destroying existing stockpiles, and decontaminating areas affected by these compounds.[67,127] Current large-scale destruction techniques include incineration[87] and neutralization by base hydrolysis, but these strategies come with additional challenges regarding safe transport and toxic byproducts.[26] Therefore, it remains critical to continue developing new strategies and to understand the exact chemistry of agents' destruction in both vapor and condensed phases. Of particular interest are the extremely dangerous organophosphonate nerve agents Soman and Sarin.[92] Sarin, for example, has a high estimated toxicity of 35 mg min m^{-3} in humans via vapor inhalation.[128] Even beyond these dangerous compounds, many less toxic organophosphonates have found widespread industrial use as plasticizers, flame retardants, fire-resistant fluids and lubricants, and pesticides.[86,90] It is therefore important to characterize environmental impacts and remediation strategies for organophosphonate contaminants more broadly. This study adds to our fundamental understanding of the primary chemical kinetics and physical processes occurring when these compounds are exposed to rapid heating under atmospheric conditions.

In a continuation of the work presented in **Chapters 3** and **4**, the current chapter presents a detailed investigation of the laser-induced, high temperature rapid heating destruction of DIMP (**Figure 5.1**).[33,39,66] We again selected DIMP from among the class of organophosphonate simulants for two reasons. First, DIMP shares key structural similarities with the nerve agent Sarin, which is a compound of particular interest due in part to its use in urban terror attacks in Japan and its exposure to US troops abroad.[26,33] Second, it has been shown in a number of pyrolytic and thermal studies that a significant organophosphonate destruction channel yields substituted and unsubstituted carbon products resulting from the alkoxy moiety.[66,68,109,129–133] This gaseous product array is easily detectible and differentiable via mass spectrometry and FTIR analyses, which enables a robust investigation of the impact of laser heating rate, surface temperature, and atmospheric pressure on simulant destruction.

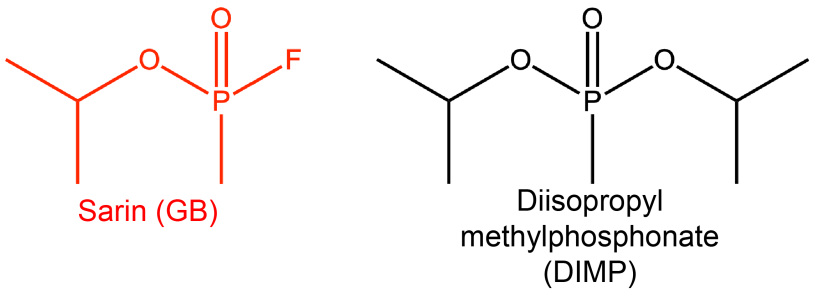

Figure 5.1: **Chemical structures of Sarin and DIMP**. Chemical structures of the nerve agent sarin (red) and the simulant DIMP (black) differ only in the replacement of fluorine with an additional oxygen and isopropyl group.

In addition to experimental and theoretical work on the thermal decomposition and combustion of these compounds,[66,68,132,134,135] this work is an extension of previous work examining oxidative[99,136] and laser destruction[137] of adsorbed chemical nerve agent simulants under UHV conditions (**Chapters 3** and **4**). As discussed, the oxidative destruction of DIMP and DMMP progress at similar rates and yield oxygen- and carbonyl-containing oligomeric product species.[99,136] Laser desorption and destruction studies of a number of Sarin simulants (DIMP, DMMP, and diethyl ethylphosphonate), demonstrated lower temperature thresholds for destruction of simulants with relatively larger phosphonate side chains.[137] On the basis of these results, we again expect that the majority of gas phase products in this study will include a variety of 1, 2, and 3-carbon products generated from the DIMP isopropyl group, with possible incorporation of atmospheric oxygen.

Using a unique atmospheric pressure ablation chamber, rapid laser heating of 10^{11} K s^{-1}, and *in situ* MS, the experiments in this chapter probe the reaction products in the prompt destruction of DIMP under atmospheric and, for the first time, oxygen-depleted atmospheric conditions. In addition to identifying product branching ratios as a function of laser power, the manipulation of oxygen content allows us to elucidate the mechanistic role of oxygen in simulant destruction. This basic understanding is critical for practical decontamination strategies that involve, for example, flame incineration, as these conditions often lead to significant oxygen depletion in the local environment.[138]

In the laser-induced thermal destruction of DIMP, we demonstrate that the resulting product

distribution depends on both surface temperature rise and atmospheric oxygen composition. More specifically, the relative production of small alkene products depends significantly on laser power; the relative yield of smaller substituted products is higher when the sample is ablated with higher laser powers. Likewise, under oxygen-depleted conditions, the relative amount of oxygenated products decreases sharply relative to alkene and alkane products. This suggests that under extreme high-temperature conditions atmospheric oxygen is incorporated directly into the products of the fragmented simulant. Such findings are directly relevant to producing novel CWA mitigation strategies and maintaining national security.

5.2 Experimental Section

Unlike the other chapters in this thesis, we conducted all experiments for this chapter in a newly constructed atmospheric-mass spectrometry apparatus, shown in **Figure 5.2**. Additional measurements were collected via *ex situ* FTIR analysis. In short, a QMS (UTI 100) occupies a high-vacuum chamber reaching base pressures of 10^{-9} Torr. This chamber samples, via a 20 cm fused silica capillary with a 25-μm inner diameter, the gaseous products produced in a small, adjacent atmospheric chamber used for laser ablation trials. A second identical inlet capillary in the atmospheric chamber ensures that atmospheric pressure is maintained during experimental sampling. The volume of the atmospheric sampling chamber is small (approximately 40 cm^3), which enables rapid diffusion of vapor products; changes in chamber contents are detected by the mass spectrometer within 300 ms. We do note that the capillary is not heated, so there is a possibility for vapor condensation of DIMP or associated products during transport. Gas phase products are, however, expected to thermalize rapidly in the atmospheric chamber, so we do not expect condensation in the capillary to be a major pathway. The large pressure differential between the two chambers also ensured consistent gas flow through the capillary, and repeated use of the same capillary showed no blockage, indicating that condensation was not happening on a large scale.

In order to prepare DIMP samples for ablation, we routinely purged the atmospheric chamber and re-opened it to atmosphere between trials. The substrate for all experiments was a highly

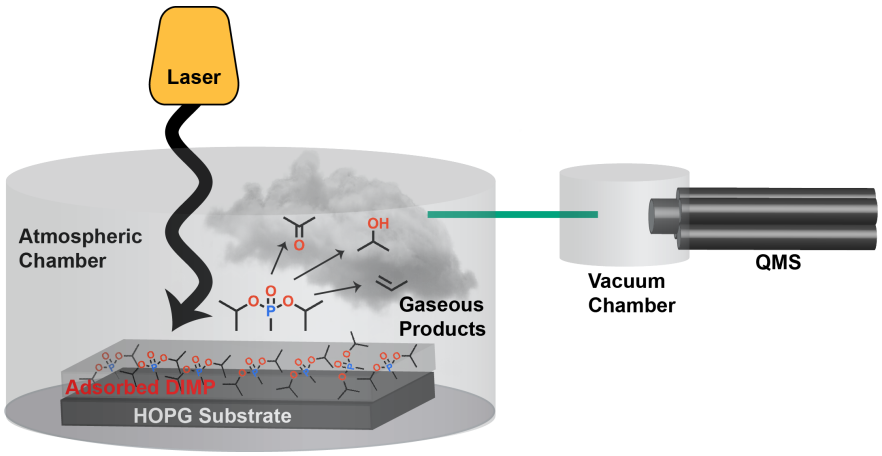

Figure 5.2: **Schematic layout of atmospheric ablation chamber**. We conducted laser ablation experiments in a joint atmospheric and high vacuum apparatus. We ablated condensed DIMP simulant films in an atmospheric chamber with a Nd:YAG laser; gaseous products are transported via capillary (green) to a high vacuum chamber containing a QMS for analysis.

ordered pyrolytic graphite crystal (HOPG, Bruker). In addition to chamber purging, we exfoliated the HOPG surface between trials to ensure reproducible surface quality and composition. To begin each experiment, we deposited 10 μL of DIMP (Alfa Aesar) on the HOPG surface and sealed the chamber. A background mass scan was then collected; final product analysis was performed on the background-subtracted spectra collected following ablation.

We ablated DIMP films with pulses from a Nd:YAG laser (Quanta-Ray GCR 130) producing near-IR photons at 1064 nm. To estimate the surface temperature on the HOPG substrate induced by the laser pulse, we carried out the following calculation for one-dimensional heat flow into a semi-infinite slab of material (transverse propagation of the beam is large compared to the depth of heat conduction into the film). Assuming that the optical absorption coefficient of HOPG is large (on the order of 10^4 – 10^6 cm^{-1}),[139–142] the surface temperature of the HOPG surface at time t can be calculated as:[143]

$$T(0,t) = \frac{2F_0}{K}\left(\frac{\kappa t}{\pi}\right)^{1/2} \tag{5.1}$$

In **Equation 5.1**, F_0 is the absorbed incident flux from the laser, K is the thermal conductivity of HOPG and κ is the thermal diffusivity (reported as 290 W m^{-1} K^{-1} and 0.000165 m^2 s, respec-

tively).[144] In practice, the total pulsed laser power is first measured with a Scientech calorimeter (Model 38-0101). We then convert this output to pulse energy by incorporating the pulse frequency (20 Hz) and scaling to the duration of individual pulses (8 ns). Pulse energies in this study range from 0.103 to 0.244 J. This total flux is further scaled to the reflection coefficient of HOPG (reported as 0.21 at 300 K).[139] With this model, peak laser powers raise the crystal temperature to approximately 2830 $\pm$ 110 K at a heating rate of 3.2 $\times$ 10^{11} K s^{-1}. The error cited for temperature is a standard propagation including error from the calorimeter measurement, pulse width, and HOPG reflection coefficient. We note that simulant films were ablated for 2 minutes at 20 Hz in order to generate sufficient product signal for analysis. However, product signals (propene at m/z = 41, for example) were detected for single pulse ablations and thermocouple measurements of the HOPG crystal show a steady-state temperature rise of only approximately 350 K as a result of the extended ablation. We therefore assume that the modest temperature rise caused by extended ablation is negligible compared to the high temperatures during each individual pulse.

MS analyses involved a series of steps illustrated with representative data in **Figure 5.3**. To begin, background spectra were subtracted from post-ablation spectra (**Figure 5.3a**). Next, the MALDIquant R package was used for data smoothing (using a 7-point Savitzky-Golay-filter, **Figure 5.3b**) and peak detection.[145,146] In order to deconvolve the spectra into individual product contributions, it was first necessary to build a library of fragmentation patterns for the proposed products. To this end, mass spectra were collected for propene (Sigma Aldrich), acetone, and isopropyl alcohol (IPA, both from Thermo Fisher). The spectra for additional products, ethylene and acetylene, were obtained from reference data from the National Institute of Standards and Technology (NIST).[147] Once this library was complete, the relative product contributions for the ablated spectra were determined using a least-squares analysis (**Figure 5.3c**). We note that though present in the background-subtracted spectra, large peaks associated with atmospheric gases like N_2, O_2, Ar, and so forth, were excluded from this deconvolution procedure because of the difficulty separating trace product signals from atmospheric contributions. The omission of m/z = 27 and 28 in particular made it difficult to distinguish ethylene and acetylene. Therefore, all discussions herein

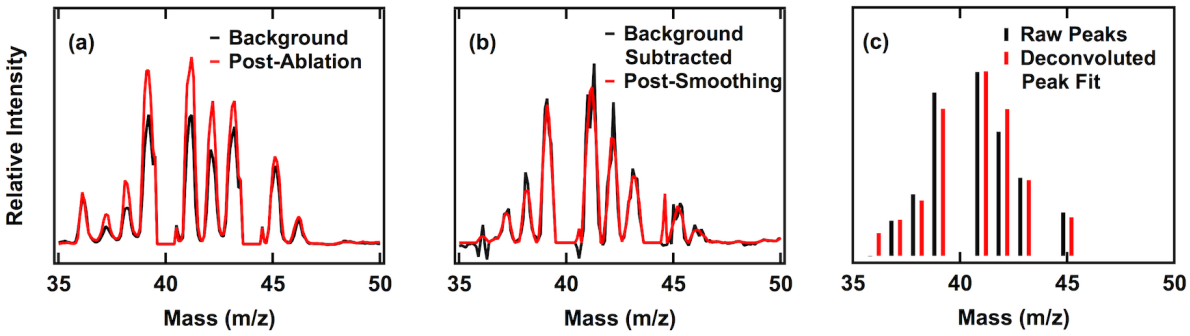

Figure 5.3: **Representative analysis of DIMP mass spectra**. We process and analyze MS of ablated DIMP in three steps. Background spectra are subtracted from post-ablation spectra (a). These background-subtracted spectra are smoothed (red, b) and peaks are detected (black bars, c). A least-squares procedure is used to determine relative product yields and reproduce the ablated spectra (red bars, c).

will group these two-carbon products together.

In addition to MS, we used a second modular chamber for concurrent *ex situ* FTIR analysis of ablated products. To begin these experiments, we purged a 150 cm^3 IR cell with ZnSe windows to approximately 25 mTorr. We then connected the chamber via a leak valve to an analogous atmospheric chamber for simulant ablation. Following the ablation procedure, the valve was opened, allowing the evolved gaseous products to escape into the purged chamber. The contents of the unheated chamber were analyzed using a Nicolet iS50 infrared spectrophotometer (Thermo Fisher) and a liquid-nitrogen-cooled MCT/A detector. We averaged all such FTIR spectra over 200 scans at 4 cm^{-1} resolution; peak fitting analysis utilized Gaussian peaks atop cubic baselines.

5.3 Results and Discussion

5.3.1 FTIR Product Analysis

Previous investigations into the thermal destruction of DIMP have consistently identified a number of products including propene, IPA, and ethylene. These studies include destruction via pyrolysis, combustion, exposure to a corona discharge, dissociative adsorption, laser ablation, and so forth.[66,68,76,126,127,148] While this provides a reasonable set of products to look for, the current

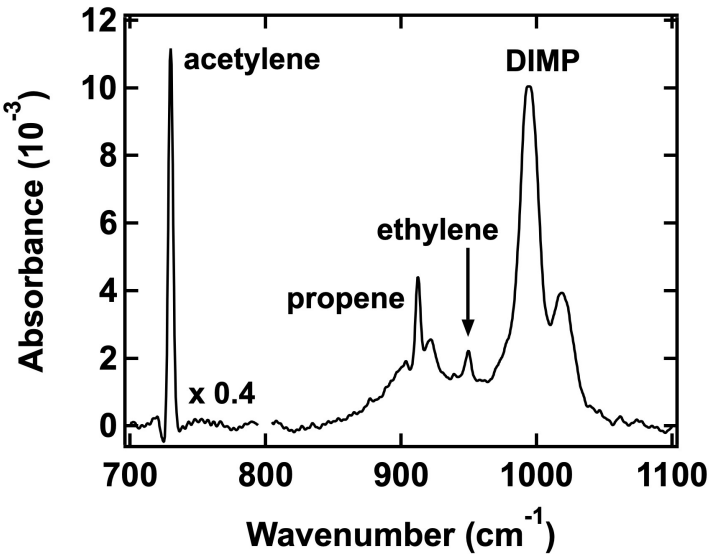

Figure 5.4: **Representative FTIR spectrum of ablated DIMP**. Following ablation to approximately 2720 K, FTIR spectra show clear evidence of residual DIMP as well as acetylene, propene, and ethylene products.

work represents the first direct study of rapid laser heating (on the order of 10^{11} K s^{-1}) of adsorbed liquid DIMP under atmospheric pressure and oxygen-depleted conditions. It is therefore necessary to firmly establish the full range of products before attempting to assess branching ratios; this was done using *ex situ* FTIR. The representative spectrum of ablated DIMP in **Figure 5.4** shows clear evidence of propene, ethylene, acetylene, as well as contributions from unreacted DIMP or other partially decomposed organophosphonate fragments such as isopropyl methylphosphonate (IMP). In addition to the prominent phosphonate P-O-C stretching modes at 995 and 1020 cm^{-1}, we observe significant signal intensity from propene's $=CH_2$ wagging mode (912 cm^{-1}) and the bending modes of acetylene and ethylene (730 cm^{-1} and 949 cm^{-1}, respectively). All peaks referenced herein are consistent with those reported for the corresponding molecules in the gas phase.[39,101,102,147,149–152] CO is also observed, but this is difficult to uniquely assign to either DIMP or HOPG ablation. Additionally, other small product peaks are observed in the spectra beyond those highlighted in **Figure 5.4**, but we were not able to clearly establish their identities using FTIR alone.

In both FTIR and the following MS analyses, we note that the scope of our experiment did not

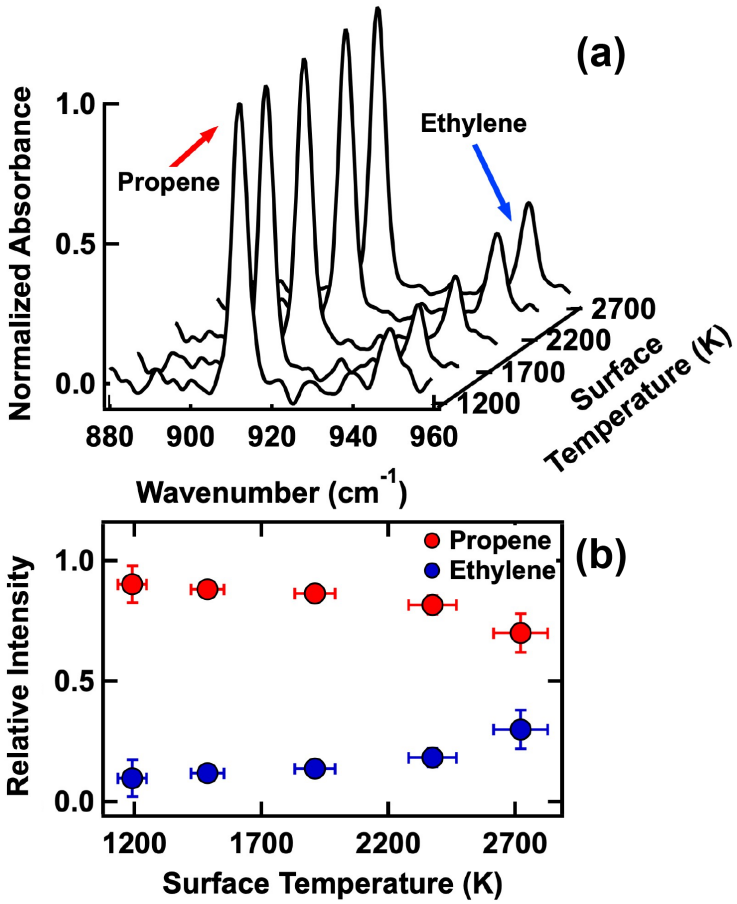

Figure 5.5: **FTIR - product distribution with increased surface temperature**. Relative production of ethylene and propene changes as a function of laser ablation power. FTIR spectra normalized to propene height (a) demonstrate increases in relative ethylene production as surface ablation temperature increases. Baseline and other product peaks have been subtracted for clarity. The relative integrated area of the associated peaks (b) shows that this trend is observed throughout the temperature range explored in this study (error bars represent the standard deviation of at least three trials at each ablation temperature).

include direct quantification of condensed-phase products or parent molecules remaining on the HOPG substrate or in the atmospheric chamber. Similar to other studies, however, our gas-phase product analysis suggests that it is primarily phosphorus-containing products that remain following thermal destruction.[66,153] In addition to unreacted DIMP, these products likely include IMP and methylphosphonic acid (MPA).

As laser power (and thereby HOPG surface temperature) is increased, an interesting trend emerges in the relative distribution of products. When we normalize spectra to the height of the

propene peak, we see a corresponding relative increase in the height of ethylene (**Figure 5.5a**). If the relative areas of these two peaks are plotted as a function of HOPG surface temperature (**Figure 5.5b**), it becomes clear that as the ablation temperature increases, ethylene production increases relative to propene. The same trend is observed for relative propene and acetylene production. Without precise absorption cross-sections for these compounds it is difficult to quantify the absolute amount of each product formed. It is clear, however, that higher temperatures lead to a higher yield of smaller substituted carbon products.

5.3.2 Effects of Varying Surface Temperature

The results described in the preceding section were easily replicated with *in situ* mass spectrometry. However, it is important to note that the MS data reveal some additional minor products unidentified in the FTIR data. FTIR spectra provided no conclusive evidence of oxygenated ablation products, despite their suggested presence in other pyrolytic and thermal decomposition studies of DIMP.[68,76,126] Background subtracted mass spectra of ablated DIMP, however, show clear increases in m/z = 43 and m/z = 45 (acetone and IPA, respectively). The yield of both of these products is consistently small relative to propene and ethylene/acetylene, so their absence in FTIR spectra may simply be due to lack of sensitivity. Therefore, mass spectra are deconvoluted into contributions from four observed products: propene, ethylene/acetylene, acetone, and IPA. **Figure 5.6** shows the least-squares fit for the data collected in three representative trials at different ablation powers. When the data are normalized to propene signal (m/z = 41), there is a clear corresponding relative increase in the amount of the smaller acetylene and ethylene products. In other words, these results again suggest that peak surface temperatures impact the extent of bond cleavage and identity of destruction products.

5.3.3 Effects of Varying Atmospheric Oxygen

In order to probe the role of atmospheric oxygen in DIMP destruction, we performed a series of experiments with variable partial pressures of oxygen. Following simulant deposition, the sampling

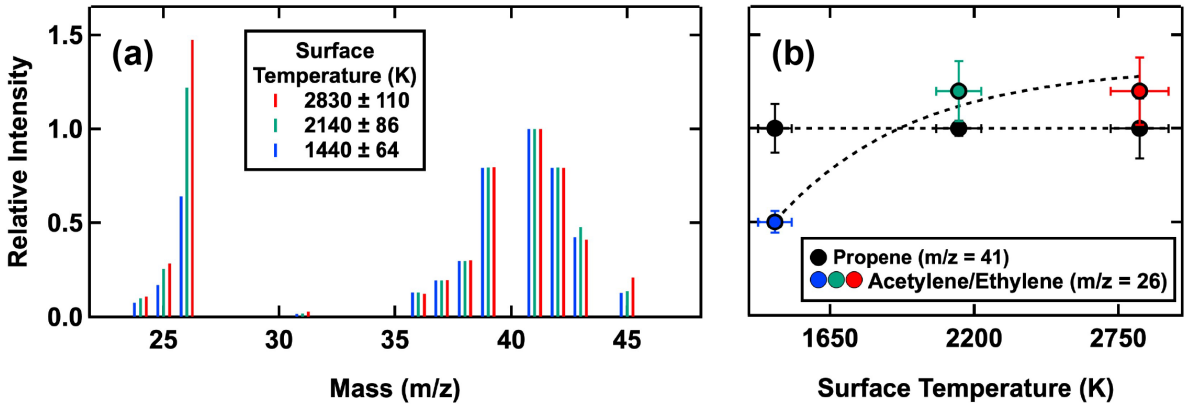

Figure 5.6: **MS - product distribution with increased surface temperature**. Reproduced representative mass spectra (a) from a least-squares fit of the data (normalized to propene signal at m/z = 41) show an increase in low molecular weight products (ethylene and acetylene) as laser power is increased. This can also be seen in the normalized relative intensities of propene and acetylene/ethylene (m/z = 26) averaged across all trials (b). Ablation surface temperatures are 1440 K (blue), 2140 K (green), and 2830 K (red). Dotted line is drawn to guide the eye.

chamber was carefully purged with N_2 until a desired oxygen pressure was reached (as measured with the QMS). The chamber, however, was still maintained at atmospheric pressure. After ablation at the highest laser powers, the results in **Figure 5.7** show that the presence of oxygenated products plummets nearly to zero when atmospheric oxygen is reduced. Signals associated with both acetone (m/z = 43) and IPA (m/z = 45) decrease sharply relative to propene (m/z = 41). *This observation is of critical importance; it demonstrates clearly that atmospheric oxygen is incorporated directly into the fragmenting DIMP molecule.*

5.3.4 Mechanism of Destruction

We summarize the effects of varying both ablation surface temperature and atmospheric composition in **Table 5.1**. Each entry represents the average of at least three similar trials. In brief, we observe that higher ablation temperatures lead to an increase in the relative production of shorter chain substituted products (ethylene/acetylene vs. propene). Additionally, a reduction in available atmospheric oxygen leads to a decrease in the relative production of oxygenated products (acetone and IPA vs. propene). These results inform the following discussion of the mechanisms underlying

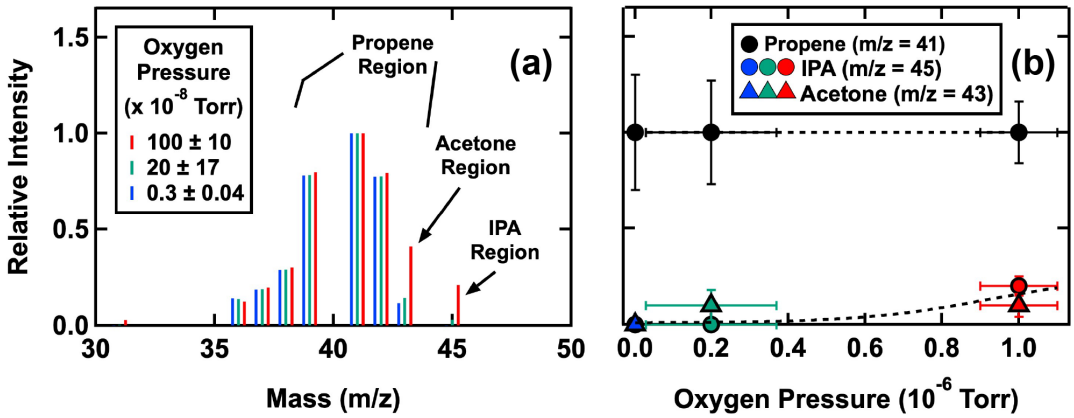

Figure 5.7: **MS - product distribution with decreased atmospheric oxygen**. Reproduced representative mass spectra (a) from a least-squares fit of the data (normalized to propene signal at m/z = 41) show a sharp decrease in oxygenated products as available oxygen decreases. This can also be seen in the normalized relative intensities of propene, IPA (m/z = 45) and acetone (m/z = 43) averaged across all trials (b). Recorded oxygen pressures in the QMS chamber were 1×10^{-6} Torr under atmospheric ablation conditions (red), 2×10^{-7} under low oxygen conditions (green), and 3×10^{-9} Torr under oxygen-depleted conditions (blue). Dotted line is drawn to guide the eye.

the thermal destruction of condensed-phase DIMP.

To begin, it has been proposed experimentally and theoretically that that the primary pyrolytic destruction step for DIMP and other similar molecules is a unimolecular decomposition to IMP and propene via a six-membered ring transition state.[66,154–156] Moreover, propene production has been observed under a variety of high temperature conditions, beginning with temperatures as low as 700 K, which is lower than the ablation range studied here.[66,137] In vacuum studies, propene is also produced as a result of dissociative adsorption of DIMP.[76,109] Essentially, many studies agree that a major step in DIMP destruction involves the formation of propene. On the other hand, few studies have identified direct mechanisms that yield smaller substituted products from DIMP's initial dissociation (and indeed no single initial bond scission is enough to yield a two-carbon product from DIMP directly). Instead, it is likely that the smaller products (ethylene, acetylene, methane, etc) are produced as secondary destruction products of propene.[157,158] The results of this work present evidence that indeed propene is likely one of the first products, and that higher ablation temperatures increase the relative extent of further fragmentation.

The results of the oxygen study add interesting detail to the existing mechanistic picture.

Chamber Conditions		Relative Product Contributions			
Oxygen (Torr)	***T_s (K)***	***IPA***	***Acetone***	***Propene***	***Ethylene/Acetylene***
$(1\pm0.1)\times10^{-6}$	2830 ± 110	0.2 ± 0.05	0.1 ± 0.06	1 ± 0.16	1.2 ± 0.18
$(1\pm0.1)\times10^{-6}$	2140 ± 86	0.2 ± 0.03	0.1 ± 0.12	1 ± 0.04	1.2 ± 0.16
$(1\pm0.1)\times10^{-6}$	1440 ± 64	0.1 ± 0.08	0.4 ± 0.13	1 ± 0.13	0.5 ± 0.06
$(1\pm0.1)\times10^{-6}$	2830 ± 110	0.2 ± 0.05	0.1 ± 0.06	1 ± 0.16	1.2 ± 0.18
$(2\pm1.7)\times10^{-7}$	2830 ± 110	0.0 ± 0.03	0.1 ± 0.08	1 ± 0.27	4.2 ± 0.86
$(3\pm0.4)\times10^{-9}$	2830 ± 110	0.0 ± 0.0	0.0 ± 0.0	1 ± 0.30	7.0 ± 1.49

Table 5.1: **Normalized product ratios following DIMP ablation**. Summary of all DIMP ablation experiments performed, normalized to propene production. As surface temperature is increased, the relative ratio of ethylene and acetylene to propene increases. As available oxygen is decreased, the relative production of IPA and acetone decreases.

Zegers and Fisher proposed a two-step pyrolysis mechanism for DIMP, beginning with the unimolecular decomposition that yields propene. The second step involves transfer of a hydrogen from the phosphorous hydroxyl group to the oxygen of the isopropoxy group, yielding IPA and methyl dioxophosphorane.[66,68] Our observations suggest, however, that this intermolecular step may not be the primary mechanism for IPA formation at these high-temperature, fast-heating, and condensed-phase conditions. Instead, atmospheric O_2 or radicals formed from thermal dissociation may abstract hydrogens or break bonds in the DIMP molecule directly. For example, if an alkyl radical forms upon scission of the P-O-C bond, atmospheric O_2 can readily add to generate an alkoxy radical. This species, in turn, is expected to react or decompose readily to form both the observed acetone and IPA.[122,159,160] The direct incorporation of oxygen from the atmosphere in this proposed mechanism would account for the observed dependence on oxygen pressure in the ablation chamber in the production of oxygenated products.

5.4 Conclusion

Building on work investigating pyrolysis, dissociative adsorption, and laser ablation of chemical warfare agents and their simulants, this study presents a comprehensive look at rapid thermal ablation of condensed DIMP under atmospheric pressure conditions. Decomposition products observed include propene, ethylene, acetylene, IPA, and acetone, which are well in line with existing

literature on thermal destruction of organophosphonates. Product distributions varied significantly when both laser power (HOPG surface temperature) and oxygen content were altered; higher ablation powers led to higher temperatures, which increased the extent of secondary fragmentation in alkene and alkyne products observed. Lower oxygen partial pressures led to a sharp decrease in oxygenated products, suggesting that a dominating mechanism in this system involves direct incorporation of atmospheric oxygen into product fragments.

Though Sarin, unlike DIMP, includes a fluorine substituent on the central phosphorus atom, there is reason to believe the results highlighted here have direct relevance for Sarin's thermal destruction. Experimental work with simulants and nerve agents has shown significant correlation between bond frequency and desorption energies, suggesting that simulants like DIMP are indeed appropriate for modeling the chemistry of toxic agents.[33] Perhaps more importantly, pyrolytic simulations of Sarin have confirmed that thermal destruction begins with the same six-center intermediate that leads to propene elimination.[68] Therefore we expect that the chemistry observed in these temperature-jump experiments is relatively generalizable to Sarin and other organophosphonates.

In addition to validating the applicability of these results on live nerve agents, extensions of this work may include tracking the destruction temperature thresholds and product distributions for additional simulants and simulant mixtures, as well as the impact of incorporating less absorptive or reactive substrates. In general, this work continues to shed light on the basic mechanisms of organophosphonate thermal destruction, related to those encountered under high temperature rapid heating blast conditions. These results are critical for the accurate modeling of environmental persistence and implementation of mitigation strategies for chemical warfare agents and other organophosphonate pesticides.

Chapter 6

Sticking Probability of High-Energy Methane on Crystalline, Amorphous, and Porous Amorphous Ice Films

We present research detailing the sticking probability of CH_4 on various D_2O ices of terrestrial and astrophysical interest using a combination of time-resolved RAIRS and King and Wells mass spectrometry techniques. As the incident translational energy of CH_4 increases (up to 1.8 eV), the sticking probability decreases for all ice films studied, which include high-density, non-porous amorphous (np-ASW) and crystalline (CI) films as well as porous amorphous (p-ASW) films with various pore morphologies. Importantly, sticking probabilities for all p-ASW films diverge and remain higher than either np-ASW or CI films at the highest translational energies studied. This trend is consistent across all porous morphologies studied and does not depend on pore size or orientation relative to the substrate. We propose that in addition to offering slightly higher binding energies the porous network in the D_2O film is very efficient at dissipating the energy of the incident CH_4 molecule. These results offer a clear picture of the initial adsorption of small molecules on various icy interfaces; a quantitative understanding of these mechanisms is essential for the accurate modeling of many astrophysical processes occurring on the surface of icy dust particles.

6.1 Introduction

To create accurate models of the chemical and physical processes occurring in atmospheric and terrestrial environments, it is necessary to examine molecular and atomic adsorption onto frozen water ices.[161,162] Furthermore, understanding the interactions between gas molecules and different molecular ices can help to classify the composition and the history of complex multicomponent ices.[163] Adsorption on icy surfaces, in astrophysical environments for instance, is a critical first step in a variety of recombination and addition reactions, some resulting in the formation of small organic molecules.[164,165]

Ice can exist in a variety of crystalline and amorphous forms. Crystalline (CI) water ice with its hexagonal lattice is the most common form of snow and ice on Earth[166] and can also be found in warmer astrophysical environments.[167] Amorphous solid water (ASW), on the other hand, is the most abundant form of water in astrophysical environments[168] and is present in comets, planetary rings, and interstellar clouds.[22] ASW can be classified into two types: high-density nonporous (np-ASW) and low-density porous (p-ASW) based on its pore structure.[169] In general, ASW morphology plays a significant role in the adsorption of volatile gas species within astrophysical ices.[170–172] Although not yet found in such environments, p-ASW can exist as the result of heterogeneous molecular synthesis occurring on dust grains in the interstellar medium (ISM).[173] Exposure to ultraviolet light, X-rays, cosmic radiation, or thermal processing can also induce morphological changes in astrophysical ices[162,172–174] Over time and as a result of these processes, ASW ices can become CI and vice versa. Because of this, there is an interest in understanding the precise role of surface morphology in gaseous adsorption.[175]

In this work we use high-energy projectiles to examine adsorption mechanisms on various astrophysical ices. A particular focus is on porous amorphous water ices and how the pore structure influences the energy accommodation and uptake of incident molecules. In general, a molecule impacting a surface adsorbs if it loses enough of its kinetic energy to the lattice upon impact.[176] Accurate measurements of sticking probabilities are essential because a higher sticking probability

can lead to greater observed reactivity as has been shown other molecules on amorphous ices.[177]

We present the first study examining the sticking probability of CH_4 as a function of translational beam energy on p-ASW of varying porosities, np-ASW, and CI D_2O ice films under UHV conditions using the King and Wells method and molecular beam techniques (**Subsection 2.2.3**).[8] Molecular beams enable tunable control of incident energy, and thus precise knowledge of the sticking process.[178] We chose CH_4 for this work primarily due to its known presence in many astrophysical environments, including its potential incorporation in icy clathrates found in outer solar system bodies such as Titan.[173,179,180] Within those environments, reactions involving CH_4 can be a significant contributor to the formation of complex organic molecules.[181] Additionally, CH_4 will hopefully allow us to exclusively probe adsorption phenomena, because its light mass and lower momenta may preclude direct embedding underneath the surface.[23,182,183] We demonstrate that for the highest energy beam (1.8 eV), the sticking probability is higher for p-ASW than np-ASW and CI ices. For the p-ASW ices, we also determine that there is no difference in sticking probability as a result of increased porosity.

Our results build upon previous work in our group focused on the sticking probability of D_2O and H_2O on CI for incident translation energies ranging from 0.3 to 0.7 eV.[184] The sticking probability was near unity for those measurements and did not change as a function of water ice morphology or surface temperatures ranging from 140 to 155 K. By using CH_4 and expanding the water ice morphology to include amorphous water ices with and without pores as well as higher incident translational energies, our measurements provide a more complete understanding of the dynamics of sticking between projectiles and water ices. Such work is critical to creating accurate models of these processes occurring in atmospheric and terrestrial environments between water ices and CH_4. By examining the initial part of the uptake process, these results provide insight into the adsorption-desorption equilibrium for ices in the troposphere.[185] Beyond these astrophysical and environmental applications, the adsorption of molecules into solid materials is an important first step in many dynamic processes at interfaces in fields such as photo-catalysis, radiation chemistry, waste processing, and advanced materials synthesis.[170] Many commercial catalysts are porous

within these fields; these pore structures enable efficient sticking and transport of molecules.[186]

6.2 Experimental Section

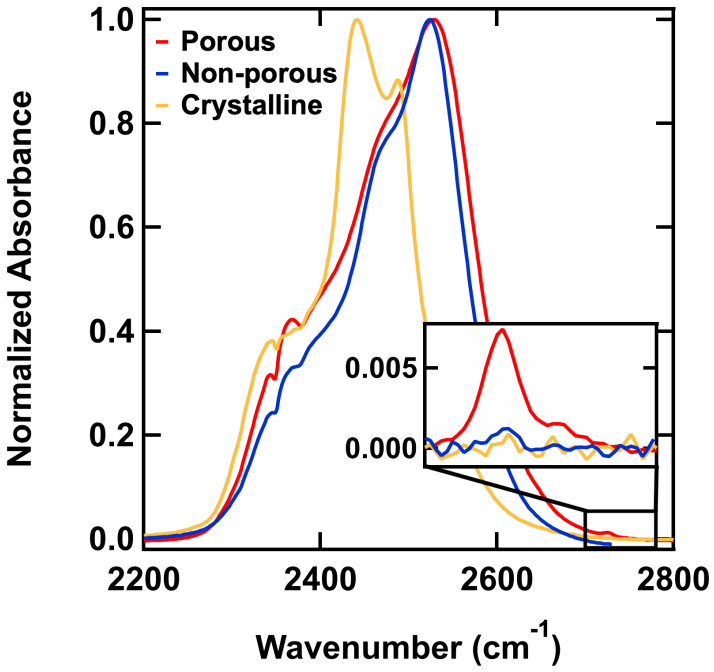

Figure 6.1: **Representative RAIR spectra of different water morphologies**. Normalized infrared spectra of the O-D stretch distinguish porous amorphous (p-ASW, red), non-porous amorphous (np-ASW, blue), and crystalline (CI, yellow) D_2O ices on Au(111) dosed at 25 K, 107 K, and 150 K, respectively. The inset demonstrates that while dangling O-D modes are observed for both ASW films, they are significantly more intense in the p-ASW films.

We performed all of the experiments described in this chapter in the molecular beam scattering instrument described in **Chapter 2**. Our primary analytical techniques were time-resolved RAIRS and King and Wells. All RAIR spectra were analyzed with Gaussian peaks atop either linear or cubic baselines, depending on the region. Each spectrum is an average of 70-200 scans taken using 4 cm^{-1} resolution with a clean Au(111) sample for the background. For ice preparation, we used D_2O (rather than H_2O) due to its preferable O-D stretch frequency that avoids overlap with the ν_3 methane mode.[187–189]

We produced D_2O films via directed doser (**Subsection 2.4.3**). D_2O was typically leaked in at a pressure of 2.0×10^{-9} Torr, leading to an average growth rate of 0.5 ML/min.[21] The ice films used

in this study were between 150 and 300 layers thick. While backfilling the chamber to a known pressure of D_2O, we collected RAIR spectra at regular time intervals during exposure, allowing for direct quantification of film thickness from integrated intensity of the large O-D stretch between 3600 cm^{-1} and 2800 cm^{-1} (**Subsection 2.4.3**).[190,191] **Figure 6.1** shows a typical normalized O-D stretch for the three different ice films used in this study. Following literature precedent and as a result of D_2O molecule coordination differences among these films, this region can be used to distinguish p-ASW, np-ASW, and CI films.[192] In particular, the interface of p-ASW films contains a significant fraction of three- and two-coordinated surface D_2O molecules ("dangling bonds") that can be clearly resolved spectroscopically at 2725 cm^{-1} and 2740 cm^{-1} respectively. Though also present in the np-ASW film, this dangling bond region is much lower intensity, reflecting the large difference in surface areas between porous and non-porous films.[188,193–195] The temperature of the substrate during dosing dictates the water ice morphology; the substrate temperatures used for ice growth were 150 K for CI, 107 K for np-ASW, and 25 K for p-ASW.[167,168]

To produce ASW films with increased porosity, we changed the angle of the directed doser relative to surface normal.[22,196,197] The films used in this study were produced at 30°, 60°, or 70° as well as via background deposition. As characterized by Stevenson et. al.,[22] porosity increases with deposition angle, so the D_2O films dosed at 30° are less porous than those grown at 60° or 70°.[198] The pores also grow with an orientation that matches deposition angle.[196] Although films produced via background deposition (backfilling the chamber with water vapor) are as porous as those grown at 70°, the water molecules approach the surface with thermal energy and random angular orientation resulting in nonuniform pore orientation and size.[196,197] The intensities of the dangling bond spectroscopic signals are known to roughly scale with porosity, so RAIR spectra can be used to qualitatively confirm that ices with different porosities have been formed.[199,200] Unless otherwise specified in this work, "p-ASW" refers to our default porous film grown at 30°, and porous films grown at other deposition angles (60, 70 and background) will be identified as such.

We produced CH_4 beams by expanding 1% CH_4 in H_2 or neat CH_4 at stagnation pressures

of 200-400 psi through a 10 μM molybdenum pinhole. Resistively heating the beam nozzle from room temperature to 970 K resulted in CH_4 translational energies of up to 0.3 eV for the neat CH_4 beam and up to 1.8 eV for the CH_4 beam seeded in H_2. The translational energy distribution widths (ΔE/E) ranged from 12% to 21%. For one experiment (investigating the impact of embedding phenomena), we also used a beam of CF_4, produced by expanding 1% CF_4 in H_2 at stagnation pressures of 300-500 psi through a 20 μM molybdenum pinhole. Resistively heating the beam nozzle to over 950 K resulted in a CF_4 translational energy of 5.3 eV with a ΔE/E $\approx$ 40%.

As described in **Subsection 2.2.3**, we determined sticking probability using the King and Wells technique.[8,9] To conduct multiple trials with a given film, we first annealed the ice to 70 K for 30 min. While this reduced porosity slightly, it ensured that repeated King and Wells cycles did not further alter the film morphology throughout the day.[186,196,201] We also explored the generalizability of our results by comparing the sticking probabilities for CH_4 on np-ASW, p-ASW, and CI H_2O films. We note that for all the CH_4 translational energies studied, the sticking probability values were the same as those observed for D_2O ices; we did not observe any significant isotopic effect at our experimental resolution, as has been previously detected between D_2O impinging on H_2O and D_2O ices.[202]

6.3 Results

6.3.1 King and Wells

We performed King and Wells measurements of initial sticking probabilities on a prepared ice substrate held at 33.5 K for all results presented in this study. This temperature choice reflects a number of important considerations related to both the nature of the CH_4/D_2O interaction and the King and Wells method itself. As discussed by He et al., there are three potential challenges with performing King and Wells measurements for this ice system.[175] First, the liquid helium cooling of the sample manipulator may impact the pumping speed of the chamber, thereby altering the reflected portion of the beam at different sample temperatures. We avoid this by taking

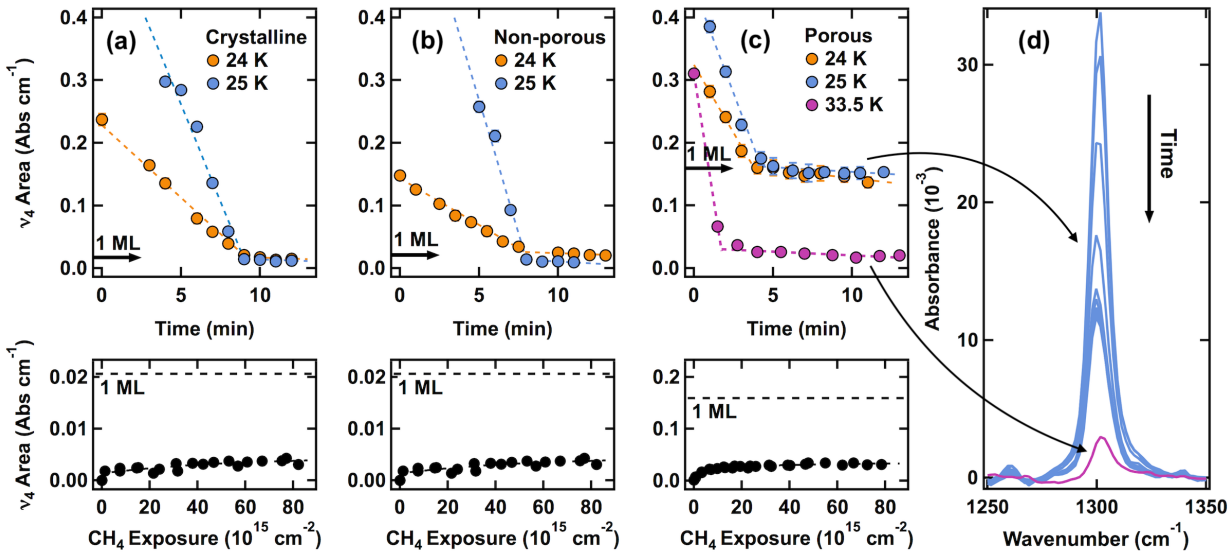

Figure 6.2: **Isothermal desorption of CH_4 from ice**. Isothermal desorption of multilayer CH_4 from crystalline (CI, a), non-porous amorphous (np-ASW, b) and porous amorphous (185 layers, c) ice films (top) allows for quantitative estimation of monolayer thickness, as measured via the integrated absorbance of the ν_4 mode. Growth of the same peak area during exposure at 33.5 K (bottom) confirms that the amount of adsorbed CH_4 is significantly less than a full monolayer for each type of ice. This is also demonstrated in the corresponding RAIR spectra for desorption a 25 K (blue, d) and 33.5 K (pink, d).

all measurements at a single sample temperature, where the unknown improvement in chamber pumping speed is consistent across experiments. Second, because CH_4 interacts with the ice surface via weak dispersion forces rather than direct chemisorption, these experiments require low surface temperatures. Furthermore, ice surfaces have a wide range of binding sites and binding energies.[203–205] These two factors present a second challenge; a well-defined saturation of the CH_4 reflected signal might be difficult to observe over short exposure time scales. Although full reflection may ultimately be observed with long exposures, CH_4 desorption as well as finite adsorption of background H_2O and D_2O at these low temperatures over long timescales compete to prevent signal saturation. As such, all initial sticking probability measurements referenced herein are calculated using the initial CH_4 indirect flux rather than the value at saturation (after surface sites are filled). These considerations, therefore, are mitigated by our experimental setup.

Beyond the aforementioned considerations, we are also specifically interested in quantifying the initial sticking probabilities in the low coverage, submonolayer regime. This is desirable be-

cause the concentrations of small molecules in the ISM are typically quite low.[206] Moreover, we want to eliminate any contribution from multilayer sticking, which occurs more readily in porous films, even at higher surface temperatures.[186,198] As such, the desired temperature regime should be high enough to restrict all sticking to submonolayer.[196] In light of these considerations, we selected 33.5 K as the surface temperature of interest. At this temperature, however, the monolayer is not perfectly stable on the surface. While this does not impact the measurements of initial sticking probabilities, CH_4 surface coverage at long exposure time scales will reflect contributions from both adsorption and desorption. By explicitly quantifying and accounting for the rates of desorption, we also account for the third concern with King and Wells measurements, which is that they typically do not have the time resolution to distinguish between molecules that are directly reflected from the surface and those that adsorb for a short time and then desorb again.

As shown in the top panels of **Figure 6.2a-c**, quantification of the monolayer was established via isothermal desorption experiments for each ice film. After dosing a multilayer film of CH_4 at 20 K, we tracked the integrated area of the ν_4 mode over time at an elevated temperature.[189,207–209] A distinct slope change is observed when multilayer desorption changes to monolayer, thereby allowing for an approximate quantification of monolayer thickness. The bottom panels of **Figure 6.2a-c** show that when we hold the surface at 33.5 K (as during a King and Wells experiment), the total amount of adsorbed CH_4 reaches a maximum far below the respective monolayer thickness for each type of ice film. Measured desorption rates for all films at 33.5 K are similar in magnitude to the incident CH_4 flux, so this steady-state maximum indicates that only a small fraction of the monolayer is stable on the surface over long timescales (as shown in **Figure 6.2c** in pink).

Figure 6.2 highlights another important feature of this system, which is that the monolayer thickness (and uptake at 33.5 K) on the porous film is significantly higher than uptake on either CI or np-ASW films (likely due to the increased surface area).[210] This effect has been well-documented previously – Kimmel et. al. demonstrated, for example, that a 50 layer film of p-ASW deposited at 30° sees a total CH_4 adsorption of 2 monolayer equivalents.[196] On this basis one might expect, therefore, that a 185 layer film (as used in **Figure 6.2c**) would likewise adsorb

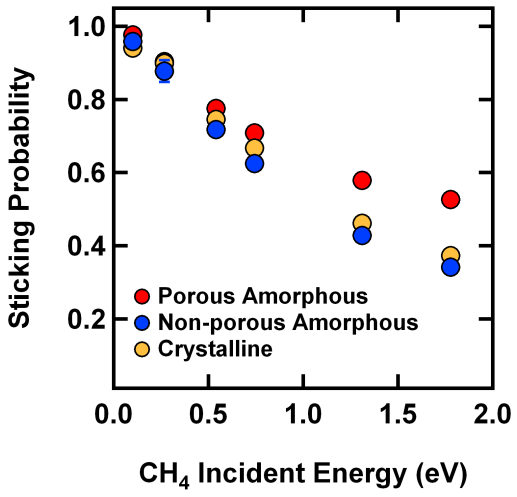

Figure 6.3: **CH_4 sticking probabilities - p-ASW, np-ASW, and CI**. Sticking probabilities for CH_4 on porous (p-ASW, red), non-porous (np-ASW, blue) and crystalline (CI, yellow) D_2O films held at 33.5 K. Sticking probability decreases for all films as incident CH_4 energy increases, but remains higher for the porous film. Error bars represent the standard deviation of at least three measurements on at least two different days.

roughly 7-8 monolayers of CH_4. Indeed, the data show that the p-ASW monolayer adsorption is almost exactly 8 times that of the CI and np-ASW films. Similarly, steady-state adsorptions at 33.5 K are on the order of 10^{14} CH_4 cm^{-1} on the p-ASW films and 10^{13} CH_4 cm^{-1} on CI and np-ASW films.

Figure 6.3 contains the measured sticking probabilities for CH_4 on crystalline (CI), non-porous (np-ASW), and porous (p-ASW) D_2O films. Clearly, as the CH_4 incident energy increases, the observed trend on the porous film diverges from both CI and np-ASW; sticking probabilities remain significantly higher for the porous film. This divergence will be discussed in further detail below. First, however, it is important to note that crystalline and non-porous films display nearly identical sticking probability trends throughout the range of incident energies studied. This insensitivity to morphology (CI versus np-ASW) has been observed in other experimental and theoretical systems, including D_2O sticking on H_2O and D_2O,[202] H_2O sticking on H_2O,[176] and CO sticking on H_2O.[166,211] The theoretical work of Al-Halabi et. al., for example shows not only that the sticking of CO is nearly equal between np-ASW and CI H_2O films, but also an exponential decay of sticking probability with incident translational energy that is roughly comparable to that measured

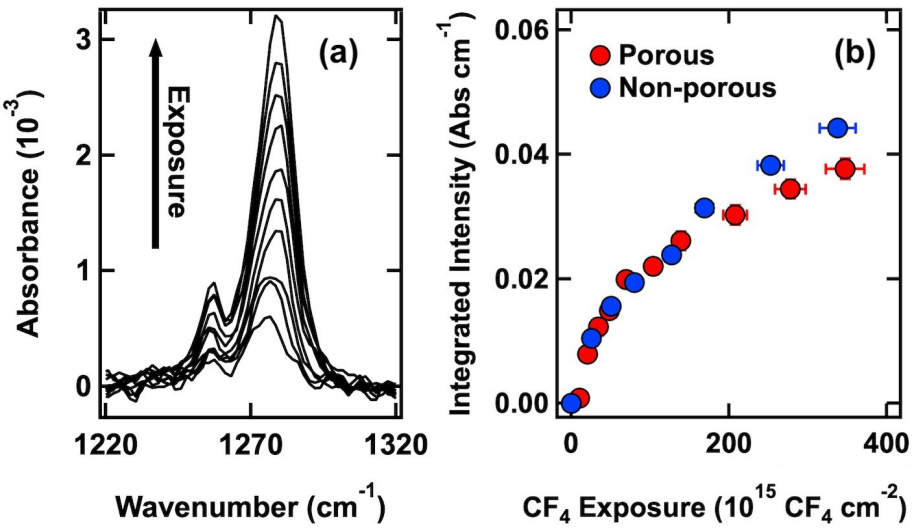

Figure 6.4: **CF_4 embedding in p-ASW and np-ASW**. (a) RAIR spectra collected throughout CF_4 exposure show clear signal growth at 1276 and 1257 cm^{-1}. (b) The integrated area of these CF_4 peaks is proportional to the amount of CF_4 that remains embedded in the surface. Both p-ASW and np-ASW films show similar rates of uptake, indicating that the barrier for ballistic embedding into porous films matches that established in previous works for non-porous films. This figure highlights the trend for a porous film deposited at 30° from surface normal, but there are no significant differences in embedding rates for any of the porous films studied in this work.

in this study.[166]

It is important, when discussing adsorption to both porous and non-porous films, to elucidate the contribution of any penetration of the incident CH_4 into the bulk ice. Previous work in our lab identified a significant activated uptake channel for incident projectiles in the ice bulk (termed "embedding").[23,182,183] After investigating this process for a range of molecules in np-ASW H_2O, we established a clear momentum barrier for this channel (embedding probabilities in CI films were significantly lower than those observed for np-ASW). In general, the momenta reached in the current chapter (using the relatively light CH_4) are well below this barrier, so no embedding is expected in either np-ASW or CI films. There is, however, the question whether the use of D_2O (rather than H_2O) or a more porous ice morphology will effectively lower this barrier, making direct comparisons of sticking probabilities across more challenging films. To examine this, we exposed both porous and non-porous D_2O ice films to beams of 5.3 eV CF_4. We selected CF_4 because it has a higher mass and has been successfully used in previous embedding experiments.

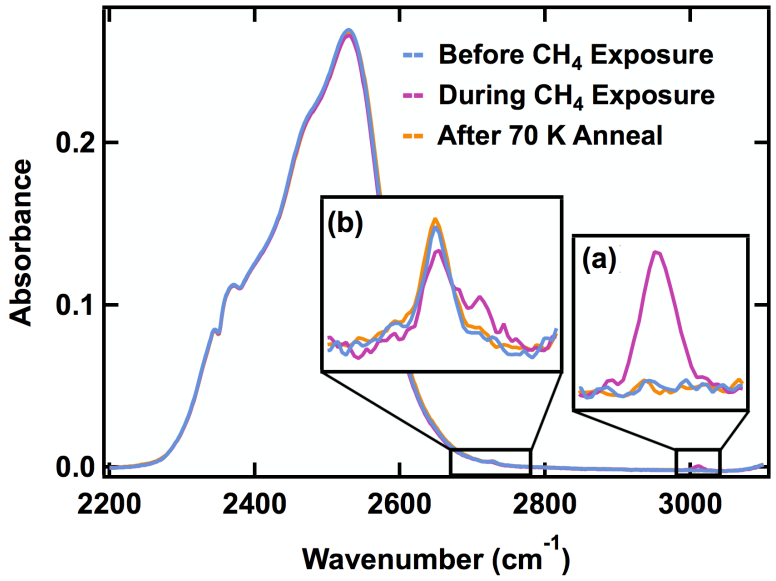

Figure 6.5: **D_2O films before, during, and after CH_4 exposure**. RAIR spectra of D_2O films are unchanged by CH_4 exposure and subsequent anneal. During exposure, some CH_4 adsorbs to the surface (a), and the dangling O-D stretching mode is slightly red-shifted (b). Annealing to 70 K removes all CH_4 and leaves the original D_2O film unchanged.

All such ballistic embedding experiments were performed with the films held at 70 K to mimic ice preparation conditions used during sticking probability experiments and to preclude a significant surface adsorption channel for CF_4 on the ice. RAIR spectra were collected at regular intervals during exposure to quantify the increase in stable, embedded CF_4 within the ice film (**Figure 6.4a**). These growth rates closely match data collected in previous works, indicating no major differences between D_2O and H_2O ice films (**Figure 6.4b**). Furthermore, the rates of embedding are nearly identical for both p-ASW and np-ASW. Therefore, we expect the previously reported momentum barrier for np-ASW to hold for p-ASW, preventing CH_4 embedding in all of the ice films discussed herein. Indeed, RAIR spectra collected during anneal cycles to 70 K after King and Wells experiments (as well as RGA monitoring of ice desorption at the end of the day) confirm that there is no discernible uptake of CH_4 into the ice bulk; all CH_4 is surface adsorbed.

Though we have demonstrated that there are no differences in embedding phenomena, there are other ways in which CH_4 may interact differently with the p-ASW structure, thereby impacting the observed sticking probability. First, we observe no discernible sputtering of the water film by

the CH_4 beam. Though sputtering of astrophysical ices has been reported, the impinging species in these works are typically either charged and/or significantly higher in energy.[212–216] In other words, we do not expect the momentum transfer for the CH_4/D_2O system to be significant enough to desorb water molecules from the surface, nor is there any possibility for electronic sputtering. Second, there is also a large body of research investigating the impact of fast, heavy ions on the morphology of ice films. Specifically, high energy ions (mimicking the effect of cosmic rays) have been shown to compact the pores of vapor-deposited ices.[203,217–219] Even the relatively low energy release of H_2 recombination (4.5 eV) on the surface of ice can have a similar compaction effect.[193] Though it appears unlikely, it is important to investigate the possible impact that CH_4 may have on the morphology of the porous D_2O films used in this study. **Figure 6.5** depicts representative regions from RAIR spectra of the film before, during, and following CH_4 exposure. Upon exposure to CH_4 (**Figure 6.5a**), there is a slight red shift in intensity of the dangling O-D mode (**Figure 6.5b**). This shift is well documented in FTIR studies of sequential CH_4/H_2O depositions, and indicates that some of the surface D_2O molecules are coordinating with the adsorbed CH_4.[187,195] After annealing the sample back to 70 K following the experiment, however, all CH_4 desorbs and there are no lasting changes in the O-D stretch or the dangling O-D peaks. This indicates that the water film height, morphology, and porosity are not impacted by CH_4 sticking experiments, even at the highest energies studied (1.8 eV).

6.3.2 Amorphous Films, Varied Porosity

In the previous section, we established that sticking probabilities of CH_4 are higher for p-ASW films than either np-ASW or CI films at high incident energies. This comparison, however, only includes porous films deposited at 30° relative to surface normal. **Figure 6.6** depicts the sticking probabilities for CH_4 on a variety of porous films, including those deposited via directed doser (at 30°, 60°, and 70° from surface normal) as well as via background deposition. Surprisingly, there is no strong variation in sticking probabilities for CH_4 on any of these films, despite the expected differences in pore orientation and film density.[197,220]

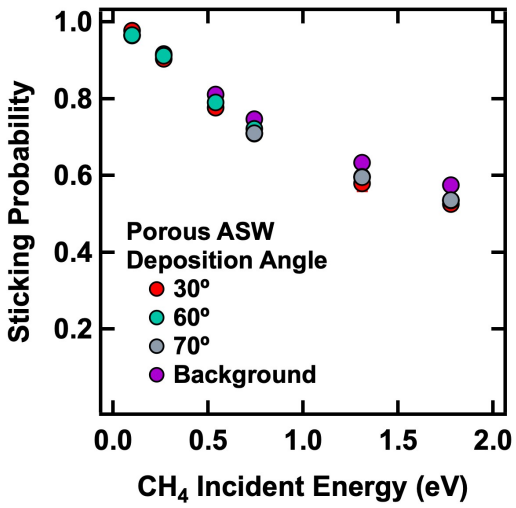

Figure 6.6: **CH_4 sticking probabilities - porous films**. Sticking probabilities are shown for CH_4 impinging on porous D_2O films held at 33.5 K, deposited via directed doser at 30° (red), 60° (green), and 70° (gray) relative to surface normal as well as via background deposition (purple). For the incident energies studied, there are no clear differences in sticking probabilities for these films. Error bars represent the standard deviation of at least three measurements on at least two different days.

To further understand these results, it is possible to quantify CH_4 coverage on a given surface during a period of exposure and compare it across films. We can estimate the amount of adsorbed CH_4 at a given time t_1 using the following equation:

$$N_{CH_4} = (P_2 - P_1)(t_1 - t_0) - \int_{t_0}^{t_1} P(t)\,\mathrm{d}x \tag{6.1}$$

In **Equation 6.1**, P_2 is the indirect CH_4 flux when the beam is blocked from the substrate, P_1 is the background CH_4 pressure when the beam is closed, and t_0 is the time at which the flag is removed and the film is fully exposed to CH_4. The last term is a simple numerical integration of the raw King and Wells pressure reading between those two time values. In doing this analysis for high translational energy CH_4 beams (1.8 eV), we find that in the first seconds of exposure (corresponding to a total exposure of $(5.0 \pm 0.4) \times 10^{14}$ CH_4 cm^{-2}), CI and np-ASW films have adsorbed $(1.0 \pm 0.1) \times 10^{14}$ CH_4 cm^{-2}, while 200 ML porous films (at all deposition angles) have accumulated $(1.8 \pm 0.3) \times 10^{14}$ CH_4 cm^{-2}. This increase is the result of both increased

surface area and higher initial sticking probabilities on porous films at these beam energies, and the difference only widens as exposure continues. The difference in uptake is illustrated qualitatively in **Figure 6.7a**, which depicts normalized King and Wells data for representative trials on np-ASW, CI, and p-ASW films. To aid in visual comparison, the data have been normalized in both axes by incident flux. Clearly, the porous film adsorbs more CH_4 before desorption takes over.

In **Figure 6.7b** the results of a similar coverage analysis are displayed for all porous ices. In this depiction, total coverage is scaled further by surface area to give an approximate "fractional coverage". Relative surface area is defined via the integrated intensity of the dangling O-D feature. As we discuss in **Figure 6.1**, this feature provides a reasonable measure of porosity and is related to the total surface area of the film.[199,200] Though the initial sticking probability is consistent across porous films, the relative accumulation of CH_4 is 1-2 times higher for films deposited at 30° and via background deposition than those deposited at 60° or 70°. The roots of this behavior will be addressed further in **Section 6.4** below.

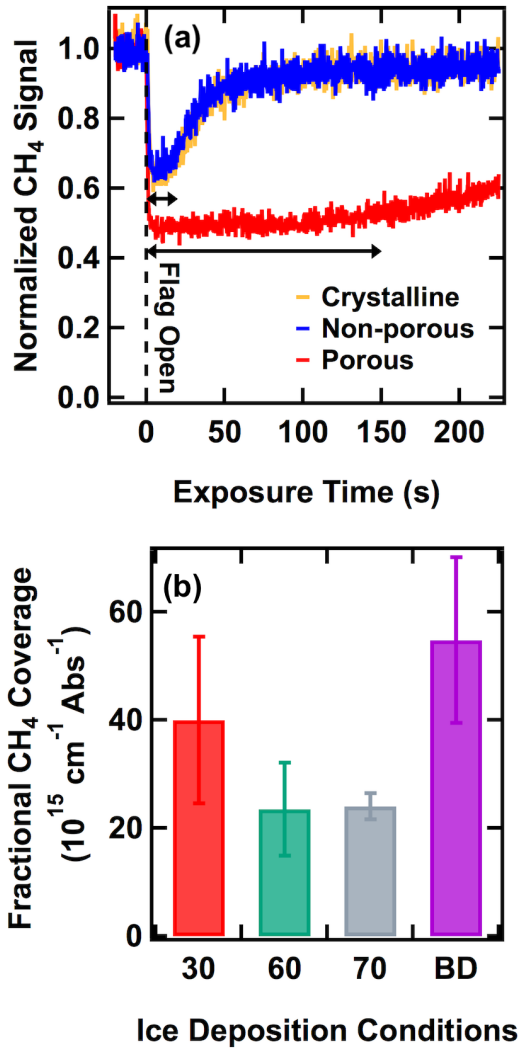

Figure 6.7: **CH_4 uptake and fractional coverage on ice**. Representative, normalized King and Wells data for all films studied show a clear increase in CH_4 uptake on porous films relative to CI and np-ASW. (a) Total uptake on a porous film (p-ASW, red) is nearly an order of magnitude higher than on either crystalline (CI, yellow) or non-porous (np-ASW, blue). Time and intensity axes are normalized to the incident flux. (b) Fractional CH_4 coverage is higher for porous films deposited at 30° or via background deposition (red, purple) than for those deposited at 60° or 70° (green, gray). We define fractional coverage as the total adsorbed CH_4 scaled by the integrated areas of the dangling bond feature. All data were selected from trials using 1.8 eV CH_4 beams.

6.4 Discussion

There are two new, significant findings to come out of this work. The first is that the sticking probability of CH_4 on p-ASW D_2O films does not decay as fast as it does on CI and np-ASW D_2O films. The second is that under our energetic conditions, the sticking probability trend does not depend on the type of porous ice film used. What follows is a qualitative discussion of why these trends occur and how future studies might further refine the proposed conclusions.

Sticking probabilities for a particular system are known to depend on both the binding energy between the surface and the adsorbate as well as the surface conditions (morphology, temperature, etc).[165] Binding energies for a variety of molecules on different ices of astrochemical interest have been widely reported. As discussed, the low-coverage binding energy for CH_4 on np-ASW ice has been reported in the range of 0.06 – 0.14 eV.[195,201,206,221] Additionally, differences in binding energy for CO (CH_4 and CO are expected to have similar binding interactions on ice)[201] between CI and np-ASW are small and on the order of 0.01 eV at most.[166,222] This suggests a partial explanation for the similarity in sticking probabilities between these two ice films. Binding energies on porous films, on the other hand, may be higher than those for either np-ASW or CI ice interfaces. Many studies assert that the binding energy distribution for molecules on porous films is wider and peaks at higher values.[164,206,223,224] This idea is refined by Zubkov et al., who concluded that while the distribution of binding sites on the surface is independent of film thickness and porosity, the lower fractional coverages of adsorbates on porous films (due to their increased surface area) lead to adsorbates interacting with more higher energy binding sites.[186] In short, it is likely that at the low coverages investigated here, CH_4 binds somewhat more strongly to the porous films.

Binding energy, however, is not a sufficient explanation on its own. Whatever the variation may be for the different ice films, all available reported binding energies for CO and CH_4 are less than 0.2 eV. This is significantly lower than most of the incident energies studied here, suggesting that there must be an additional mechanism for energy accommodation by the surface. Indeed,

theoretical work has shown that energy dissipation into ice films is incredibly facile under similar conditions.[166,225] *We suggest, therefore, that it is the distinct morphology of the porous films that is largely responsible for the observed divergence in sticking probabilities at high incident energies*. Desorption studies from a variety of porous substrates have found that desorption kinetics are governed by diffusive motion within pores and multiple collisions with pore walls.[226,227] Indeed, the energy-dissipating effects of these pore wall collisions have been previously cited in studies of molecular or atomic interactions with ice;[228] Zubkov et al. also found that prior to desorption, molecules on porous ice experience hundreds of desorption-readsorption attempts (as compared to just one attempt on non-porous).[186] Perhaps the most significant evidence of this energy accommodation by pore walls was demonstrated in a study of HD recombination. Hornekaer et al. found that on porous ice, a significant fraction of newly formed HD remained adsorbed to the surface, indicating that the porous network was extremely efficient at dissipating the 4.5 eV recombination energy.[229] This is in contrast to a non-porous film, which saw almost zero retention of the HD molecules following recombination. In summary, the higher sticking probabilities for CH_4 on p-ASW relative to np-ASW and CI likely result from diffusion on and multiple collisions with pore walls, leading to a more efficient dissipation of incident translational energy. It is possible, then, that the sticking probability as discussed here on porous films is more of an uptake coefficient; a measure of advantageous decelleration induced by the physical pore structure, rather than a higher capacity for site-specific energy accommodation on different types of icy surfaces.

In order to discuss CH_4 coverage, it is important to mention the impact of desorption. As mentioned previously, only a fraction of a CH_4 monolayer can remain stably adsorbed on the surface at 33.5 K. Therefore, we expect the increase in reflected signal after the first few seconds (after initial sticking is measured) to be a result of both directly reflected CH_4 and steadily desorbing CH_4. Ultimately, when the reflected signal levels off at long exposure timescales, adsorption and desorption are occurring at equal rates. Measured isothermal, low-coverage desorption rates for all porous films studied here are roughly equivalent and comparable in magnitude to the incident flux, making it possible to compare coverages across these films despite the competing rates of

adsorption and desorption.

At normal incidence, this study showed that porous films of any orientation are equally efficient at dissipating the energy of impinging CH_4, but these films adsorb relatively different amounts of CH_4, depending on deposition conditions. The invariance in sticking probability across films of different porosities suggests that the D_2O pore surface is equally efficient at accommodating the incident energy of the CH_4 molecules, regardless of how that pore is oriented relative to the incident beam. These results also suggest, however, that incident CH_4 is not sampling the full surface area of the pore network of 60° and 70° films before beginning to desorb. This can perhaps be understood in terms of pore geometry and size. Films deposited at 30° have lower total surface areas, but they also have pores that are closer to perpendicular to the substrate.[22,220] Relatively more of the pore surface area, therefore, is accessible to the incident beam. Likewise background deposited films have a distribution of pore sizes and orientations; some fraction of which will be perpendicular or near-perpendicular to the substrate. On the other hand, the more tilted, wider pores of the 60° and 70° films present fewer surface sites for the incident beam. *So while CH_4 may undergo multiple collisions with the pore structure before sticking, these coverage results indicate that adsorbed CH_4 is not necessarily diffusing fully into the pore structure and filling up all available surface sites, particularly on the more angled porous film structures*. A future experiment that explores the angular dependence of sticking and uptake on these porous films would be a significant step toward identifying the relative importance of factors such as pore orientation and size.

6.5 Conclusion

In this chapter we present detailed sticking probability measurements for high translational energy CH_4 impinging on a variety of D_2O ice films at 33.5 K. We confirm that at the energies studied, CH_4 is unable to either embed in the bulk or significantly impact the morphology of any ice, including low-density porous films. As incident translational energy increases, the sticking probability decreases for all films. However, CH_4 sticks with greater probability to p-ASW films than

it does to either CI or np-ASW films at the same energies. Furthermore, we observe no substantial changes in sticking probability when changing the exact morphology (pore orientation and size) of the porous film used. Even though there may be slight changes in binding energies between CH_4 and the different films, we propose that the porous morphology is largely responsible for this observed divergence. Multiple collisions with pore walls are likely efficient at dissipating the incident energy of the CH_4 projectile. This conclusion is supported by the fact that porous films with more beam-accessible pore surfaces (films deposited at 30° and via background deposition) accumulate relatively more CH_4 during exposure than do films with fewer accessible pore surfaces (deposited at 60° and 70°).

These results are further evidence that the morphology of ice films (and other industrial substrates) critically influences the adsorption and subsequent reactivity of incident molecules. Even if not universally porous, small cracks, fissures, and other morphological deformities in the surface of astrophysical ices may lead to an increased uptake of gaseous molecules, thereby impacting phenomena including the outgassing of comets, chemical reactions in the ISM, and thermal and electrical processing of icy dust grains.[166,228,229]

Chapter 7

Reverse Water-Gas Shift Chemistry inside a Supersonic Molecular Beam Nozzle

In this chapter, we show that resistive heating of the metal surface of a supersonic molecular beam nozzle is very effective in converting CO_2 diluted in H_2 to CO and H_2O via the reverse water-gas shift (RWGS) reaction at temperatures that preclude simple pyrolysis. The conversion of CO_2 to CO, referred to herein as "RWGS yield," exceeds 80% at nozzle temperature above 1000 K, with a detectable methane byproduct. The stainless-steel surface of the nozzle appears to facilitate the reaction as a heterogeneous catalyst. Reaction yield is observed to increase with higher nozzle temperature and, when the gas mixture contains a significant excess of H_2, decrease with increasing in nozzle stagnation pressure. The inverse dependence of the reaction on stagnation pressure is used to propose a reaction mechanism. Additional kinetic control over the mechanism is afforded by adjusting reactant partial pressures and residence times inside the nozzle reactor, highlighting this method's utility in screening heterogeneous catalysis reactions with fine control over mass flow rates, pressure, and temperature. The results of this study, therefore, present a route to efficient, high pressure, inline catalysis as well as a method to rapidly assess the viability of new catalysts in development.

7.1 Introduction

Thermodynamic equilibrium of the system containing carbon dioxide, hydrogen, water vapor, and carbon monoxide is at the center of mass production of high-demand chemicals including ammonia and methanol.[230,231] The direct reaction of carbon dioxide with hydrogen is an endothermic reaction known as the reverse water-gas shift reaction (RWGS). The RWGS reaction is endothermic by 41 kJ mol^{-1}, expressed by the equation:[232]

$$CO_2 + H_2 \rightarrow CO + H_2O \tag{7.1}$$

This reaction has not attracted as much attention as its forward-direction counterpart, but the RWGS reaction, particularly at high temperatures, can often play a role in the overall observed kinetics. RWGS conversion is typically below 50% under typical experimental conditions[232–236] and extraneous alcohol or hydrocarbon byproducts often accompany the desired products. These byproducts come from Fischer-Tropsch reactions branching from intermediate steps in the RWGS reaction.[237,238]

Two general methods are employed for the water-gas shift reactions: high-temperature pyrolysis and heterogeneous catalysis.[233,234,239–242] The former typically requires temperatures above 1000 K to overcome the energetic barrier. The latter is generally efficient for a variety of metal and metal-oxide catalysts.[241] The experimental conditions in the current study produce a facile route for high conversion yield of CO_2 to CO as measured by TOF-MS. Unique to this study is the use of a supersonic molecular beam as the reactor. The nozzle's stainless-steel surface serves as the heterogeneous catalyst and the products are sampled via TOF-MS after exiting the beam's hot nozzle.

This beam-as-reactor method has been used to generate radical reactants via pyrolytic unimolecular dissociation[243,244] as well as to study catalytic hydrocarbon formation. Shebaro et al. reported large hydrocarbons, including benzene, in the product stream of a supersonic beam of ethane at elevated nozzle temperatures.[245,246] Romm et al. expanded upon this work; they eluci-

dated the interplay of kinetic and thermodynamic control of methane pyrolysis in a heated nozzle by identifying changes in products under different flow conditions.[247,248]

In the current chapter, we use a similar setup to sample the RWGS reaction products. Unlike prior work sampling reaction products via TOF-MS following desorption from a surface, we feed the reactive mixture of H_2 and CO_2 into the hot stainless-steel nozzle of the supersonic beam source, which serves as the catalytic site.[249–252] Downstream, with the QMS along the direct line-of-sight from the differentially pumped beam, we measure conversion yields of CO_2 to CO of ≈50% by 800 K; the yield is above 80% by 1000 K. We discuss the reaction mechanism and examine the extent of extraneous Fischer-Tropsch reactivity under these conditions. We also determine the extent of kinetic control over the product stream afforded by our experimental conditions.

7.2 Experimental Section

We performed all of the experiments described in this chapter in the molecular beam scattering instrument described in **Chapter 2**. A gas mixture of 10%, 50%, or 88% CO_2 diluted in H_2 flows into a 316 stainless-steel nozzle gland fitted with a 20 μm diameter pinhole made of molybdenum. We also tested platinum pinholes to confirm that the pinhole material had no impact on reaction yield. Using the configuration described in **Subsection 2.3.4**, we were able to heat the nozzle to 1025 K and reach stagnation pressures up to 450 psi. After changing either the nozzle temperature or stagnation pressure we allowed the beam at least 30 minutes to equilibrate prior to data acquisition. Our primary analytical technique was TOF-MS, using square-wave (SQW) modulation of the beam (50% duty cycle) and the inline QMS located in the UHV chamber.

7.2.1 Calculating RWGS Yield

Quantifying CO_2 to CO conversion involves comparison of SQW modulated data at m/z = 28 and m/z = 44 at room and elevated temperatures. Because we used SQW-modulated data, we derived total intensity at any given m/z value from the difference in the sums of four consecutive 200 μs

bins with the beam passing and blocked by the chopper wheel. Once we collected these four data points, the calculation for RWGS yield is identical to the procedure described in **Subsection 2.3.3** for calculating the dissociation of O_2 to O(^{3}P). The key difference is that the relevant ionizations are now:

$$CO_2 + e^- \xrightarrow{\sigma_D} CO^+ + O + 2e^- \tag{7.2}$$

$$CO_2 + e^- \xrightarrow{\sigma_{CO_2}} CO_2^+ + 2e^- \tag{7.3}$$

$$CO + e^- \xrightarrow{\sigma_{CO}} CO^+ + 2e^- \tag{7.4}$$

Once we plug these values into the analogous versions of **Equation 2.13 and 2.16**, the relative number density between CO and CO_2 (R) can be written as:

$$R = \frac{N_{28}}{N_{44}} = \left(\frac{\eta_H}{\eta_L} - 1\right)\left(\frac{\sigma_D}{\sigma_{CO}}\right) \tag{7.5}$$

As is the case for O_2, the only cross-section values that remain are the dissociative detachment of CO_2 to CO^+ (σ_D) and ionization of CO (σ_{CO}); for irradiation with 100 eV electrons, these values are 2.25 and 1.82 Å^2, respectively.[253,254] Finally, the fraction of CO_2 converted to CO, defined here as the RWGS yield, is a function of R:

$$\frac{N_{CO}}{N_{CO} + N_{CO_2}} = \frac{R}{R+1} \tag{7.6}$$

7.3 Results and Discussion

7.3.1 Evidence for RWGS Reaction

Reactivity is evident in comparing representative SQW modulated data in **Figure 7.1** obtained from a supersonic beam with a stagnation pressure of 250 psi. Near room temperature, when no reaction is expected, there are the anticipated signals at m/z = 28 and m/z = 44, attributed entirely

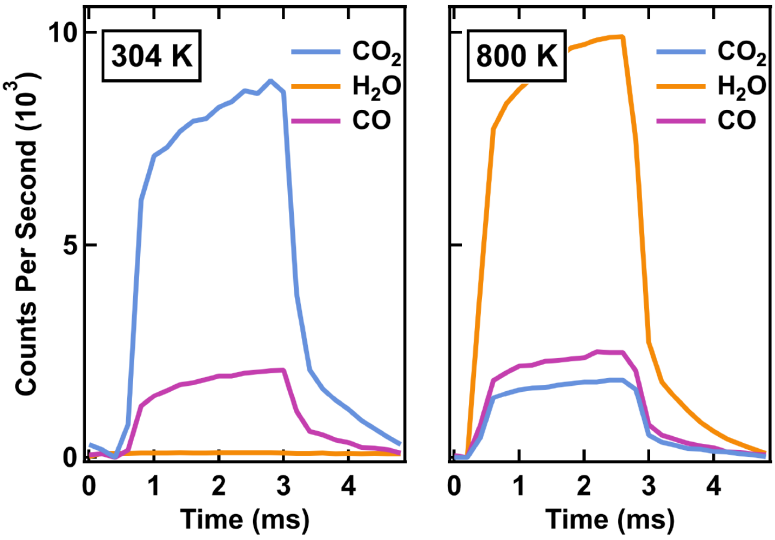

Figure 7.1: **Representative MS of room and high temperature beam composition**. Representative square wave TOF-MS signals at m/z = 18 (H_2O, yellow), 28 (CO, pink), and 44 (CO_2, blue). At room temperature (left), the only contribution to signal intensity at m/z = 28 is the dissociative ionization of CO_2. Upon heating the nozzle to 800 K (right), RWGS reactivity is evidenced by a dramatic increase in the ratio of CO to CO_2, as well as new signal intensity at m/z = 18 (attributed to H_2O formation). These data were collected using the 10% CO_2 gas mixture at 250 psi.

to the ionization and dissociative detachment of CO_2 in the beam. Upon heating the nozzle to 800 K, however, the CO_2 intensity drops significantly, while the signal at m/z = 28 increases. We also observe new signal intensity at m/z = 18, due to H_2O formation in the nozzle. This indicates significant RWGS reactivity.

Though the RWGS reaction is the primary mechanism, we also observe some evidence that secondary reaction channels are active at the highest temperatures studied. For example, we see significant signal intensity at m/z = 15 that cannot be attributed to the initial gas mixture. Shown in **Figure 7.2**, the normalized intensity at m/z = 15 increases with nozzle temperature, peaking near 800 K before starting to decrease thereafter. Moreover, after extended use at the highest temperatures studied (weeks of operation with consistent daily use), the nozzle eventually clogs with soot (or coke) and must be taken apart and sonicated to continue.

Under our reaction conditions, both Fischer-Tropsch or CO_2 methanation (Sabatier) reactions are possible explanations for this observation.[255,256] In monitoring the product stream, however,

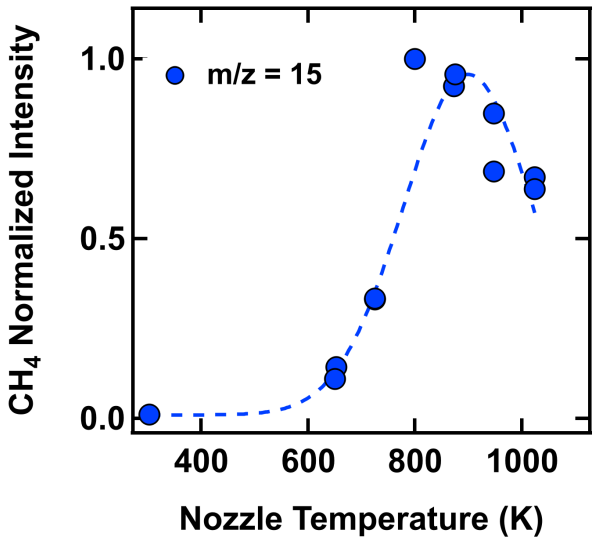

Figure 7.2: **CH_4 in product stream at high temperatures**. TOF-MS signal at m/z = 15 is observed at high temperatures in the nozzle, likely corresponding to the generation of methane. Above 800 K, the relative amount of methane in the product stream decreases, perhaps signaling the loss of methane due to coupling Fischer-Tropsch processes. These data were collected using the 10% CO_2 gas mixture at 250 psi. Dotted line is drawn to guide the eye.

we do not see any major evidence of Fischer-Tropsch byproducts such as formaldehyde and ethanol (m/z = 29 and 31, respectively) or other large, unsaturated hydrocarbons. This makes sense, as significant Fischer-Tropsch reactivity would necessarily consume any CO generated by the RWGS reaction. Any trace Fischer-Tropsch reactivity that is taking place is likely, under our conditions, to have high methane selectivity anyway due to our high temperatures and H_2/CO ratios, as well as the nozzle acting as an un-promoted iron-based catalyst.[257–259] It is possible that the decrease in methane signal above 800 K is due to some methane coupling in the nozzle,[245–248] contributing to the eventual clogging, but in general it appears that the most significant secondary reaction is simply the production of methane or other surface carbide species directly from CO_2 and H_2.[260–262]

Notably, the stainless-steel nozzle does not exhibit considerable RWGS catalytic activity until it has been thermally annealed under vacuum for dozens of hours. **Figure 7.3** demonstrates the effect of vacuum annealing of the nozzle at 800 K on the RWGS yield. The yield, as measured using a nozzle temperature of 800 K and stagnation pressure of 250 psi, is essentially zero with no treatment, and has leveled off near 50% after 180 hours of vacuum annealing at 800 K. This observation

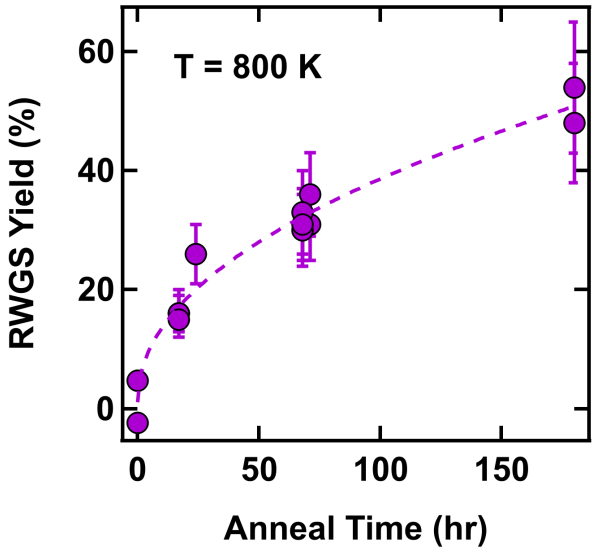

Figure 7.3: **RWGS yield increases with anneal time**. The 316 stainless-steel nozzle does not show appreciable catalytic activity of any kind until it has been annealed at 800 K under vacuum. The RWGS yield (for 10% CO_2 gas mixture at a stagnation pressure of 250 psi) reaches 50% after roughly 180 hours of vacuum annealing at 800 K. Dotted line drawn to guide the eye. Error bars represent one standard deviation.

can be rationalized by considering the stainless steel surface. As produced, the passive property of stainless steel derives from iron and chromium oxide surface layers. Annealing under vacuum, however, can significantly alter the composition of the surface. At modest vacuum annealing temperatures, (500 – 800 K), the surface sees a decrease in graphitic and hydrocarbon contamination as well as an increase in chromium content.[263–267] Both of these effects may be crucial in maintaining a high number of active sites on the catalytic substrate. Mixed iron and chromium oxides are common catalysts for both the forward and reverse water-gas shift reactions.[230,241,268,269] Many researchers have also highlighted the significant role chromium plays in stabilizing the surface and preventing sintering (and the associated loss of catalytic surface area).[230,268,270,271] We conclude, therefore, that vacuum annealing increases the surface chromium content, thereby enabling the high-yield RWGS reaction.

At constant stagnation pressure, RWGS yield is obtained only at high nozzle temperatures. This is expected from the reaction's endothermicity. Shown in **Figure 7.4**, once the nozzle temperature exceeds 650 K, conversion of CO_2 to CO is observed, and the total conversion increases

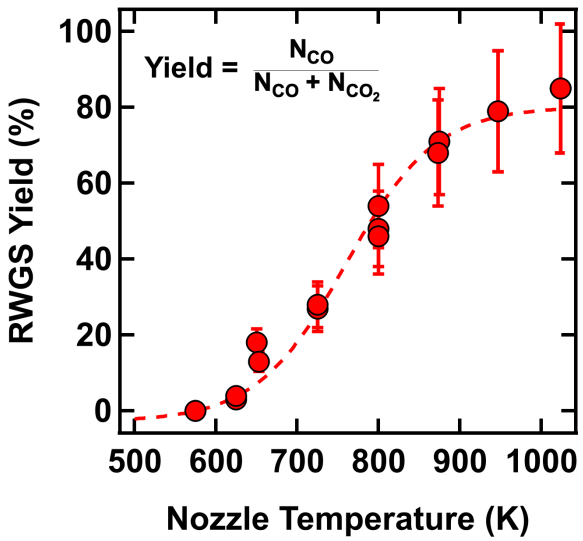

Figure 7.4: **RWGS yield increases with nozzle temperature**. Given the endothermic nature of the reaction, increasing the nozzle temperature leads to a higher RWGS yield for the 10% CO_2 gas mixture at a constant stagnation pressure of 250 psi. Dotted line drawn to guide the eye. Error bars represent one standard deviation.

with increasing temperature throughout the entire range studied in this work. While hydrocarbons are evidently produced to some extent, the total conversion of CO_2 to CO is very high above 800 K, reaching above 80% by 1025 K. It is worth noting, however, that the yield appears to plateau at the lowest and highest temperatures studied. The fact that there is no significant yield below 650 K suggests a thermally activated process; likely the dissociation of H_2.[272–275] It is less likely that this activation arises from a sudden freeing of surface active sites for dissociative adsorption; CO and CO_2 are present in such dilute amounts, and their desorption from Fe-based surfaces typically occurs at slightly higher temperatures.[276–279] At the highest temperatures studied, on the other hand, increases in reaction yield appear to slow. Again, this behavior may be understood by considering the composition of the stainless steel interface at these temperatures. While modest annealing temperatures lead to chromium enrichment as discussed above, temperatures above 1000-1100 K lead to a significant depletion in surface chromium levels.[264,265,280–282] A loss of active sites, therefore, may explain why peak reactive yields do not exceed 85%.

7.3.2 Reaction Mechanism and Kinetic Control

The mechanisms of RWGS reactions have been studied both in the gas phase and over catalysts.[233,235,236,239,241] Several early investigations suggested surface-mediated processes, with the mechanism broadly classified as either regenerative or associative.[233,236] Reported mechanisms are frequently dependent upon catalyst composition and reaction temperature, and considerable dispute remains in mechanistic studies.[231,233,256] In light of our current results and utilizing some key assumptions, we attempt to describe the RWGS reaction mechanism taking place within our nozzle. High-temperature pyrolysis would require temperatures higher than those studied here, so we can assert that a surface-specific process is taking place.[237,239] Several authors have studied RWGS reactivity under similar temperature and pressure conditions with inert quartz reactors and conversion was typically less than 0.1%.[232,235] Bustamante and co-workers compared yields for quartz and metallic chambers; they found a dramatic increase in catalytic activity with a metallic surface, resulting in conversion rates of up to 55% at 1173 K under ambient pressure.[232,283] They concluded that the metal surfaces of the reactor directly catalyzed the reaction. Similarly, surface-facilitated reactions utilizing supersonic beams have also been demonstrated in other studies. For example, Romm et al. reported close to 100% conversion of ethane to heavier hydrocarbons in a supersonic nozzle beam; their proposed mechanism relied heavily on surface-mediated hydrogen abstraction processes.[247,248]

Based on the above discussion, we postulate one possible mechanism, wherein the (*) subscript denotes a surface site and X* is a surface-adsorbed X species:

$$\textbf{(1)} \quad H_{2(g)} + 2* \rightleftharpoons 2H*$$
$$\textbf{(2)} \quad CO_{2(g)} + * \rightleftharpoons CO_2*$$
$$\textbf{(3)} \quad CO_2* + * \rightarrow CO* + O*$$
$$\textbf{(4)} \quad O* + 2H* \rightleftharpoons H_2O* + 2*$$
$$\textbf{(5)} \quad CO* \rightarrow CO_{(g)} + *$$
$$\textbf{(6)} \quad H_2O* \rightarrow H_2O_{(g)} + *$$

Figure 7.5: **Proposed RWGS reaction mechanism**. Proposed mechanism for high pressure, high temperature RWGS reaction for a 10% CO_2 in H_2 gas mixture in a stainless steel beam nozzle reactor.

This mechanism is based on the frequently-cited redox mechanisms for high-temperature WGS catalysis in both the forward and reverse directions.[230,236,269,284] Given the large excess of H_2 in our reaction mixture and the relatively facile dissociation on steel, we assume that the limiting step under our reaction conditions is the dissociation of CO_2 (**Figure 7.5**, step 3). Therefore, the overall rate can be represented by:

$$Rate = \frac{\mathrm{d}P_{CO}}{\mathrm{d}t} = k_3 \theta_{CO_2^*} \theta^* \tag{7.7}$$

Additionally, the fractional coverage of adsorbed CO_2 ($\theta_{CO_2^*}$) can be determined from the equilibrium in step 2 (**Figure 7.5**):

$$\theta_{CO_2^*} = K_2 P_{CO_2} \theta^* \tag{7.8}$$

By combining these two equations and assuming that hydrogen coverage on the surface remains approximately constant and CO_2 is competing for the remaining sites, we can derive a rate expression:

$$Rate = \frac{\mathrm{d}P_{CO}}{\mathrm{d}t} = \frac{k_3 K_2 P_{CO_2}}{(1 + K_2 P_{CO_2})^2} \tag{7.9}$$

Though we do not measure rates directly in this study, we can approximate them by recognizing that nozzle residence times do not change as a function of stagnation pressure.[11] Therefore, measuring yield as a function of CO_2 partial pressure allows us to partially assess the feasibility of this rate law. These results are shown in **Figure 7.6**, where RWGS reaction yield is observed to decrease as a function of CO_2 partial pressure. **Equation 7.9** is a good fit for the data, but our limited pressure range makes it difficult to say with certainty that this predicted rate law completely describes the reaction. It is clear, however, that there is a small negative power dependence for the rate on CO_2 partial pressure. This has been observed occasionally in previous studies,[230,285] but we note that it is common for WGS power rate laws to change significantly across different catalyst systems, temperatures, and relative reactant pressures. In other words, **Equation 7.9** may only be

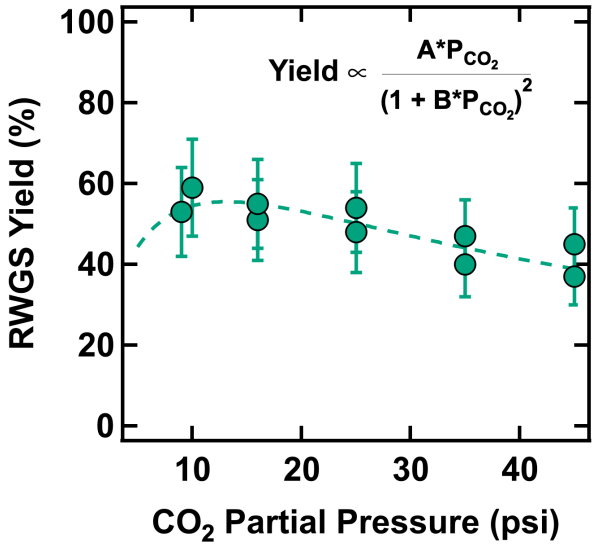

Figure 7.6: **RWGS yield decreases with CO_2 partial pressure**. RWGS yield decreases as a function of CO_2 partial pressure (10% CO_2 in H_2 gas mixture) at a constant nozzle temperature of 800 K. Dashed line is a fit of the data to **Equation 7.9**, which is a proposed mechanism for the reaction assuming CO_2 dissociation on the metal surface is the rate-limiting step.

appropriate for the data in this particular pressure, temperature, and reaction mixture regime.

The challenge of establishing a universal mechanism for this reaction is highlighted when we consider that the dissociation of H_2 (**Figure 7.5**, step 1) can also be a key step, depending on reaction conditions. In the 10% mixture, H_2 drastically outnumbers the CO_2. Given the facile splitting of H_2 on the stainless steel, we assume that the oxygen atoms left from the dissociative chemisorption of CO_2 can generate water immediately (**Figure 7.5**, step 4). Strengthening this argument are a series of experiments we performed with two additional mixtures of CO_2 and H_2: 50% and 88% CO_2 diluted in H_2. The results in **Figure 7.7** show that the RWGS yields for the less dilute mixtures are significantly lower than the 10% mixture over the same high temperature range. Though the yield may be decreasing in part due to the increase in CO_2 partial pressures for the 50% and 88% mixture (as discussed for **Figure 7.6**), it also appears that excess H_2 is critical in facilitating high yields. Without an excess of H_2 in the feed gas, the rate-limiting step may change, leading to a slowdown in CO production; though CO_2 may be able to adsorb more readily, the number of hydrogen atoms on the surface available for reaction will also decrease.

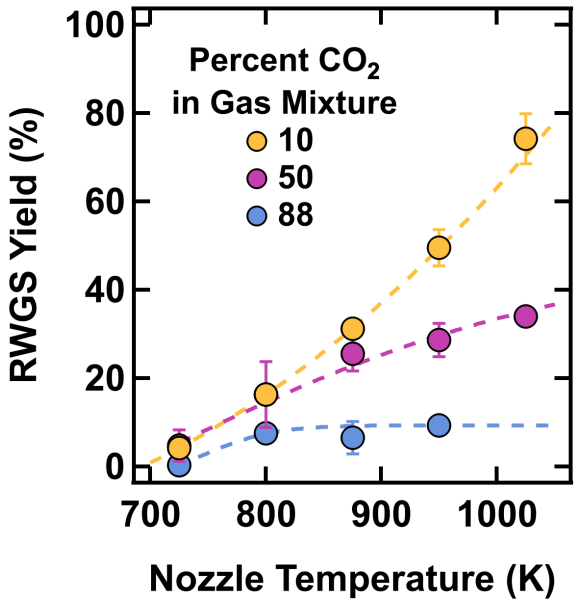

Figure 7.7: **RWGS yield impacted by CO_2/H_2 ratio**. Representative RWGS yields for various mixtures of CO_2 and H_2 at varying temperatures and constant stagnation pressure (250 psi). Without an excess of H_2 in the feed gas, the reduction of CO_2 to CO relative to the dilute 10% mixture plummets at high temperature. Dotted lines drawn to guide the eye.

7.4 Conclusion

Utilizing a supersonic expansion from a heated stainless steel nozzle, we demonstrate selective CO_2 reduction to CO by H_2 involved in the RWGS reaction. This reaction exhibits conversion yields above 80% at nozzle temperatures above 1000 K. The yield of the reaction increases as nozzle temperature increases and decreases with higher stagnation pressure (and CO_2 partial pressure). The stainless-steel surface was found to serve as a heterogeneous catalyst for the reaction. A small amount of methane is formed as a byproduct, and is likely further converted to heavier hydrocarbons when the nozzle temperature is above 800 K.

We propose a mechanism for the reaction under our conditions and probe its applicability through precise control of reaction mixture, residence time in the nozzle reactor, and nozzle temperature. In addition to characterizing the RWGS reaction catalyzed on stainless steel under high pressure conditions, this supersonic expansion technique also provides broad opportunities to

screen various catalytic reactions under variable pressure and temperature conditions. It is feasible for this technique to facilitate such reactions with surface-generated gas-phase radicals, followed by rapid desorption and cooling of the intermediate products. This method, therefore, affords a rapid, quantitative, and comprehensive screening ansatz of catalytic efficiency.

Chapter 8

Reaction Kinetics and Influence of Film Morphology on the Oxidation of Propene Thin Films by O(^{3}P) Atomic Oxygen

We present results detailing the oxidative reactivity of condensed propene thin films, with particular attention to epoxide product formation due to its importance in the industrial production of polyurethane plastics and trace presence of these species in the interstellar medium. After exposing films to a supersonic beam of ground state atomic oxygen, O(^{3}P), RAIR spectra confirm significant propene reactivity yielding products including propylene oxide, propanal, and a small amount of acetone. In addition to identifying these primary products, we discuss experimentally-determined activation energy barriers for reaction in the condensed propene system. Interestingly, we identify significant differences in propene film crystallinity as a result of substrate deposition temperature; lower deposition temperatures ($\leq$44 K) yield a more amorphous film, whereas higher temperatures ($>$59 K) yield a more ordered, crystalline film. Very little oxidative reactivity is observed in the amorphous propene film, suggesting that film structure has a substantial impact on observed reactivity by impeding or allowing efficient O(^{3}P) diffusion. Overall, this work provides fundamental mechanistic insight into the diffusion and reactivity of atomic oxygen in condensed films of small, unsaturated hydrocarbons. The results also emphasize limitations of condensed phase reactions that rely on reactant diffusion; film composition, morphology, and thickness can significantly limit reactivity despite low reaction barriers.

8.1 Introduction

The reaction of atomic oxygen, O(^{3}P), with small alkenes is important across many fields including smog formation in the atmosphere, combustion processes, and chemical complexity in astrophysical ices.[158,286] These reactions also play a critical role in the formation of polycyclic aromatic hydrocarbons and soot.[287] Additionally, the products formed from oxygen addition across double bonds are often significant industrial intermediates. Propylene oxide, for example, is a key intermediate in the manufacturing of polyurethane plastics and other products.[288,289] It is one of the top chemicals produced worldwide by mass,[290] and there is immense interest in optimizing the economic and environmental efficiency of its production.[291–293]

The gas phase reaction between alkenes (including propene) and oxygen has been well-studied, beginning as early as the 1950's.[294–298] It is well established, for example, that the reaction begins with oxygen addition across the double bond, forming a triplet biradical intermediate. This primary product species then progresses through a number of reaction channels including intersystem crossing (ISC) from the triplet to the singlet potential energy surface (PES) to form singlet products. Recently, a comprehensive study from Leonori *et al.* used crossed molecular beams and complementary *ab initio* electronic structure calculations to identify complete branching ratios, energetic barriers, and potential energy surfaces for the O(^{3}P) + propene reaction.[299,300] This study and others have highlighted the temperature dependent role of ISC in the gas phase reaction; the fraction of products formed via ISC decreases with increasing temperature.[296,299,300] Despite this rigorous work in the gas phase, however, there still remains limited mechanistic and kinetic data available for the oxidation of condensed alkene films. In the few early studies of this system,[301–304] primary products and reaction rates were identified, but the experimental conditions utilized thick, uncharacterized propene films and were limited to temperatures above 70 K (propene phase may have been unclear).

Understanding reactions between condensed alkenes and oxygen at cold temperatures is also important for astrophysical applications due to the trace presence of these species in the interstellar

medium.[305] It is thought that reactions on interstellar dust grains below 77 K facilitate the formation of many such molecules with abundances that cannot be explained by gas phase chemistry alone.[162,306,307] To date, only gaseous propene has been observed in a dark interstellar cloud[308] and on Titan,[309] but molecules formed on dust grains (possibly due to exposure to ionizing radiation)[310] could desorb and contribute to these measured gas phase concentrations.[311] Additionally, propylene oxide, one of the major products in the O(^{3}P) + propene reaction, has been detected spectroscopically in the interstellar medium[312] as well as produced in a laboratory simulation experiment by exposure of propylene ices at 5 K to energetic electrons.[313] Such studies indicate that oxygen atom addition and insertion reaction pathways could activate a novel channel for chemical complexity in ices that are too cold for radicals to diffuse and react.[314,315]

In this chapter we use the RF plasma source described in **Subsection 2.3.3**, to generate a supersonic expansion of ground state atomic oxygen, O(^{3}P), which is then exposed to condensed propene films. We track reaction product formation in real time with *in situ* RAIRS, which allows us to determine the activation energy for this process. We find that in the condensed phase, propene reacts readily with O(^{3}P) to form primarily the partial oxidation products propylene oxide and propanal. Additionally, we present the first study highlighting the specific impact of alkene film morphology on oxidative reactivity. Specifically, oxygen is unable to react with more disordered, amorphous propene films.

Overall, the work in this chapter provides fundamental insight into the diffusion and reactivity of ground state atomic oxygen in condensed films of small, unsaturated hydrocarbons. By employing cryogenic conditions and thin films of propene, we can simulate interstellar conditions which can aid in modeling reactivity on interstellar dust grains. Additionally, the kinetic and mechanistic detail gained from this reaction will inform polyurethane plastic manufacturing. This work also broadly highlights the possible challenges with condensed phase reactivity in which film structure and morphology may significantly limit reactant diffusion and reactivity in thicker films.

8.2 Experimental Section

We performed all of the experiments described in this chapter in the molecular beam scattering instrument described in **Chapter 2**. Our primary analytical technique was time-resolved RAIRS. All RAIR spectra were analyzed with Gaussian peaks atop cubic baselines. Each spectrum is an average of 300-500 scans taken using 4 cm^{-1} resolution with the clean Au(111) sample as the reference background. Between experiments, we cleaned the Au(111) crystal via a 15 min sputter and anneal cycle, as described in **Subsection 2.4.2**.

Using the beam dosing method outlined in **Subsection 2.4.3**, we dosed propene on the Au(111) substrate at surface temperatures ranging from 44 K to 59 K, where propene desorption is negligible. Dosing conditions resulted in a typical incident propene flux of 2.6×10^{15} molecules cm^{-2} s^{-1}, corresponding to a deposition rate of approximated 2.4 layers s^{-1} (assuming one monolayer is roughly 10^{15} molecules cm^{-2}).[21] Because we used a neat propene beam, we were able to quantify propene flux using the procedure from **Subsection 2.3.2**. We performed this measurement and calculation at room temperature to ensure no additional pumping capacity was added by the cold sample manipulator. Following this measurement, we used the same beam to establish a conversion to propene film thickness by monitoring propene growth on the cold crystal via RAIRS as a function of exposure and calculating an absorption cross-section for the $=CH_2$ wagging mode (γ_w), comprised of two peaks: a large, sharp peak at 919 cm^{-1} and a smaller shoulder at 914 cm^{-1}. Our calculated cross-section is in good agreement with previously reported values.[147,152,316,317] Propene film thicknesses are herein reported in layers; films throughout this chapter ranged from 10 to 240 layers (specific thicknesses are noted). The beam source was thoroughly pumped out and purged prior to turning on the oxygen source to avoid trace propene contaminants during exposure.

Finally, we generated atomic oxygen using the RF beam source described in **Section 2.3.3**. Our gas was a mixture of 5% O_2 in Ne mixture, and typical experimental conditions resulted in an $O(^3P)$ flux of 8.4×10^{14} atoms cm^{-2} s^{-1}. The translational energies were 0.12 eV, with energy widths of approximately 0.06 eV. While it would be desirable to explore the reaction with higher

incident translational energies by substituting a seeded mixture of O_2 in He, doing so would reduce O_2 dissociation and introduce O(^{1}D) to the beam, which is a more reactive species.[82] 45 Thus, for this experiment, 5% O_2 in Ne remains the optimal gas mixture.

8.3 Results and Discussion

8.3.1 Spectral Evidence of Reactivity and Product Formation

Condensed propene reacts readily with O(^{3}P). **Figure 8.1** shows typical RAIR spectra of a 66-layer propene film at 54 K before and after extended exposure to O(^{3}P). Prior to exposure, spectral features are easily correlated with gas-phase and condensed-phase peak assignments.[152,317–320] As shown by the dashed line in **Figure 8.1a**, the most intense features at 919 cm^{-1} and 914 cm^{-1} are assigned to the =CH_2 wagging mode of propene (γ_w) with a smaller feature at 1003 cm^{-1} corresponding to the CC bending mode.[151,321,322] Unless otherwise stated, changes in the integrated areas of the features at 914 cm^{-1} and 919 cm^{-1} are used throughout the rest of this study to track propene reaction progress (corresponding to oxidation of the propene double bond). A second region is highlighted in **Figure 8.1b** at 1643 cm^{-1}, corresponding to the propene C=C stretch.[323] A third region highlighted in **Figure 8.1c** shows additional CH, CH_2 and CH_3 stretching modes that are smaller in intensity.[324] The two largest peaks at 3075 cm^{-1} and 2977 cm^{-1} correspond to the CH_2 and CH_2 + CH stretching modes, respectively.[320,324] Other notable features in this stretching region are peaks at 2939 cm^{-1} and 2964 cm^{-1} assigned to CH_3 stretching,[318,322] and a peak at 3009 cm^{-1} assigned to CH stretching.[320]

Following 1×10^{18} atoms cm^{-2} of oxygen exposure, the aforementioned propene peaks change dramatically, many of them decaying in intensity. At the same time, there is significant growth of novel features that represent oxygenated products. Most notably in the solid line in **Figure 8.1a**, the spectral signature at 830 cm^{-1} is assigned to the ring deformation mode of propylene oxide (δ_{C_2O}).[325–328] New peaks (1730 cm^{-1} and 1693 cm^{-1}) in **Figure 8.1b** are similarly assigned to the C=O stretching frequency of propanal ($\nu_{C=O}$).[329–331] Additionally, there is a small

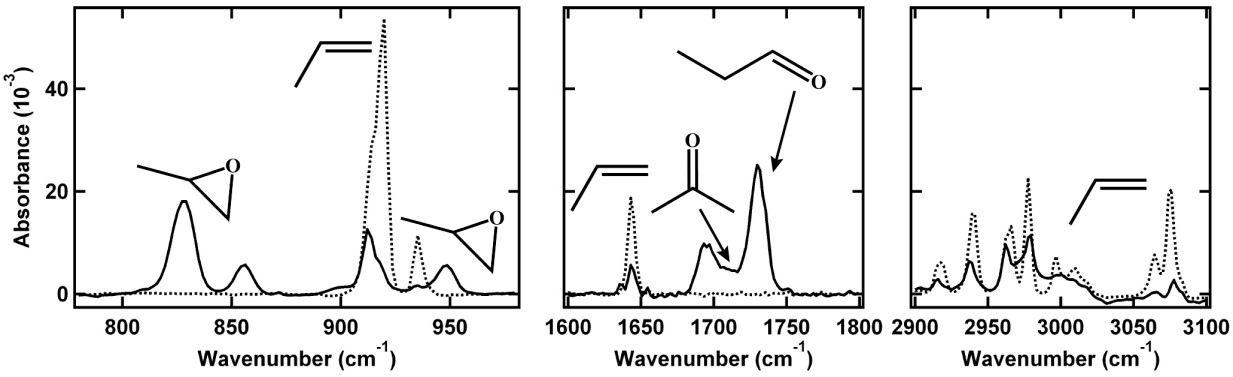

Figure 8.1: **Representative RAIR spectra of pristine and reacted propene**. RAIR spectra of characteristic regions of a 66-layer propene film before (dashed line) and after exposure to O(^{3}P) (solid line, total exposure 1×10^{18} atoms cm^{-2}). As a result of exposure, the total signal intensity is observed to decrease for the CH_2 wagging (919 cm^{-1} and 914 cm^{-1}, a), C=C stretching (1643 cm^{-1}, b), and CH, CH_2 and CH_3 stretching (3009 cm^{-1}, 3075 cm^{-1} 2977 cm^{-1}, 2939 cm^{-1}, and 2964 cm^{-1}, c) modes of propene. New peaks grow in upon exposure corresponding to propylene oxide (830 cm^{-1}, a), acetone (1709 cm^{-1}, b), and propanal (1730 cm^{-1} and 1693 cm^{-1}, b).

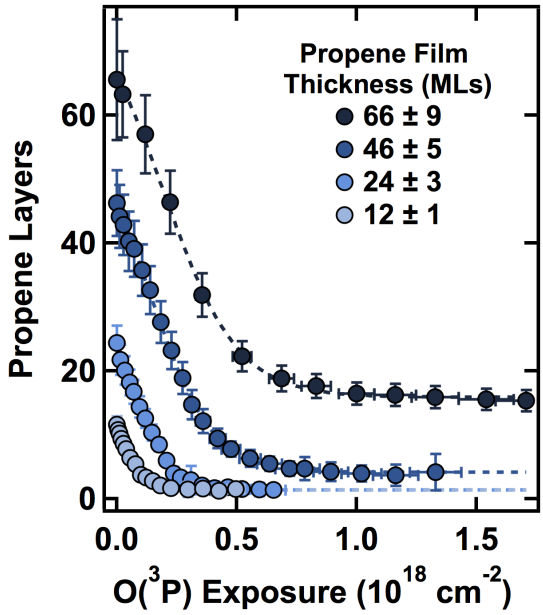

Figure 8.2: **Propene oxidation - propene consumption**. Changes in the number of propene layers on the surface (as determined via the integrated area of the =CH_2 wagging mode, γ_w) when films of varying thicknesses are exposed to O(^{3}P) at 54 K demonstrate initial reactivity that slows upon extended exposure. O(^{3}P) is only able to fully react the film when the initial film has fewer than 24 layers of propene. Dotted lines are drawn to guide the eye.

amount of acetone produced, confirmed spectroscopically by growth of a new peak at 1709 cm^{-1}, corresponding to its C=O stretching mode.[332,333]

To determine the role of film thickness in product formation and oxidative reactivity, propene films of increasing thickness ranging from 12 to 66 layers were dosed at 59 K and exposed to O(^{3}P) at 54 K. **Figure 8.2** depicts the decrease in the integrated area of the γ_w peak as these films are exposed. There is a clear period of initial linear reactivity for all films with a rate that is independent of the starting thickness. From these initial reactivity measurements, we estimate that $\approx$1 propene molecule reacts for every 100 oxygen atoms reaching the film surface. Given the observed rate of reaction and calculated barriers (below), this low reaction probability is perhaps surprising. We estimate, however, that at our surface temperatures, the sticking probability of oxygen atoms is on the order of 20% or less. This estimate was performed using the King and Wells technique[8] and thus explains why not every oxygen atom reaching the film is able to react. **Figure 8.2** also shows that after this initial period of exposure there is a stark drop in reactivity. In the 12 and 24 layer films, the reaction tails off because oxygen reacts with propene completely down to the Au(111) substrate. In thicker films, however, oxygen is unable to fully react with the propene in more buried layers. Moreover, the total reacted depth is inconsistent for both the 46 and 66-layer films (reaction complete at 4 layers and 23 layers remaining, respectively). This suggests that oxygen reactivity is connected to initial propene film thickness and that the reaction does not progress by simple layer-by-layer consumption of propene.

These results indicate that for films with fewer than 70 layers (**Figure 8.2**), the initial reactivity of O(^{3}P) + propene is linear and independent of film thickness. However, when examining thicker propene films (70 – 240 layers), the initial linear rate slows slightly (**Figure 8.3a**). When plotting the initial rates as a function of propene film thickness in layers, we see that initial propene reactivity plateaus for films greater than 150 layers (**Figure 8.3b**). We note that frequencies of the γ_w mode do not shift upon increased propene deposition, confirming that there are no major changes in film structure or optical effects as coverage increases.[334] Rather, we propose that these changes in initial reaction rates can be attributed to increased barriers for oxygen diffusion within the film,

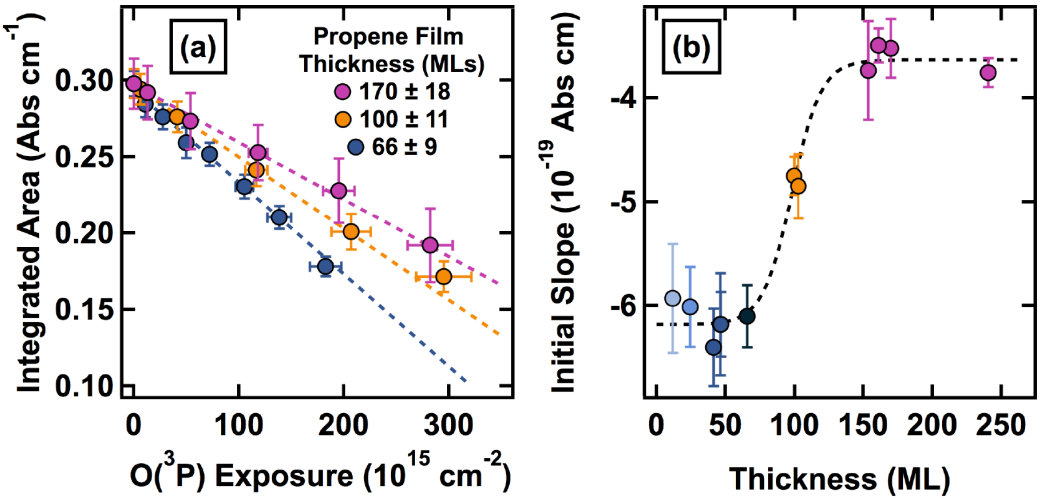

Figure 8.3: **Initial reaction rate varies with film thickness**. Integrated areas of the γ_w peak corresponding to 66, 100, and 170-layer thick propene films (a) show that the initial O(^{3}P) reactivity is linear with rates that depend on thickness. Taking these initial rates from (a) and including rates for films up to 240 layers (b) demonstrates that that this initial rate slows for films greater than 70 layers, but reaches a steady value for films greater than 150 layers. Dotted line in (b) is drawn to guide the eye.

as discussed in the following section (**8.3.2**).

Throughout oxygen exposure, propene disappearance is coupled to the growth of new spectral features corresponding to propylene oxide, propanal, and a small amount of acetone (**Figure 8.1**). Product growth is immediately observed upon O(^{3}P) exposure by monitoring the integrated areas of propylene oxide's δ_{C_2O} mode (**Figure 8.4a**) and propanal's $\nu_{C=O}$ mode (**Figure 8.4b**). We see that not only is there more propylene oxide and propanal formed in thicker films, but that the rate of formation of these products does not change with increasing film thickness (up to 70 ML). During exposure at 54 K, the Au(111) substrate temperature is such that propene and our products (propanal and propylene oxide) are stable on the surface.[313,323,331] Even though our film composition changes (decrease in propene, increase in propanal and propylene oxide), there is limited desorption of products, and thus our overall film thickness is likely comparable throughout. We detect no distortion or shifting of RAIR peaks as exposure continues and products form. Additionally, we expect that the index of refraction is comparable for alkene ices and oxygen hydrocarbons,[335] so we primarily attribute changes in peak intensity to reactivity and possibly molecular orientation,

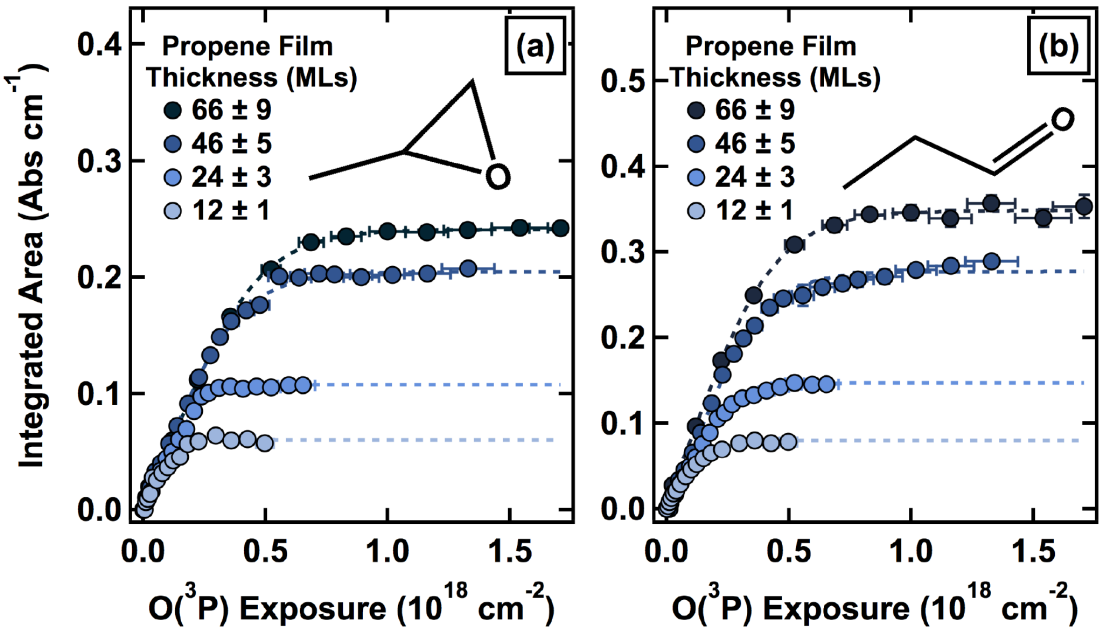

Figure 8.4: **Propene oxidation - product formation**. Integrated area of the propylene oxide ring deformation peak (δ_{C_2O}, a) and propanal C=O peak ($\nu_{C=O}$, b) for propene films of varying thickness exposed to O(^{3}P) at 54 K demonstrate that the primary products grow in with a similar linear rate. More product is formed in reactions with thicker films. Dotted lines are drawn to guide the eye.

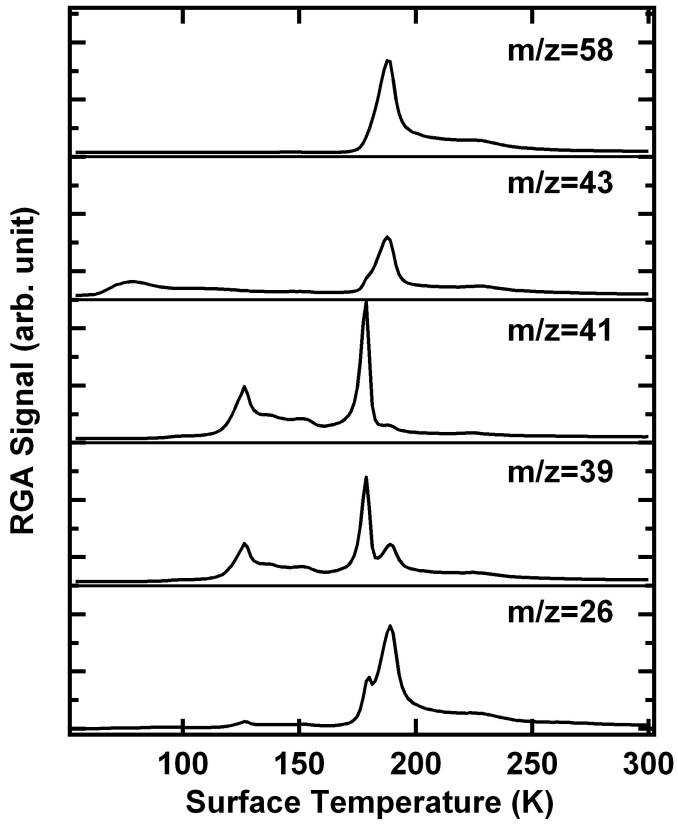

Figure 8.5: **TPD of propene oxidation products**. TPD of a 46-layer propene film after exposure to 1×10^{18} atoms cm^{-2} of O(^{3}P) confirms the presence of propanal (m/z = 26, 58), propylene oxide (m/z = 26, 43, 58), and acetone (m/z = 43). There is also some propene left on the surface (m/z = 39, 41).

rather than optical effects as our films are likely less than 100 nm thick.[336]

In addition to RAIRS, temperature programmed desorption (TPD) data can help to confirm product identities and their relative stabilities on the surface (**Figure 8.5**). For the 46-layer film, O(^{3}P) is unable to fully react the film down to the substrate (**Figure 8.2**), and there are correspondingly low-temperature desorption features for unreacted propene at m/z = 39 and 41. As shown in **Figure 8.5**, these first desorption features peak at 119 K, closely matching previous studies for propene on Au(111).[323] Although it is difficult to quantitatively differentiate our products due to significantly overlapping cracking patterns, we can assign m/z = 43 to acetone and propylene oxide, m/z = 26 to propanal and propylene oxide, and m/z = 58 to propanal, propylene oxide, and acetone. As shown in **Figure 8.5**, acetone appears to be the least stable with a small desorption

feature at 78 K, while propanal and propylene oxide have major desorption features at around 175 K.[331,337] From this analysis, it is clear that propanal and propylene oxide are not only our major products in the condensed phase, but also more stable on the surface. It is possible that these products are in weakly bound multilayer films, while there is less than a monolayer of acetone.[333] We also note that we do not identify any high-molecular weight polymeric or oligomeric species which suggests that our intermediate product species are not long lived on the surface.

8.3.2 Effect of Surface Temperature

In addition to characterizing film reactivity and product formation, we can use the initial reaction rates at surface temperatures ranging from 44 K to 59 K to calculate the activation energy for the disappearance of propene (films of ≈30 layers thick). The $=CH_2$ wagging mode of propene is comprised of two features at 919 cm^{-1} and 914 cm^{-1}. Upon exposure to O(^{3}P), **Figure 8.6a** depicts the loss of integrated area of 919 cm^{-1} peak for four different surface temperatures (all films dosed at 59 K). A corresponding Arrhenius plot is shown in **Figure 8.6b**; the calculated activation energy for the removal of propene's double bond is 0.41 ± 0.05 kcal mol^{-1}. Under our experimental conditions, this activation energy is similar to or less than those reported in gas phase studies of the same system.[338–340] However, because this value is calculated simply from the disappearance of propene, it is possibly a convolution of three different reaction steps, each of which will be explored in detail below.

The first challenge hidden within the measured activation energy is a question of product formation and reaction mechanism. The observed product distribution for the O(^{3}P) + propene reaction is well supported by a mechanism[341,342] (**Figure 8.7**) in which O(^{3}P) attacks the double bond to form a triplet biradical intermediate. It is important to note that our reaction products (acetone, propanal, and propylene oxide) are singlet species. As outlined by the PES in Leonori et al,[299] it is clear that our reaction proceeds almost 100% via ISC to the singlet surface, leading to our observed products. This can be accounted for by recent studies[299,343] demonstrating that ISC and nonadiabatic effects become increasingly important as reaction temperature decreases.[344]

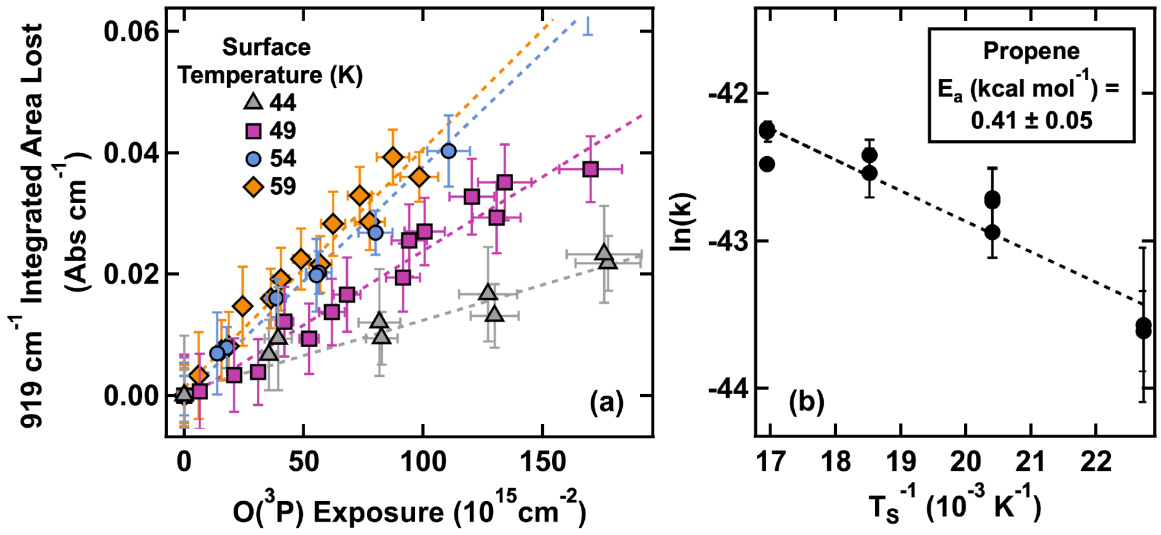

Figure 8.6: **Reaction kinetics - propene consumption**. Integrated area lost from the 919 cm^{-1} peak (part of the $=CH_2$ wagging mode, γ_w) corresponding to ≈30-layer thick propene films exposed to O(^{3}P) (a) provides initial linear reaction rates for surface temperatures ranging from 44 K to 59 K. These rates are fit to an Arrhenius model (b), giving an experimental activation energy of 0.41 ± 0.05 kcal mol^{-1}.

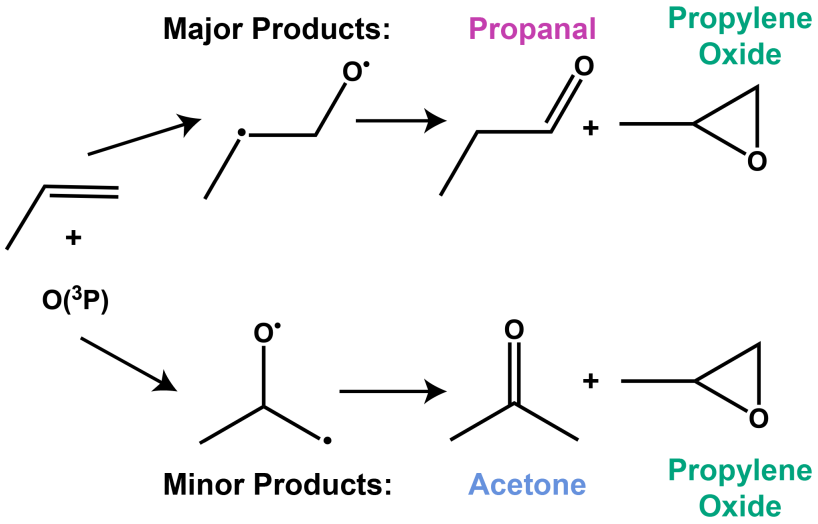

Figure 8.7: **Propene reaction mechanism**. Reported mechanism for the O(^{3}P) reaction with condensed propene: O(^{3}P) is expected to preferentially attack the least substituted side of the double bond to form a triplet biradical intermediate that progresses, via ISC, to the final products propylene oxide and propanal.

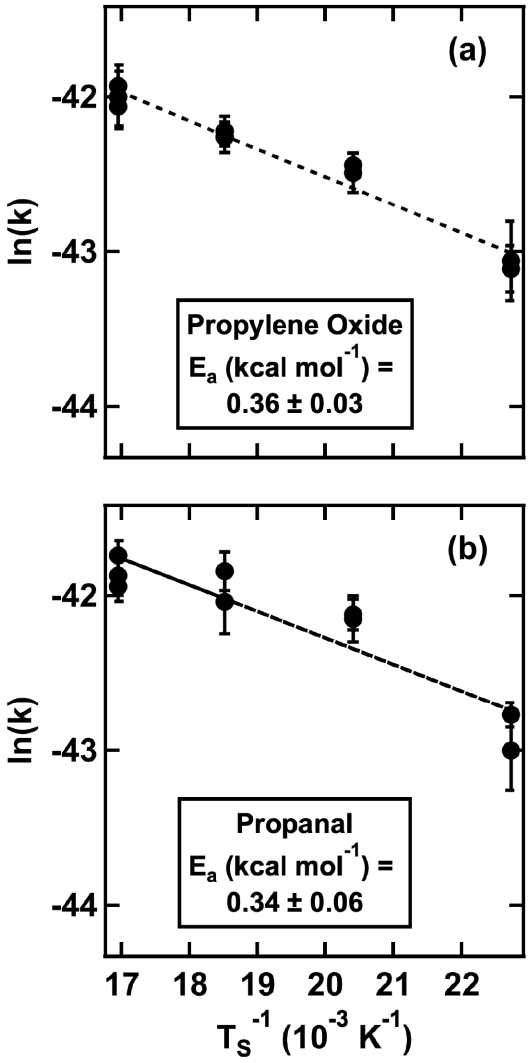

Figure 8.8: **Reaction kinetics - product formation**. Initial rate constants of propylene oxide (a) and propanal (b) formation from 30-layer thick propene films exposed to O(^{3}P) over temperatures ranging from 44 to 59 K are fit to an Arrhenius model. The experimental activation energies are 0.36 ± 0.03 kcal mol^{-1} and 0.34 ± 0.06 kcal mol^{-1} for propylene oxide and propanal formation respectively.

As mentioned above, however, the measured activation energy for propene oxidation may include barrier contributions for oxygen addition to either side of the double bond (**Figure 8.7**). To parse these contributions, we perform the same Arrhenius analysis on product formation, using the integrated area of propylene oxide's δ_{C_2O} mode and propanal's $\nu_{C=O}$ mode as a function of O(^{3}P) exposure. Propylene oxide is a major product in both addition channels, while propanal should only be formed from addition of oxygen to the terminal propene carbon.

The results of this analysis show that the activation energy for propylene oxide formation is 0.36 ± 0.03 kcal mol^{-1} (**Figure 8.8a**) and 0.34 ± 0.06 kcal mol^{-1} for propanal formation (**Figure 8.8a**). These values are in good agreement with one another, and they are also within error of the measured activation energy for destruction of propene's double bond (0.41 ± 0.05 kcal mol^{-1}). This suggests that not only is oxygen addition to the terminal carbon the dominating pathway, obeying Cvetanovic's rules for oxygen addition to alkenes,[341] but the addition step itself is rate limiting.[302] This makes sense for our low temperature, condensed phase environment given that in the gas phase the barrier for O(^{3}P) addition is three times higher for the central carbon compared to the terminal carbon.[299]

To further assess the mechanism, we examine changes in the CH region associated with the terminal and central carbons. This analysis is shown for a representative 46-layer film, but these trends are consistent for films of varying thicknesses. In particular, as shown in **Figure 8.9a**, we track changes in peaks at 2977 cm^{-1} (CH_2 + CH stretching) and 3075 cm^{-1} (CH_2 stretching). We integrated these two peaks as a function of O(^{3}P) exposure and normalized their intensity to the pristine film (**Figure 8.9b**). When oxygen atoms are introduced into the film, there is a clear decay in intensity for both peaks, again supporting that atomic oxygen is easily able to react with the condensed propene. The relative reaction rates in **Figure 8.9b** suggest that reactivity is greater for the 3075 cm^{-1} peak corresponding to only CH_2 stretches (green) compared to the 2977 cm^{-1} peak corresponding to CH_2 + CH stretches (orange). This can be interpreted as again reinforcing that oxygen addition to the terminal carbon is the dominant pathway. We also note that because we are using RAIRS, this trend may also be linked to a change in average molecular orientation;

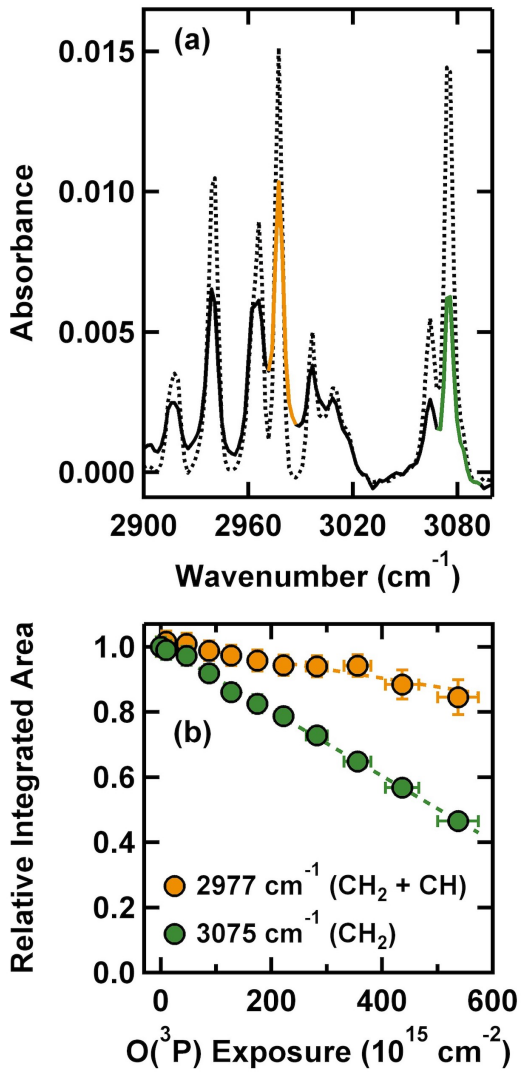

Figure 8.9: **Propene reactivity in the CH region**. (a) RAIR spectra of the CH region of a 46-layer propene film before (dashed line) and after exposure to $O(^3P)$ (solid line, total exposure 5×10^{17} atoms cm^{-2}) at 54 K shows significant reactivity. (b) Normalized intensities as a function of exposure demonstrate different rates of reaction for peaks at 2977 cm^{-1} (orange, CH_2 + CH stretching mode) and 3075 cm^{-1} (green, CH_2 stretching mode).

this is, however, unlikely to be a significant contribution due to the thick, polycrystalline nature of the film.[319]

Also complicating this analysis is a small decrease in intensity of the peaks at 2939 cm^{-1} and 2964 cm^{-1} corresponding to the CH_3 stretching modes. This suggests that although oxygen addition is the dominant mechanism, hydrogen abstraction may be a minor secondary pathway. Gas phase studies found that H abstraction was unable to compete with oxygen addition,[114] and although barriers in the condensed phase are often lower, we do not expect that H abstraction is a significant contribution to the overall reaction mechanism. H abstraction would necessarily yield a highly reactive hydroxyl radical,[287] which we see no evidence for in our product analysis. Moreover, abstraction leaves behind a carbon-centered radical that could easily continue to react with other molecules in the film or with oxygen species in the beam. It is possible that a small amount of acrolein is formed through this channel, but it is certainly only a minor contribution.

The second challenge with quantifying a reaction barrier for this system in the condensed phase is the potential contribution of oxygen diffusion. To untangle this contribution, we return to the difference in initial reaction rates observed between thin ($<$70 layer) and thick ($>$150 layer) films). By performing the same Arrhenius analysis again on 150 ML films, we find that the activation energy for the reaction of propene's double bond is 1.06 ± 0.11 kcal mol^{-1}. This is significantly higher than the calculated barrier for $\approx$30-layer propene films (0.41 kcal mol^{-1}), suggesting that oxygen diffusion through the film plays a significant role in the observed reaction in thicker films.[341,345–347] The thinnest propene films ($<$70 layers) may contain more small defects, grain boundaries, and islands that allow oxygen more ready access to the bulk. In other words, the reaction is not diffusion controlled for thin films because there is less need for diffusion: the surface is likely inhomogeneous with exposed propene islands.[348] Higher reactivity at defects and grain boundaries is well documented,[349,350] and as with other thick molecular films, self-similarity may not be achieved until a certain thickness is reached (often $>$100 layers).[22,183,190,351] Our results, therefore, suggest that propene films reach self-similarity at approximately 150 layers, at which point oxygen diffusion becomes limiting.

8.3.3 *Effect of Propene Film Structure*

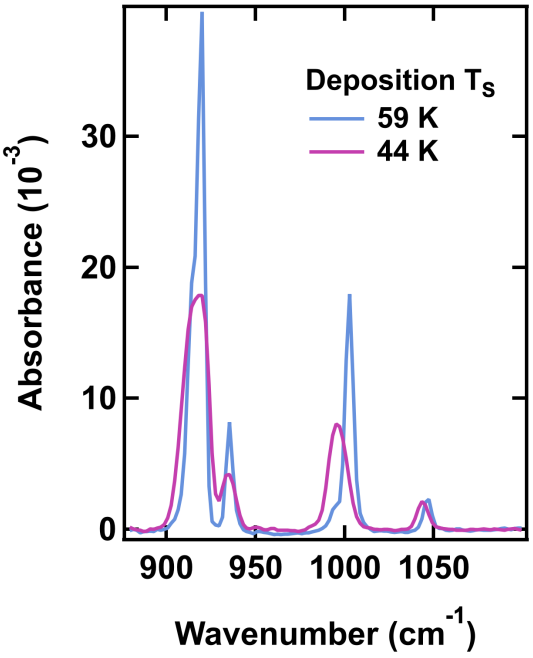

Figure 8.10: **Crystalline vs. amorphous propene - RAIR spectra**. RAIR spectra of characteristic regions of 46-layer condensed propene films demonstrate that films deposited at 44 K (pink) are significantly different than films deposited at 59 K (blue). The peaks corresponding to the γ_w mode, the C=C wagging mode, the CH_2 twisting + CH out of plane bending mode, and the CH_3 rock + CH out of plane mode in the low-temperature film are generally broader and red-shifted from the analogous high-temperature film. Such shifts indicate a more disordered and amorphous film.

For all experiments mentioned thus far, propene films were deposited at a surface temperature of 59 K and exposed to oxygen at temperatures between 44 and 59 K. However, as shown in **Figure 8.10**, the deposition substrate temperature has a profound impact on the RAIR spectra of the pristine propene film, indicating a significant difference in film morphology. This is true regardless of film thickness. The spectral differences between a propene film produced at 59 K and one produced at 44 K can be summarized as follows: The γ_w peak broadens and red shifts by 2 cm^{-1} to 918 cm^{-1}, the C=C wagging mode red shifts by 2 cm^{-1} to 933 cm^{-1}, the CH_2 twisting + CH out of plane bending mode red shifts by 7 cm^{-1} to 995 cm^{-1}, and the CH_3 rock + CH out of plane bending mode red shifts by 4 cm^{-1} to 1043 cm^{-1}. These alkene modes are known to be sensitive to the conformation of the molecule and local changes within the environment.[352] In

general, the peak shifts and broadening observed for the propene film dosed at 44 K compared to the propene film at 59 K is attributed to increased film disorder.[318,323,353] Red shifts may also be a result of increased intermolecular interactions with surrounding propene molecules, resulting in a slight weakening of the $=CH_2$ bond.

Although this is, to our knowledge, the first spectral evidence of differing morphologies of condensed propene, it is not unusual for deposition conditions to influence mobility during film deposition, leading to different film phases at different temperatures and dosing rates. There is vast literature, for example, on the growth of amorphous solid water and crystalline water ice films whereby crystalline films are only possible at higher substrate temperatures where there is enough mobility for water molecules to rearrange during dosing or upon annealing.[22,196,220,354] Similarly for alkenes, amorphous (produced at 12 K) and crystalline (produced at 70 K) acetylene have been clearly identified spectroscopically.[355] Upon warming the amorphous acetylene from 12 K, an irreversible change was detected in the spectra between 40 K and 50 K indicating that the amorphous acetylene ice was converted to a more crystalline form. Such spectral changes between amorphous and crystalline have also been detected for ethane and ethylene;[335] warming films to 60 K always resulted in crystallization. Based on the similarities between our observations and these studies, we will use the terms "amorphous" and "crystalline" to differentiate the films deposited below 44 K or at 59 K, respectively as propene films are less ordered when deposited below 44 K and more highly ordered at 59 K.

To determine how propene structure impacts oxidative reactivity, a crystalline film dosed at 59 K and an amorphous film dosed at 44 K were exposed to $O(^3P)$ at an intermediate temperature of 49 K (**Figure 8.11**). At 49 K, both propene films structurally remain the same as when deposited, the amorphous film is unable to irreversibly change to a crystalline structure and vice versa. As expected, the reaction rate for the crystalline film (blue) is linear as oxygen reacts with the film. On the other hand, the amorphous film grown at 44 K is largely unreactive. There is a very short initial period of reactivity, which we attribute to $O(^3P)$ reacting with the disordered propene surface layers at the vacuum interface. After this, however, there is little to no reaction despite extended

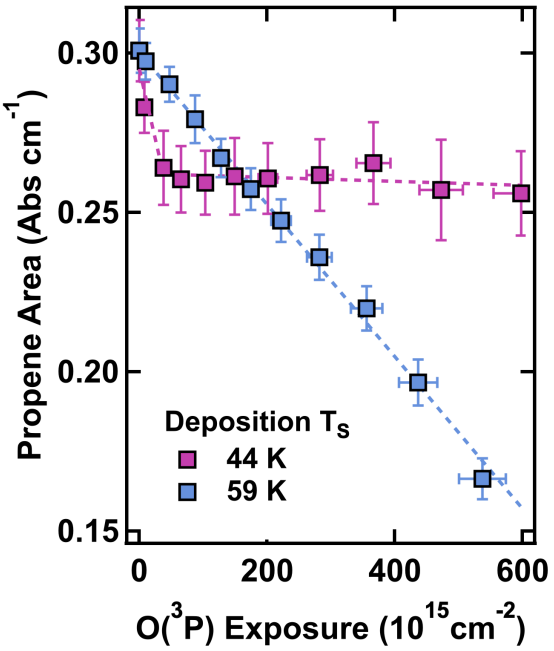

Figure 8.11: **Crystalline vs. amorphous propene - reactivity**. Changes in the integrated area of the γ_w mode for a 46-layer propene film dosed at 44 K (pink) and 59 K (blue) and exposed to O(^{3}P) at 49 K demonstrate that while films dosed at 44 K do experience some initial reactivity, O(^{3}P) is unable to penetrate into the bulk of the film; diffusion and reaction occurs more readily for propene films deposited at 59 K.

exposure; this is true for all RAIR spectral regions, including the CH. It is interesting to note that the initial reaction rate of the amorphous film is faster than the rate in the crystalline film. This may further support the "amorphous" vs. "crystalline" designation of the two films. A more amorphous film typically presents a larger exposed surface area (due to islands, microporous pockets, and under-coordinated surface molecules) than the crystalline film.[200,221] A larger surface area would provide more accessible surface propene molecules and thus a faster observable rate of initial reaction before oxygen penetration into the bulk becomes necessary for continued reaction.

Beyond the first seconds of reactivity, it is quite surprising that reactivity plateaus so drastically for the amorphous film. These results suggest that oxygen is unable to diffuse into the propene bulk when the film has a more amorphous structure. This behavior is supported by previous studies examining oxidative reactivity of self-assembled monolayers (SAMs)[84,356,357] that found that a more compact and less mobile film structure was not as reactive. Additionally, it has been suggested that

film density plays a role in observed spectroscopic band strengths, as is the case for amorphous methane.[358] Thus, the lower intensity of the peaks corresponding to amorphous propene could indicate increased density compared to the crystalline propene film. Although larger diffusion barriers in amorphous films are less common, there are polymer films where the amorphous regions are denser and this trend has been observed.[359,360] This suggests that our amorphous propene film may be packed more closely, making it less accessible to the permeating oxygen. We know from previous studies that monolayer propene molecules organize with the double bond nearly parallel to the Au(111) substrate.[323] This molecular orientation also appears to propagate to thicker multilayer crystalline propene films as well.[318] Thus, it is possible that in this crystalline propene structure, the molecules are organized in such a way that intermolecular-spacing affords easy access for oxygen to diffuse into the film and encounter propene's double bond.[361] It is also likely that our propene films are polycrystalline, and that grain boundaries further facilitate diffusion.[84]

RAIR spectra of the amorphous and crystalline forms of propene are easily differentiated, allowing us to probe the amorphous to crystallization transition directly and extract an activation energy for the process. We dosed amorphous propene films (70-layers thick) at 44 K and subjected them to isothermal annealing at 50, 51, 51.5, 52, 53, 54, and 55 K. Spectra collected every 60-90 seconds during the anneal clearly demonstrate a sharp phase transition (**Figure 8.12a**), evidenced by a sharpening of the peak at 919 cm^{-1} and a decrease in relative intensity of the 914 cm^{-1} shoulder. The crystallization process occurs over a time scale of 5-30 minutes, depending on the temperature.

We established rate constants for the crystallization by tracking the change in intensity at 919 cm^{-1} throughout the anneal. As shown in **Figure 8.12a**, the crystallizing spectra have multiple isobectic points where the spectra overlap, indicating a linear combination of crystalline and amorphous states.[362] Thus, the relative intensity of this point to both the starting fully amorphous film and the ending fully crystalline film can be used to establish the crystalline fraction of the film at any point in time.

This analysis is shown for a representative trial at each temperature by the dotted data in **Figure**

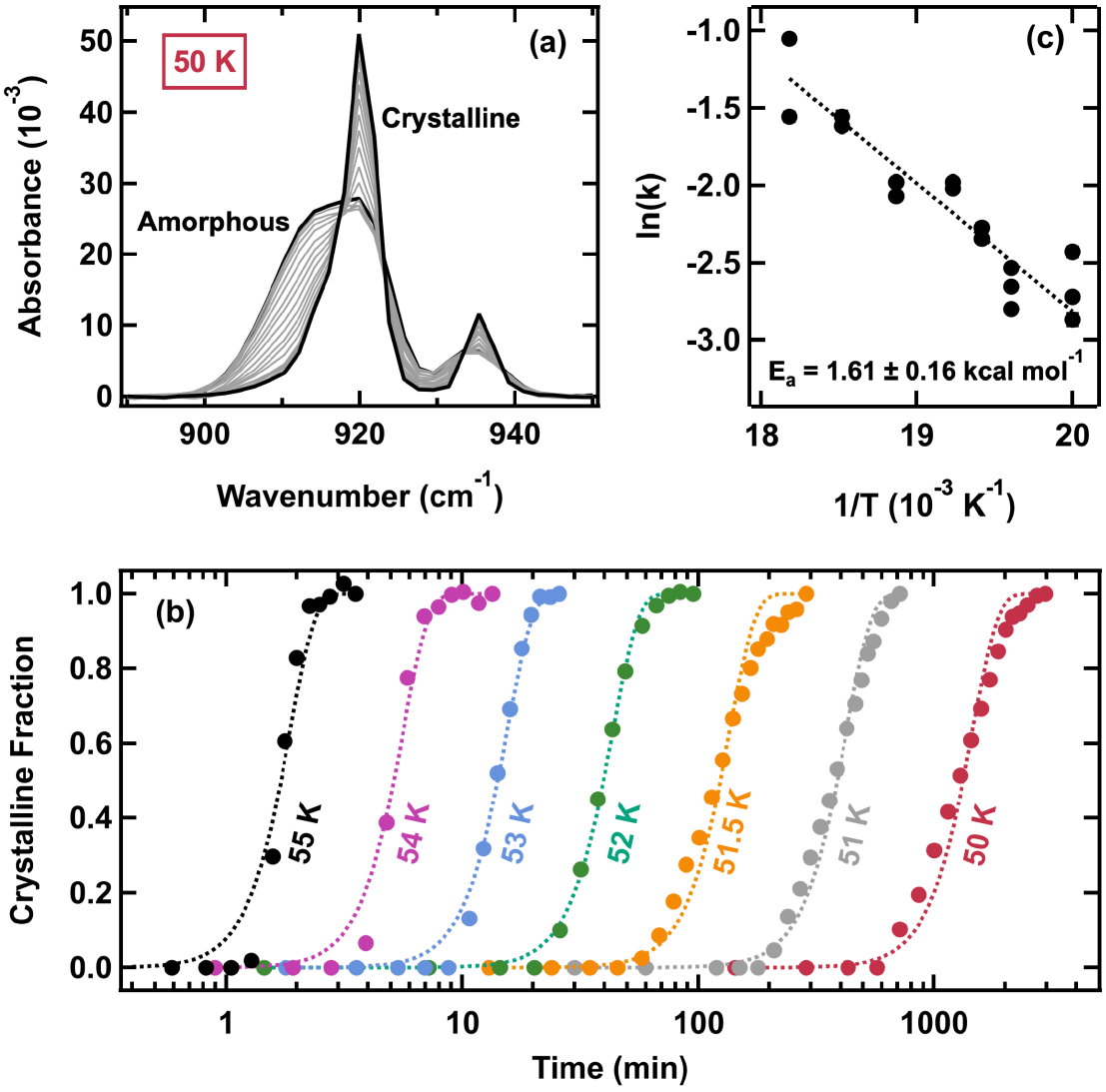

Figure 8.12: **Propene crystallization kinetics**. (a) Time-resolved RAIR spectra of 70-layer propene films isothermally annealed at 50 K indicate a transition from amorphous to crystalline propene. (b) Representative crystalline fractions versus annealing time (dots) are fit to the Avrami equation (**Equation 8.1**, dashed lines), using k as a fit parameter and a n value of 4 (see text for details). Crystalline fractions are established using the relative intensities of the corresponding spectra at 919 cm^{-1}. (c) Rate constants (k) are fit to an Arrhenius equation, yielding an activation of 1.61 $\pm$ 0.16 kcal mol^{-1} for the crystallization of propene.

8.12b. The corresponding fit (illustrated by a dashed line) is the integrated form of the Avrami equation:[363–365]

$$x(t) = 1 - e^{-(kt)^n} \tag{8.1}$$

This form of the Avrami equation is commonly used to describe phase transformation by nucleation and gives the crystallized fraction of a material ($x(t)$) as a function of time during isothermal annealing. In **Equation 8.1**, k is the crystallization rate constant (experimental fit parameter) and n is a parameter related to the crystallization mechanism.[362] A value of n = 4 fits the data well, suggesting that the nucleation rate is constant and that there is isotropic three-dimensional growth of the crystalline phase.[366,367] We note, however, that the value of n has little impact on the calculated activation energy for propene crystallization, which is the focus of this analysis.

We calculated an activation energy for the crystallization by assuming that the crystallization rate constants have an Arrhenius-like temperature dependence. This plot is shown in in **Figure 8.12c**; the corresponding analysis gives an activation energy of 1.61 $\pm$ 0.16 kcal mol^{-1}. This activation energy is much lower than those reported for water[362] or methanol[368] ices ($\approx$17-23 kcal mol^{-1}) indicating a low barrier for this irreversible change to crystalline propene. One possible explanation for this low value is that our amorphous propene might actually be in a metastable state, similar to what has been observed in ethane, ethylene, and acetylene ices.[335,355] However, since we do not observe any additional spectral differences between propene deposited between 20 K and 44 K, this seems unlikely. A second, more plausible explanation for the difference may be that the prope ne films used are thin ($\approx$70 layers); water film crystallization kinetics, for example, are only independent of thickness for films greater than 300 layers.[369]

Regardless, this analysis highlights a number of interesting features of the propene system. First, the Avrami fitting procedure and low activation energy barrier suggests that crystallization occurs rapidly, with nucleation occurring randomly (i.e. the weak physisorption interaction between propene and the Au(111) substrate is not the dominating factor in crystallization nucleation). Additionally, we demonstrate the general feasibility of using isothermal annealing and correspond-

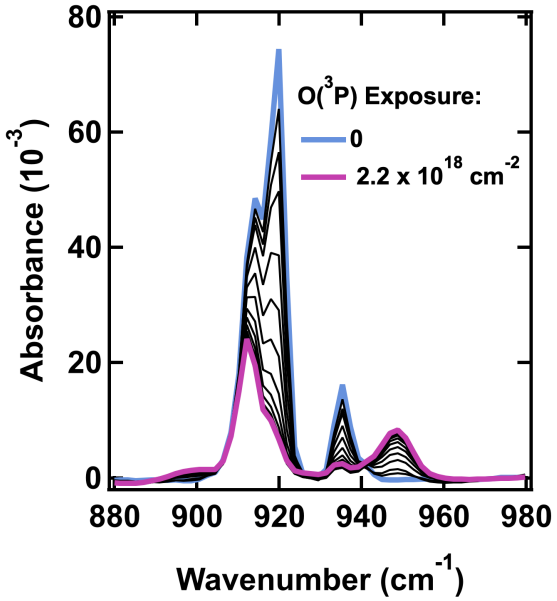

Figure 8.13: **Crystalline propene oxidation - γ_w mode**. Upon exposure to O(^{3}P), RAIR spectra of the γ_w propene mode shows a faster rate of intensity decrease for the higher wavenumber peak (919 cm^{-1}), indicating that there may be multiple domains within the propene film and that some of them are more accessible to O(^{3}P) reactivity.

ing spectra to determine alkene crystalline activation energies, which can be useful in discussing the relative stabilities of solids, liquids, and supercooled liquids.[368]

The discovery of multiple propene phases may also help to explain the observations from **Figure 8.2**, in which O(^{3}P) is unable to fully erode thicker films and the total reacted depth is inconsistent among thicker films. When propene films crystallize (**Figure 8.12a**), RAIR spectra show a dramatic change in the relative intensity of the γ_w mode; the 914 cm^{-1} shoulder decreases in intensity while the 919 cm^{-1} peak increases. During oxidation, this bluer peak (919 cm^{-1}) is consumed more readily (**Figure 8.13**). This may indicate that within "crystalline" films, there is not uniform O(^{3}P) reactivity within the film. Instead, it is possible that due to inhomogeneity in film organization, there are certain domains of increased order or accessibility where oxygen diffusion and reaction occurs more readily. *Our results, therefore, show broadly that film structure can have a dramatic impact on observed reactivity by impeding or allowing efficient reactant diffusion.*

8.4 Conclusion

The oxidative reactivity of condensed propene films at cryogenic surface temperatures has been characterized using time resolved RAIRS. We find that in the condensed phase, propene reacts readily with O(^{3}P) to form primarily propylene oxide and propanal, supporting a mechanism where oxygen almost always preferentially adds to the least substituted side of the double bond. Following addition, the triplet biradical intermediate undergoes ISC at a likelihood of close to 100% to form the singlet products: propanal, propylene oxide, and a small amount of acetone. The activation energy for the loss of propene in the O(^{3}P) + propene reaction for 30-layer thick films is 0.41 0.05 kcal mol^{-1} while the activation energy for propylene oxide formation is 0.36 $\pm$ 0.03 kcal mol^{-1} and 0.34 $\pm$ 0.06 kcal mol^{-1} for propanal formation. When examining thicker films (150 ML), we find that the activation energy for the reaction of propene's double bond is 1.06 $\pm$ 0.11 kcal mol^{-1} which suggests that oxygen diffusion through the film plays a significant role in the observed reaction. Interestingly, it is possible to spectroscopically differentiate two forms of propene: an amorphous form present at lower deposition temperatures ($<$44 K) and a crystalline form present at 59 K. Little reactivity is observed when the propene film is more disordered. Additionally, since RAIR spectra of the amorphous and crystalline forms of propene are easily differentiated, it is possible probe the amorphous to crystallization transition directly and extract an activation energy for this process.

Overall, this work provides fundamental mechanistic insight into the diffusion and reactivity of ground state atomic oxygen in condensed films of small, unsaturated hydrocarbons. Our results indicate that despite low reaction barriers for oxygen diffusion, film composition and morphology can have significant impact on reactant diffusion and subsequent reactivity. In general, such work informs the development of novel industrial processes used in the production of polyurethane plastics as well as shed light on possible chemical pathways in frozen astrophysical environments. In addition to these applications, an important future extension of this work may be to consider conformationally ordered, vinyl-containing films in which molecular orientation relative to the im-

pinging oxygen atom can be controlled, allowing for precise, stereodynamic tuning of reaction kinetics.

Appendix A

Appendices

Appendices **A1 - A7** contain the raw data for all figures reproduced in this thesis, organized by chapter in which the figure appears. Many figures include data points that represent the average of some collected value across numerous trials; the associated appendix figures include a table in the caption detailing the raw data used.

Appendix **A8** details the copyright attribution for all work reproduced in this thesis that has been published or submitted for publication.

A1 Experimental Methods (Chapter 2)

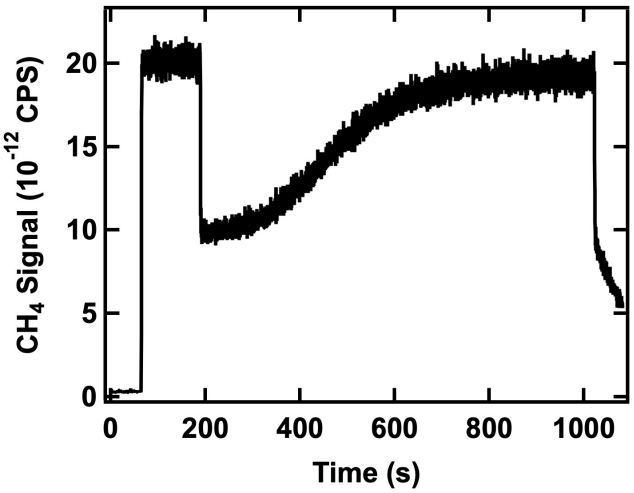

Figure A1.1: **Raw RGA data for Figure 2.4**. Signal intensity for a beam of CH_4 (seeded in H_2) exposed to a thick film of p-ASW D_2O. The beam nozzle is heated to 970 K, resulting in an energy of 1.8 eV (*Data file: 040618.R05*).

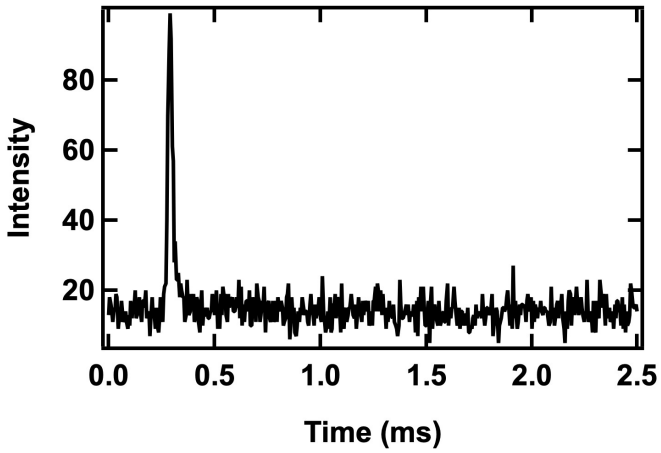

Figure A1.2: **Raw TOF data for Figure 2.6**. QMS signal intensity for a beam of CH_4 (seeded in H_2, 400 K) is collected as a function of time. $t = 0$ when the beam passes through the rotating chopper slit at 1% duty-cycle modulation. (*Data file: 040918T.F05*).

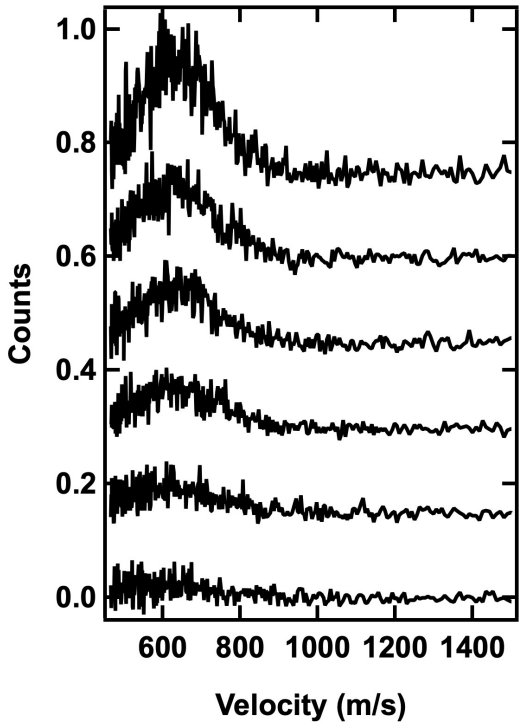

Figure A1.3: **Raw TOF data for Figure 2.7**. We collect a series of TOF spectra for a neat beam (CO_2, in this case) at various backing pressures and find the linear relationship between the integrated area of these curves and the calculated beam flux. We then use the slope of this fit to convert TOF peak area to absolute flux for seeded beams. (*Data files: 082917T.F01-6*).

A2 Oxidation, Destruction, and Persistence of Multilayer Dimethyl Methylphosphonate Films during Exposure to O(^{3}P) Atomic Oxygen (Chapter 3)

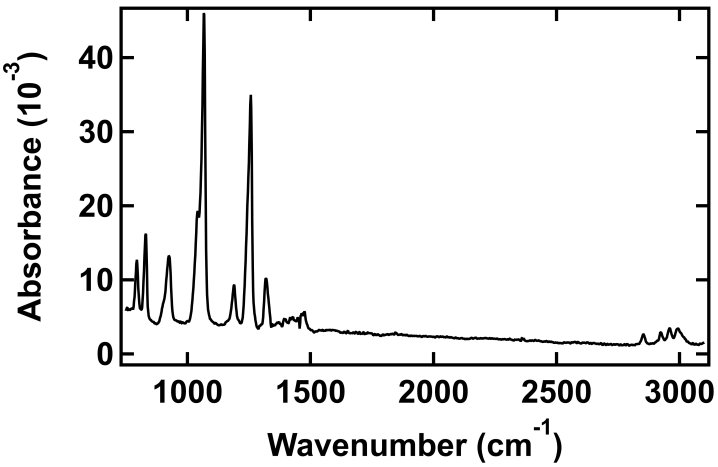

Figure A2.1: **Raw RAIR spectrum for Figure 3.1**. Raw RAIR spectrum of a forty-layer thick DMMP film on single-crystal Au(111). We dosed the film via directed doser while the crystal was held at 155 K. (*Data file: 081215A.IR01*).

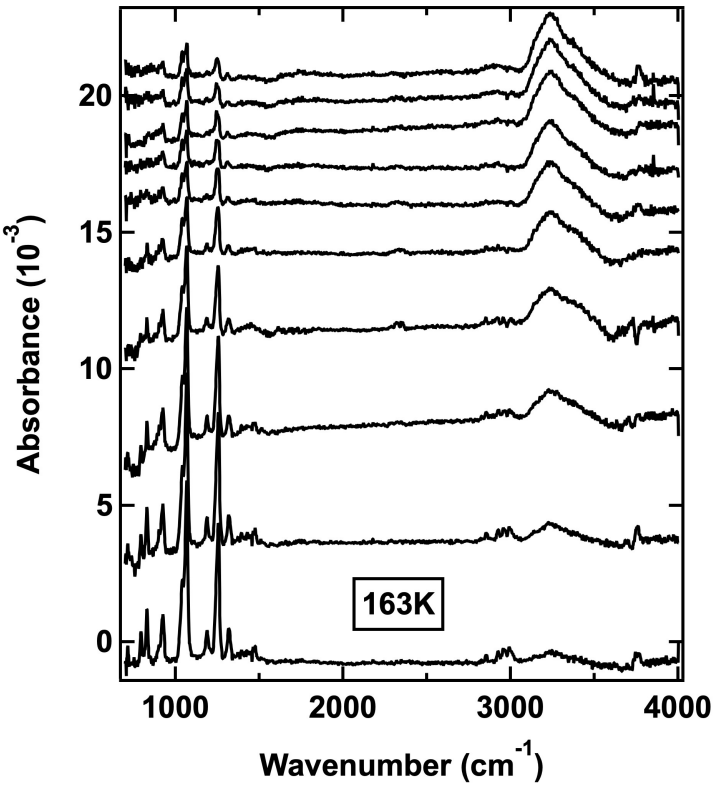

Figure A2.2: **Raw RAIR spectra for Figure 3.2 - 163 K**. A multilayer DMMP film desorbs slowly at 163 K; we collect spectra at regular time intervals and track the P-O-C modes at 1041 and 1066 cm^{-1} and compile the integrated areas in the 163 K panel of **Figure 3.2**. (*Data files: 042815B.IR01-10*).

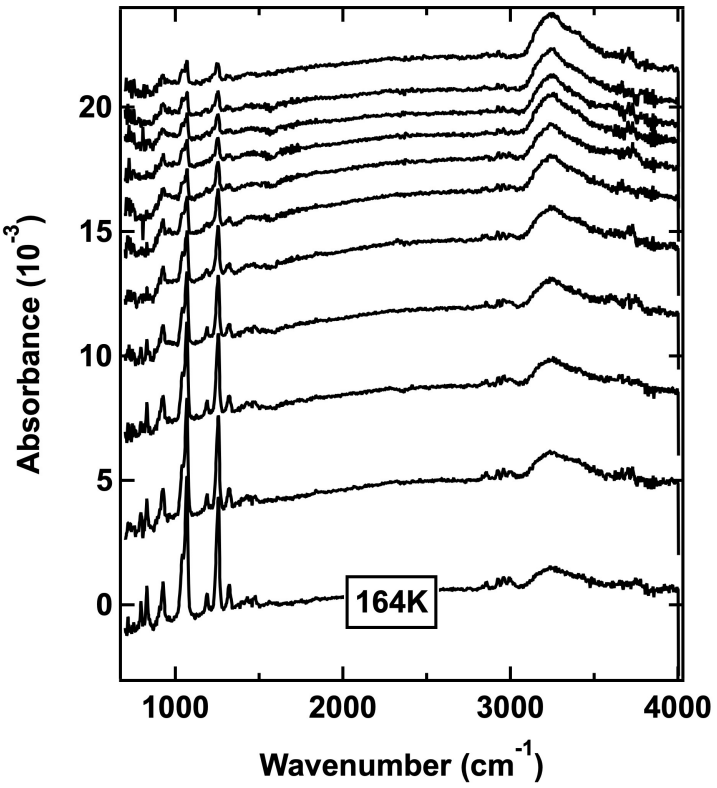

Figure A2.3: **Raw RAIR spectra for Figure 3.2 - 164 K**. A multilayer DMMP film desorbs slowly at 164 K; we collect spectra at regular time intervals and track the P-O-C modes at 1041 and 1066 cm^{-1} and compile the integrated areas in the 164 K panel of **Figure 3.2**. (*Data files: 043015B.IR01-11*).

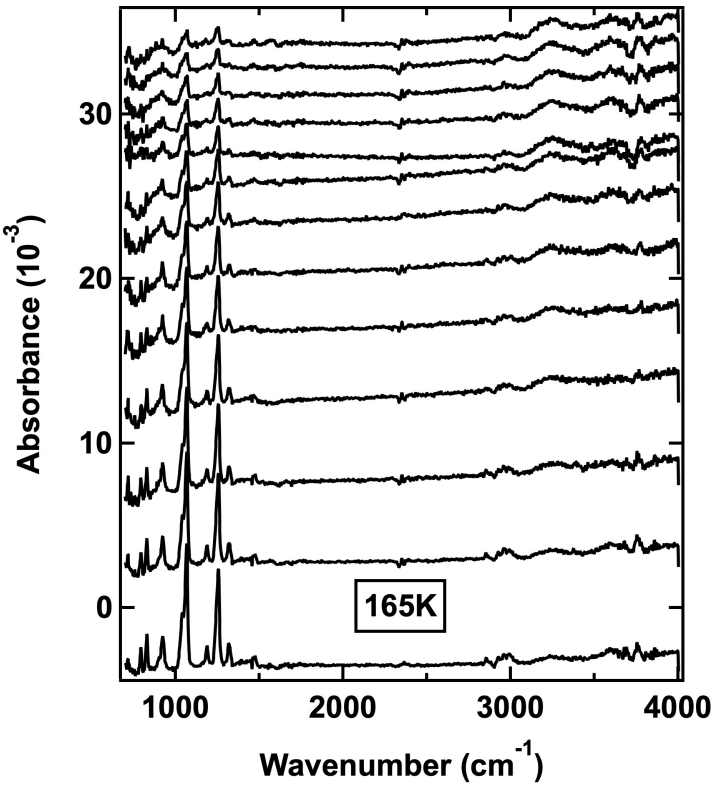

Figure A2.4: **Raw RAIR spectra for Figure 3.2 - 165 K**. A multilayer DMMP film desorbs slowly at 165 K; we collect spectra at regular time intervals and track the P-O-C modes at 1041 and 1066 cm^{-1} and compile the integrated areas in the 165 K panel of **Figure 3.2**. (*Data files: 050415A.IR02-14*).

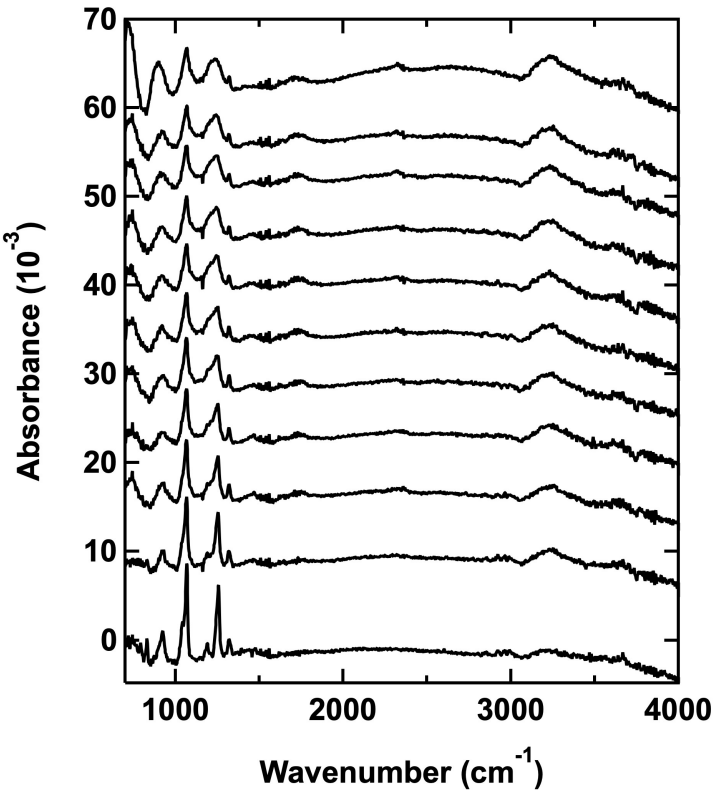

Figure A2.5: **Raw RAIR spectra for Figures 3.3 and 3.4**. A 6-layer DMMP film changes dramatically on exposure to O(^{3}P). We integrate each spectra in the P-O-C and P=O regions over the course of 106 minutes of exposure. The corresponding areas are discussed in **Figure 3.3b**. **Figure 3.4** details the relative intensities of the peaks comprising the P=O region. (*Data files: 082815A.IR01-10*).

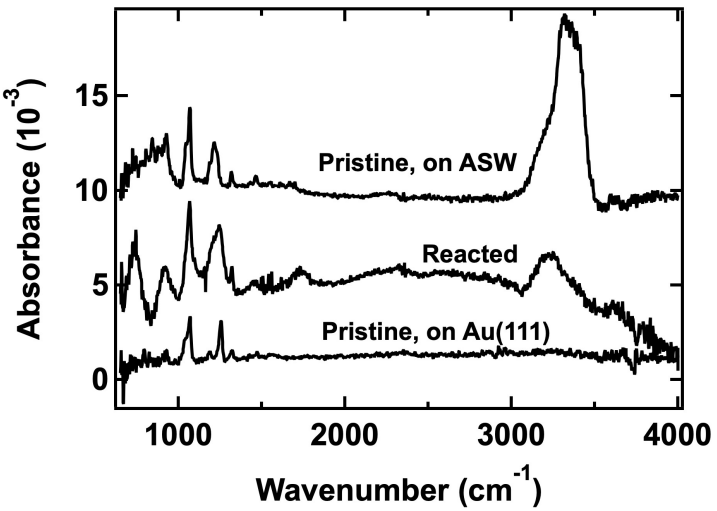

Figure A2.6: **Raw RAIR spectra for Figure 3.5**. We collected spectra of DMMP films (<10 layers) in three different regimes: as deposited on Au(111), following reaction with O(^{3}P), and as deposited on a thick film of amorphous solid water (ASW) ice. We prepare the ASW film *via* background deposition at a crystal temperature of 123 K. (*Data files: 082815A.IR08 (Reacted), 061215B.IR02 (Pristine, on Au(111)), 061115D.IR01 (Pristine, on ASW)*).

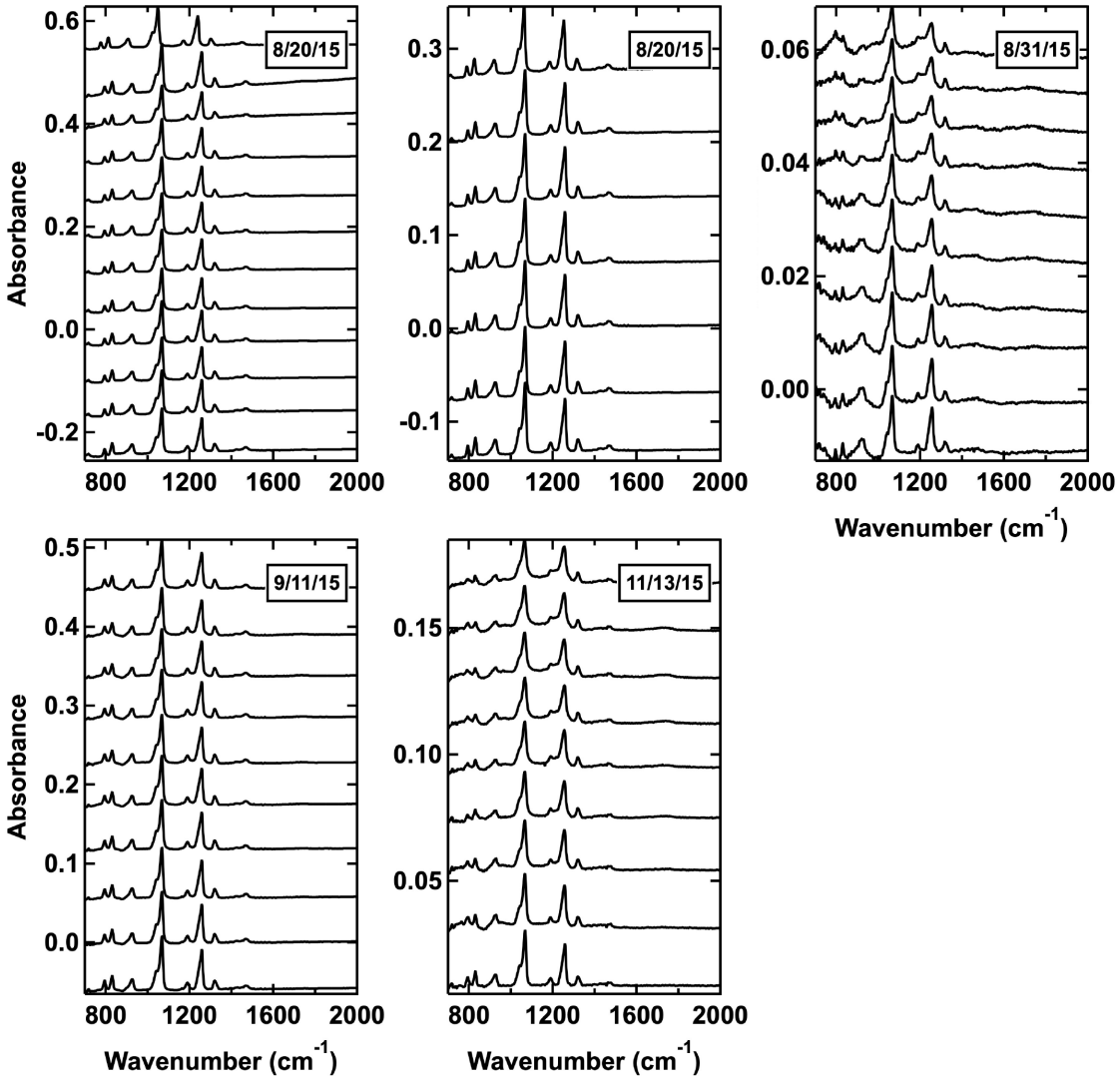

Figure A2.7: **Raw RAIR spectra for Figure 3.6**. We tracked the integrated areas of the P-O-C modes (1041 and 1066 cm^{-1}) from these spectra in **Figure 3.6** as DMMP films are exposed to O(^{3}P). For visual clarity, the spectra are truncated at 2000 cm^{-1} in this figure. (*Data files: 082015B.IR02-12 (39 layers), 082015B.IR13-19 (34 layers), 083115A.IR02-11 (6 layers), 091115A.IR01-10 (36 layers), 111315A.IR01-10 (12 layers)*).

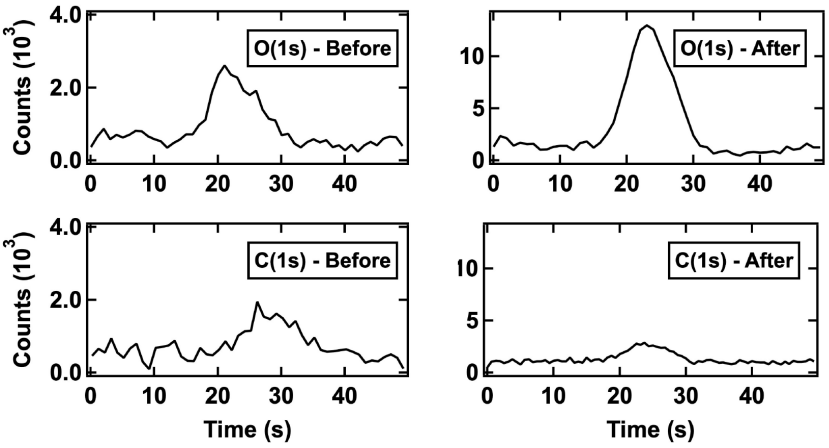

Figure A2.8: **Raw XPS spectra for Figure 3.7**. We collected XPS spectra of the O(1s) and C(1s) regions of a 15-layer DMMP film as deposited ("before") and following reaction with O(^{3}P) ("after"). We used different films for each collection due to X-ray-induced film damage. (*Data files: 100115.X02 (C(1s), before), 100115.X01 (O(1s), before) 090215.X01 (C(1s), after), 090215.X02 (O(1s), after)*).

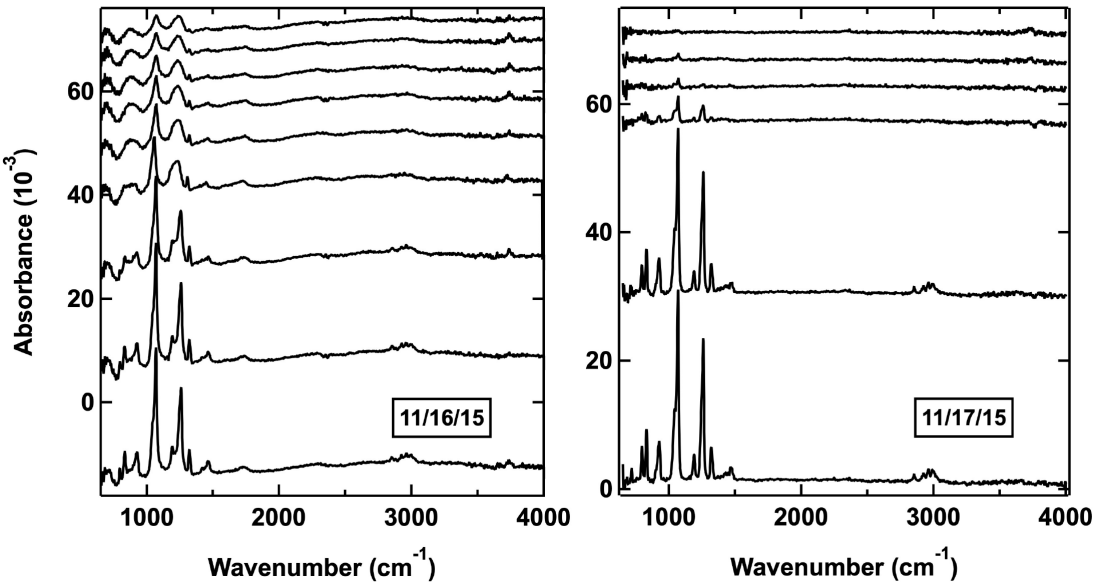

Figure A2.9: **Raw RAIR spectra for Figure 3.8**. We collected spectra of a pristine ("as deposited") and reacted ("exposed to O(^{3}P)") DMMP films (15 layers) at 10 K intervals during stepped programmed desorption experiments. (*Data files: 111615B.IR01-09 (reacted), 111715A.IR02-07 (pristine)*).

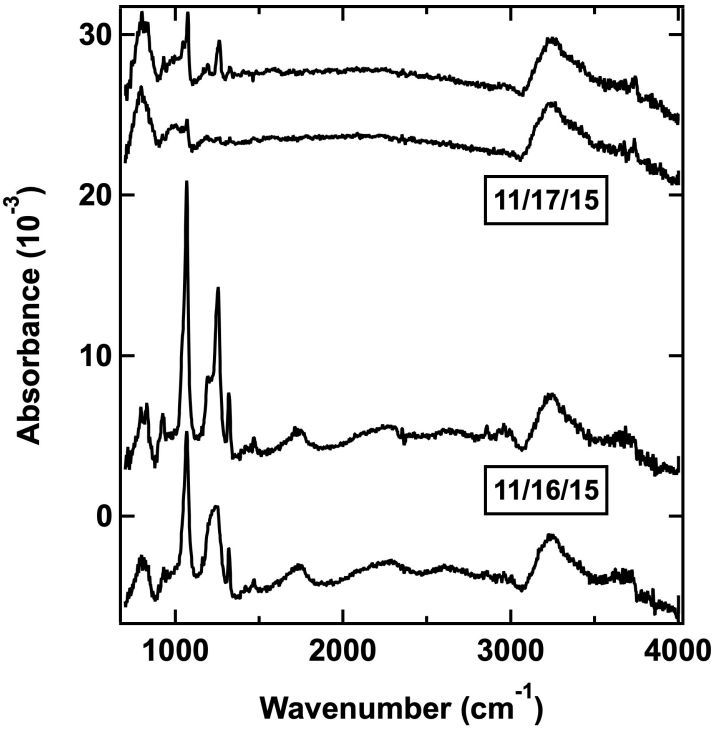

Figure A2.10: **Raw RAIR spectra for Figure 3.9**. These spectra are a subset of those collected for **Figure 3.8**; we examine the P=O region for the spectra at 185 and 195 K as the DMMP desorbs. (*Data files: 111615B.IR03-04 (reacted), 111715A.IR04-05 (pristine)*).

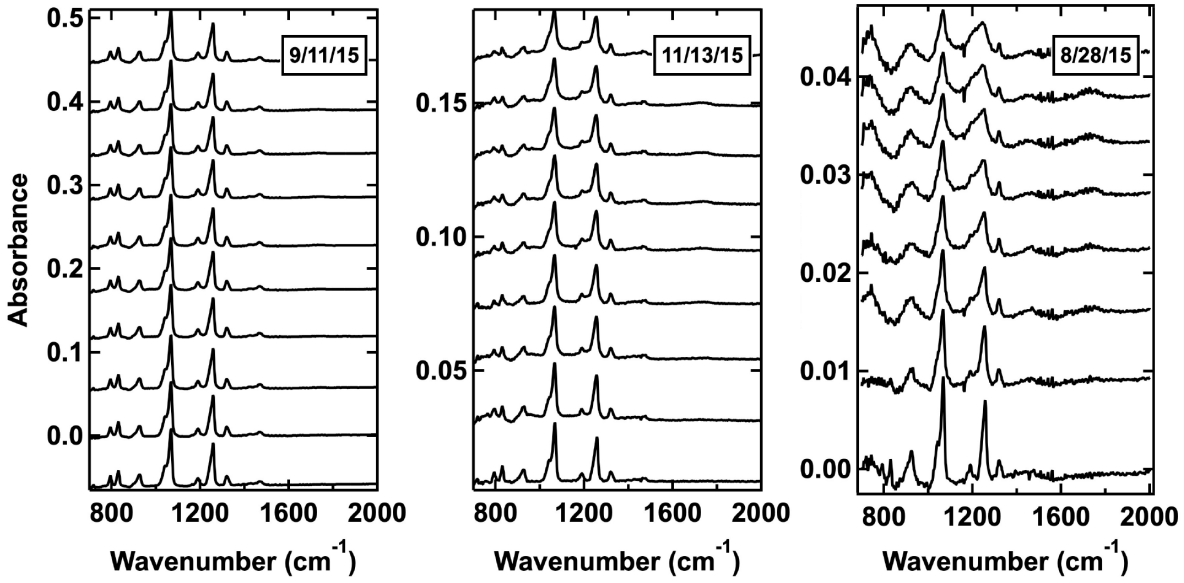

Figure A2.11: **Raw RAIR spectra for Figure 3.10**. We examine the change in integrated area in the P=O and P-O-C regions for DMMP films of varying thicknesses as they are exposed to O(^{3}P). (*Data files: 082815A.IR01-08 (6 layers), 111315B.IR01-09 (12 layers), 091115A.IR01-10 (36 layers)*).

A3 Oxidative Destruction of Multilayer Diisopropyl Methylphosphonate Films by O(^{3}P) Atomic Oxygen (Chapter 4)

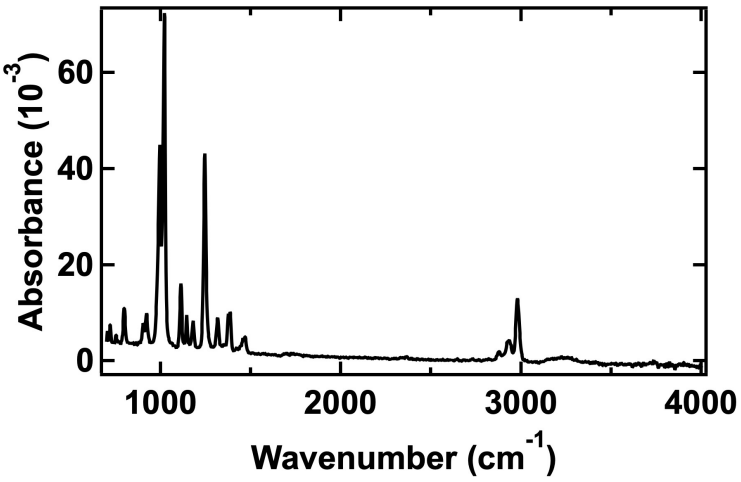

Figure A3.1: **Raw RAIR spectrum for Figure 4.1**. Raw RAIR spectrum of a thirty-layer DIMP film on single-crystal Au(111). Unless otherwise stated, all films in this chapter were deposited via beam dosing while the crystal was held at 165 K, and then annealed to 182 K. All O(^{3}P) exposure was similarly performed with the film at 165 K. (*Data file: 072716A.IR01*).

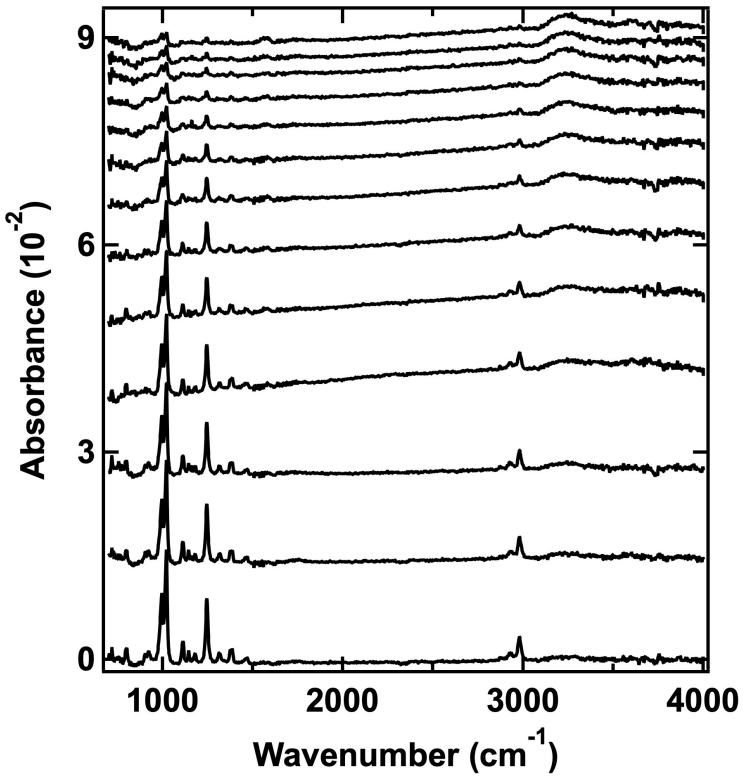

Figure A3.2: **Raw RAIR spectra for Figure 4.2**. Raw RAIR spectra of a six-layer DIMP film as it desorbs at 174 K. (*Data files: 070616A.IR02-14*).

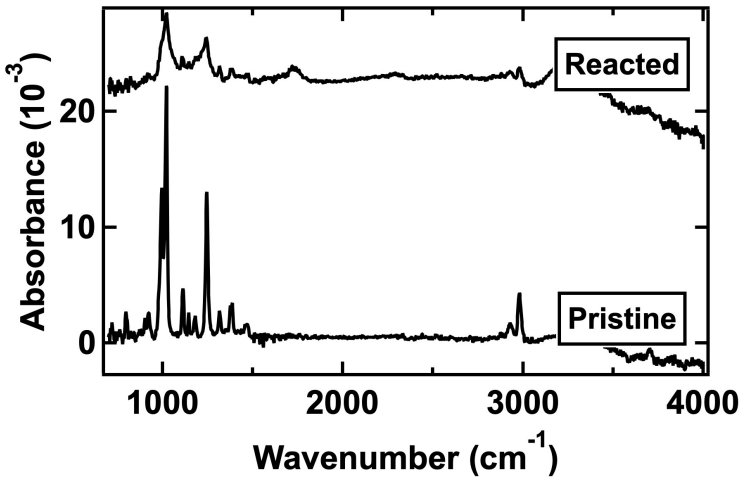

Figure A3.3: **Raw RAIR spectra for Figure 4.3**. Raw RAIR spectra of a seven-layer DIMP film before ("pristine") and after ("reacted") exposure to 1×10^{21} O(^{3}P) atoms cm^{-2}. (*Data files: 102716.IR01 (pristine), 102716A.IR03 (reacted)*).

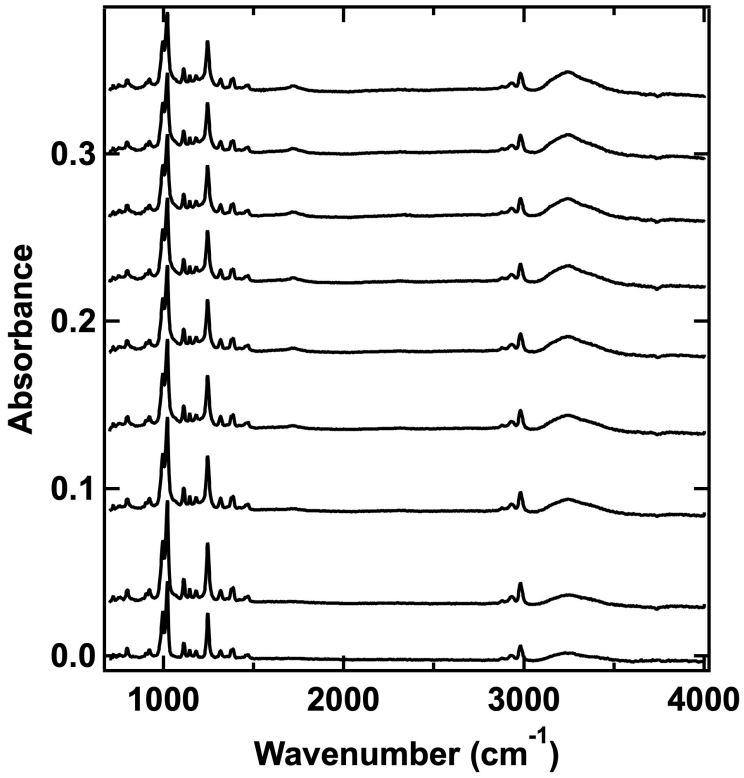

Figure A3.4: **Raw RAIR spectra for Figure 4.4**. Raw RAIR spectra of a 27-layer DIMP film during O(^{3}P) exposure; we track the integrated areas of the P=O and P-O-C regions. Total exposure was 2.4×10^{21} O(^{3}P) atoms cm^{-2}. (*Data files: 112916A.IR01-09*).

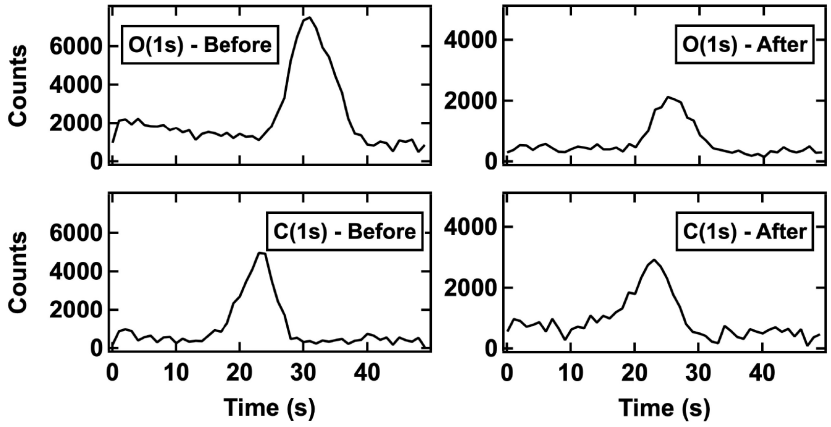

Figure A3.5: **Raw XPS spectra for Figure 4.5**. We collected XPS spectra of the O(1s) and C(1s) regions of a 17-layer DIMP film as deposited ("before") and following reaction with O(^{3}P) ("after"). We used different films for each collection due to X-ray-induced film damage. (*Data files: 102616.X02 (O(1s), before), 102616.X01 (C(1s), before) 102716.X05 (O(1s), after), 102716.X01 (C(1s), after)*).

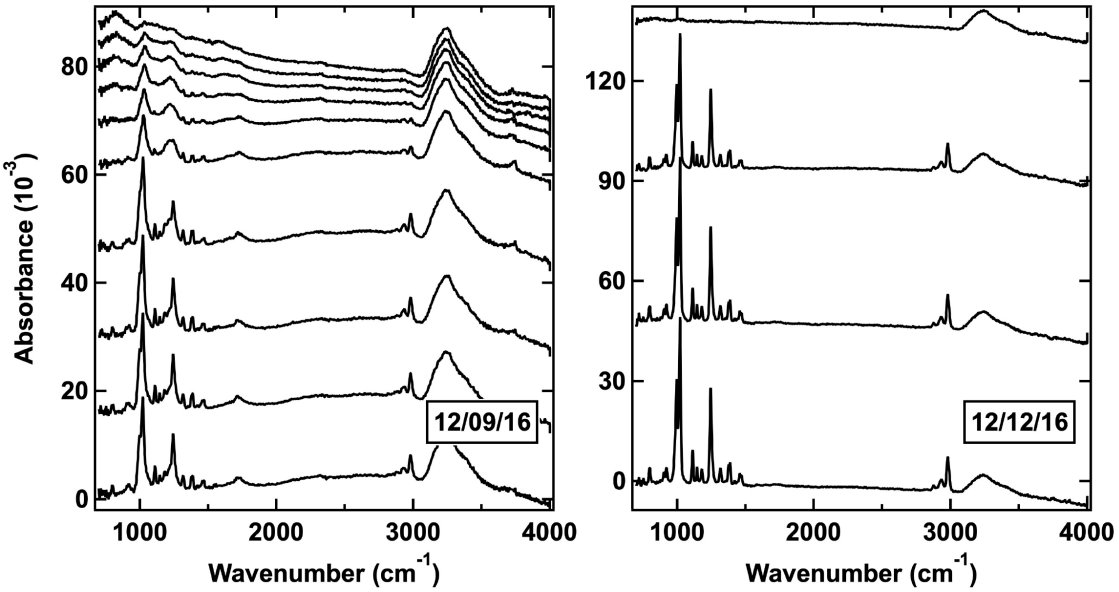

Figure A3.6: **Raw RAIR spectra for Figure 4.7**. We collected spectra of a pristine ("as deposited") and reacted ("exposed to O(^{3}P)") DIMP films (17 layers) at 10 K intervals during stepped programmed desorption experiments from 165 K to 355 K. (*Data files: 120916.IR06-15 (reacted), 121216A.IR01-04 (pristine)*).

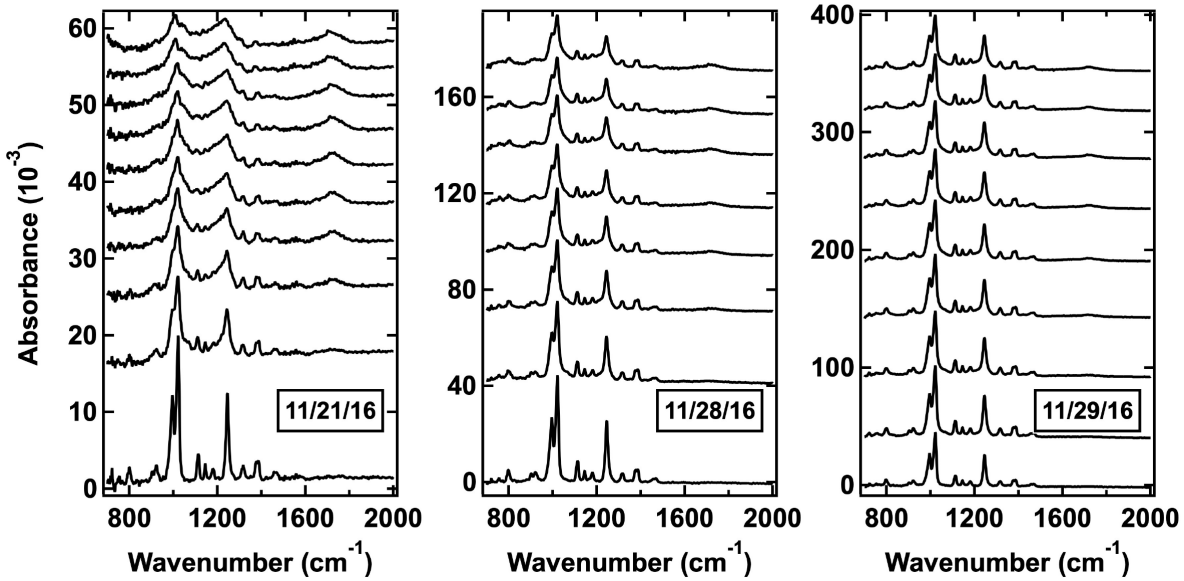

Figure A3.7: **Raw RAIR spectra for Figure 4.8**. We examine the change in integrated area in the P-O-C region for DIMP films of varying thicknesses as they are exposed to O(^{3}P). (*Data files: 112116A.IR01-10 (7 layers), 112816A.IR01-08 (17 layers), 112916A.IR01-09 (27 layers)*).

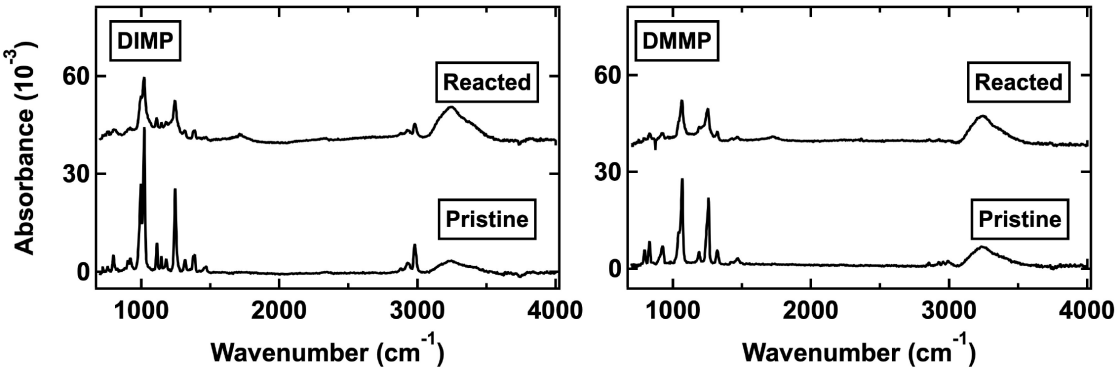

Figure A3.8: **Raw RAIR spectra for Figure 4.9**. We compare the qualitative changes in pristine and reacted DIMP and DMMP films. Both films are approximately 12-17 layers thick. (*Data files: 112816A.IR01,11 (DIMP), 122116A.IR01,07 (DMMP)*).

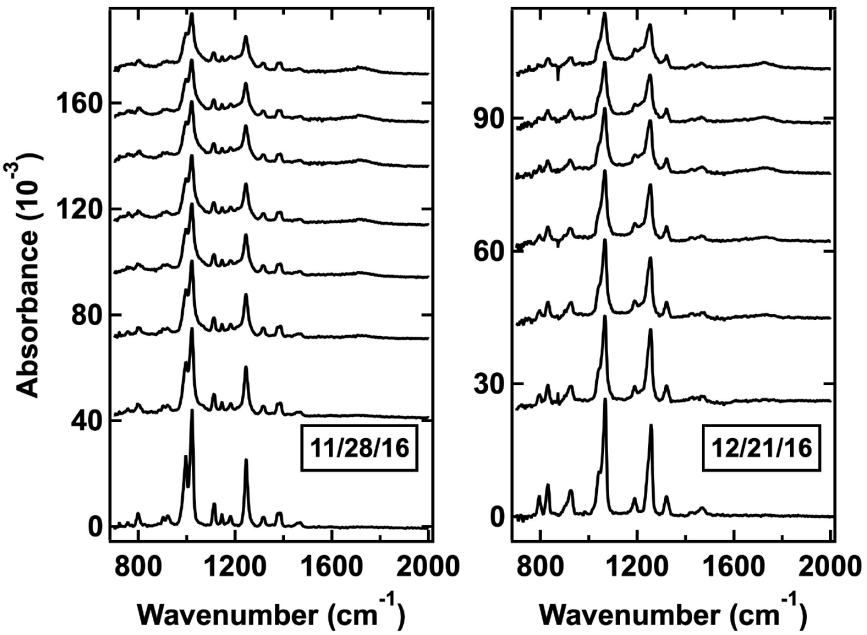

Figure A3.9: **Raw RAIR spectra for Figure 4.8**. We examine the change in integrated area in the P-O-C region for both DMMP (12 layers) and DIMP (17 layers) films as they are exposed to O(^{3}P) at 155 K. O(^{3}P) flux for DIMP was 1.3×10^{17} cm^{-2} s^{-1}, total exposure of 280 minutes. O(^{3}P) flux for DMMP was 2.1×10^{17} cm^{-2} s^{-1}, total exposure of 100 minutes. (*Data files: 112816A.IR01-08 (DIMP, 17 layers), 122116A.IR01-07 (DMMP, 12 layers)*).

A4 Rapid Laser-Induced Temperature Jump Decomposition of the Nerve Agent Simulant Diisopropyl Methylphosphonate under Atmospheric Conditions (Chapter 5)

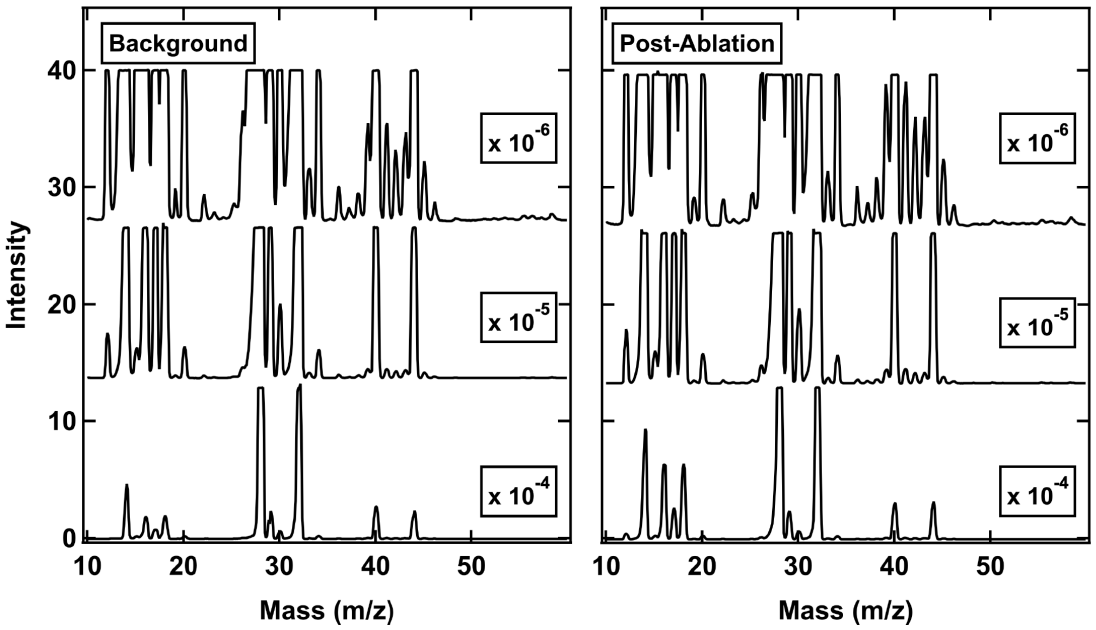

Figure A4.1: **Raw MS for Figure 5.3**. To collect one full mass sweep with the proper resolution, we compile three separate spectra collected with three different magnifications (nominally $\times 10^{-4}$, $\times 10^{-5}$, and $\times 10^{-6}$ Torr, although we do not use these absolute pressure values for comparison; we simply scale each scan to the same relative order of magnitude and compile a single spectra). Following simulant ablation, we collect and compile three more spectra to get a mass scan of the gaseous products. (*Data files: 073118F01-F03 (background), 073118F04-F06 (post-ablation)*).

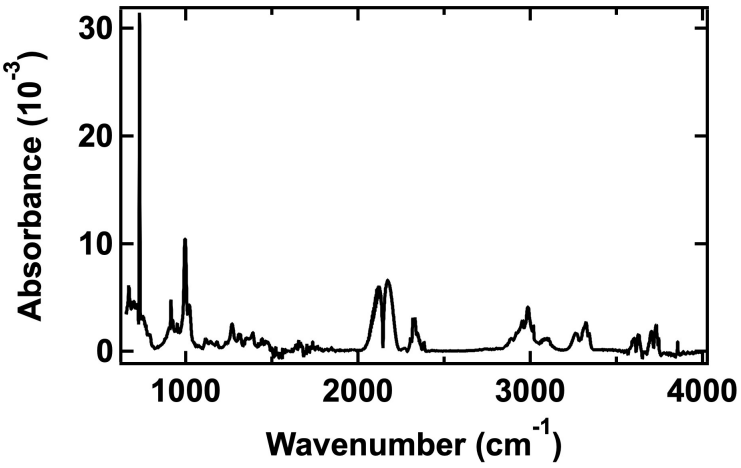

Figure A4.2: **Raw FTIR spectrum for Figure 5.4**. Following ablation in the atmospheric chamber, gaseous products flow into an evacuated chamber. We collect FTIR spectra of the contents of this chamber; this representative spectrum was collected after DIMP ablation to approximately 2720 K. (*Data file: 072718A.IR03*).

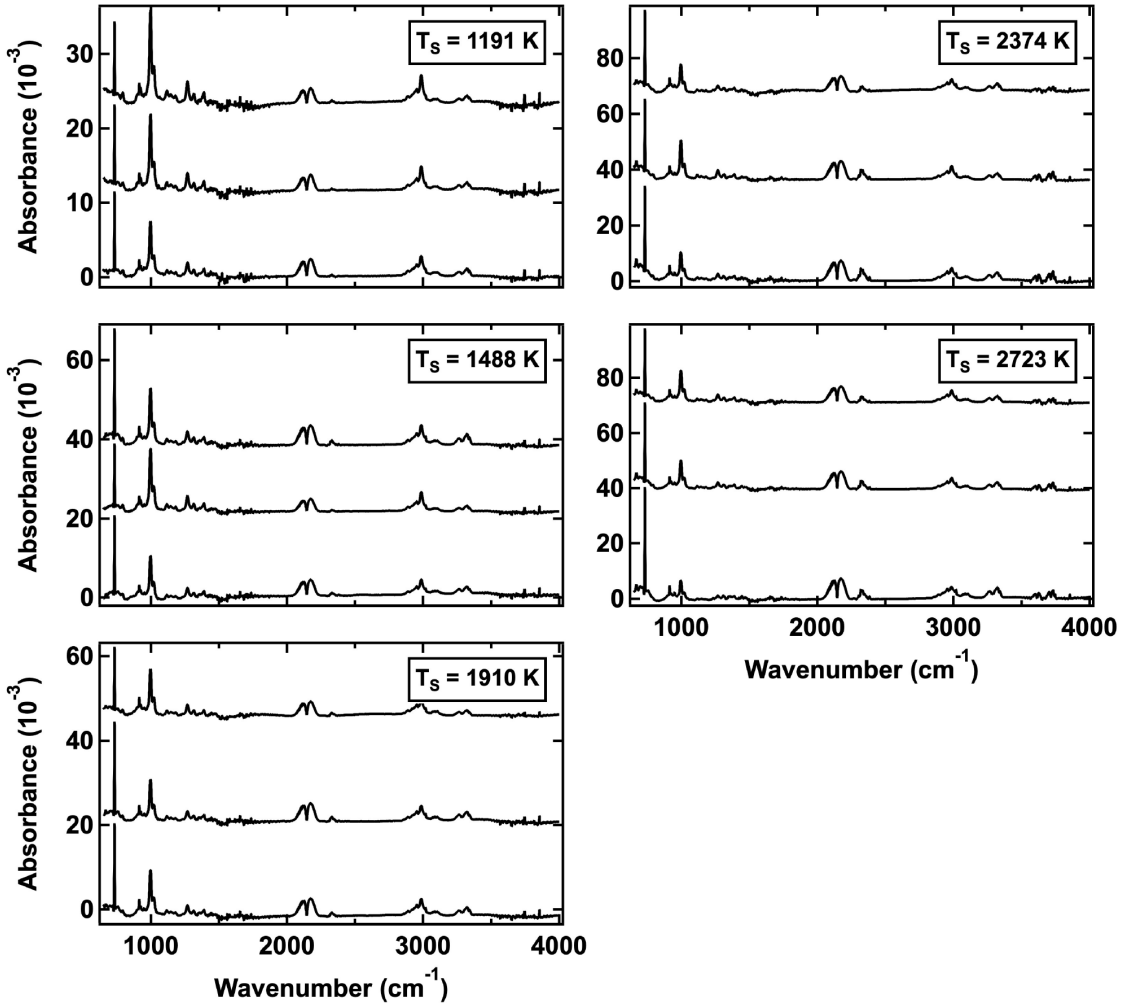

Figure A4.3: **Raw FTIR spectra for Figure 5.5**. We ablated DIMP at five different temperatures and collected FTIR spectra of the associated gaseous products. One spectra from each set is displayed in **Figure 5.5a**, and we average the relevant integrated areas (propene's $=CH_2$ wagging mode and ethylene's bending mode) from all three spectra at each temperature to create the plot in **Figure 5.5b**. (*Data files: 072518A.IR02-04 (1191 K), 072518A.IR05-07 (1488 K), 072618A.IR02-03 and 072718B.IR01 (1910 K), 0727618A.IR05-06 and 072718B.IR02 (2374 K), 072718A.IR01-03 (2723 K)*).

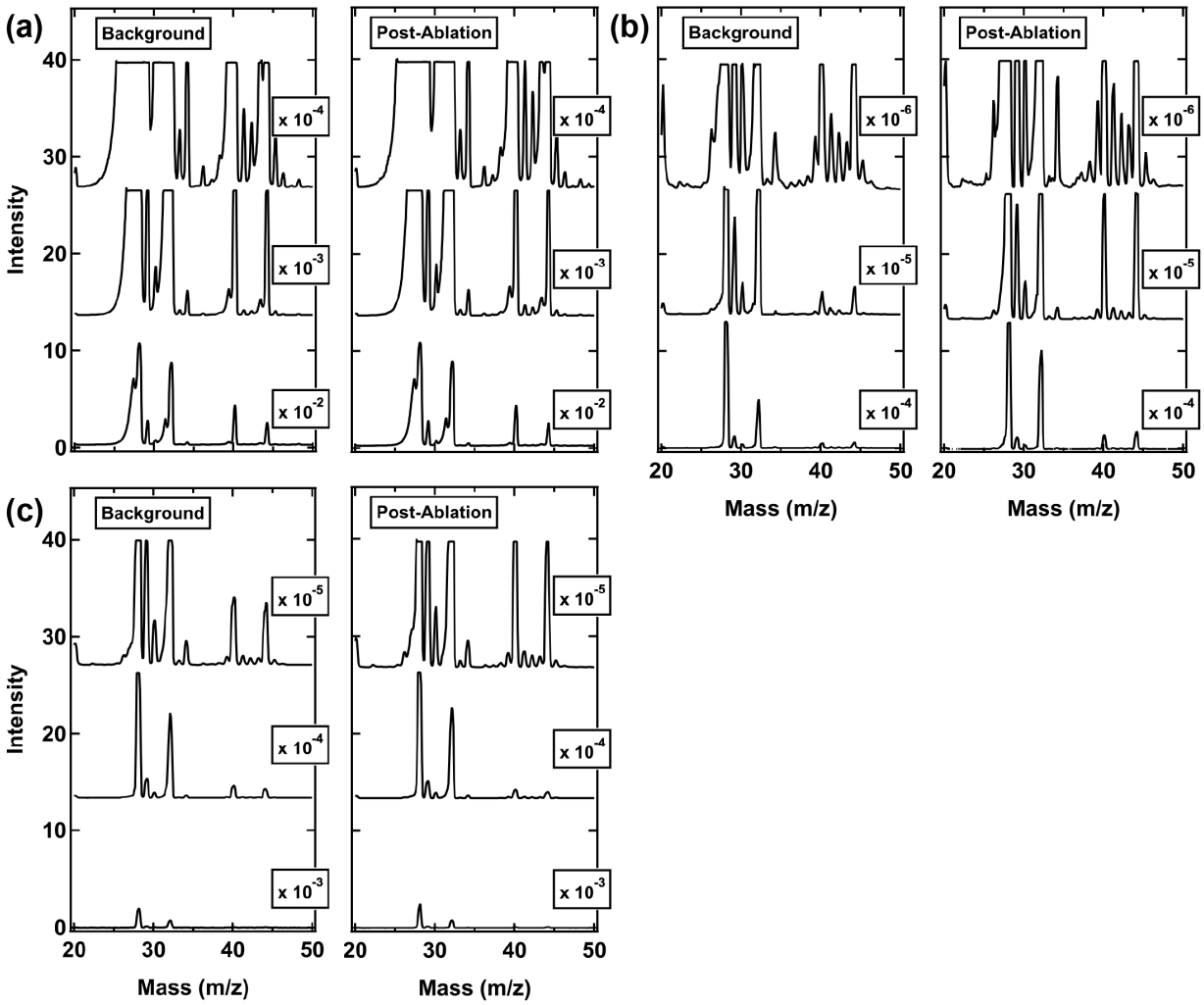

Figure A4.4: **Raw MS for Figure 5.6 - 1440 K**. We ablated DIMP at three different temperatures and collected *in situ* mass spectra of the associated gaseous products. **Figure 5.6a** contains the least-squares fit to the *080318B* data set, and the 1440 K data points in **Figure 5.6b** are the average amounts of propene and acetylene/ethylene present in spectra collected at this ablation temperature. (*Data files: 061418S01-06 (a), 080218E01-06 (b), 080318B01-06 (c)*).

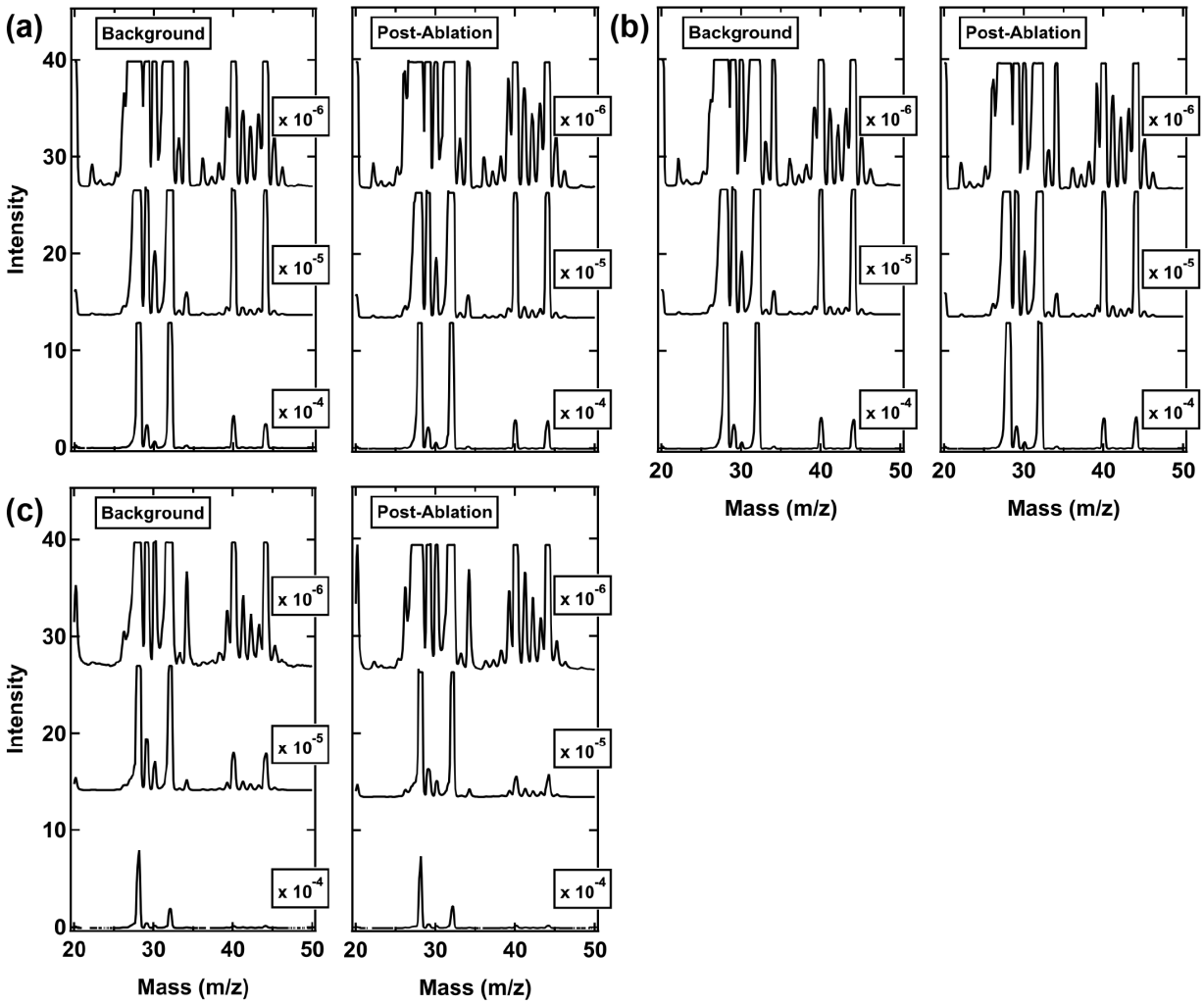

Figure A4.5: **Raw MS for Figure 5.6 - 2140 K**. We ablated DIMP at three different temperatures and collected *in situ* mass spectra of the associated gaseous products. **Figure 5.6a** contains the least-squares fit to the *073118G* data set, and the 2140 K data points in **Figure 5.6b** are the average amounts of propene and acetylene/ethylene present in spectra collected at this ablation temperature. (*Data files: 073118G01-06 (a), 073118H01-06 (b), 080218D01-06 (c)*).

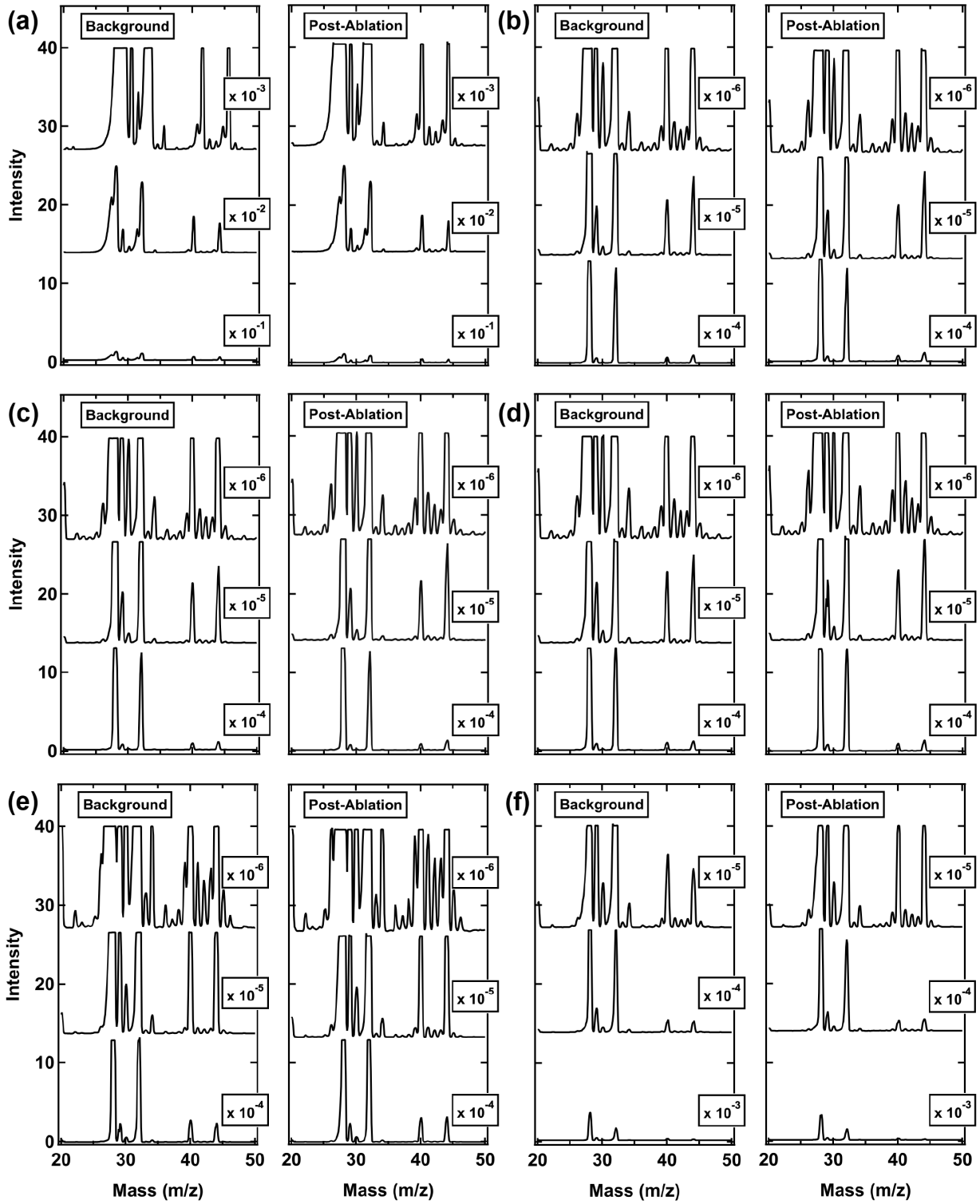

Figure A4.6: **Raw MS for Figure 5.6 - 2830 K**.

Figure A4.6: **Raw MS for Figure 5.6 - 2830 K**. We ablated DIMP at three different temperatures and collected *in situ* mass spectra of the associated gaseous products. **Figure 5.6a** contains the least-squares fit to the *073118F* data set, and the 2830 K data points in **Figure 5.6b** are the average amounts of propene and acetylene/ethylene present in spectra collected at this ablation temperature. Note: This data is also used as the atmospheric data in **Figure 5.7** (Oxygen pressure of 1×10^{-6} Torr). (*Data files: 061318S09-14 (a), 072718B01-06 (b), 072718C01-06 (c), 072718D01-06 (d), 073118F01-06 (e), 080318A01-06 (f)*).

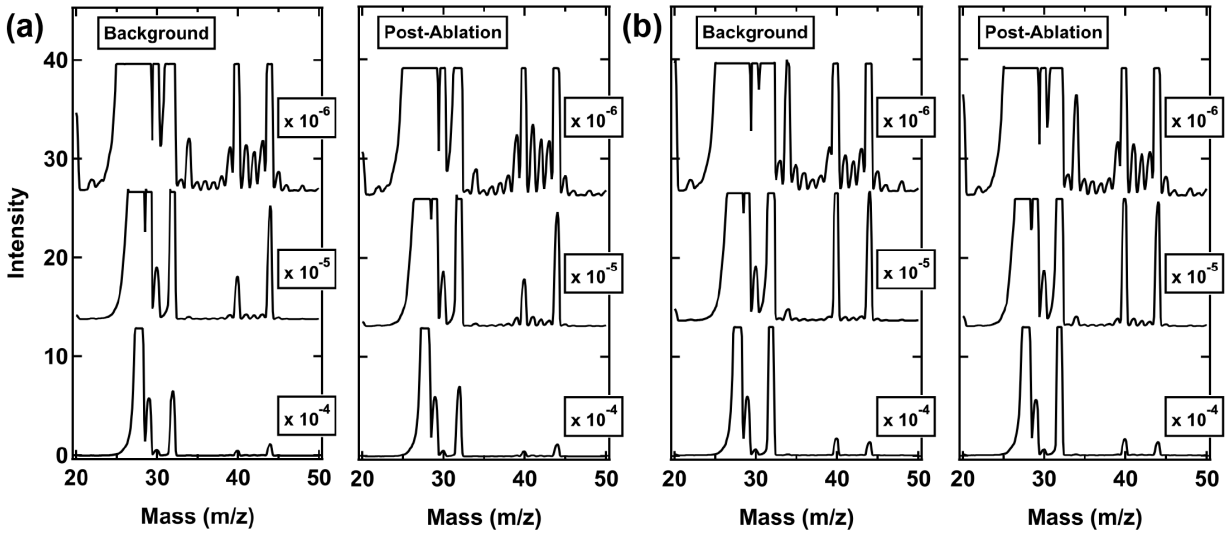

Figure A4.7: **Raw MS for Figure 5.7 - 2 $\times$ 10^{-7} Torr**. We ablated DIMP under three different atmospheric oxygen pressures and collected *in situ* mass spectra of the associated gaseous products. **Figure 5.7a** contains the least-squares fit to the *081418B* data set, and the 2×10^{-7} Torr data points in **Figure 5.7b** are the average amounts of propene and acetylene/ethylene present in spectra collected under these conditions. (*Data files: 081318F01-06 (a), 081418B01-06 (b)*).

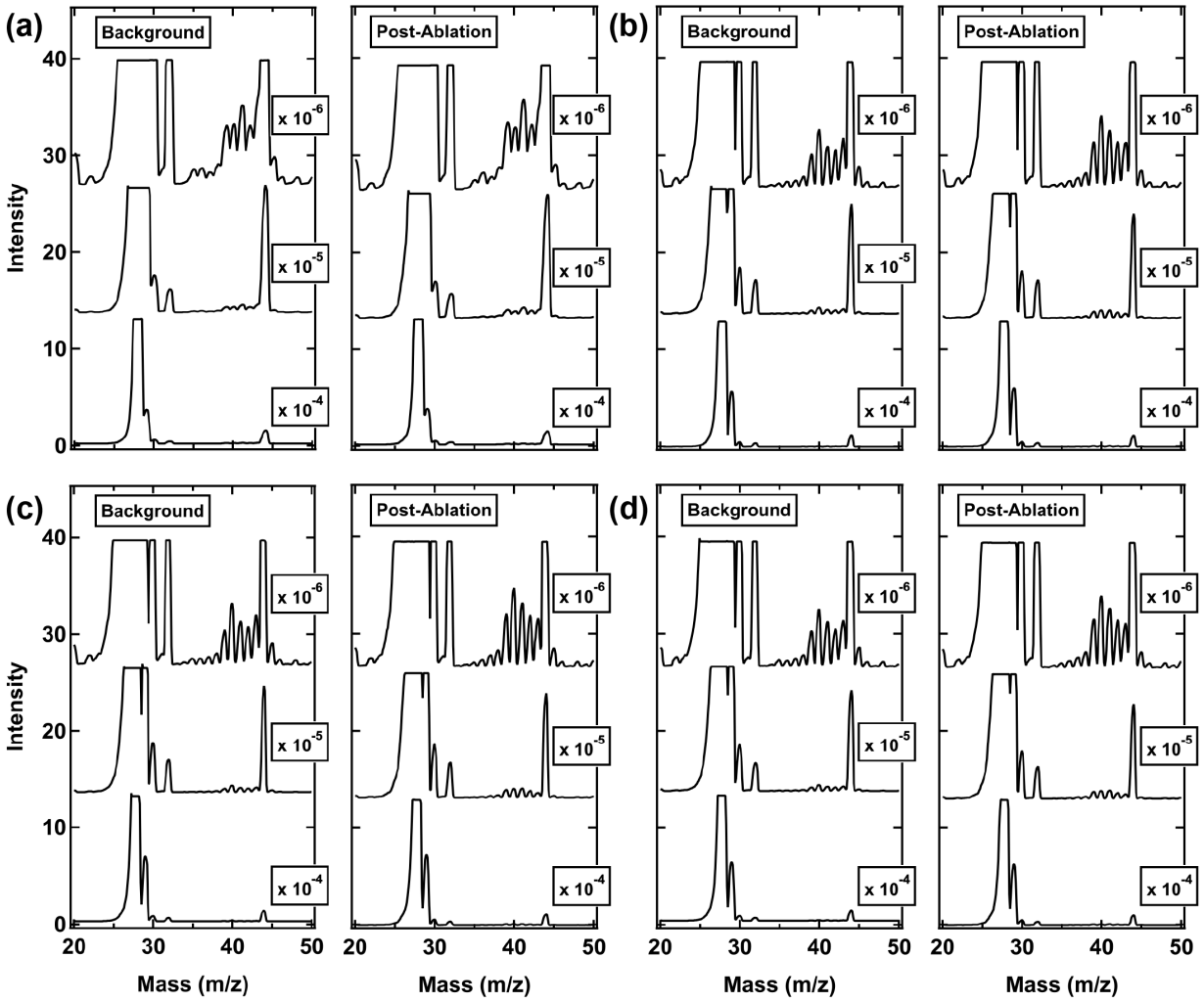

Figure A4.8: **Raw MS for Figure 5.7 - 3 $\times$ 10^{-9} Torr**. We ablated DIMP at three different atmospheric oxygen pressures and collected *in situ* mass spectra of the associated gaseous products. **Figure 5.7a** contains the least-squares fit to the *080918H* data set, and the 3 $\times$ 10^{-9} Torr data points in **Figure 5.7b** are the average amounts of propene and acetylene/ethylene present in spectra collected under these conditions. (*Data files: 080918H01-06 (a), 081318C01-06 (b), 081318D01-06 (c), 081318E01-06 (d)*).

A5 Sticking Probability of High-Energy Methane on Crystalline, Amorphous, and Porous Amorphous Ice Films (Chapter 6)

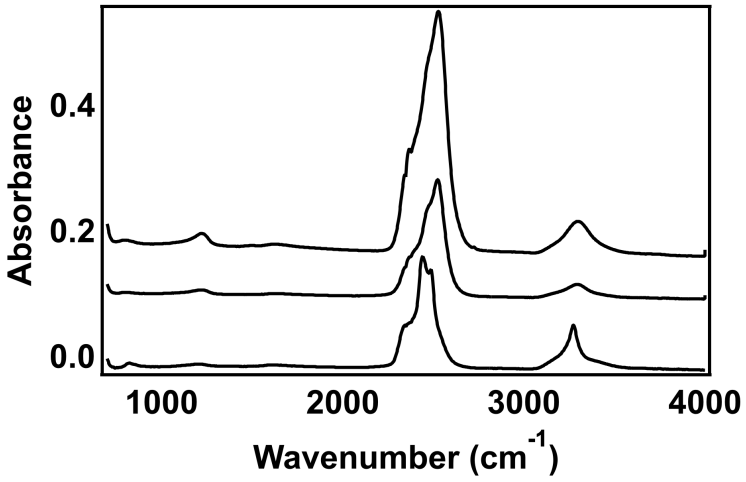

Figure A5.1: **Raw RAIR spectra for Figure 6.1**. The shape of the O-D stretching region varies with different ice morphologies (p-ASW, np-ASW, and CI). We also use the integrated area of the small "dangling-bond" region between 2700 and 2780 cm^{-1} to determine surface area and degree of porosity. Each spectrum is a representative example of each film type with a thickness between 150 and 250 layers, deposited via directed doser at a crystal temperature of 25, 107, and 150 K for p-ASW, np-ASW, and CI, respectively. (*Data files: 040218A.IR06 (p-ASW), 042018A.IR01 (np-ASW), 050918A.IR36 (CI*).

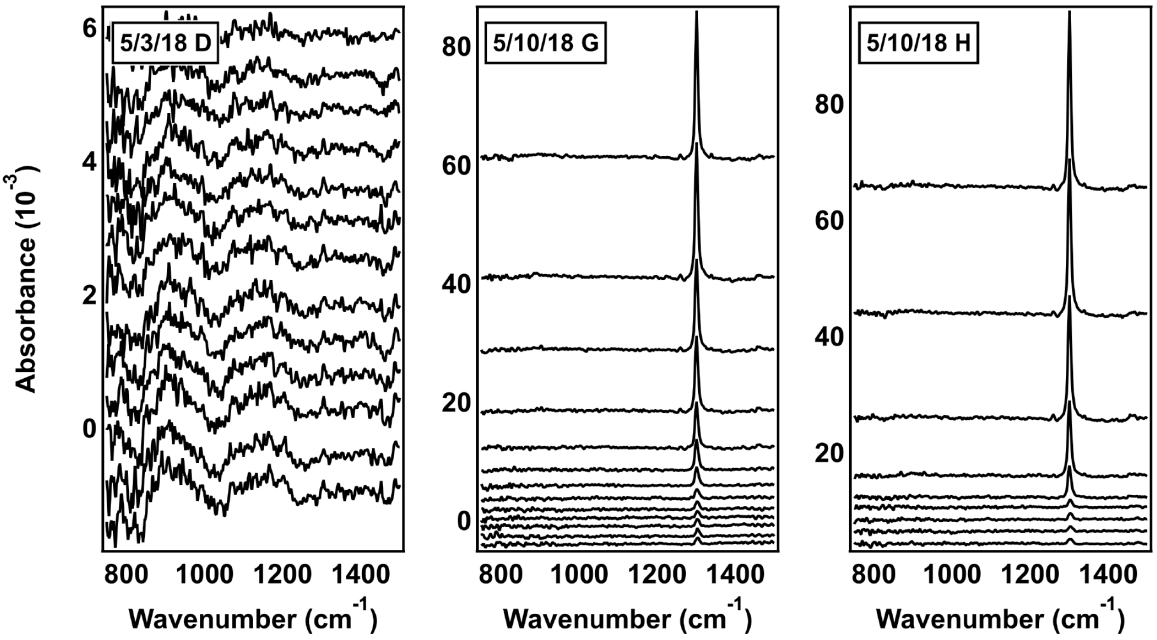

Figure A5.2: **Raw RAIR spectra for Figure 6.2a - CI films**. We tracked the integrated area of methane's ν_4 mode (1305 cm^{-1}) during adsorption and desorption experiments. In the top panel of **Figure 6.2a**, we isothermally desorb a multilayer film of methane on a CI film at 24 and 25 K; the change in desorption slope indicates the height of the monolayer. In the bottom panel, we watch as a small amount of methane (RT beam) grows in on a CI film held at 33.5 K. (*Data files: 051018G.IR01-16 (desorption, 24 K), 051018H.IR01-09 (desorption, 25 K), 050318D.IR01-13 (adsorption, 33.5 K)*).

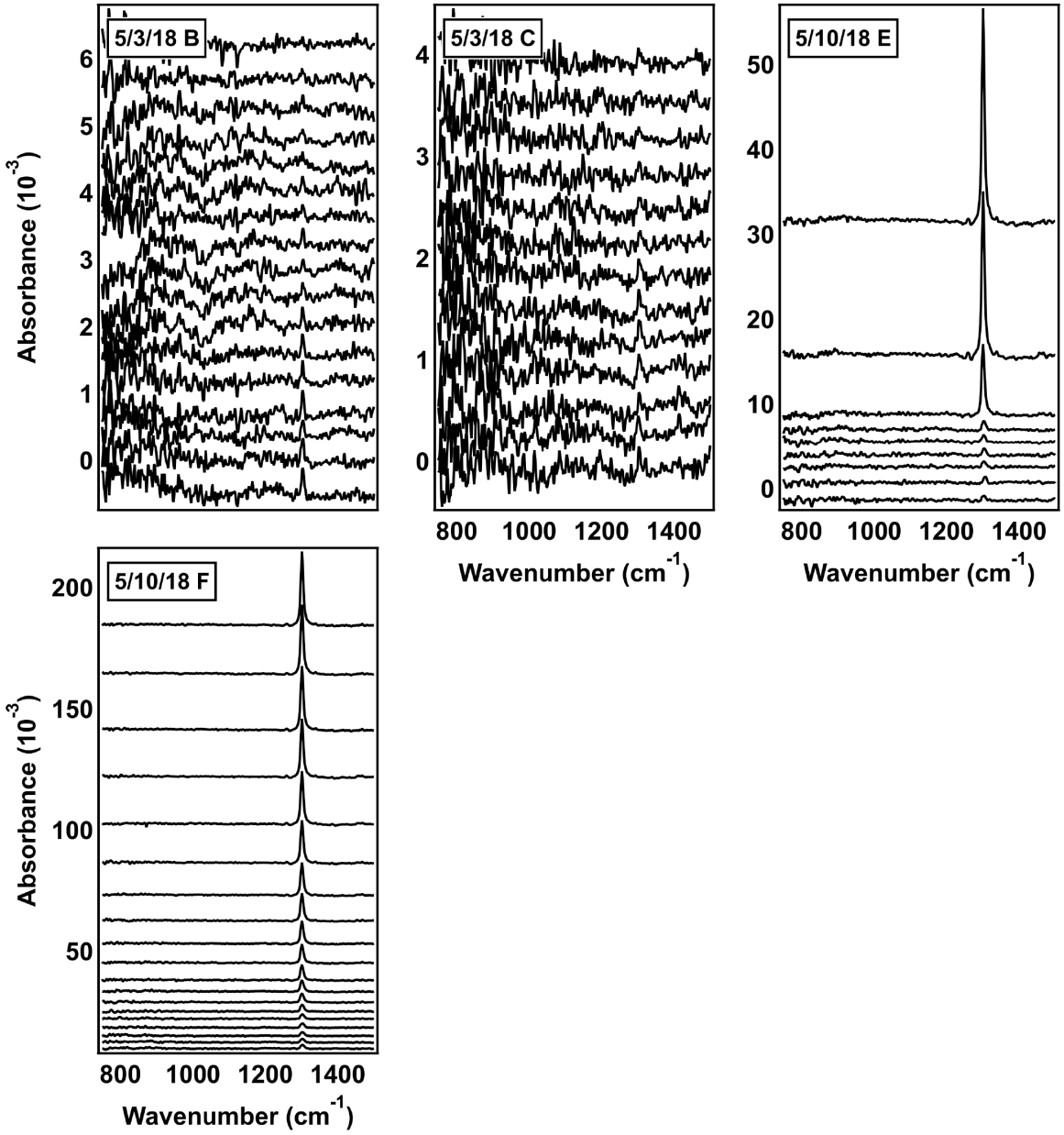

Figure A5.3: **Raw RAIR spectra for Figure 6.2b - np-ASW films**. We tracked the integrated area of methane's ν_4 mode (1305 cm^{-1}) during adsorption and desorption experiments. In the top panel of **Figure 6.2b**, we isothermally desorb a multilayer film of methane on a np-ASW film at 24 and 25 K; the change in desorption slope indicates the height of the monolayer. In the bottom panel, we watch as a small amount of methane (RT beam) grows in on a np-ASW film held at 33.5 K. (*Data files: 051018F.IR08-29 (desorption, 24 K), 051018E.IR01-10 (desorption, 25 K), 050318B.IR01-17 (adsorption, 33.5 K), 050318C.IR01-13 (adsorption, 33.5 K)*).

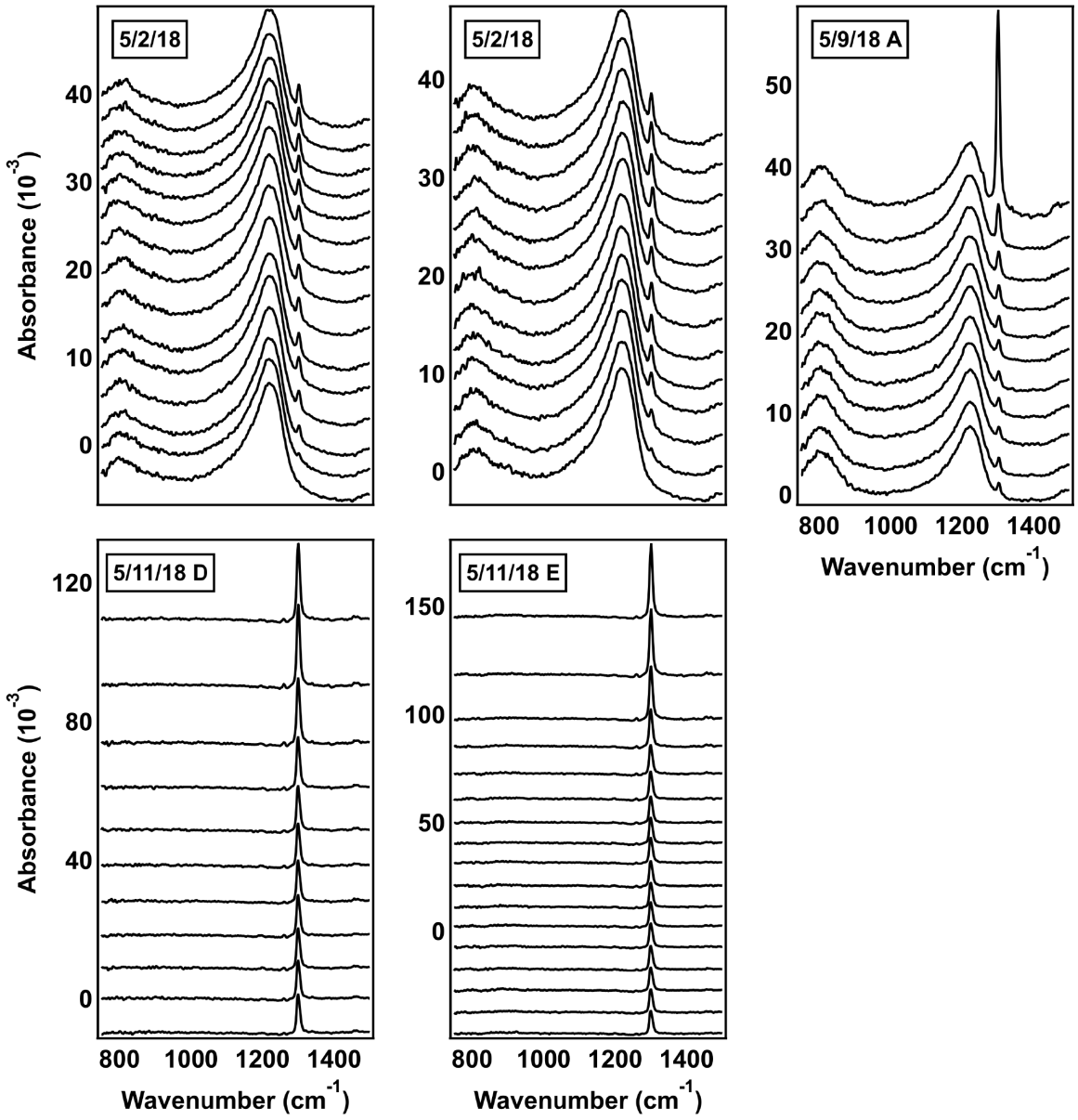

Figure A5.4: **Raw RAIR spectra for Figure 6.2c and d - p-ASW films**. We tracked the integrated area of methane's ν_4 mode (1305 cm^{-1}) during adsorption and desorption experiments. In the top panel of **Figure 6.2c**, we isothermally desorb a multilayer film of methane on a p-ASW film at 24, 25, and 33.5 K; the change in desorption slope indicates the height of the monolayer. In the bottom panel, we watch as a small amount of methane (RT beam) grows in on a p-ASW film held at 33.5 K. The spectra in **Figure 6.2d** are from the same data sets. (*Data files: 051118D.IR01-11 (desorption, 24 K), 051118E.IR01-17 (desorption, 25 K), 050918A.25-35 (desorption, 33.5 K), 050218A.IR18-32 (adsorption, 33.5 K), 050218A.IR33-45 (adsorption, 33.5 K)*).

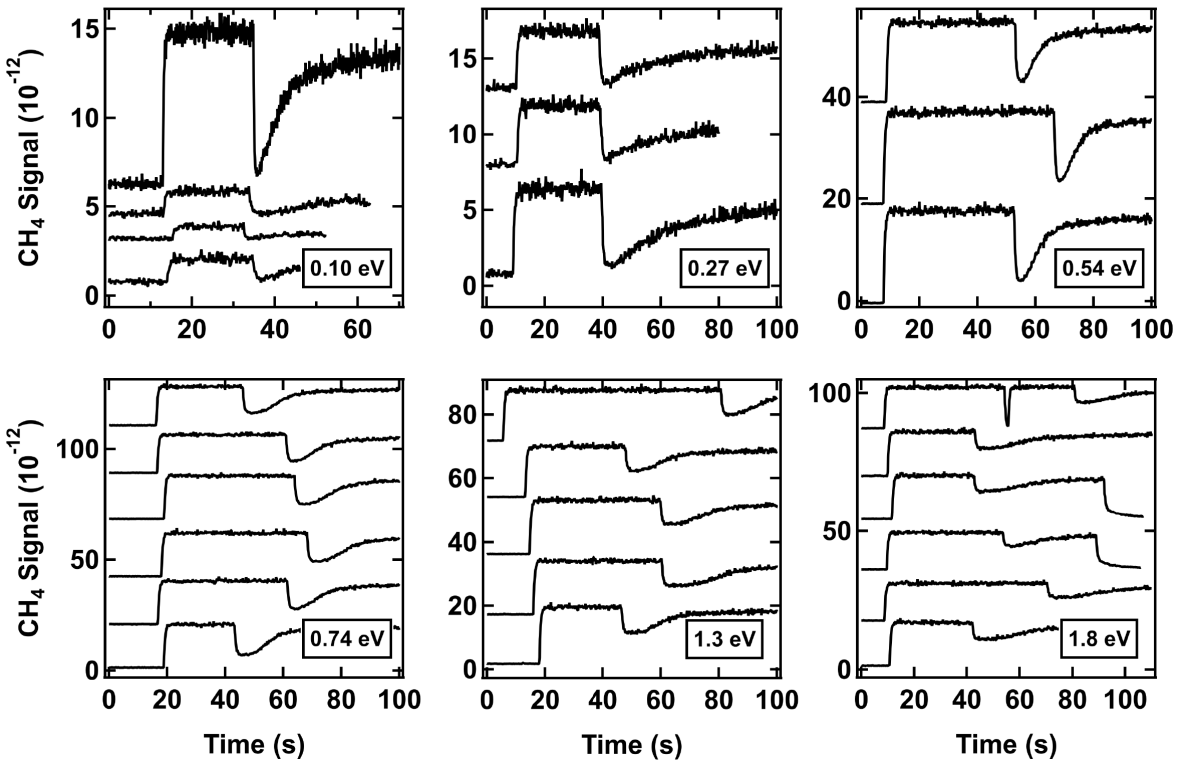

Figure A5.5: **Raw King and Wells data for Figure 6.3 - CI films**. Using the procedure outlined in **Subsection 2.2.3**, we collect the RGA signal at m/z = 15 as a CI film is exposed to a heated beam of CH_4 (0.10 and 0.27 eV) or CH_4 seeded in H_2 (0.54, 0.74, 1.3, 1.8 eV). We use the drop in intensity to calculate the initial sticking probability; each yellow data point in **Figure 6.3** represents the average value across all trials with a particular beam energy.

0.10 eV	0.27 eV	0.54 eV	0.74 ev	1.3 eV	1.8 eV
060818.R07	042418.R08	050218.R05	041818.R02	041818.R04	041818.R03
061118.R04	060818.R05	050218.R06	041818.R05	042518.R13	041918.R03
061118.R09	060818.R06	050318.R06	042318.R11	042518.R14	041918.R04
061118.R10			043018.R07	043018.R05	042718.R05
			043018.R08	043018.R06	042718.R06
			043018.R09		042718.R10
					043018.R04

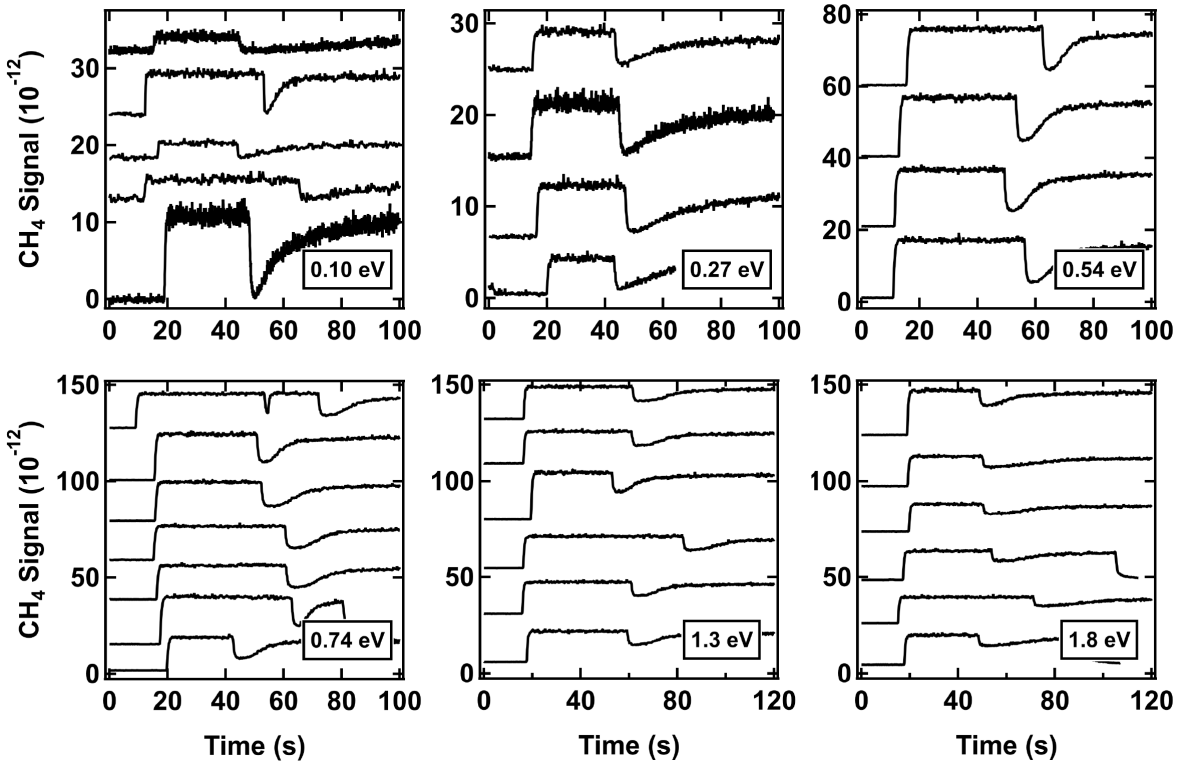

Figure A5.6: **Raw King and Wells data for Figure 6.3 - np-ASW films**. Using the procedure outlined in **Subsection 2.2.3**, we collect the RGA signal at m/z = 15 as a np-ASW film is exposed to a heated beam of CH_4 (0.10 and 0.27 eV) or CH_4 seeded in H_2 (0.54, 0.74, 1.3, 1.8 eV). We use the drop in intensity to calculate the initial sticking probability; each blue data point in **Figure 6.3** represents the average value across all trials with a particular beam energy.

0.10 eV	0.27 eV	0.54 eV	0.74 ev	1.3 eV	1.8 eV
040518.R05	042418.R06	050318.R02	041518.R02	041718.R04	041718.R03
040518.R06	042418.R07	050318.R03	041718.R02	041718.R07	041718.R06
040518.R08	060818.R02	050318.R04	041718.R05	042318.R05	042018.R02
042418.R04	060818.R03	050318.R05	042318.R02	042318.R06	042018.R03
042418.R05			042318.R03	042318.R07	042018.R04
			042318.R04	042718.R03	042718.R04
			042718.R02		

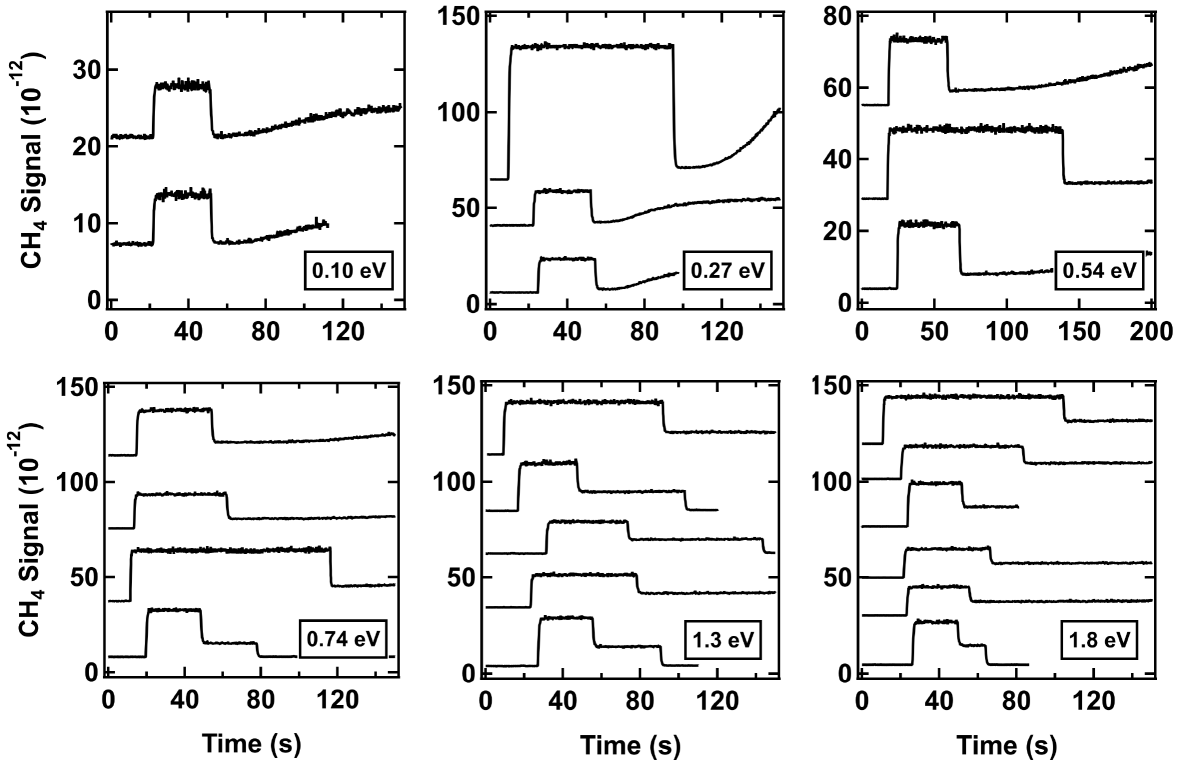

Figure A5.7: **Raw King and Wells data for Figure 6.3 - p-ASW films**. Using the procedure outlined in **Subsection 2.2.3**, we collect the RGA signal at m/z = 15 as a p-ASW (30° deposition) film is exposed to a heated beam of CH_4 (0.10 and 0.27 eV) or CH_4 seeded in H_2 (0.54, 0.74, 1.3, 1.8 eV). We use the drop in intensity to calculate the initial sticking probability; each red data point in **Figure 6.3** represents the average value across all trials with a particular beam energy.

0.10 eV	0.27 eV	0.54 eV	0.74 ev	1.3 eV	1.8 eV
042518.R02	040618.R09	050218.R02	040618.R03	040618.R07	040618.R05
042518.R03	042518.R04	050218.R03	041318.R02	041318.R09	041318.R04
	042518.R05	050218.R04	042518.R07	041318.R12	041318.R08
			042518.R08	042518.R11	042518.R09
				042518.R12	042518.R10
					043018.R02

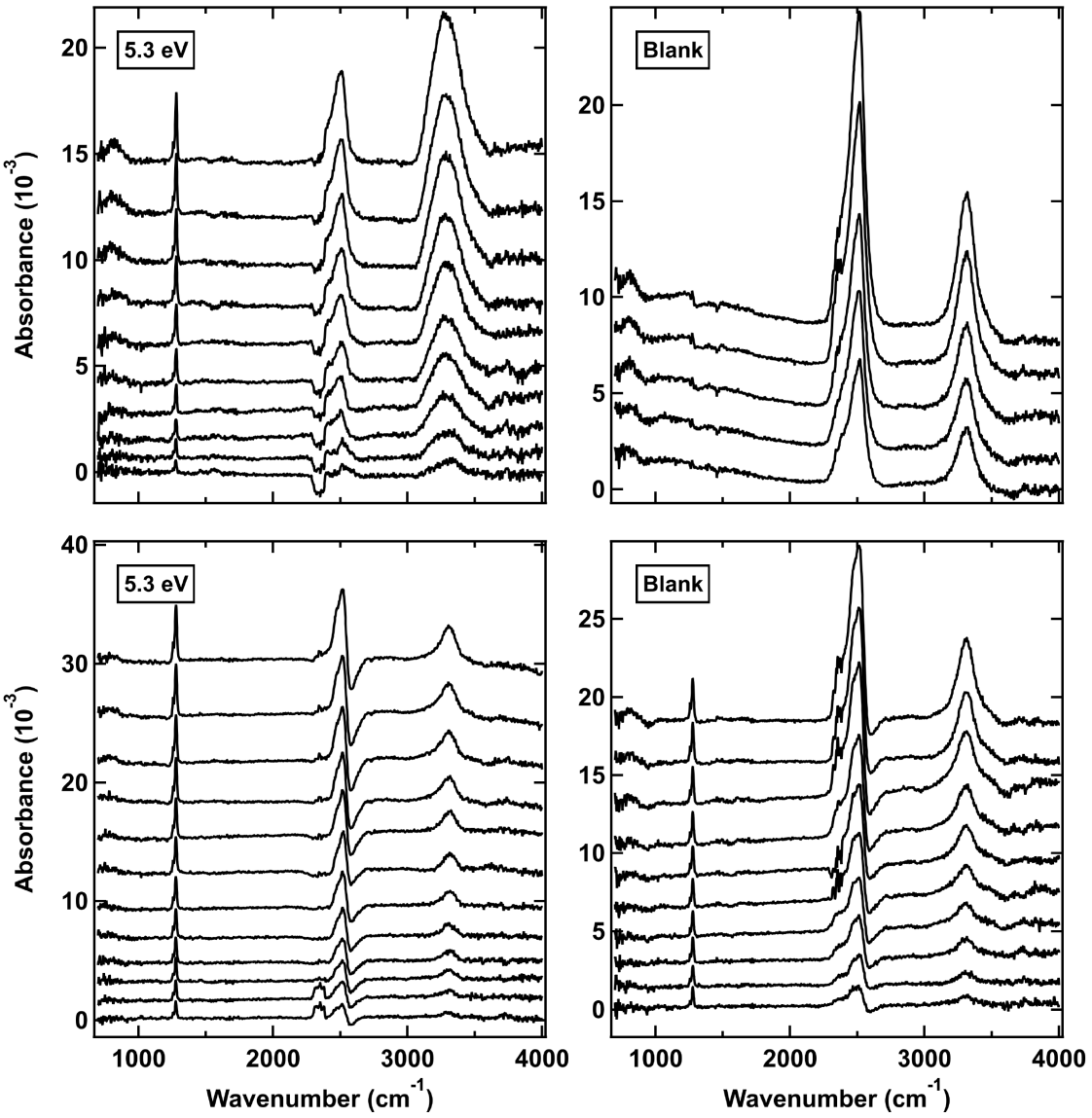

Figure A5.8: **Raw RAIR spectra for Figure 6.4**. We tracked the growth rate of CF_4 embedded in np-ASW (top) and p-ASW (bottom) films via the integrated area of modes at 1276 and 1257 cm^{-1}. We performed embedding experiments with a beam energy of 5.3 eV and the ice film held at 70 K. We also performed corresponding blank trials with a room temperature beam ($\approx$0.11 eV) to quantify any small contributions to the signal from CF_4 surface adsorption. (*Data files: 031218B.IR01-10 (np-ASW, 5.3 eV), 013118B.IR04-08 (np-ASW, blank), 031418B.IR01-12 (p-ASW, 5.3 eV), 031518B.IR01-10 (p-ASW, blank)*).

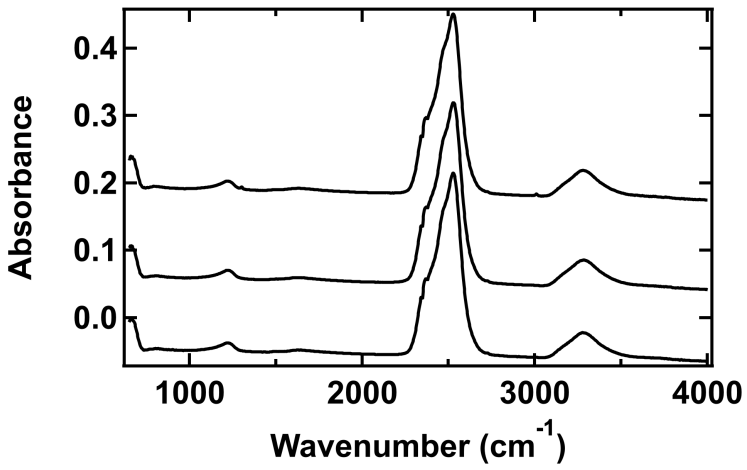

Figure A5.9: **Raw RAIR spectra for Figure 6.5**. Spectra collected before, during and after exposure to a seeded, 0.54 eV CH_4/H_2 beam illustrate any minor changes in the underlying water structure as a result of CH_4 exposure. (*Data files: 050218A.IR33 (before CH_4 exposure), 050218A.IR45 (during CH_4 exposure), 050218A.IR46 (after anneal)*).

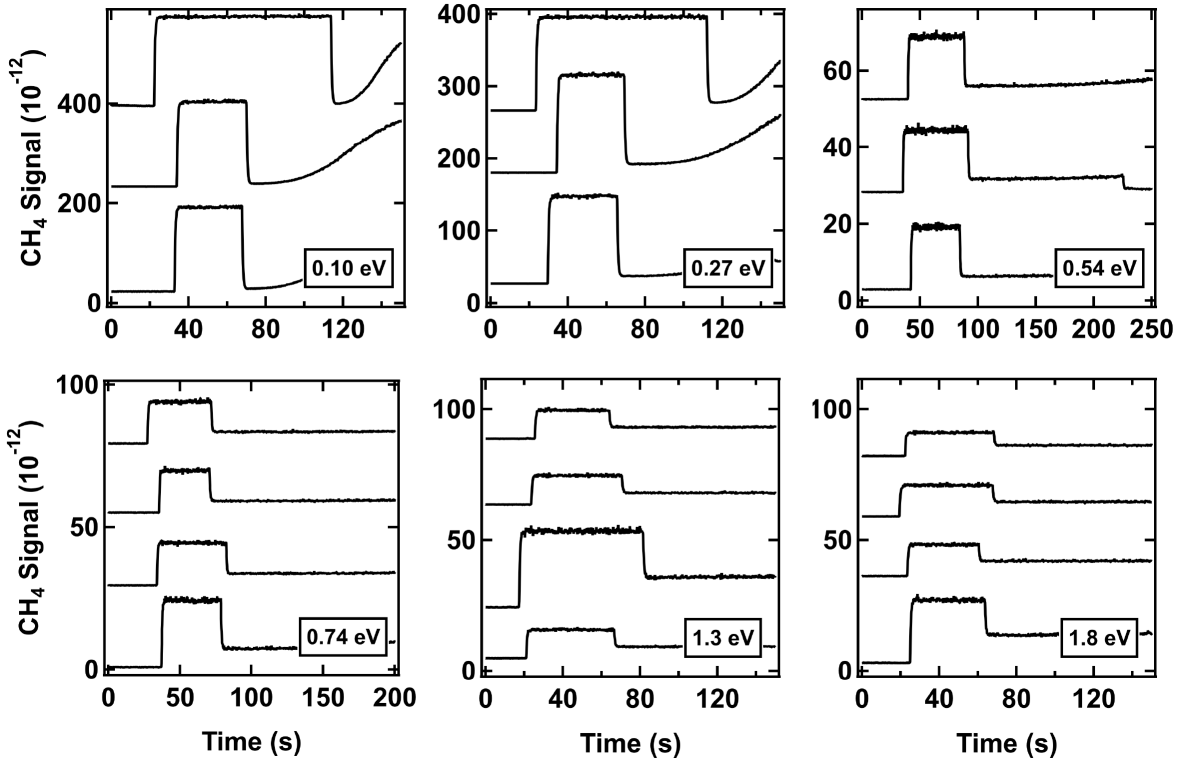

Figure A5.10: **Raw King and Wells data for Figure 6.6 - 60° films**. Using the procedure outlined in **Subsection 2.2.3**, we collect the RGA signal at m/z = 15 as a p-ASW (60° deposition) film is exposed to a heated beam of CH_4 (0.10 and 0.27 eV) or CH_4 seeded in H_2 (0.54, 0.74, 1.3, 1.8 eV). We use the drop in intensity to calculate the initial sticking probability; each green data point in **Figure 6.6** represents the average value across all trials with a particular beam energy.

0.10 eV	0.27 eV	0.54 eV	0.74 ev	1.3 eV	1.8 eV
040818.R02	050718.R14	050718.R02	040918.R02	040918.R04	040918.R03
050718.R16	050718.R15	050718.R03	050718.R05	050718.R08	050718.R11
050718.R17	040818.R03	050718.R04	050718.R06	050718.R09	050718.R12
			050718.R07	050718.R10	050718.R13

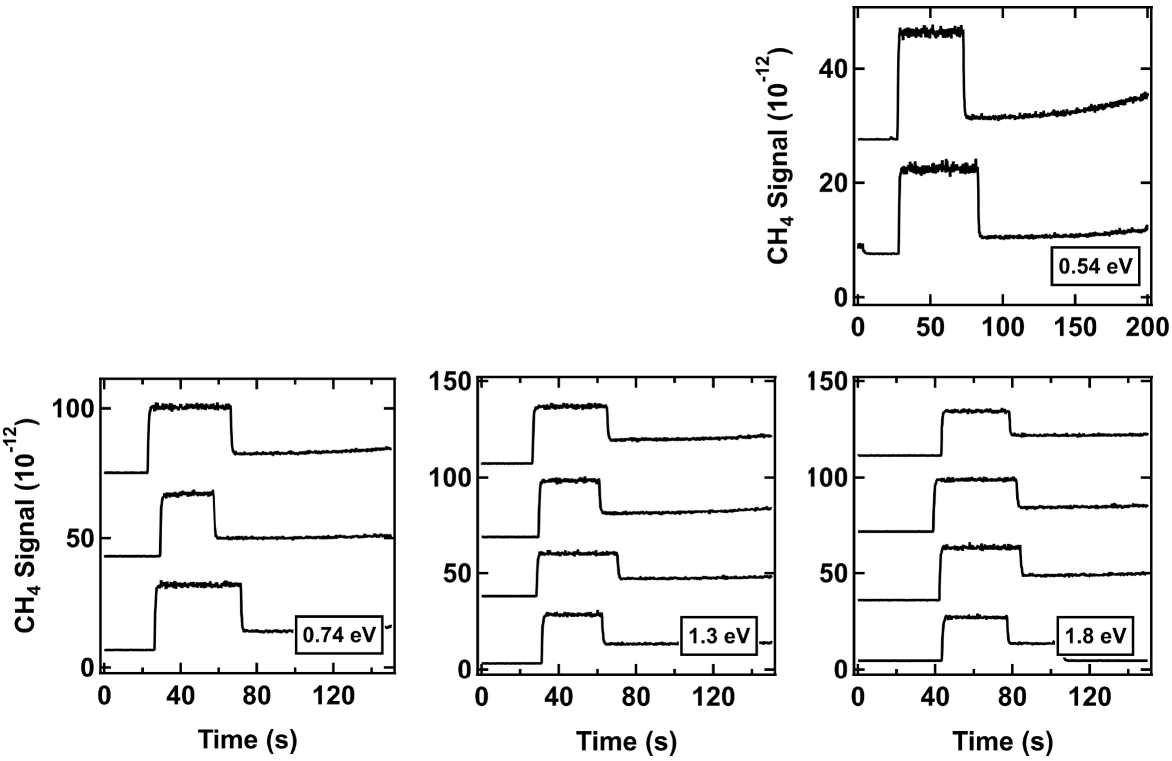

Figure A5.11: **Raw King and Wells data for Figure 6.6 - 70° films**. Using the procedure outlined in **Subsection 2.2.3**, we collect the RGA signal at m/z = 15 as a p-ASW (70° deposition) film is exposed to a heated beam of CH_4 seeded in H_2 (0.54, 0.74, 1.3, 1.8 eV). We use the drop in intensity to calculate the initial sticking probability; each gray data point in **Figure 6.6** represents the average value across all trials with a particular beam energy.

0.54 eV	0.74 ev	1.3 eV	1.8 eV
051418.R02	041118.R02	041118.R04	041118.R03
051418.R03	051518.R02	041118.R04	041118.R06
	051518.R03	051518.R05	051518.R07
		051518.R06	051518.R08

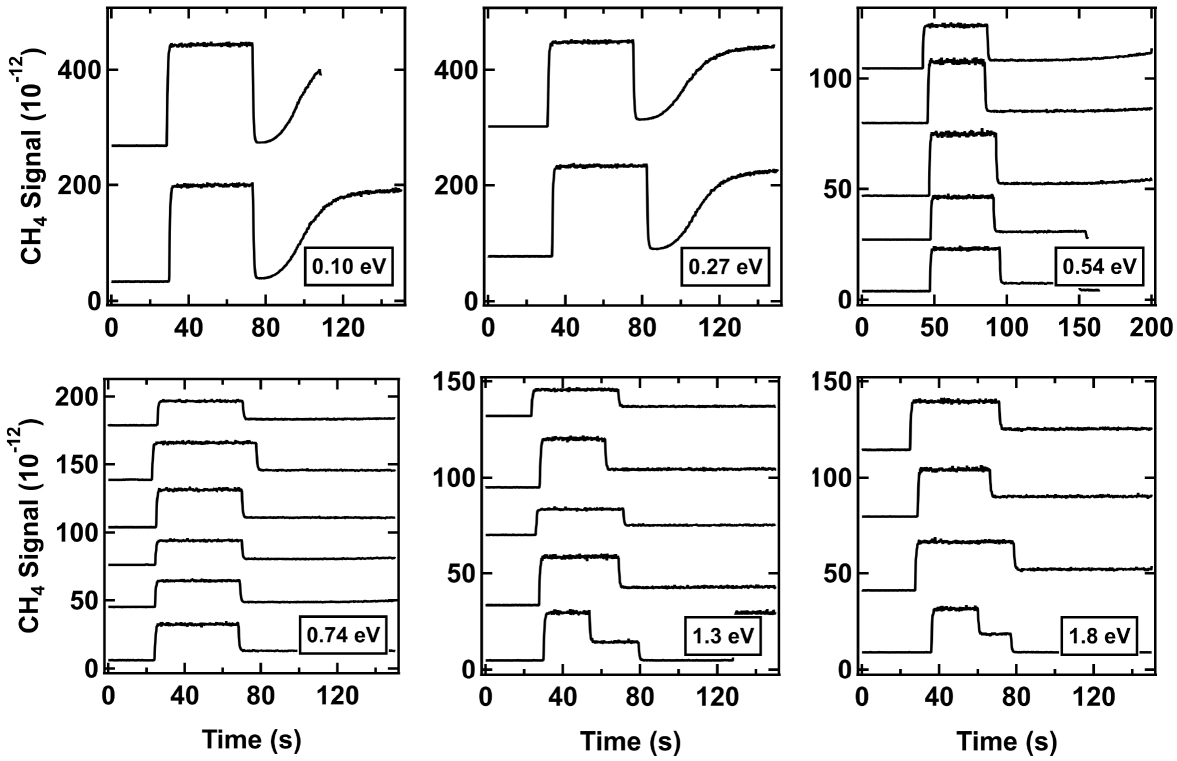

Figure A5.12: **Raw King and Wells data for Figure 6.6 - BD films**. Using the procedure outlined in **Subsection 2.2.3**, we collect the RGA signal at m/z = 15 as a p-ASW (background deposition) film is exposed to a heated beam of CH_4 (0.10 and 0.27 eV) or CH_4 seeded in H_2 (0.54, 0.74, 1.3, 1.8 eV). We use the drop in intensity to calculate the initial sticking probability; each purple data point in **Figure 6.6** represents the average value across all trials with a particular beam energy.

0.10 eV	0.27 eV	0.54 eV	0.74 ev	1.3 eV	1.8 eV
050818.R11	050818.R09	050818.R02	041218.R02	041218.R04	041218.R03
050818.R12	050818.R10	050818.R03	050818.R05	050818.R07	051618.R09
		050818.R04	050818.R06	050818.R08	051618.R10
		051618.R02	051618.R04	051618.R07	051618.R11
		051618.R03	051618.R05	051618.R08	
			051618.R06		

Figure A5.13: **Raw King and Wells data for Figure 6.7**. All data listed here already appears in **Figures A5.2 - A5.4** and **A5.10 - A5.12**. I have just highlighted the data that we used for calculating the values reported in the text of **Subsection 6.3.2** and included in **Figure 6.7**.

Panel A	**Panel B - 30°**	**Panel B - 60°**	**Panel B - 70°**	**Panel B - BD**
041818.R03	050218.R02	050718.R11	041118.R03	051618.R02
042518.R09	050218.R03	040918.R03	051518.R07	051618.R03
041718.R06	050218.R04	050718.R02	051518.R08	051618.R09
	040618.R05		051418.R03	051618.R10
	042518.R09			050818.R02
	043018.R02			

A6 Reverse Water-Gas Shift Chemistry inside a Supersonic Molecular Beam Nozzle (Chapter 7)

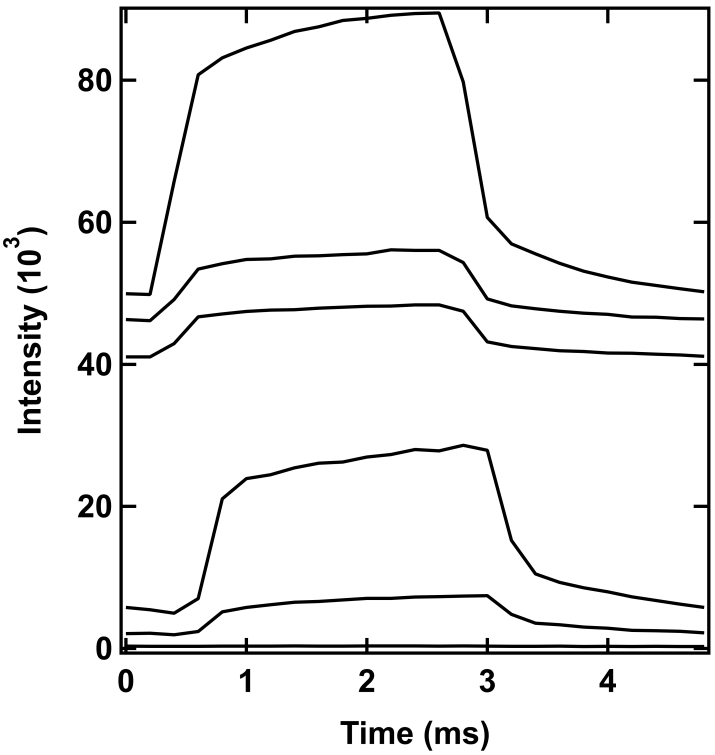

Figure A6.1: **Raw MS for Figure 7.1**. We collected mass spectra for CO, CO_2, and H_2O (m/z = 28, 44, 18, respectively) with square wave modulation of the molecular beam. Both sets were collected with a beam pressure of 250 psi. (*Data files: 030117T.F03-05 (304 K), 0222817T.F03-05 (800 K)*).

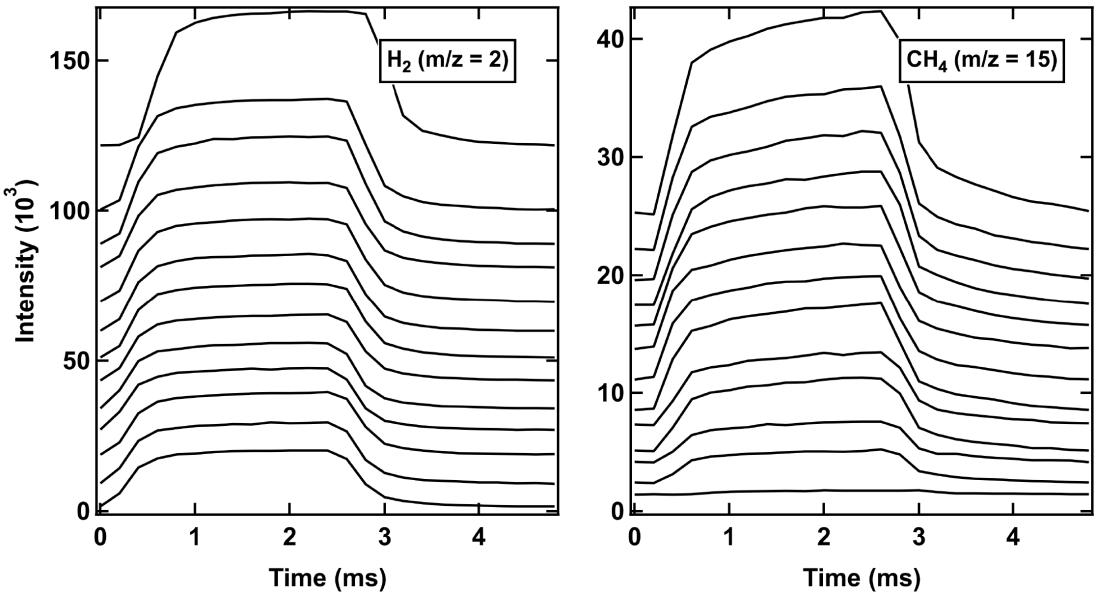

Figure A6.2: **Raw MS for Figure 7.2**. We collected mass spectra for H_2 and CH_4 (m/z = 2 and 15, respectively) with square wave modulation of the molecular beam. The raw CH_4 signal intensity is normalized to the H_2 signal for the same trial and then further normalized to 1. Beam nozzle temperatures vary, but all data was collected with a stagnation pressure of 250 psi.

300 K	**650 K**	**725 K**	**800 K**
030117T.F01-02	022817T.F53-54	030117T.F11-12	022817T.F01-02
	030117T.F06-07	030117T.F21-22	022817T.F28-29
875 K	**950 K**	**1025 K**	
022817T.F63-64	030117T.F31-32	030117T.F42-43	
030117T.F16-17	030117T.F37-38	030117T.F47-48	

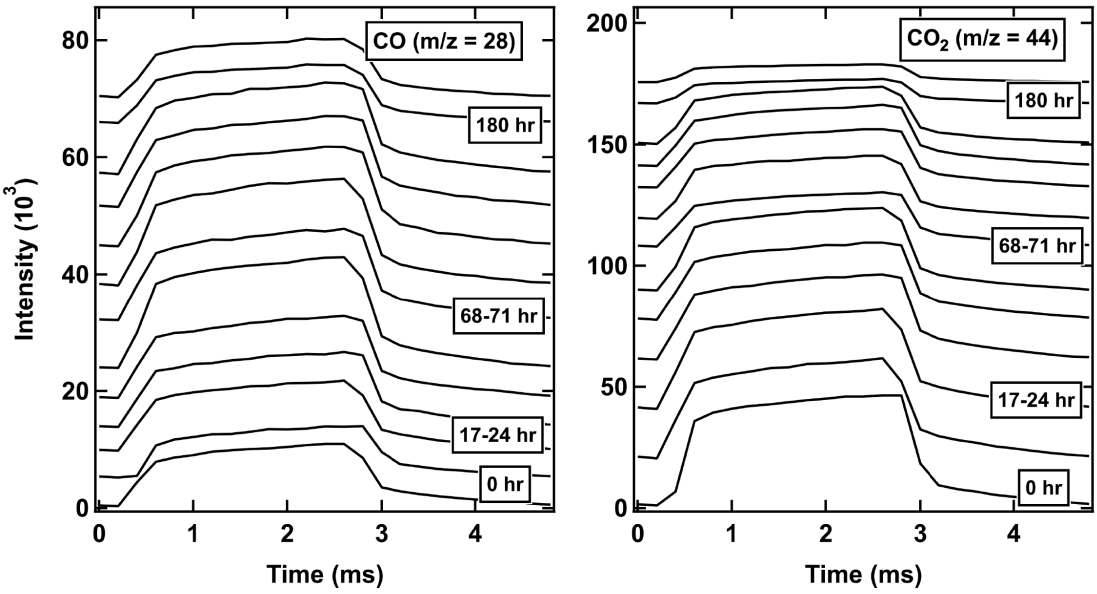

Figure A6.3: **Raw MS for Figure 7.3**. We collected mass spectra for CO and CO_2 (m/z = 28 and 44, respectively) with square wave modulation of the molecular beam. We established RWGS yield by comparing the relative intensities of these two masses to a corresponding measurement at room temperature (see **Equation 7.5** for details). All trials were collected at 800 K with a stagnation pressure of 250 psi (unless otherwise noted below).

0 hr	17-24 hr	68-71 hr	180 hr
021717T.F04-05	021817T.F04-05	022017T.F04-05	022817T.F31-32
020317T.F19-20 (420 psi)	020917T.F04-05 (420 psi)	022017T.F29-30	022817T.F04-05
	021017T.F09-10 (420 psi)	021317T.F14-15	
	021017T.F24-25 (420 psi)	021317T.F04-05	
		021317T.F09-10	

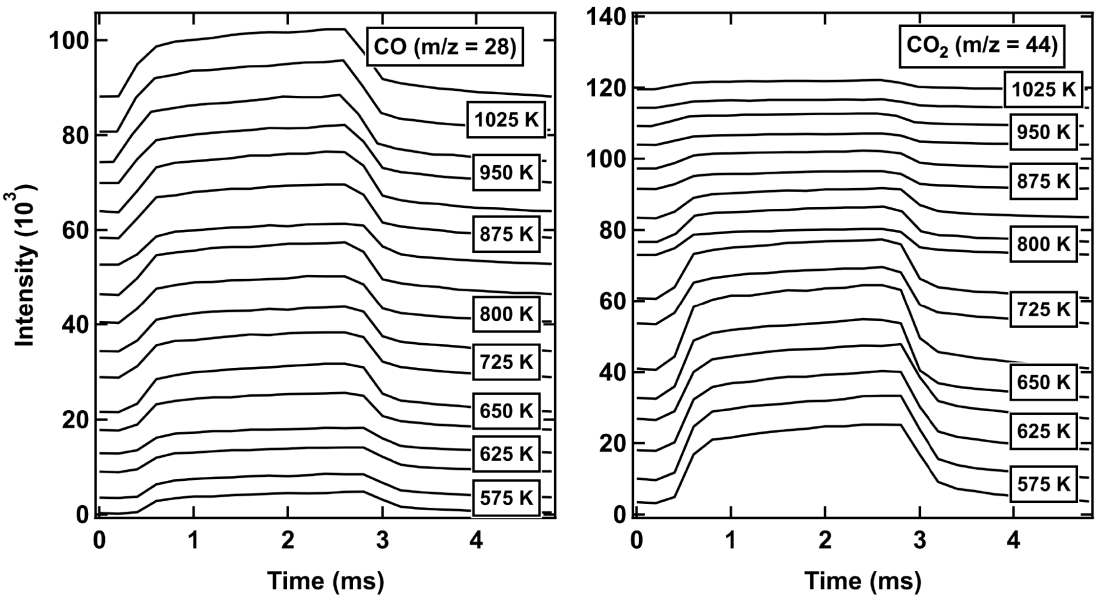

Figure A6.4: **Raw MS for Figure 7.4**. We collected mass spectra for CO and CO_2 (m/z = 28 and 44, respectively) with square wave modulation of the molecular beam. We established RWGS yield by comparing the relative intensities of these two masses to a corresponding measurement at room temperature (see **Equation 7.5** for details). Though nozzle temperature varies, all trials were collected with a stagnation pressure of 250 psi and a nozzle that had been vacuum annealed for 180 hours or more.

575 K	**625 K**	**650 K**	**725 K**
031317T.F09-10	031317T.F14-15	022817T.F56-57	030117T.F14-15
031317T.F24-25	031317T.F19-20	030117T.F09-10	030117T.F24-25
800 K	**875 K**	**950 K**	**1025 K**
022817T.F04-05	030117T.F19-20	030117T.F34-35	030117T.F45-46
022817T.F31-32		030117T.F40-41	030117T.F50-51
031318T.F04-05			

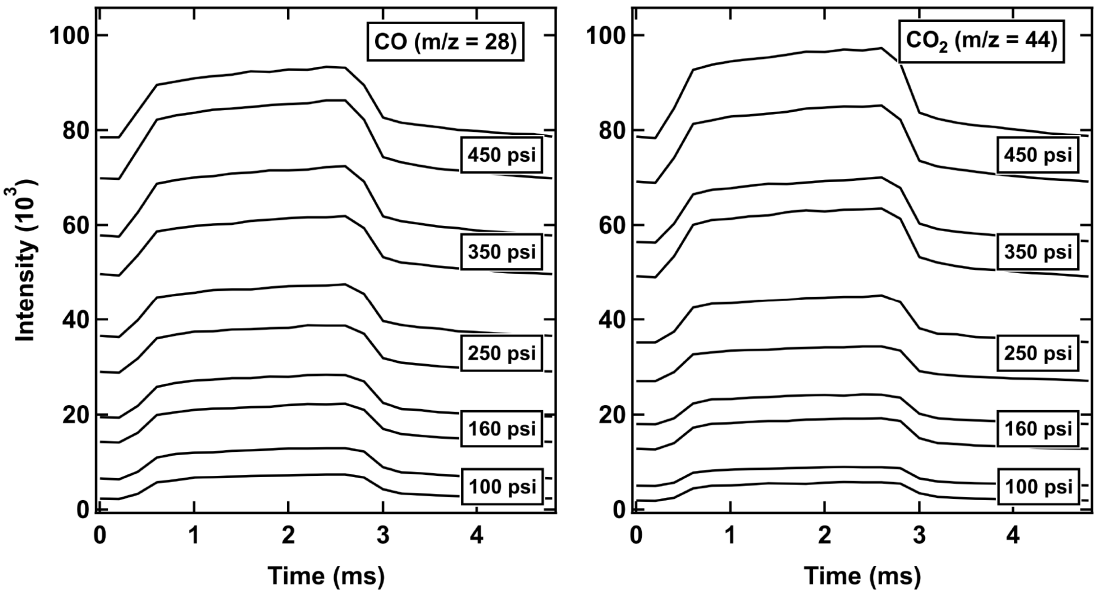

Figure A6.5: **Raw MS for Figure 7.6**. We collected mass spectra for CO and CO_2 (m/z = 28 and 44, respectively) with square wave modulation of the molecular beam. We established RWGS yield by comparing the relative intensities of these two masses to a corresponding measurement at room temperature (see **Equation 7.5** for details). All trials were collected at 800 K, with a stagnation pressure of 250 psi, and a nozzle that had been vacuum annealed for 180 hours or more.

90 psi	160 psi	250 psi	350 psi	450 psi
022817T.F21-22	022817T.F26-27	022817T.F04-05	022817T.F10-11	022817T.F16-17
022817T.F46-47	022817T.F51-52	022817T.F31-32	022817T.F36-37	022817T.F41-42

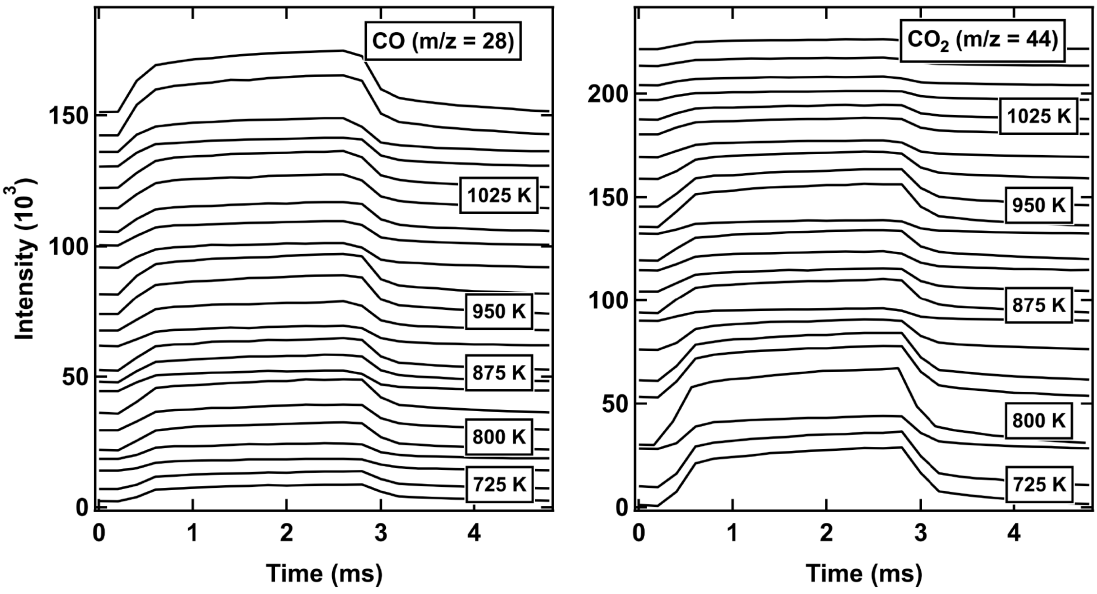

Figure A6.6: **Raw MS for Figure 7.7** - 10% CO_2 mixture. We collected mass spectra for CO and CO_2 (m/z = 28 and 44, respectively) with square wave modulation of the molecular beam. We established RWGS yield by comparing the relative intensities of these two masses to a corresponding measurement at room temperature (see **Equation 7.5** for details). All trials were collected at 800 K, with a stagnation pressure of 150-250 psi, and a nozzle that had been vacuum annealed for 180 hours or more.

90 psi	160 psi	250 psi	350 psi	450 psi
041717T.F44-45	041717T.F04-05	041717T.F19-20	041717T.F24-25	041717T.F54-55
041717T.F49-50	041717T.F09-10	041717T.F34-35	041717T.F29-30	041717T.F59-60
042517T.F49-50	041717T.F14-15	042417T.F24-25	042117T.F05-06	042117T.F10-11
		042517T.F14-15	042417T.F04-5	042417T.F19-20
			042517T.F19-20	042517T.F24-25
			042517T.F39-40	042517T.F34-35

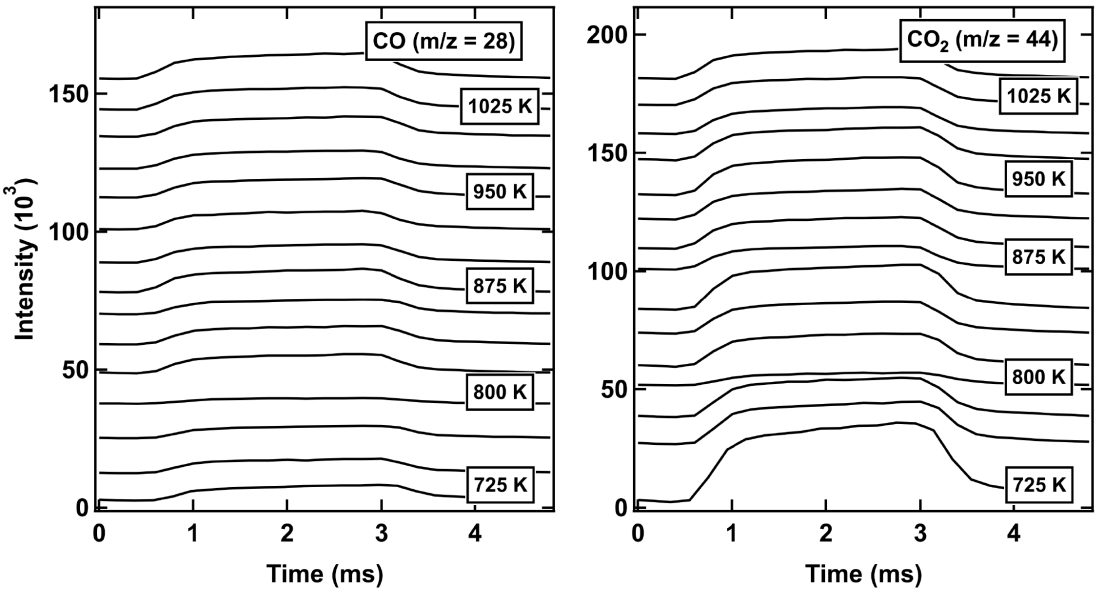

Figure A6.7: **Raw MS for Figure 7.7** - 50% CO_2 mixture. We collected mass spectra for CO and CO_2 (m/z = 28 and 44, respectively) with square wave modulation of the molecular beam. We established RWGS yield by comparing the relative intensities of these two masses to a corresponding measurement at room temperature (see **Equation 7.5** for details). All trials were collected at 800 K, with a stagnation pressure of 150-250 psi, and a nozzle that had been vacuum annealed for 180 hours or more.

90 psi	160 psi	250 psi	350 psi	450 psi
042617T.F04-05	042517T.F44-45	042617T.F21-22	042617T.F26-27	042617T.F31-32
042617T.F61-62	042617T.F16-17	042617T.F51-52	042617T.F46-47	042617T.F41-42
042717T.F09-10	042617T.F5657	042717T.F19-20	042717T.F24-25	
	042717T.F14-15			
	042718T.F28-29			

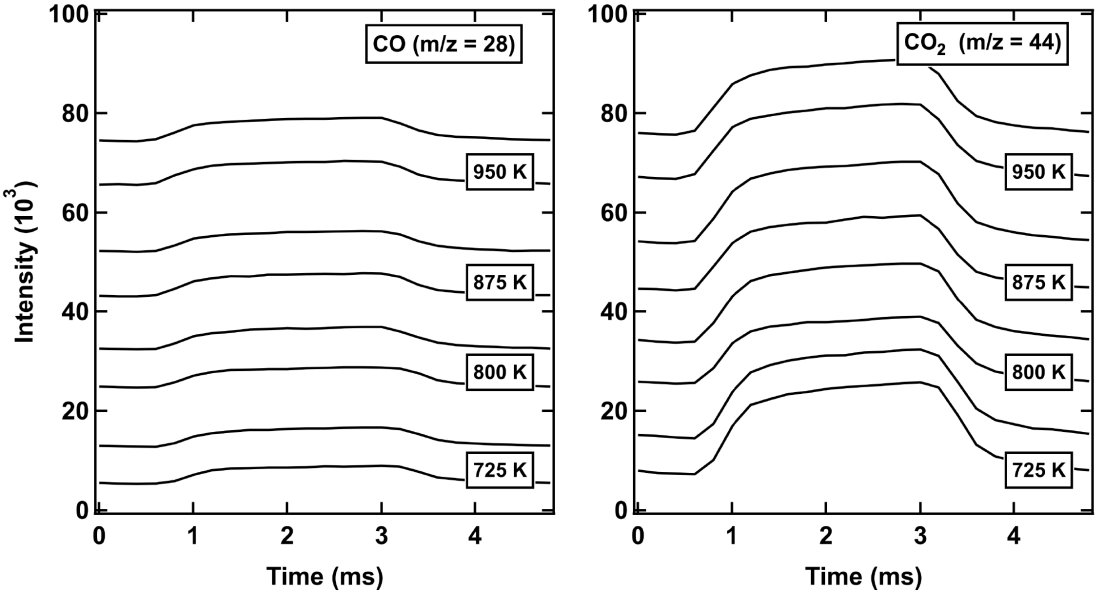

Figure A6.8: **Raw MS for Figure 7.7** - 88% CO_2 mixture. We collected mass spectra for CO and CO_2 (m/z = 28 and 44, respectively) with square wave modulation of the molecular beam. We established RWGS yield by comparing the relative intensities of these two masses to a corresponding measurement at room temperature (see **Equation 7.5** for details). All trials were collected at 800 K, with a stagnation pressure of 150-250 psi, and a nozzle that had been vacuum annealed for 180 hours or more.

90 psi	160 psi	250 psi	350 psi	450 psi
031617T.F11-12	031617T.F04-05	031617T.F36-37	031617T.F41-42	
031617T.F26-27	031617T.F31-32	031617T.F51-52	031617T.F46-47	

A7 Reaction Kinetics and Influence of Film Morphology on the Oxidation of Propene Thin Films by O(^{3}P) Atomic Oxygen (Chapter 8)

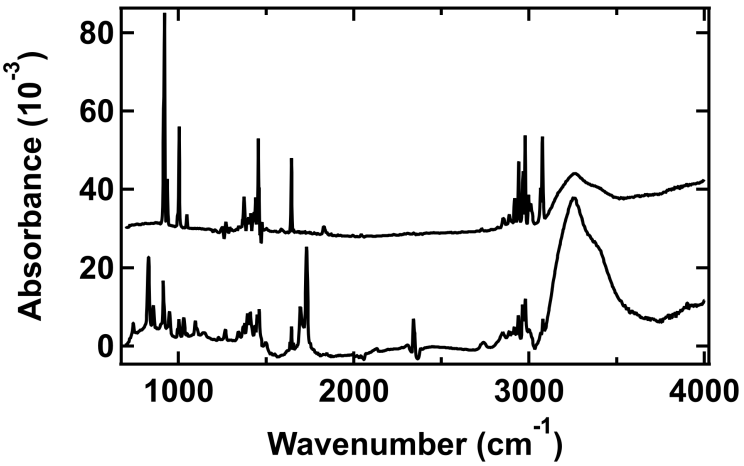

Figure A7.1: **Raw RAIR spectra for Figure 8.1**. Both spectra correspond to a 66-layer propene film, deposited on the crystal at 59 K via molecular beam dosing. The "pristine" spectrum was collected immediately after deposition, and the "reacted" spectrum after exposing the film to 1 ± 10^{18} O(^{3}P) atoms cm^{-2} while the crystal is held at 54 K. (*Data files: 040819A.IR02 (pristine), 040819A.IR16 (reacted)*).

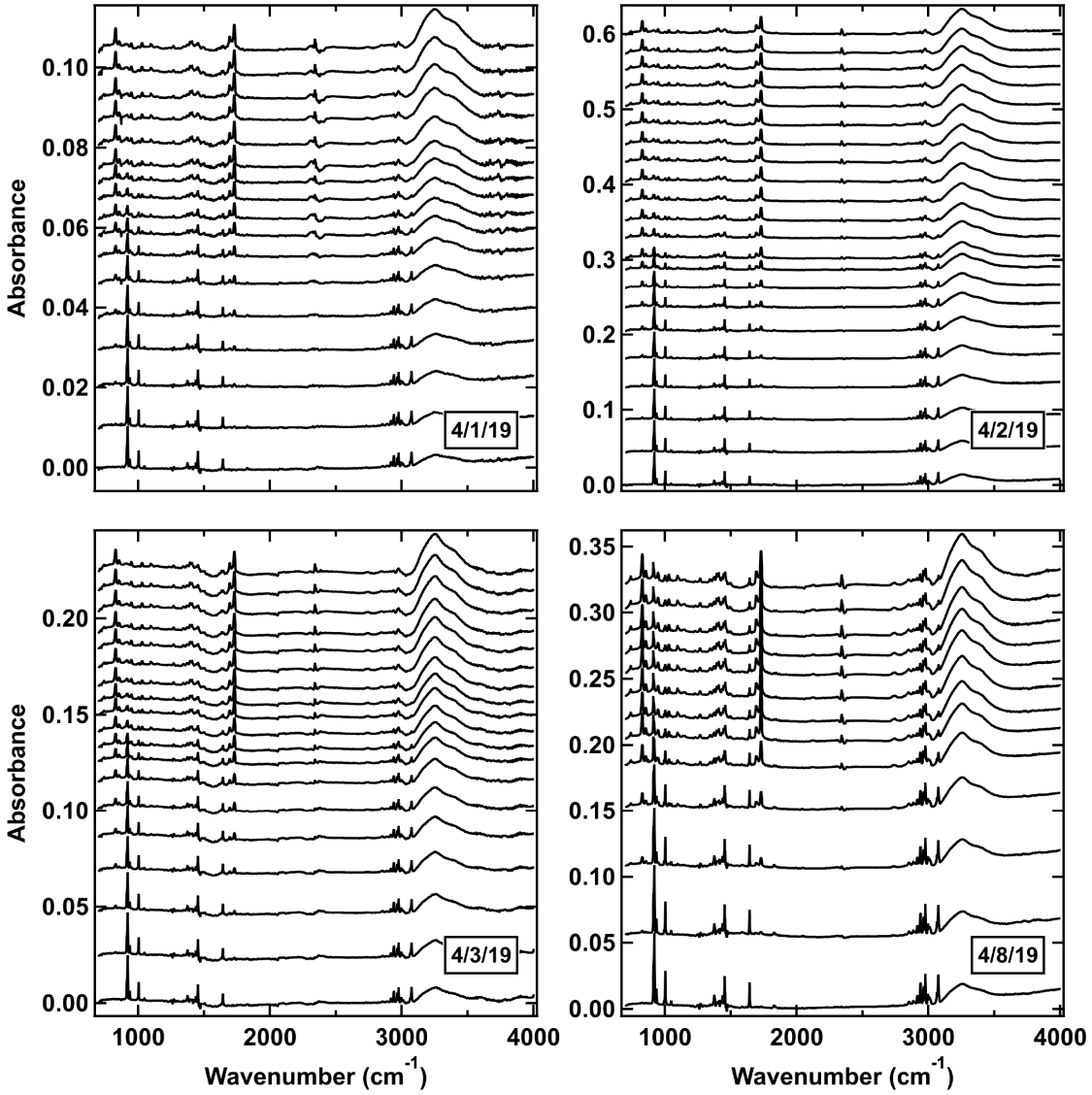

Figure A7.2: **Raw RAIR spectra for Figure 8.2 and 8.4**. After depositing a propene film with a desired thickness on the crystal at 59 K, we collect spectra at regular time intervals during exposure to O(^{3}P) with the crystal held at 54 K. **Figure 8.2** contains the integrated areas of the 914 - 919 cm^{-1} region, corresponding to the loss of propene's double bond. **Figure 8.4** contains the integrated areas of peaks at 827 and 1730 cm^{-1}, corresponding to the appearance of propylene oxide and propanal, respectively. (*Data files: 040119B.IR02-19 (12 layers), 040319A.IR02-20 (24 layers), 040219A.IR02-23 (46 layers), 040819A.IR04-16 (66 layers)*).

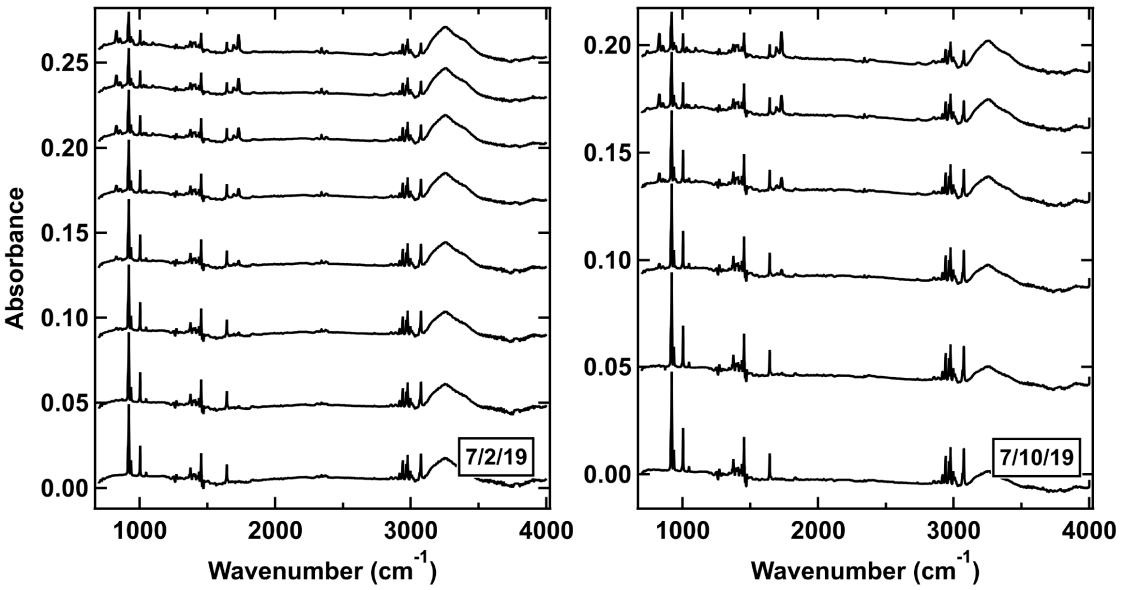

Figure A7.3: **Raw RAIR spectra for Figure 8.3 - 35-46 layers**. As the propene film is exposed to $O(^3P)$, we track the loss of spectral intensity in the 914 - 919 cm^{-1} region (corresponding to the loss of propene's double bond). We use the change in intensity to calculate an initial rate of reactivity. The surface is held to 59 K during deposition and 54 K during exposure; this figure corresponds to trials with propene films between 35 and 46 layers thick. Note: the data presented in **Figure 8.3** includes the trials displayed in **Figure A7.2**. (*Data files: 070219A.IR02-09, 071019A.IR02-07*).

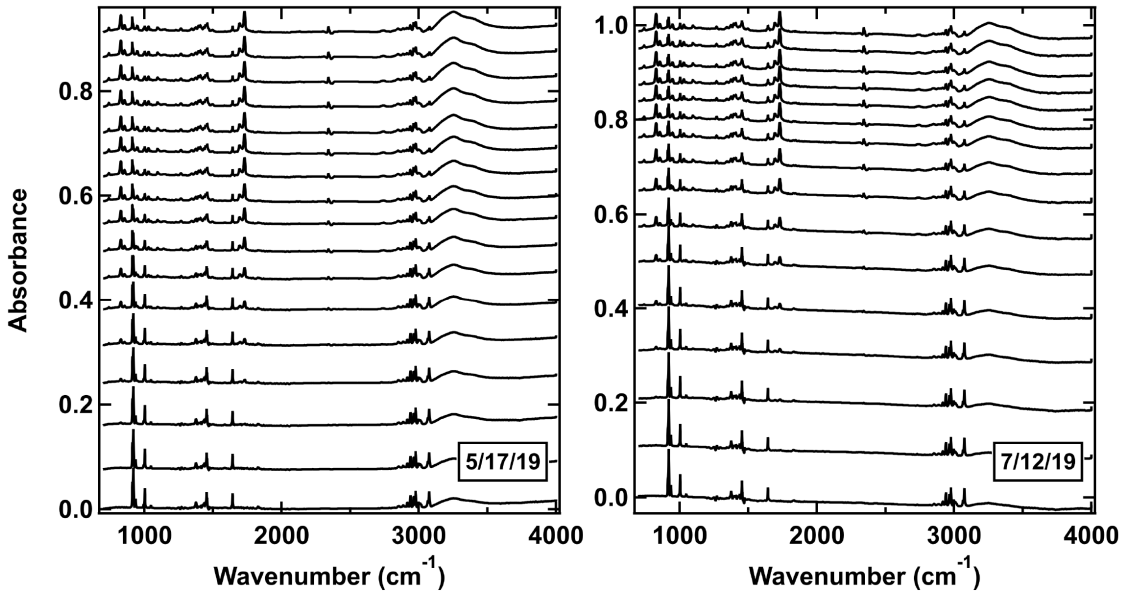

Figure A7.4: **Raw RAIR spectra for Figure 8.3 - 100 layers**. As the propene film is exposed to O(^{3}P), we track the loss of spectral intensity in the 914 - 919 cm^{-1} region (corresponding to the loss of propene's double bond). We use the change in intensity to calculate an initial rate of reactivity. The surface is held to 59 K during deposition and 54 K during exposure; this figure corresponds to trials with propene films that are 100 layers thick. (*Data files: 051719A.IR04-20, 071219A.IR02-17*).

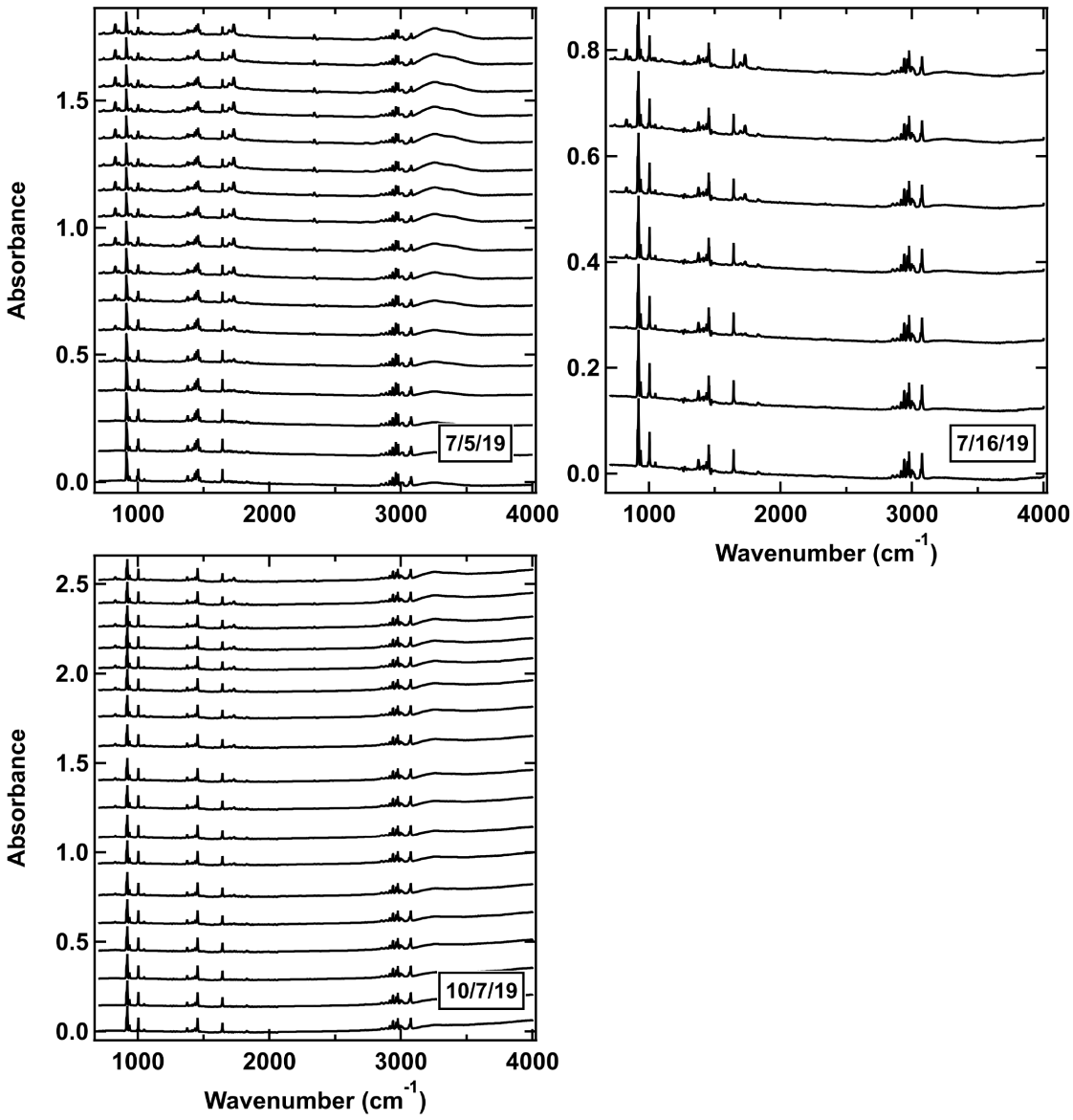

Figure A7.5: **Raw RAIR spectra for Figure 8.3 - 155-170 layers**. As the propene film is exposed to O(^{3}P), we track the loss of spectral intensity in the 914 - 919 cm^{-1} region (corresponding to the loss of propene's double bond). We use the change in intensity to calculate an initial rate of reactivity. The surface is held to 59 K during deposition and 54 K during exposure; this figure corresponds to trials with propene films between 155 and 170 layers thick. (*Data files: 071619B.IR02-08, 100719A.IR02-19, and 070519A.IR02-18*).

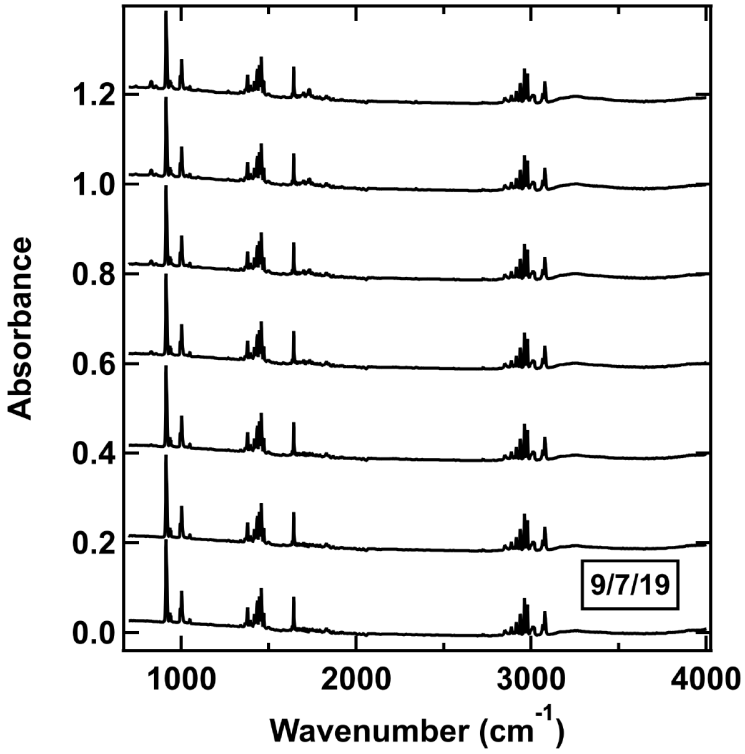

Figure A7.6: **Raw RAIR spectra for Figure 8.3 - 240 layers**. As the propene film is exposed to O(^{3}P), we track the loss of spectral intensity in the 914 - 919 cm^{-1} region (corresponding to the loss of propene's double bond). We use the change in intensity to calculate an initial rate of reactivity. The surface is held to 59 K during deposition and 54 K during exposure, this figure corresponds to trials with propene films that are 240 layers thick. (*Data files: 090719A.IR02-07*).

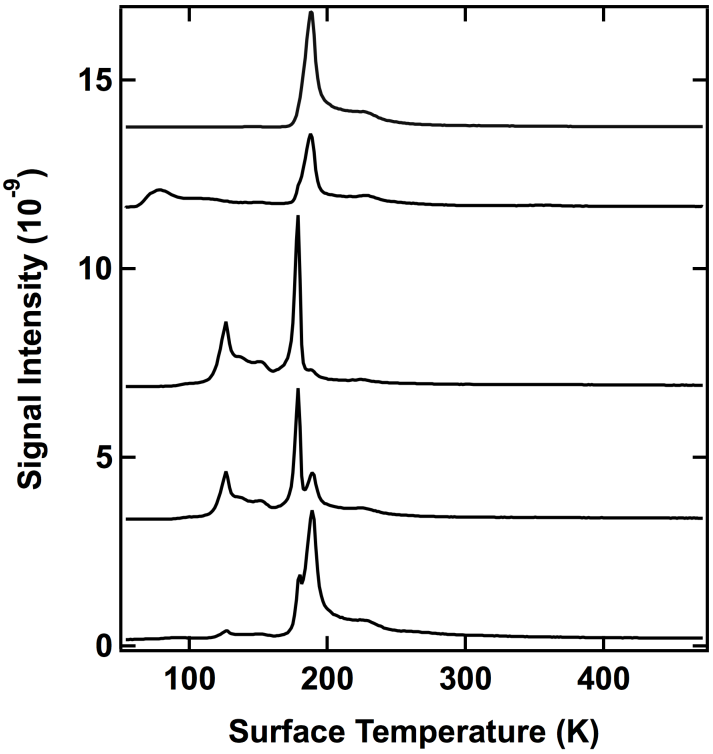

Figure A7.7: **Raw TPD spectra for Figure 8.5**. After exposing a 46-layer propene film to 1 $\times$ 10^{18} atoms cm^{-2}, we track QMS signal (RGA) as the surface temperature is After exposing a 46-layer propene film to 1 $\times$ 10^{18} atoms cm^{-2} O(^{3}P), we track QMS signal (RGA) as the surface temperature is increased at a rate of $\approx$1 K s^{-1}. (*Data file: 040219_TPD01.txt*).

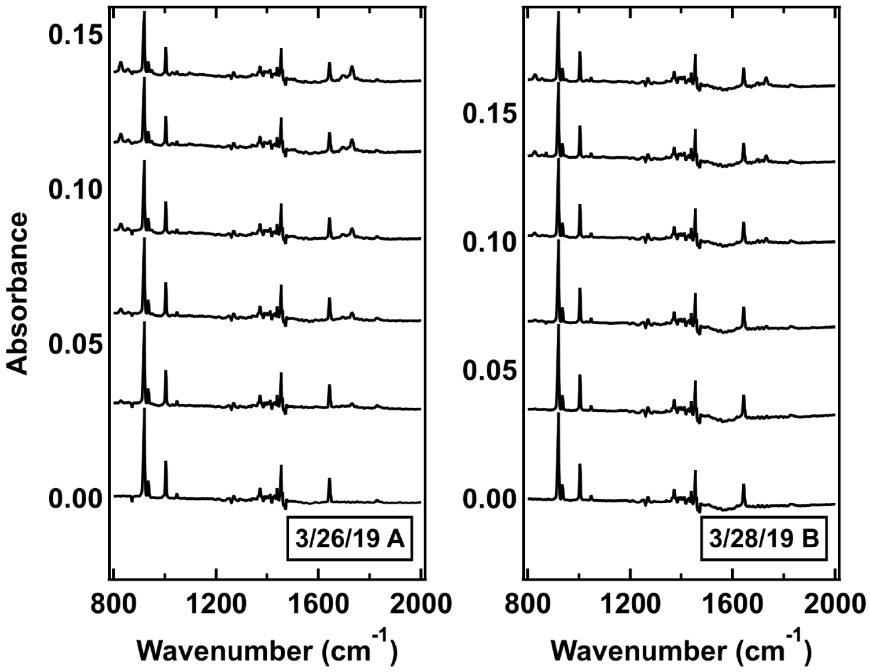

Figure A7.8: **Raw RAIR spectra for Figure 8.6 and 8.8 - 44 K**. As the propene film is exposed to O(^{3}P), we track the loss of spectral intensity in the 914 - 919 cm^{-1} region (corresponding to the loss of propene's double bond). All films are 30 layers thick, and the surface is held to 59 K during deposition and 44 K during exposure. (*Data files: 032619A.IR02-07 and 032819B.IR02-07*).

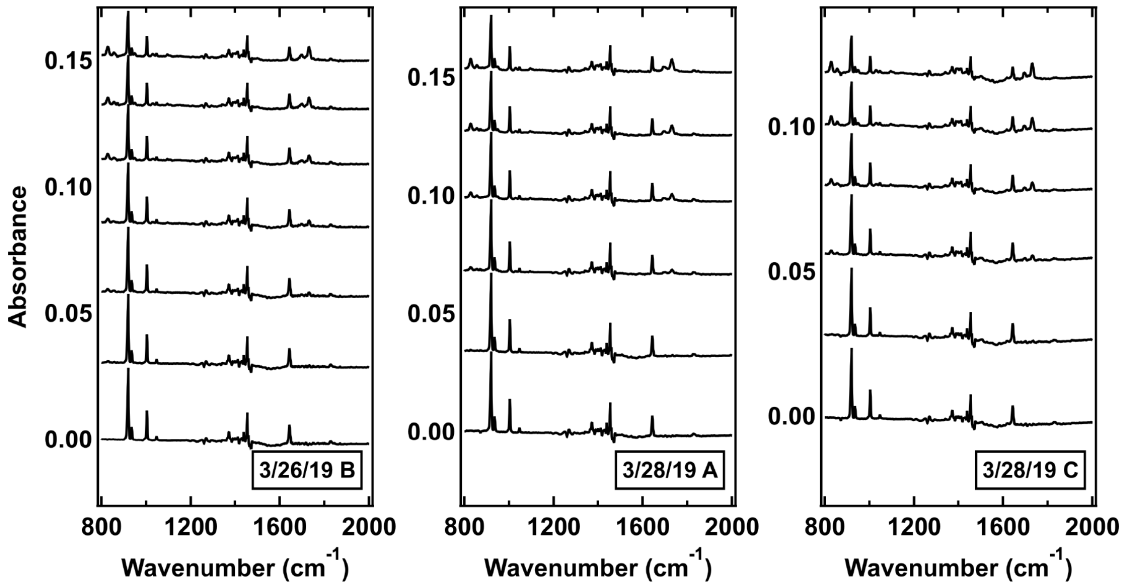

Figure A7.9: **Raw RAIR spectra for Figure 8.6 and 8.8 - 49 K**. As the propene film is exposed to O(^{3}P), we track the loss of spectral intensity in the 914 - 919 cm^{-1} region (corresponding to the loss of propene's double bond). All films are 30 layers thick, and the surface is held to 59 K during deposition and 49 K during exposure. (*Data files: 032619B.IR02-07, 032819A.IR02-07, and 032819C.IR02-07*).

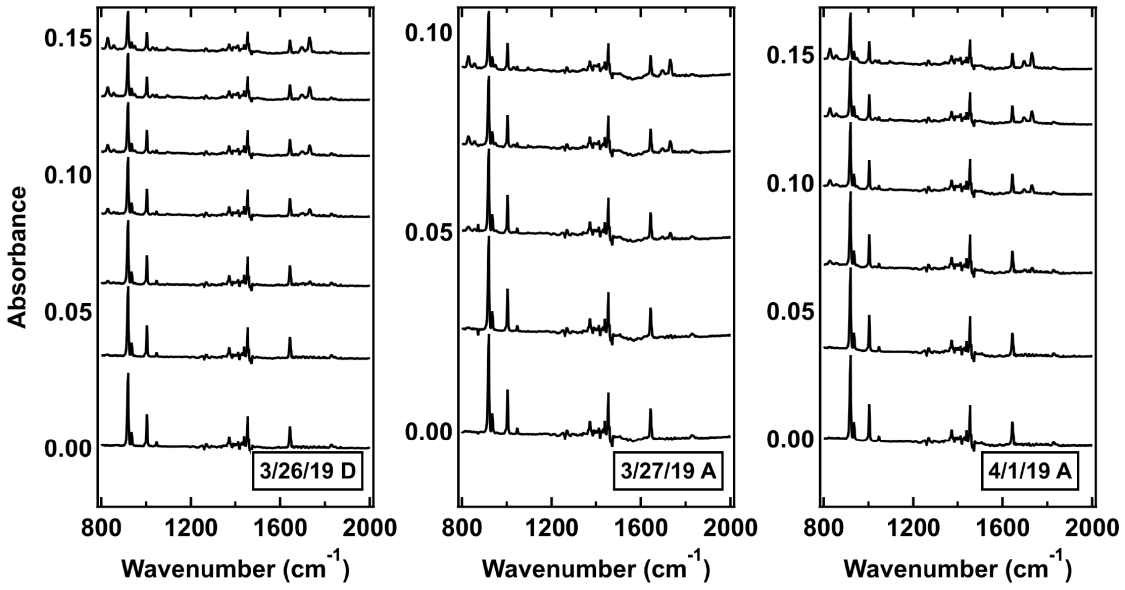

Figure A7.10: **Raw RAIR spectra for Figure 8.6 and 8.8 - 59 K**. As the propene film is exposed to O(^{3}P), we track the loss of spectral intensity in the 914 - 919 cm^{-1} region (corresponding to the loss of propene's double bond). All films are 30 layers thick, and the surface is held to 59 K during deposition and 59 K during exposure. (*Data files: 032619D.IR02-08, 032719A.IR02-06, and 040119A.IR02-07*).

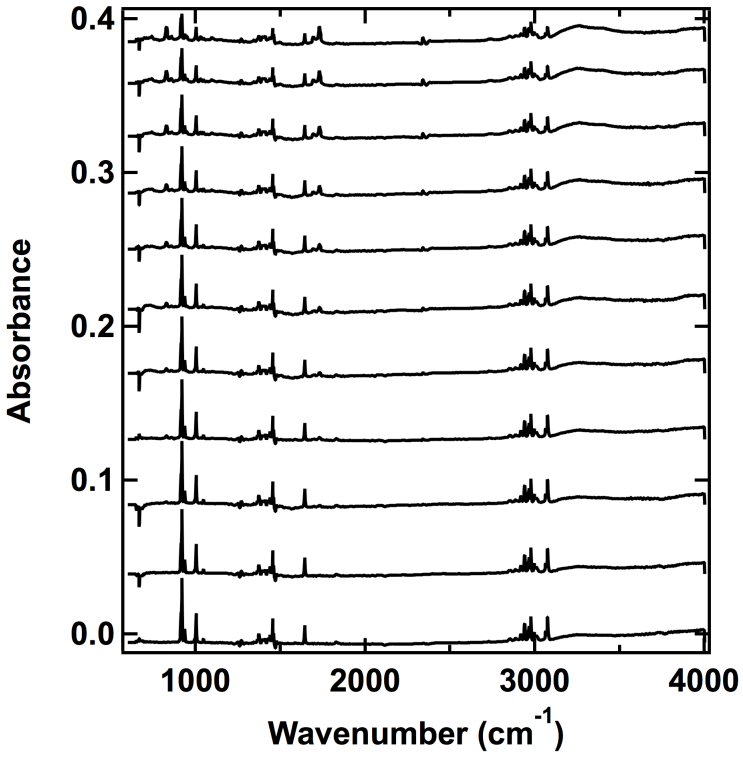

Figure A7.11: **Raw RAIR spectra for Figure 8.9**. As a 46-layer propene film is exposed to O(^{3}P), we track changes and loss of spectral intensity in the CH peaks located at 2939, 2964, 2977, and 3075 cm^{-1}. (*Data files: 053119A.IR03-13*).

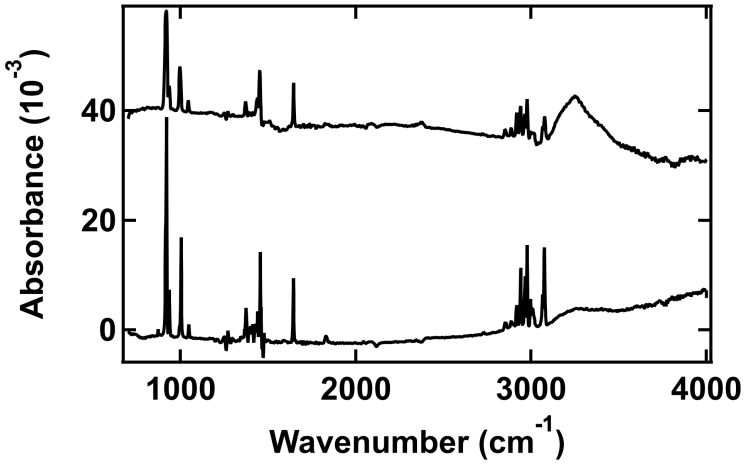

Figure A7.12: **Raw RAIR spectra for Figure 8.10**. We collected spectra of two "pristine", 19-layer propene films: one deposited with the crystal held to 59 K, and one with the crystal at 44 K. Both spectra were collected at 49 K. (*Data files: 053019A.IR02 (44 K) and 053119A.IR02 (59 K)*).

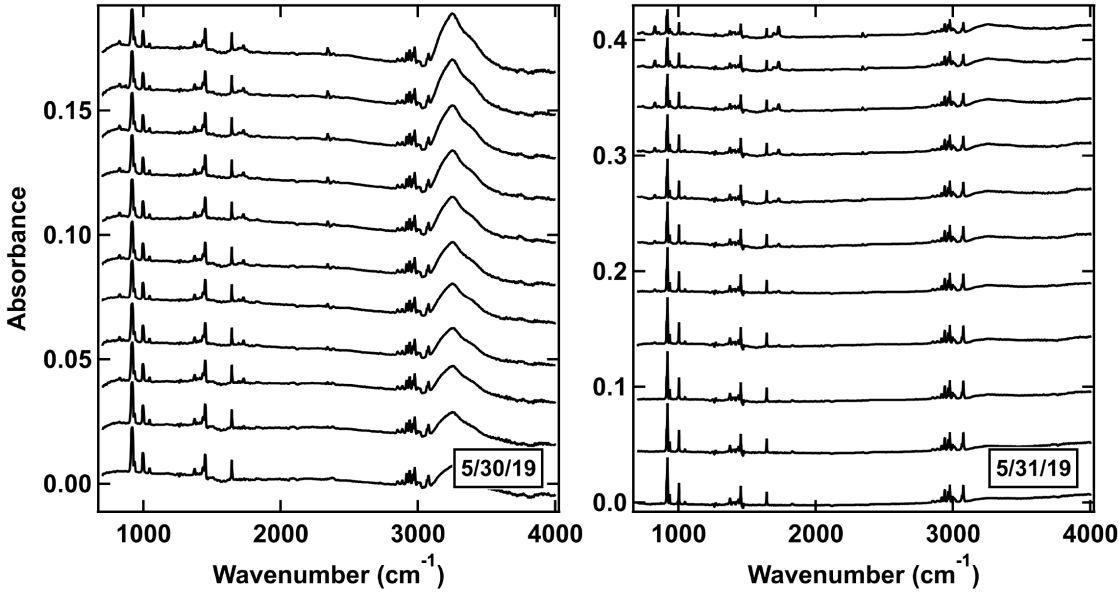

Figure A7.13: **Raw RAIR spectra for Figure 8.11**. We collected spectra at regular time intervals as two 19-layer propene films are exposed to O(^{3}P): one film was deposited with the crystal held to 59 K, and one with the crystal at 44 K. Both films were exposed to O(^{3}P) at 49 K. (*Data files: 053019A.IR02 (44 K) and 053119A.IR02 (59 K)*).

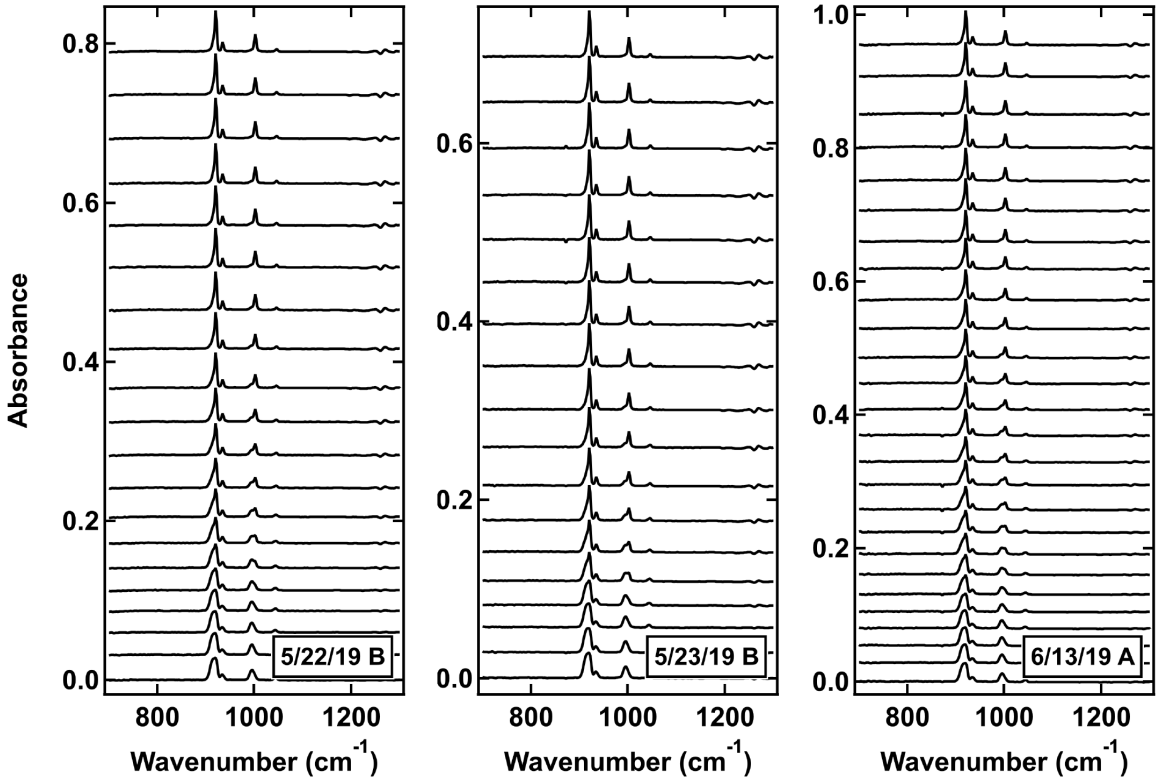

Figure A7.14: **Raw RAIR spectra for Figure 8.12 - 50 K**. We collected spectra at regular time intervals as 24-layer propene films (deposited at 44 K) are isothermally annealed to 50 K. (*Data files: 052219B.IR02-21, 052319B.IR02-19, and 061319A.IR02-27*).

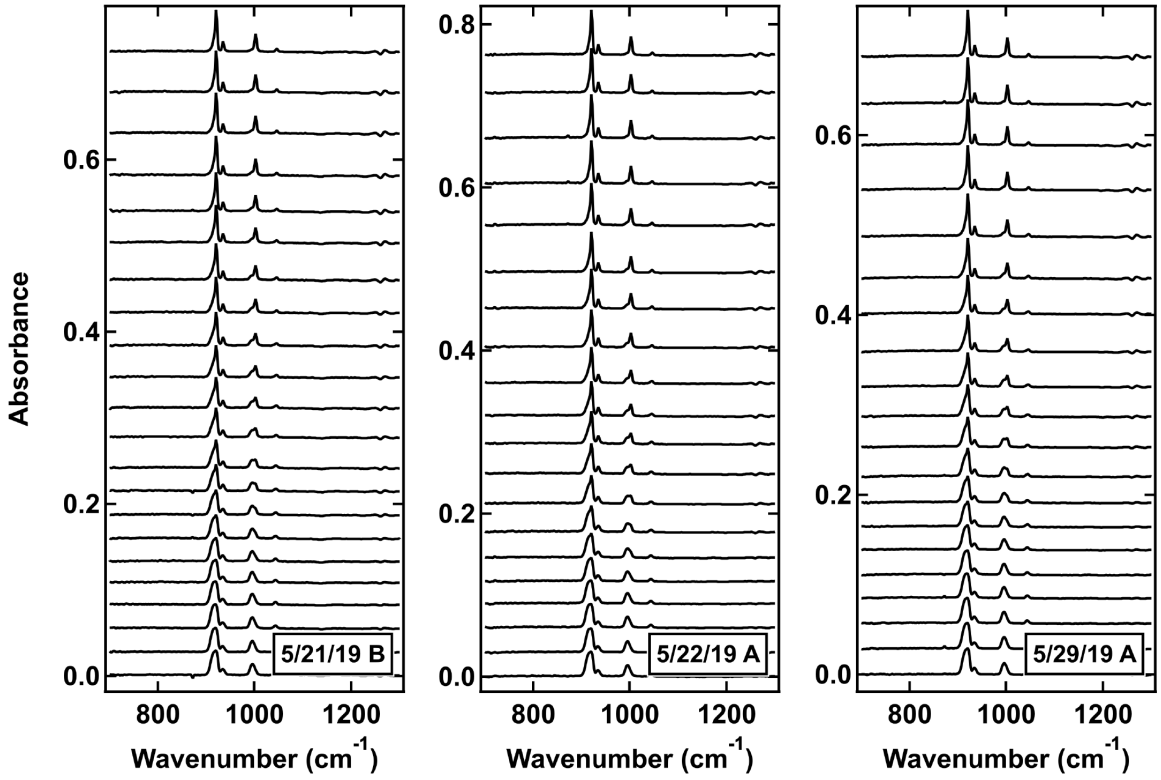

Figure A7.15: **Raw RAIR spectra for Figure 8.12 - 51 K**. We collected spectra at regular time intervals as 24-layer propene films (deposited at 44 K) are isothermally annealed to 51 K. (*Data files: 052119B.IR02-24, 052219A.IR02-21, and 052919A.IR02-21*).

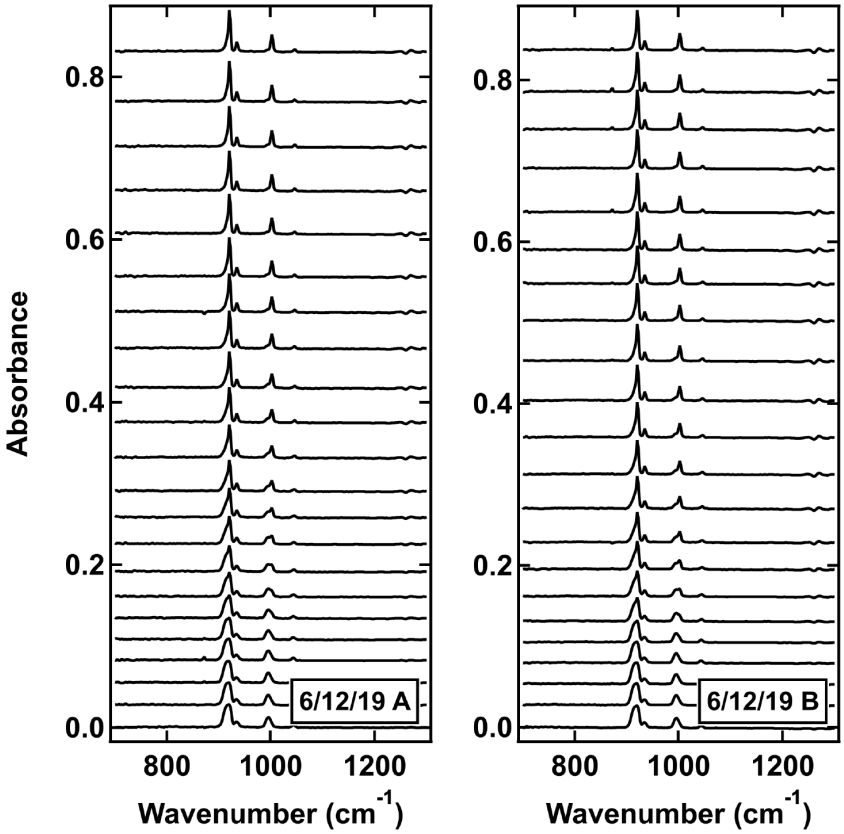

Figure A7.16: **Raw RAIR spectra for Figure 8.12 - 51.5 K**. We collected spectra at regular time intervals as 24-layer propene films (deposited at 44 K) are isothermally annealed to 51.5 K. (*Data files: 061219A.IR02-23 and 061219B.IR02-23*).

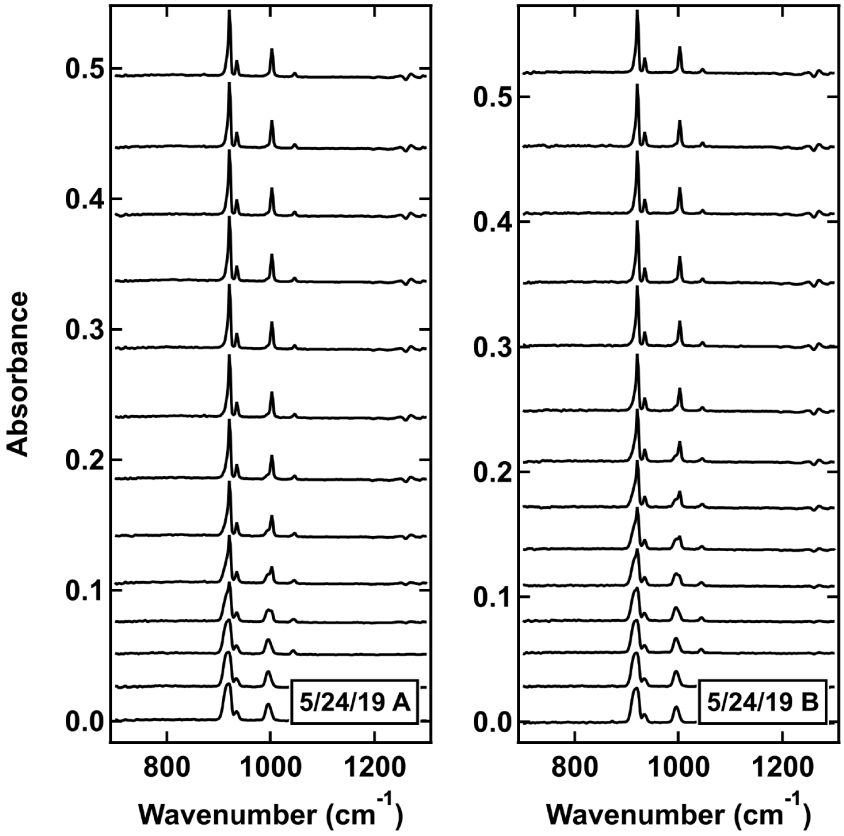

Figure A7.17: **Raw RAIR spectra for Figure 8.12 - 52 K**. We collected spectra at regular time intervals as 24-layer propene films (deposited at 44 K) are isothermally annealed to 52 K. (*Data files: 052419B.IR02-14 and 052419A.IR02-14*).

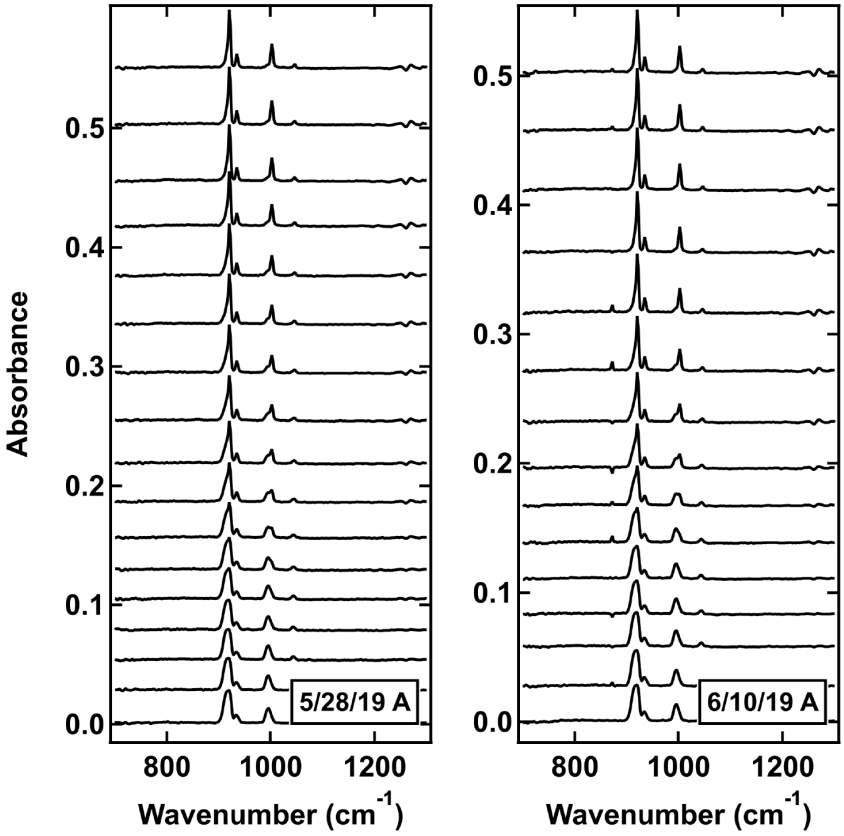

Figure A7.18: **Raw RAIR spectra for Figure 8.12 - 53 K**. We collected spectra at regular time intervals as 24-layer propene films (deposited at 44 K) are isothermally annealed to 53 K. (*Data files: 061019A.IR02-16 and 052819A.IR02-18*).

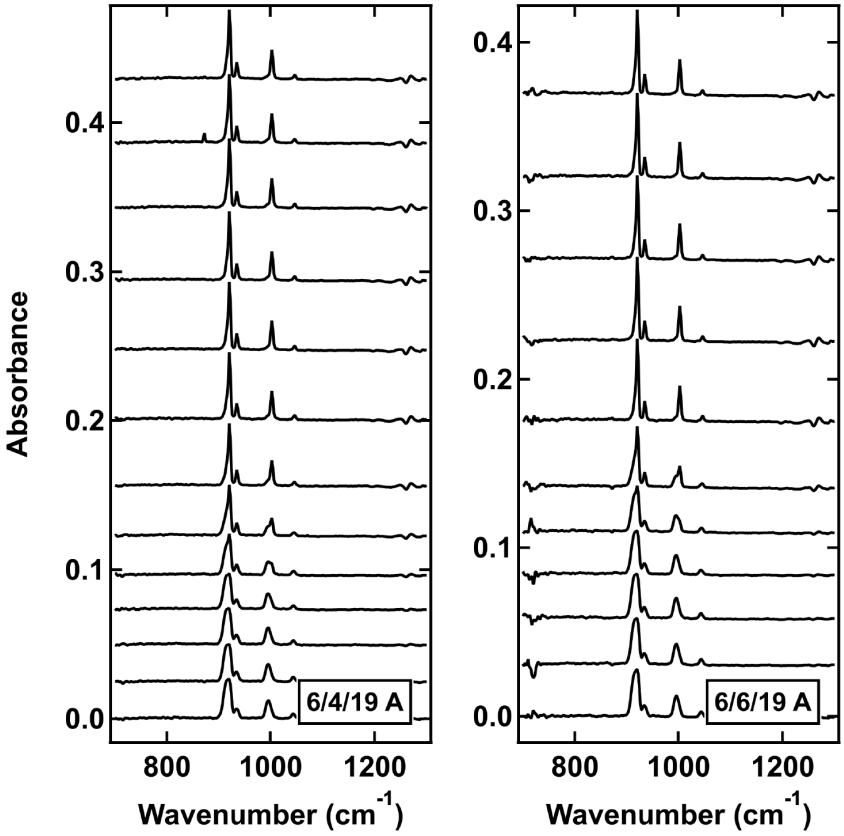

Figure A7.19: **Raw RAIR spectra for Figure 8.12 - 54 K**. We collected spectra at regular time intervals as 24-layer propene films (deposited at 44 K) are isothermally annealed to 54 K. (*Data files: 060419A.IR02-14 and 060619A.IR02-14*).

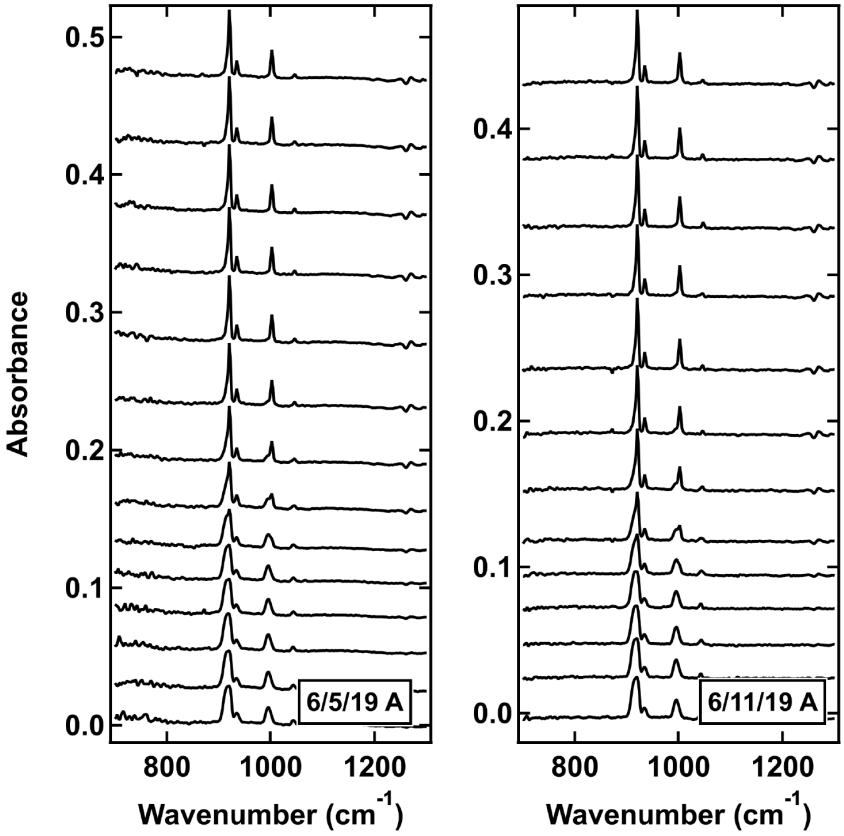

Figure A7.20: **Raw RAIR spectra for Figure 8.12 - 55 K**. We collected spectra at regular time intervals as 24-layer propene films (deposited at 44 K) are isothermally annealed to 55 K. (*Data files: 060519A.IR02-15 and 061119A.IR02-14*).

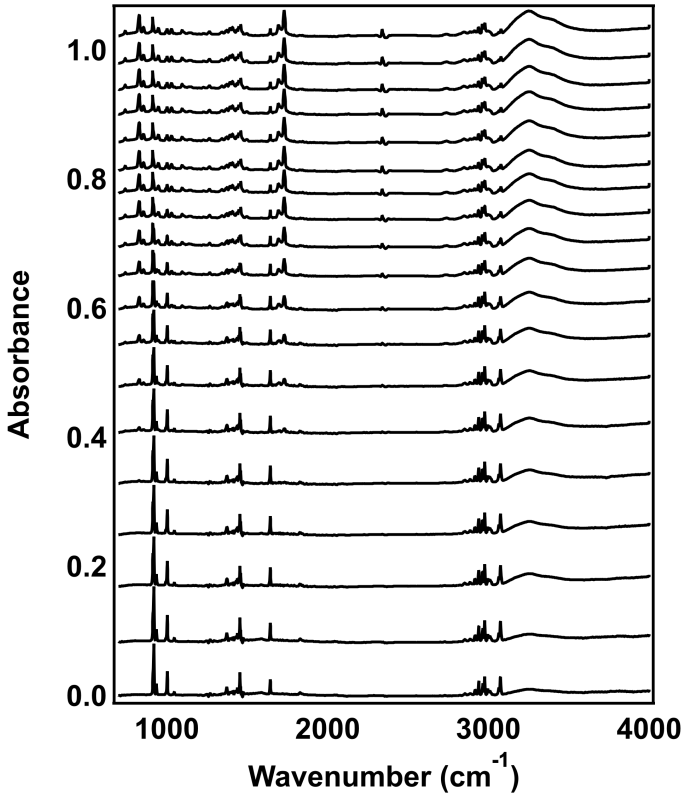

Figure A7.21: **Raw RAIR spectra for Figure 8.13**. We collected spectra at regular time intervals as a 40-layer "crystalline" propene film (deposited at 59 K) is exposed to O(^{3}P). Again, we track the nature of the loss of spectral intensity in the 914 - 919 cm^{-1} region (corresponding to the loss of propene's double bond). (*Data files: 051719A.IR02-20*).

A8 Copyright Attribution

Chapter 3 is adapted with permission from Langlois, G. G.; Thompson, R. S.; Li, W.; Sibener, S. J. Oxidation, Destruction, and Persistence of Multilayer Dimethyl Methylphosphonate Films during Exposure to O(^{3}P) Atomic Oxygen. *The Journal of Physical Chemistry C* **2016**, *120*, 16863–16870. Copyright 2016 American Chemical Society.[99]

Chapter 4 is adapted with permission from Thompson, R. S.; Langlois, G. G.; Sibener, S. J. Oxidative Destruction of Multilayer Diisopropyl Methylphosphonate Films by O(^{3}P) Atomic Oxygen. *The Journal of Physical Chemistry B* **2017**, *122*, 455–463. Copyright 2017 American Chemical Society.[370]

Chapter 5 is adapted with permission from Thompson, R. S.; Brann, M. R.; Purdy, E. H.; Graham, J. D.; McMillan, A. A.; Sibener, S. J. Rapid Laser-Induced Temperature Jump Decomposition of the Nerve Agent Simulant Diisopropyl Methylphosphonate under Atmospheric Conditions. *The Journal of Physical Chemistry C* **2019**, *123*, 21564–21570. Copyright 2019 American Chemical Society.[371]

Chapter 6 is adapted with permission from Thompson, R. S.; Brann, M. R.; Sibener, S. J. Sticking Probability of High-Energy Methane on Crystalline, Amorphous, and Porous Amorphous Ice Films. *The Journal of Physical Chemistry C* **2019**, *123*, 17855–17863. Copyright 2019 American Chemical Society.[354]

Chapter 7 has been submitted for publication to *Applied Surface Science*.

Chapter 8 is currently under revision for publication to *The Journal of Physical Chemistry C*.

References

(1) Suëtaka, W.; Yates, J. T. In *Surface Infrared and Raman Spectroscopy*; Springer US: Boston, MA, 1995, pp 13–116.

(2) Aroca, R. In *Surface-Enhanced Vibrational Spectroscopy*; John Wiley & Sons, Ltd: 2007, pp 35–71.

(3) Greenler, R. G. Reflection method for obtaining the infrared spectrum of a thin layer on a metal surface. *The Journal of Chemical Physics* **1969**, *50*, 1963–1968.

(4) Tolstoy, V. P.; Chernyshova, I. V.; Skryshevsky, V. A. In *Handbook of infrared spectroscopy of ultrathin films*; Wiley-Interscience: 2003, pp 1–70.

(5) Ratner, B. D.; Castner, D. G. In *Surface Analysis – The Principal Techniques*, Vickerman, J. C., Gilmore, I. S., Eds.; John Wiley & Sons, Ltd: Chichester, UK, 2009, pp 47–112.

(6) Moulder, J. F.; Stickle, W. F.; Sobol, P. E.; Bomben, K. D. In *Handbook of X-ray Photoelectron Spectroscopy*, Chastain, J., Ed.; Perkin-Elmer Corporation: 1981, pp 1–29.

(7) Crist, V. B. In *Handbooks of Monochromatic XPS Spectra*; XPS International, LLC: Mountain View, California, 1999, pp 17–21.

(8) King, D. A.; Wells, M. G. Molecular beam investigation of adsorption kinetics on bulk metal targets: Nitrogen on tungsten. *Surface Science* **1972**, *29*, 454–482.

(9) Matar, E.; Bergeron, H.; Dulieu, F.; Chaabouni, H.; Accolla, M.; Lemaire, J. L. Gas temperature dependent sticking of hydrogen on cold amorphous water ice surfaces of interstellar interest. *The Journal of Chemical Physics* **2010**, *133*, 104507\1–10.

(10) Kolasinki, K. W. In *Surface Science: Foundations of Catalysis and Nanoscience*, Third; John Wiley & Sons, Ltd: Chichester, UK, 2012, pp 115–183.

(11) Scoles, G. In *Atomic and Molecular Beam Methods, Volume 1*, Bassi, D., Buck, U., Laine, D., Eds.; Oxford University Press: New York, 1988, pp 14–53.

(12) Anderson, J. B.; Fenn, J. B. Velocity distributions in molecular beams from nozzle sources. *Physics of Fluids* **1965**, *8*, 780–787.

(13) Livesey, R. G. In *Foundations of vacuum science and technology*, Lafferty, J. M., Ed.; Wiley: 1998, pp 81–105.

(14) Zheng, S. *Conductance Calculation - Molecular Flow, Long Tube of Circular Cross Section*; tech. rep.; 1993, pp 1–4.

(15) Saksaganskiĭ, G. L. In *Molecular flow in complex vacuum systems*; Gordon and Breach Science Publishers: 1988, pp 1–31.

(16) Sibener, S. J.; Buss, R. J.; Casavecchia, P.; Hirooka, T.; Lee, Y. T. A crossed molecular beams investigation of the reactions O(^{3} ¡i¿P¡/i¿)+ C $_6$ H $_6$, C $_6$ D $_6$. *The Journal of Chemical Physics* **1980**, *72*, 4341–4349.

(17) Alagia, M.; Aquilanti, V.; Ascenzi, D.; Balucani, N.; Cappelletti, D.; Cartechini, L.; Casavecchia, P.; Pirani, F.; Sanchini, G.; Volpi, G. G. Magnetic Analysis of Supersonic Beams of Atomic Oxygen, Nitrogen, and Chlorine Generated from a Radio-Frequency Discharge. *Israel Journal of Chemistry* **1997**, *37*, 329–342.

(18) Casavecchia, P.; Balucani, N.; Volpi, G. G. In *The Chemical Dynamics and Kinetics of Small Radicals*, Wagner, A., Liu, K., Eds.; World Scientific Publishing Company: 1996; Chapter 9, pp 365–426.

(19) Hanke, F.; Björk, J. Structure and local reactivity of the Au(111) surface reconstruction. *Physical Review B* **2013**, *87*, 235422\1–6.

(20) Yang, J.; Cui, W.; Li, Y.; Xie, G.; Zhang, N.; Wang, R.; Hu, T.; Zhang, H. Investigation of argon ion sputtering on the secondary electron emission from gold samples. *Applied Surface Science* **2016**, *382*, 88–92.

(21) Callen, B.; Griffiths, K.; Memmert, U.; Harrington, D.; Bushby, S.; Norton, P. The adsorption of water on Ni(110): Monolayer, bilayer and related phenomena. *Surface Science* **1990**, *230*, 159–174.

(22) Stevenson, K. P.; Kimmel, G. A.; Dohnalek, Z.; Smith, R. S.; Kay, B. D. Controlling the morphology of amorphous solid water. *Science* **1999**, *283*, 1505–1507.

(23) Gibson, K. D.; Langlois, G. G.; Li, W.; Killelea, D. R.; Sibener, S. J. Molecular interactions with ice: Molecular embedding, adsorption, detection, and release. *The Journal of Chemical Physics* **2014**, *141*, 18C514\1–11.

(24) Henderson, M. A. The interaction of water with solid surfaces: fundamental aspects revisited. *Surface Science Reports* **2002**, *46*, 1–308.

(25) Bothe, M. A. In *The New Chemical Weapons Convention: Implementation and Prospects*, Bothe, M., Ronzitti, N., Rosas, A., Eds.; Kluwer Law International: Cambridge, MA, 1999, pp 1–16.

(26) Jang, Y. J.; Kim, K.; Tsay, O. G.; Atwood, D. A.; Churchill, D. G. Destruction and Detection of Chemical Warfare Agents. *Chemical Reviews* **2011**, *111*, 5345–5403.

(27) Davies, P. R.; Newton, N. G. The chemisorption of organophosphorus compounds at an Al(111) surface. *Applied Surface Science* **2001**, *181*, 296–306.

(28) Ekerdt, J. G.; Klabunde, K. J.; Shapley, J. R.; White, J. M.; Yates, J. T. J. Surface Chemistry of Organophosphorus Compunds. *The Journal of Physical Chemistry* **1988**, *92*, 6182–6188.

(29) Hegde, R. I.; Greenlief, C. M.; White, J. M. Surface Chemistry of Dimethyl Methylphosphonate on Rh(100). *Journal of Physical Chemistry A* **1985**, *89*, 2886–2891.

(30) Henderson, M. A.; White, J. M. Adsorption and Decomposition of Dimethyl Methylphosphonate on Platinum(111). *Journal of the American Chemical Society* **1988**, *110*, 6939–1947.

(31) Smentkowski, V. S.; Hagans, P.; Yates, J. T. Study of the Catalytic Destruction of Dimethyl Methylphosphonate: Oxidation over Mo(110). *The Journal of Physical Chemistry* **1988**, *92*, 6351–6357.

(32) Chen, D. A.; Ratliff, J. S.; Hu, X.; Gordon, W. O.; Senanayake, S. D.; Mullins, D. R. Dimethyl methylphosphonate decomposition on fully oxidized and partially reduced ceria thin films. *Surface Science* **2010**, *604*, 574–587.

(33) Davis, E. D.; Gordon, W. O.; Wilmsmeyer, A. R.; Troya, D.; Morris, J. R. Chemical Warfare Agent Surface Adsorption: Hydrogen Bonding of Sarin and Soman to Amorphous Silica. *Journal of Physical Chemistry Letters* **2014**, *5*, 1393–1399.

(34) Kim, C.; Lad, R.; Tripp, C. Interaction of organophosphorous compounds with TiO_2 and WO_3 surfaces probed by vibrational spectroscopy. *Sensors and Actuators B: Chemical* **2001**, *76*, 442–448.

(35) Mitchell, M. B.; Sheinker, V. N.; Mintz, E. A. Adsorption and Decomposition of Dimethyl Methylphosphonate on Metal Oxides. *The Journal of Physical Chemistry B* **1997**, *101*, 11192–11203.

(36) Panayotov, D. A.; Morris, J. R. Thermal decomposition of a chemical warfare agent simulant (DMMP) on TiO_2: Adsorbate reactions with lattice oxygen as studied by infrared spectroscopy. *The Journal of Physical Chemistry C* **2009**, *113*, 15684–15691.

(37) Panayotov, D. A.; Morris, J. R. Uptake of a chemical warfare agent simulant (DMMP) on TiO_2: Reactive adsorption and active site poisoning. *Langmuir* **2009**, *25*, 3652–3658.

(38) Segal, S. R.; Cao, L.; Suib, S. L.; Tang, X.; Satyapal, S. Thermal Decomposition of Dimethyl Methylphosphonate over Manganese Oxide Catalysts. *Journal of Catalysis* **2001**, *198*, 66–76.

(39) Wilmsmeyer, A. R.; Gordon, W. O.; Davis, E. D.; Troya, D.; Mantooth, B. A.; Lalain, T. A.; Morris, J. R. Infrared spectra and binding energies of chemical warfare nerve agent simulants on the surface of amorphous silica. *The Journal of Physical Chemistry C* **2013**, *117*, 15685–15697.

(40) Wilmsmeyer, A. R.; Uzarski, J.; Barrie, P. J.; Morris, J. R. Interactions and binding energies of dimethyl methylphosphonate and dimethyl chlorophosphate with amorphous silica. *Langmuir* **2012**, *28*, 10962–10967.

(41) Gordon, W. O.; Tissue, B. M.; Morris, J. R. Adsorption and Decomposition of Dimethyl Methylphosphonate on Y_2O_3 Nanoparticles. *The Journal of Physical Chemistry C* **2007**, *111*, 3233–3240.

(42) Bermudez, V. M. Investigation of the Interaction of γ-Al2O3 with Aqueous Solutions of Dimethyl Methylphosphonate Using Infrared Multiple Internal Reflection Spectroscopy. *Langmuir* **2013**, *29*, 1483–1489.

(43) Bermudez, V. M. Effect of humidity on the interaction of dimethyl methylphosphonate (DMMP) vapor with SiO2 and Al2O3 surfaces, studied using infrared attenuated total reflection spectroscopy. *Langmuir* **2010**, *26*, 18144–18154.

(44) Li, Y.-x.; Klabunde, K. J. Nanoscale Metal Oxide Particles as Chemical Reagents. Destructive Adsorption of a Chemical Agent Simulant, Dimethyl Methylphosphonate, on Heat-Treated Magnesium Oxide. *Langmuir* **1991**, *7*, 1388–1393.

(45) Panayotov, D. A.; Morris, J. R. Catalytic Degradation of a Chemical Warfare Agent Simulant: Reaction Mechanisms on TiO_2-Supported Au Nanoparticles. *Journal of Physical Chemistry C* **2008**, *112*, 7496–7502.

(46) Mattsson, A.; Lejon, C.; Štengl, V.; Bakardjieva, S.; Opluštil, F.; Andersson, P. O.; Österlund, L. Photodegradation of DMMP and CEES on zirconium doped titania nanoparticles. *Applied Catalysis B: Environmental* **2009**, *92*, 401–410.

(47) Bertilsson, L.; Engquist, I.; Liedberg, B. Interaction of Dimethyl Methylphosphonate with Alkanethiolate Monolayers Studied by Temperature-Programmed Desorption and Infrared Spectroscopy. *J. Phys. Chem. B* **1997**, *101*, 6021–6027.

(48) Bertilsson, L.; Potje-Kamloth, K.; Liess, H.-D.; Liedberg, B. On the Adsorption of Dimethyl Methylphosphonate on Self-Assembled Alkanethiolate Monolayers: Influence of Humidity. *Langmuir* **1999**, *15*, 1128–1135.

(49) Bertilsson, L.; Potje-Kamloth, K.; Lieβ, H.-D. Molecular interaction of DMMP and water vapor with mixed self-assembled monolayers studied by IR spectroscopy and SAW devices. *Thin Solid Films* **1996**, *284-285*, 882–887.

(50) Ferguson-McPherson, M. K.; Low, E. R.; Esker, A. R.; Morris, J. R. Sorption of dimethyl methylphosphonate within langmuir-blodgett films of trisilanolphenyl polyhedral oligomeric silsesquioxane. *The Journal of Physical Chemistry B* **2005**, *109*, 18914–18920.

(51) Bermudez, V. Quantum-chemical study of the adsorption of DMMP and Sarin on γ-Al_2O_3. *The Journal of Physical Chemistry C* **2007**, *111*, 3719–3728.

(52) Bermudez, V. M. Computational study of the adsorption of trichlorophosphate, dimethyl methylphosphonate, and sarin on amorphous SiO_2. *The Journal of Physical Chemistry C* **2007**, *111*, 9314–9323.

(53) Bermudez, V. M. Computational Study of Environmental Effects in the Adsorption of DMMP, Sarin, and VX on γ-Al_2O_3: Photolysis and Surface Hydroxylation. *The Journal of Physical Chemistry C* **2009**, *113*, 1917–1930.

(54) Quenneville, J.; Taylor, R. S.; Van Duin, A. C. T. Reactive Molecular Dynamics Studies of DMMP Adsorption and Reactivity on Amorphous Silica Surfaces. *The Journal of Physical Chemistry C* **2010**, *114*, 18894–18902.

(55) Yang, L.; Taylor, R.; de Jong, W. A.; Hase, W. L. A Model DMMP/TiO_2 (110) Intermolecular Potential Energy Function Developed from ab Initio Calculations. *The The Journal of Physical Chemistry C* **2011**, *115*, 12403–12413.

(56) Troya, D.; Edwards, A. C.; Morris, J. R. Theoretical study of the adsorption of organophosphorous compounds to models of a silica surface. *The Journal of Physical Chemistry C* **2013**, *117*, 14625–14634.

(57) Taylor, D. E.; Runge, K.; Cory, M. G.; Burns, D. S.; Vasey, J. L.; Hearn, J. D.; Gri, K.; Henley, M. V. Surface Binding of Organophosphates on Silica: Comparing Experiment and Theory. *The Journal of Physical Chemistry C* **2013**, *117*, 2699–2708.

(58) Michalkova, A.; Ilchenko, M.; Gorb, L.; Leszczynski, J. Theoretical Study of the Adsorption and Decomposition of Sarin on Magnesium Oxide. *The Journal of Physical Chemistry B* **2004**, *108*, 5294–5303.

(59) Mitchell, M. B.; Sheinker, V. N.; Cox, W. W. Room temperature reaction of ozone and dimethyl methylphosphonate (DMMP) on alumina-supported iron oxide. *The Journal of Physical Chemistry C* **2007**, *111*, 9417–9426.

(60) Mitchell, M. B.; Sheinker, V. N.; Cox Jr., W. W.; Hardcastle, K. Sustained room temperature decomposition of dimethyl methylphosphonate (DMMP) by O_3 on alumina-supported MnO_x. *The Journal of Physical Chemistry C* **2011**, *115*, 11514–11524.

(61) Li, Z.; Li, Y.; Cao, P.; Zhao, H. Surface Decontamination of Chemical Agent Surrogates Using an Atmospheric Pressure Air Flow Plasma Jet. *Plasma Science and Technology* **2013**, *15*, 696–701.

(62) Moeller, T. M.; Alexander, M. L.; Engelhard, M. H.; Gaspar, D. J.; Luna, M. L.; Irving, P. M. Surface Decontamination of Simulated Chemical Warfare Agents Using a Nonequilibrium Plasma With Off-Gas Monitoring. *IEEE Transactions on Plasma Science* **2002**, *30*, 1454–1459.

(63) Kim, D. B.; Gweon, B.; Moon, S. Y.; Choe, W. Decontamination of the chemical warfare agent simulant dimethyl methylphosphonate by means of large-area low-temperature atmospheric pressure plasma. *Current Applied Physics* **2009**, *9*, 1093–1096.

(64) Zhu, W.-C.; Wang, B.-R.; Xi, H.-L.; Pu, Y.-K. Decontamination of VX Surrogate Malathion by Atmospheric Pressure Radio-frequency Plasma Jet. *Plasma Chemistry and Plasma Processing* **2010**, *30*, 381–389.

(65) Herrmann, H. W.; Henins, I.; Park, J.; Selwyn, G. S. Decontamination of chemical and biological warfare (CBW) agents using an atmospheric pressure plasma jet (APPJ). *Physics of Plasmas* **1999**, *6*, 2284–2289.

(66) Zegers, E.; Fisher, E. Gas-Phase Pyrolysis of Diisopropyl Methylphosphonate. *Combustion and Flame* **1998**, *115*, 230–240.

(67) Korobeinichev, O. P.; Ilyin, S. B.; Shvartsberg, V. M.; Chernov, A. A. The destruction chemistry of organophosphorus compounds in flames—I: quantitative determination of final phosphorus-containing species in hydrogen-oxygen flames. *Combustion and Flame* **1999**, *118*, 718–726.

(68) Glaude, P.; Melius, C.; Pitz, W.; Westbrook, C. Detailed chemical kinetic reaction mechanisms for incineration of organophosphorus and fluoroorganophosphorus compounds. *Proceedings of the Combustion Institute* **2002**, *29*, 2469–2476.

(69) Liang, S.; Hemberger, P.; Neisius, N. M.; Bodi, A.; Grützmacher, H.; Levalois-Grützmacher, J.; Gaan, S. Elucidating the Thermal Decomposition of Dimethyl Methylphosphonate by Vacuum Ultraviolet (VUV) Photoionization: Pathways to the PO Radical, a Key Species in Flame-Retardant Mechanisms. *Chemistry - A European Journal* **2015**, *21*, 1073–1080.

(70) Korobeinichev, O.; Shvartsberg, V.; Shmakov, A.; Bolshova, T.; Jayaweera, T.; Melius, C.; Pitz, W.; Westbrook, C.; Curran, H. Flame inhibition by phosphorus-containing compounds in lean and rich propane flames. *Proceedings of the Combustion Institute* **2005**, *30*, 2353–2360.

(71) Conforti, P. F.; Braunstein, M.; Stearns, J. A.; Dodd, J. A. Collision dynamics of O(^{3}P) + DMMP using a specific reaction parameters potential form. *The Journal of Physical Chemistry A* **2012**, *116*, 2506–2518.

(72) Conforti, P. F.; Braunstein, M.; Dodd, J. A. Energetics and dynamics of the reactions of O(^{3}P) with dimethyl methylphosphonate and sarin. *The Journal of Physical Chemistry A* **2009**, *113*, 13752–13761.

(73) Davisson, M.; Love, A.; Vance, A.; Reynolds, J. Environmental fate of organophosphorus compounds related to chemical weapons., Livermore, CA, 2005.

(74) Fitch, J. P.; Raber, E.; Imbro, D. R. Technology challenges in responding to biological or chemical attacks in the civilian sector. *Science* **2003**, *302*, 1350–1354.

(75) Gibson, K. D.; Sibener, S. J. Scattering Dynamics, Survival, and Dispersal of Dimethyl Methylphosphonate Interacting with the Surface of Multilayer Graphene. *Journal of Physical Chemistry A* **2016**, DOI: 10.1021/acs.jpca.5b12419.

(76) Templeton, M.; Weinberg, W. Decomposition of phosphonate esters adsorbed on aluminum oxide. *Journal of the American Chemical Society* **1985**, *107*, 774–779.

(77) Eaton, G.; Harris, L.; Patel, K.; Symons, M. C. R. Infrared and Nuclear Magnetic Resonance Spectroscopic Studies on the Solvation of Trimethylphosphate and Dimethylphosphonate. *J. Chem. Soc. Faraday Trans* **1992**, *88*, 3527–3531.

(78) Herman, M. A.; Van Der Veken, B.; Barnes, A. Vibrational studies on conformational equilibrium in dimethylmethylphosphonate and methyldimethylphosphinate. *Journal of Molecular Structure* **1983**, *99*, 197–206.

(79) Lomax, S.; Barnes, A.; Van Der Veken, B. Conformational behaviour of dimethylmethylphosphonate and methyldimethylphosphinate studied by infrared spectroscopy in low-temperature matrices. *Journal of Molecular Structure* **1983**, *99*, 137–145.

(80) Vishnyakov, A.; Neimark, A. V. Molecular Model of Dimethylmethylphosphonate and Its Interactions with Water. *The Journal of Physical Chemistry A* **2004**, *108*, 1435–1439.

(81) Cuisset, A.; Mouret, G.; Pirali, O.; Roy, P.; Cazier, F.; Nouali, H.; Demaison, J. Gas-phase vibrational spectroscopy and ab initio study of organophosphorus compounds: discrimination between species and conformers. *The Journal of Physical Chemistry B* **2008**, *112*, 12516–25.

(82) Garton, D. J.; Minton, T. K.; Alagia, M.; Balucani, N.; Casavecchia, P.; Volpi, G. G. Reactive scattering of ground-state and electronically excited oxygen atoms on a liquid hydrocarbon surface. *Faraday Discussions* **1997**, *108*, 387–399.

(83) Garton, D. J.; Minton, T. K.; Alagia, M.; Balucani, N.; Casavecchia, P.; Gualberto Volpi, G. Comparative dynamics of Cl(^{2}P) and O(^{3}P) interactions with a hydrocarbon surface. *The Journal of Chemical Physics* **2000**, *112*, 5975–5984.

(84) Paz, Y.; Trakhtenberg, S.; Naaman, R. Reaction between O(^{3}P) and Organized Organic Thin-Films. *The Journal of Physical Chemistry* **1994**, *98*, 13517–13523.

(85) Thomas, L. C., *Interpretation of the Infrared Spectra of Organophosphorus Compounds*; Heyden & Son Ltd.: London, 1974.

(86) Aschmann, S. M.; Tuazon, E. C.; Atkinson, R. Atmospheric chemistry of diethyl methylphosphonate, diethyl ethylphosphonate, and triethyl phosphate. *The Journal of Physical Chemistry A* **2005**, *109*, 2282–91.

(87) Ganesan, K.; Raza, S. K.; Vijayaraghavan, R. Chemical warfare agents. *Environmental Toxicology and Pharmacology* **2010**, *2*, 166–178.

(88) Jang, Y. J.; Kim, K.; Tsay, O. G.; Atwood, D. A.; Churchill, D. G. Destruction and Detection of Chemical Warfare Agents. *Chemical Reviews* **2015**, *115*, PR1–PR76.

(89) Smith, C. S.; Metcalfe, E. A study of fire-retardant mechanisms in the gas phase by FTIR spectroscopy. *Polymer International* **2000**, *49*, 1169–1176.

(90) Szinicz, L. History of chemical and biological warfare agents. *Toxicology* **2005**, *214*, 167–181.

(91) Bartelt-Hunt, S. L.; Knappe, D. R. U.; Barlaz, M. A. A review of chemical warfare agent simulants for the study of environmental behavior. *Crit. Rev. Environ. Sci. Technol.* **2008**, *38*, 112–136.

(92) Munro, N. B.; Talmage, S. S.; Griffin, G. D.; Waters, L. C.; Watson, A. P.; King, J. F.; Hauschild, V. The sources, fate, and toxicity of chemical warfare agent degradation products. *Environmental health perspectives* **1999**, *107*, 933–74.

(93) Hu, S. X.; Yu, J. G.; Zeng, E. Y. Atmospheric degradation mechanisms of a simulant organophosphorus pesticide isopropyl methyl methylphosphonate: A theoretical consideration. *International Journal of Quantum Chemistry* **2013**, *113*, 1128–1136.

(94) Aschmann, S. M.; Tuazon, E. C.; Long, W. D.; Atkinson, R. Atmospheric chemistry of isopropyl methyl methylphosphonate and dimethyl N,N-dimethylphosphoroamidate. *The Journal of Physical Chemistry A* **2010**, *114*, 3523–3532.

(95) Martin, P.; Tuazon, E. C.; Atkinson, R.; Maughan, A. D. Atmospheric Gas-Phase Reactions of Selected Phosphorus-Containing Compounds. *The Journal of Physical Chemistry A* **2002**, *106*, 1542–1550.

(96) Liu, Y.; Liggio, J.; Harner, T.; Jantunen, L.; Shoeib, M.; Li, S. M. Heterogeneous OH initiated oxidation: A possible explanation for the persistence of organophosphate flame retardants in air. *Environmental Science and Technology* **2014**, *48*, 1041–1048.

(97) Li, Y.-x.; Klabunde, K. J. Nanoscale Metal Oxide Particles as Chemical Reagents. Destructive Adsorption of a Chemical Agent Simulant, Dimethyl Methylphosphonate, on Heat-Treated Magnesium Oxide. *Langmuir* **1991**, *7*, 1388–1393.

(98) Kim, S. H.; Kim, J. H.; Kang, B. K. Decomposition reaction of organophosphorus nerve agents on solid surfaces with atmospheric radio frequency plasma generated gaseous species. *Langmuir* **2007**, *23*, 8074–8078.

(99) Langlois, G. G.; Thompson, R. S.; Li, W.; Sibener, S. J. Oxidation, Destruction, and Persistence of Multilayer Dimethyl Methylphosphonate Films during Exposure to $O(^3P)$ Atomic Oxygen. *The Journal of Physical Chemistry C* **2016**, *120*, 16863–16870.

(100) Cory, M. G.; Taylor, D. E.; Bunte, S. W.; Runge, K.; Vasey, J. L.; Burns, D. S. Theoretical Methodology for Prediction of Tropospheric Oxidation of Dimethyl Phosphonate and Dimethyl Methylphosphonate. *The Journal of Physical Chemistry A* **2011**, *115*, 1946–1954.

(101) Guilbault, G. G.; Scheide, E.; Das, J. An Experimental Technique for Studying the Infrared Spectrum of Chemisorbed Compounds. *Spectroscopy Letters* **1968**, *1*, 167–175.

(102) Crooks, R. M.; Yang, H. C.; McEllistrem, L. J.; Thomas, R. C.; Ricco, A. J. Interactions between self-assembled monolayers and an organophosphonate Detailed study using surface acoustic wave-based mass analysis, polarization modulation-FTIR spectroscopy and ellipsometry. *Faraday Discussions* **1997**, *107*, 285–305.

(103) Mott, A. J.; Rez, P. Calculated infrared spectra of nerve agents and simulants. *Spectrochimica Acta - Part A: Molecular and Biomolecular Spectroscopy* **2012**, *91*, 256–260.

(104) Hameka, H. F.; Carrieri, A. H.; Jensen, J. O. Calculations of the Structure and the Vibrational Infrared Frequencies of Some Methylphosphonates. *Phosphorus, Sulfur, and Silicon and the Related Elements* **1992**, *66*, 1–11.

(105) Weber, M.; Nart, F. On the adsorption of ionic phosphate species on Au(111)—an in situ FTIR study. *Electrochimica Acta* **1996**, *41*, 653–659.

(106) Waghe, A.; Kanan, S. M.; Abu-Yousef, I.; Jensen, B.; Tripp, C. P. Infrared Study of UV-Irradiated Tungsten Trioxide Powders Containing Adsorbed Dimethyl Methyl Phosphonate and Trimethyl Phosphate. *Res. Chem. Intermed.* **2006**, *32*, 613.

(107) Connor, P. A.; McQuillan, A. J. Phosphate Adsorption onto TiO_2 from Aqueous Solutions: An in Situ Internal Reflection Infrared Spectroscopic Study. *Langmuir* **1999**, *15*, 1916–2921.

(108) Pleshko, N.; Boskey, A.; Mendelsohn, R. Novel infrared spectroscopic method for the determination of crystallinity of hydroxyapatite minerals. *Biophysical journal* **1991**, *60*, 786–93.

(109) Kuiper, A. E. T.; van Bokhoven, J. J. G. M.; Medema, J. The role of heterogeneity in the kinetics of a surface reaction. I. Infrared characterization of the adsorption structures of organophosphonates and their decomposition. *Journal of Catalysis* **1976**, *43*, 154–167.

(110) Burns, D. S.; Cory, M. G.; Taylor, D. E.; Bunte, S. W.; Runge, K.; Vasey, J. L. A comparison of primary and secondary hydrogen abstraction from organophosphates by hydroxyl radical. *International Journal of Chemical Kinetics* **2013**, *45*, 187–201.

(111) Aschmann, S. M.; Long, W. D.; Atkinson, R. Rate constants for the gas-phase reactions of OH radicals with dimethyl phosphonate over the temperature range of 278-351 K and for a series of other organophosphorus compounds at 280 K. *The Journal of Physical Chemistry A* **2008**, *112*, 4793–4799.

(112) Aschmann, S. M.; Long, W. D.; Atkinson, R. Temperature-dependent rate constants for the gas-phase reactions of OH radicals with 1,3,5-trimethylbenzene, triethyl phosphate, and a series of alkylphosphonates. *The Journal of Physical Chemistry A* **2006**, *110*, 7393–7400.

(113) Abbott, A.; Sierakowski, T.; Kiddle, J. J.; Clark, K. K.; Mezyk, S. P. Detailed investigation of the radical-induced destruction of chemical warfare agent simulants in aqueous solution. *The Journal of Physical Chemistry B* **2010**, *114*, 7681–7685.

(114) Atkinson, R. Gas-Phase Tropospheric Chemistry of Volatile Organic Compounds: 1. Alkanes and Alkenes. *Journal of Physical and Chemical Reference Data* **1997**, *26*, 215–290.

(115) Denisov, E. T. Solid-phase Radical Reactions and Mechanism of Oxidation of Carbon-chain Polymers. *Russian Chemical Reviews* **1978**, *47*, 572–586.

(116) Ingold, K. U. Peroxy radicals. *Accounts of Chemical Research* **1969**, *2*, 1–9.

(117) Aguila, A.; O'shea, K. E.; Tobien, T.; Asmus, K.-D. Reactions of Hydroxyl Radical with Dimethyl Methylphosphonate and Diethyl Methylphosphonate. A Fundamental Mechanistic Study. *The Journal of Physical Chemistry A* **2001**, *105*, 7834–7839.

(118) Atkinson, R.; Baulch, D. L.; Cox, R. A.; Crowley, J. N.; Hampson, R. F.; Hynes, R. G.; Jenkin, M. E.; Rossi, M. J.; Troe, J. Evaluated kinetic and photochemical data for atmospheric chemistry: Volume II - gas phase reactions of organic species. *Atmospheric Chemistry and Physics* **2006**, *6*, 3625–4055.

(119) Orlando, J. J.; Tyndall, G. S. Laboratory studies of organic peroxy radical chemistry: an overview with emphasis on recent issues of atmospheric significance. *Chemical Society Reviews* **2012**, *41*, 6294–6317.

(120) Devolder, P.; Fittschen, C.; Frenzel, A.; Hippler, H.; Poskrebyshev, G.; Striebelb, F.; Viskolczc, B.; Ehrstuhl, L. Complete falloff curves for the unimolecular decomposition of i-propoxy radicals between 330 and 408 K. *Physical Chemistry Chemical Physics* **1999**, *1*, 675–681.

(121) Peeters, J.; Fantechi, G.; Vereecken, L. A Generalized Structure-Activity Relationship for the Decomposition of (Substituted) Alkoxy Radicals. *Journal of Atmospheric Chemistry* **2004**, *48*, 59–80.

(122) Atkinson, R.; Carter, W. P. L. Reactions of alkoxy radicals under atmospheric conditions: The relative importance of decomposition versus reaction with O_2. *Journal of Atmospheric Chemistry* **1991**, *13*, 195–210.

(123) Ferenac, M. A.; Davis, A. J.; Holloway, A. S.; Dibble, T. S. Isomerization and Decomposition Reactions of Primary Alkoxy Radicals Derived from Oxygenated Solvents. *J. Phys. Chem. A* **2003**, *107*, 63.

(124) Moad, G.; Solomon, D. H., *The chemistry of radical polymerization*, 2nd; Elsevier Ltd: Kidlington, Oxford, 2006, p 639.

(125) Carlier, M.; Sochet, L.-R. Detection by E.S.R. of peroxy radicals: The importance of radical-radical reactions in the slow oxidation of butane. *Combustion and Flame* **1975**, *25*, 309–312.

(126) Korobeinichev, O. P.; Shvartsberg, V. M.; Shmakov, A. G. The chemistry of combustion of organophosphorus compounds. *Russian Chemical Reviews* **2007**, *76*, 1094–1121.

(127) Korobeinichev, O. P.; Chernov, A. A.; Sokolov, V. V.; Krasnoperov, L. N. Kinetics of destruction of diisopropyl methylphosphonate in corona discharge. *International Journal of Chemical Kinetics* **2002**, *34*, 331–337.

(128) Council, N. R. In *Review of Acute Human-Toxicity Estimates for Selected Chemical-Warfare Agents.* Washington (DC): National Academies Press (US): 1997, pp 28–34.

(129) Zegers, E. J. P.; Fisher, E. M. Gas-Phase Pyrolysis of Diethyl Methylphosphonate. *Combustion Science and Technology* **1996**, *116-117*, 69–89.

(130) Paciorek, K. J. L.; Kratzer, R. H.; Kaufman, J.; Nakahara, J. H.; Christos, T.; Hartstein, A. M. Thermal oxidative degradation studies of phosphate esters. *American Industrial Hygiene Association Journal* **1978**, *39*, 633–639.

(131) Lhomme, V.; Bruneau, C.; Soyer, N.; Brault, A. Thermal behavior of some organic phosphates. *Industrial & Engineering Chemistry Product Research and Development* **1984**, *23*, 98–102.

(132) Higgins, C. E.; Baldwin, W. H. The Thermal Decomposition of Tributyl Phosphate 1. *The Journal of Organic Chemistry* **1961**, *26*, 846–850.

(133) Bruneau, C.; Soyer, N.; Brault, A.; Kerfanto, M. Thermal degradation of tri-n-butyl phosphate. *Journal of Analytical and Applied Pyrolysis* **1981**, *3*, 71–81.

(134) Yang, L.; Shroll, R. M.; Zhang, J.; Lourderaj, U.; Hase, W. L. Theoretical investigation of mechanisms for the gas-phase unimolecular decomposition of DMMP. *The Journal of Physical Chemistry A* **2009**, *113*, 13762–13771.

(135) Glaude, P.; Curran, H.; Pitz, W.; Westbrook, C. Kinetic study of the combustion of organophosphorus compounds. *Proceedings of the Combustion Institute* **2000**, *28*, 1749–1756.

(136) Thompson, R. S.; Langlois, G. G.; Sibener, S. J. Oxidative Destruction of Multilayer Diisopropyl Methylphosphonate Films by O(^{3}P) Atomic Oxygen. *The Journal of Physical Chemistry B* **2018**, *122*, 455–463.

(137) Gibson, K. D.; Sibener, S. J. Fate of Some Chemical Warfare Simulants Adsorbed on an Inert Surface when Exposed to Rapid Laser Initiated Heating. *The Journal of Physical Chemistry C* **2018**, *122*, 24684–24689.

(138) Oppelt, E. T. Incineration Of Hazardous Waste. *JAPCA* **1987**, *37*, 558–586.

(139) Bulgakova, N.; Bulgakov, A. Pulsed laser ablation of solids: transition from normal vaporization to phase explosion. *Applied Physics A Materials Science & Processing* **2001**, *73*, 199–208.

(140) Smausz, T.; Kondász, B.; Gera, T.; Ajtai, T.; Utry, N.; Pintér, M.; Kiss-Albert, G.; Budai, J.; Bozóki, Z.; Szabó, G.; Hopp, B. Determination of UV–visible–NIR absorption coefficient of graphite bulk using direct and indirect methods. *Applied Physics A* **2017**, *123*, 633.

(141) Schultrich, B. In *Tetrahedrally Bonded Amorphous Carbon Films*; Springer, Berlin, Heidelberg: 2018, pp 585–631.

(142) Kononenko, V. V.; Kononenko, T. V.; Pimenov, S. M.; Sinyavskii, M. N.; Konov, V. I.; Dausinger, F. Effect of the pulse duration on graphitisation of diamond during laser ablation. *Quantum Electronics* **2005**, *35*, 252–256.

(143) Ready, J. F., *Effects of High-Power Laser Radiation*; Academic Press: New York, NY, 1971, pp 68–125.

(144) Windholz, R.; Molian, P. A. Nanosecond pulsed excimer laser machining of chemically vapour-deposited diamond and graphite: Part II Analysis and modelling. *Journal of Materials Science* **1998**, *33*, 523–528.

(145) Gibb, S.; Strimmer, K. MALDIquant: a versatile R package for the analysis of mass spectrometry data. *Bioinformatics* **2012**, *28*, 2270–2271.

(146) Savitzky, A.; Golay, M. J. E. Smoothing and Differentiation of Data by Simplified Least Squares Procedures. *Analytical Chemistry* **1964**, *36*, 1627–1639.

(147) Stein, S. E. In *NIST Chemistry WebBook, NIST Standard Reference Database Number 69*, Linstrom, P. J., Mallard, W. G., Eds.; NIST standard reference database; National Institute of Standards and Technology: Gaithersburg MD.

(148) Radziemski, L. J. Laser-induced photodestruction of the organo-phosphates: DIMP and DMMP. *Journal of Environmental Science and Health, Part B* **1981**, *16*, 337–361.

(149) Van Hest, M. F. A. M.; de Graaf, A.; van de Sanden, M. C. M. Use of in situ FTIR spectroscopy and mass spectrometry in an expanding hydrocarbon plasma. *Plasma Sources Science and Technology* **2000**, *9*, 615–624.

(150) Kaiser, R. I.; Roessler, K. Theoretical and Laboratory Studies on the Interaction of Cosmic-Ray Particles with Interstellar Ices. III. Suprathermal Chemistry–Induced Formation of Hydrocarbon Molecules in Solid Methane (CH_4), Ethylene (C_2H_4), and Acet. *The Astrophysical Journal* **1998**, *503*, 959–975.

(151) Silvi, B.; Labarbe, P.; Perchard, J. Spectres de vibration et coordonnées normales de quatre espèces isotopiques de propène. *Spectrochimica Acta Part A: Molecular Spectroscopy* **1973**, *29*, 263–276.

(152) Es-sebbar, E.-t.; Alrefae, M.; Farooq, A. Infrared cross-sections and integrated band intensities of propylene: Temperature-dependent studies. *Journal of Quantitative Spectroscopy and Radiative Transfer* **2014**, *133*, 559–569.

(153) Yuan, B.; Eilers, H. T-jump pyrolysis and combustion of diisopropyl methylphosphonate. *Combustion and Flame* **2019**, *199*, 69–84.

(154) Shan, X.; Vincent, J. C.; Kirkpatrick, S.; Walker, M. D.; Sambrook, M. R.; Clary, D. C. A Combined Theoretical and Experimental Study of Sarin (GB) Decomposition at High Temperatures. *The Journal of Physical Chemistry A* **2017**, *121*, 6200–6210.

(155) Ash, T.; Debnath, T.; Banu, T.; Das, A. K. Exploration of Unimolecular Gas-Phase Detoxication Pathways of Sarin and Soman: A Computational Study from the Perspective of Reaction Energetics and Kinetics. *Chemical Research in Toxicology* **2016**, *29*, 1439–1457.

(156) Hahn, D. K.; RaghuVeer, K. S.; Ortiz, J. V. Computational Tests of Models for Kinetic Parameters of Unimolecular Reactions of Organophosphorus and Organosulfur Compounds. *The Journal of Physical Chemistry A* **2011**, *115*, 14143–14152.

(157) Hidaka, Y.; Nakamura, T.; Tanaka, H.; Jinno, A.; Kawano, H.; Higashihara, T. Shock tube and modeling study of propene pyrolysis. *International Journal of Chemical Kinetics* **1992**, *24*, 761–780.

(158) Davis, S.; Law, C.; Wang, H. Propene pyrolysis and oxidation kinetics in a flow reactor and laminar flames. *Combustion and Flame* **1999**, *119*, 375–399.

(159) Milne, G. S.; Steel, C. The Gas-Phase Oxidation of Photochemically Generated Isopropyl Radicals. *The Journal of Physical Chemistry* **1968**, *72*, 3754–3761.

(160) Wijnen, M. J. H. Reactions of Alkoxy Radicals. VI. Photolysis of Isopropyl Propionate. *Journal of the American Chemical Society* **1960**, *28*, 1847–1849.

(161) Owen, T. The Contributions of Comets to Planets, Atmospheres, and Life: Insights from Cassini-Huygens, Galileo, Giotto, and Inner Planet Missions. *Space Science Reviews* **2008**, *138*, 301–316.

(162) Burke, D. J.; Brown, W. A. Ice in space: surface science investigations of the thermal desorption of model interstellar ices on dust grain analogue surfaces. *Physical Chemistry Chemical Physics* **2010**, *12*, 5947–5969.

(163) Ayotte, P.; Smith, R. S.; Stevenson, K. P.; Dohnálek, Z.; Kimmel, G. A.; Kay, B. D. Effect of porosity on the adsorption, desorption, trapping, and release of volatile gases by amorphous solid water. *Journal of Geophysical Research: Planets* **2001**, *106*, 33387–33392.

(164) Al-Halabi, A.; Van Dishoeck, E. F. Hydrogen adsorption and diffusion on amorphous solid water ice. *Monthly Notices of the Royal Astronomical Society* **2007**, *382*, 1648–1656.

(165) Hama, T.; Watanabe, N. Surface Processes on Interstellar Amorphous Solid Water: Adsorption, Diffusion, Tunneling Reactions, and Nuclear-Spin Conversion. *Chem. Rev* **2013**, *113*, 8783–8839.

(166) Al-Halabi, A.; van Dishoeck, E. F.; Kroes, G. J. Sticking of CO to crystalline and amorphous ice surfaces. *The Journal of Chemical Physics* **2004**, *120*, 3358–3367.

(167) Jenniskens, P.; Blake, D. F. Crystallization of Amorphous Water Ice in the Solar System. *The Astrophysical Journal* **1996**, *473*, 1104–1113.

(168) Jenniskens, P.; Blake, D. F.; Kouchi, A. In *Solar System Ices, Astrophysics and Space Science Library*; Springer, Dordrecht: 1998, pp 139–155.

(169) Angell, C. A. Amorphous Water. *Annu. Rev. Phys. Chem* **2004**, *55*, 559–83.

(170) Smith, R. S.; Petrik, N. G.; Kimmel, G. A.; Kay, B. D. Thermal and Nonthermal Physiochemical Processes in Nanoscale Films of Amorphous Solid Water. *Accounts of Chemical Research* **2012**, *45*, 33–42.

(171) Bossa, J.-B.; Isokoski, K.; Paardekooper, D. M.; Bonnin, M.; van der Linden, E. P.; Triemstra, T.; Cazaux, S.; Tielens, A. G. G. M.; Linnartz, H. Porosity measurements of interstellar ice mixtures using optical laser interference and extended effective medium approximations. *Astronomy & Astrophysics* **2014**, *561*, A136\1–8.

(172) Isokoski, K.; Bossa, J.-B.; Triemstra, T.; Linnartz, H. Porosity and thermal collapse measurements of H_2O, CH_3OH, CO_2, and H_2O:CO_2 ices. *Phys. Chem. Chem. Phys* **2014**, *16*, 3456–3465.

(173) Bartels-Rausch, T. et al. Ice structures, patterns, and processes: A view across the icefields. *Reviews of Modern Physics* **2012**, *84*, 885–944.

(174) Noble, J. A.; Martin, C.; Fraser, H. J.; Roubin, P.; Coussan, S. IR selective irradiations of amorphous solid water dangling modes: Irradiation vs annealing effects. *The Journal of Physical Chemistry C* **2014**, *118*, 20488–20495.

(175) He, J.; Acharyya, K.; Vidali, G. Sticking of Molecules on Nonporous Amorphous Water Ice. *The Astrophysical Journal* **2016**, *823*, 1–10.

(176) Batista, E. R.; Ayotte, P.; Bilić, A.; Kay, B. D.; Jónsson, H. What Determines the Sticking Probability of Water Molecules on Ice? *Physical Review Letters* **2005**, *95*, 223201\1–4.

(177) Watanabe, N.; Kouchi, A. Ice surface reactions: A key to chemical evolution in space. *Progress in Surface Science* **2008**, *83*, 439–489.

(178) Cardillo, M.; Balooch, M.; Stickney, R. Detailed balancing and quasi-equilibrium in the adsorption of hydrogen on copper. *Surface Science* **1975**, *50*, 263–278.

(179) Clark, R. N. In *The Science of Solar System Ices*, Gudipati, M. S., Castillo-Rogez, J., Eds.; Astrophysics and Space Science Library, Vol. 356; Springer New York: New York, NY, 2013, pp 3–46.

(180) Mousis, O.; Chassefière, E.; Holm, N. G.; Bouquet, A.; Waite, J. H.; Geppert, W. D.; Picaud, S.; Aikawa, Y.; Ali-Dib, M.; Charlou, J.-L.; Rousselot, P. Methane Clathrates in the Solar System. *Astrobiology* **2015**, *15*, 308–326.

(181) Dartois, E.; Muñoz Caro, G. M.; Deboffle, D.; Montagnac, G.; D'Hendecourt, L. Ultraviolet photoproduction of ISM dust. *Astronomy & Astrophysics* **2005**, *432*, 895–908.

(182) Langlois, G. G.; Li, W.; Gibson, K. D.; Sibener, S. J. Capture of Hyperthermal CO_2 by Amorphous Water Ice via Molecular Embedding. *The Journal of Physical Chemistry A* **2015**, *119*, 12238–12244.

(183) Gibson, K.; Killelea, D. R.; Becker, J. S.; Yuan, H.; Sibener, S. Energetic ballistic deposition of volatile gases into ice. *Chemical Physics Letters* **2012**, *531*, 18–21.

(184) Gibson, K. D.; Killelea, D. R.; Yuan, H.; Becker, J. S.; Sibener, S. J. Determination of the sticking coefficient and scattering dynamics of water on ice using molecular beam techniques. *The Journal of Chemical Physics* **2011**, *134*, 034703\1–7.

(185) Huthwelker, T.; Ammann, M.; Peter, T. The uptake of acidic gases on ice. *Chemical Reviews* **2006**, *106*, 1375–1444.

(186) Zubkov, T.; Smith, R. S.; Engstrom, T. R.; Kay, B. D. Adsorption, desorption, and diffusion of nitrogen in a model nanoporous material. I. Surface limited desorption kinetics in amorphous solid water. *The Journal of Chemical Physics* **2007**, *127*, 184707\1–11.

(187) Herrero, V. J.; Gaívez, S.; Mateánd Rafael Escribano, B. Interaction of CH_4 and H_2O in ice mixtures. *Phys. Chem. Chem. Phys* **2010**, *12*, 3164–3170.

(188) Rowland, B.; Devlin, J. P. Spectra of dangling OH groups at ice cluster surfaces and within pores of amorphous ice. *The Journal of Chemical Physics* **1991**, *94*, 812.

(189) Gálvez, Ó.; Maté, B.; Herrero, V. J.; Escribano, R. Spectroscopic Effects in CH_4/H_2O Ices. *The Astrophysical Journal* **2009**, *703*, 2101–2107.

(190) Killelea, D. R.; Gibson, K. D.; Yuan, H.; Becker, J. S.; Sibener, S. J. Dynamics of the sputtering of water from ice films by collisions with energetic xenon atoms. *The Journal of Chemical Physics* **2012**, *136*, 144705\1–8.

(191) Engquist, I.; Liedberg, B. D_2O Ice on Controlled Wettability Self-Assembled Alkanethiolate Monolayers: Cluster Formation and Substrate-Adsorbate Interaction. *J Phys Chem* **1996**, *100*, 20089–20096.

(192) Bergren, M. S.; Schuh, D.; Sceats, M. G.; Rice, S. A. The OH stretching region infrared spectra of low density amorphous solid water and polycrystalline ice Ih. *The Journal of Chemical Physics* **1978**, *69*, 3477–3482.

(193) Accolla, M.; Congiu, E.; Dulieu, F.; Manicò, G.; Chaabouni, H.; Matar, E.; Mokrane, H.; Lemaire, J. L.; Pirronello, V. Changes in the morphology of interstellar ice analogues after hydrogen atom exposure. *Physical Chemistry Chemical Physics* **2011**, *13*, 8037–8045.

(194) Maté, B.; Rodríguez-Lazcano, Y.; Herrero, V. J. Morphology and crystallization kinetics of compact (HGW) and porous (ASW) amorphous water ice. *Physical Chemistry Chemical Physics* **2012**, *14*, 10595.

(195) Raut, U.; Famá, M.; Teolis, B. D.; Baragiola, R. A. Characterization of porosity in vapor-deposited amorphous solid water from methane adsorption. *The Journal of Chemical Physics* **2007**, *127*, 204713\1–6.

(196) Kimmel, G. A.; Stevenson, K. P.; Dohnálek, Z.; Smith, R. S.; Kay, B. D.; Smith, R. S.; Kay, B. D. Control of amorphous solid water morphology using molecular beams. I. Experimental results. *The Journal of Chemical Physics* **2001**, *114*, 5284–5294.

(197) Dohnálek, Z.; Kimmel, G. A.; Ayotte, P.; Smith, R. S.; Kay, B. D. The deposition angle-dependent density of amorphous solid water films. *The Journal of Chemical Physics* **2003**, *118*, 364–372.

(198) Smith, R. S.; Zubkov, T.; Dohnálek, Z.; Kay, B. D. The Effect of the Incident Collision Energy on the Porosity of Vapor-Deposited Amorphous Solid Water Films. *The Journal of Physical Chemistry B* **2009**, *113*, 4000–4007.

(199) Buch, V.; Devlin, J. P. Spectra of dangling OH bonds in amorphous ice: Assignment to 2- and 3-coordinated surface molecules. *The Journal of Chemical Physics* **1991**, *94*, 4091–4092.

(200) Cholette, F.; Zubkov, T.; Smith, R. S.; Dohnálek, Z.; Kay, B. D.; Ayotte, P. Infrared Spectroscopy and Optical Constants of Porous Amorphous Solid Water. *The Journal of Physical Chemistry B* **2009**, *113*, 4131–4140.

(201) Smith, R. S.; May, R. A.; Kay, B. D. Desorption Kinetics of Ar, Kr, Xe, N_2, O_2, CO, Methane, Ethane, and Propane from Graphene and Amorphous Solid Water Surfaces. *The Journal of Physical Chemistry B* **2016**, *120*, 1979–1987.

(202) Morten Hundt, P.; Bisson, R.; Beck, R. D. The sticking probability of D_2O-water on ice: Isotope effects and the influence of vibrational excitation. *The Journal of Chemical Physics* **2012**, *137*, 074701–1–6.

(203) Raut, U.; Teolis, B. D.; Loeffler, M. J.; Vidal, R. A.; Famá, M.; Baragiola, R. A. Compaction of microporous amorphous solid water by ion irradiation. *The Journal of Chemical Physics* **2007**, *126*, 244511\1–5.

(204) Fayolle, E. C.; Öberg, K. I.; Cuppen, H. M.; Visser, R.; Linnartz, H. Laboratory H_2O:CO_2 ice desorption data: entrapment dependencies and its parameterization with an extended three-phase model. *A&A* **2011**, *529*, 1–11.

(205) Sandford, S. A.; Allamandola, L. J. The volume- and surface-binding energies of ice systems containing CO, CO_2 and H_2O. *Icarus* **1990**, *87*, 188–192.

(206) He, J.; Acharyya, K.; Vidali, G. Binding Energy of Molecules on Water Ice: Laboratory Measurements and Modeling. *The Astrophysical Journal* **2016**, *825*, 1–10.

(207) Hudson, R. L.; Gerakines, P. A.; Loeffler, M. J. Activation of weak IR fundamentals of two species of astrochemical interest in the T_d point group – the importance of amorphous ices. *Physical Chemistry Chemical Physics* **2015**, *17*, 12545–12552.

(208) Grundy, W.; Schmitt, B.; Quirico, E. The Temperature-Dependent Spectrum of Methane Ice I between 0.7 and 5 μm and Opportunities for Near-Infrared Remote Thermometry. *Icarus* **2002**, *155*, 486–496.

(209) Drobyshev, A.; Aldiyarov, A.; Sokolov, D. IR spectrometric studies of thin film cryovacuum condensates of methane and methane-water mixtures. *Low Temperature Physics* **2017**, *43*, 409–415.

(210) Laufer, D.; Kochavi, E.; Bar-Nun, A. Structure and dynamics of amorphous water ice. *Physical Review B* **1987**, *36*, 9219–9227.

(211) Kroes, G. J.; Andersson, S. Theory of Molecular Scattering from and Photochemistry at Ice Surfaces. *Proceedings of the International Astronomical Union* **2005**, *1*, 427–442.

(212) Pratihar, S.; Kohale, S. C.; Yang, L.; Manikandan, P.; Gibson, K. D.; Killelea, D. R.; Yuan, H.; Sibener, S. J.; Hase, W. L. Chemical Dynamics Simulations of High Energy Xenon Atom Collisions with the $\{0001\}$ Surface of Hexagonal Ice. *The Journal of Physical Chemistry C* **2013**, *117*, 2183–2193.

(213) Johnson, R.; Famá, M.; Liu, M.; Baragiola, R.; Sittler, E.; Smith, H. Sputtering of ice grains and icy satellites in Saturn's inner magnetosphere. *Planetary and Space Science* **2008**, *56*, 1238–1243.

(214) Baragiola, R.; Vidal, R.; Svendsen, W.; Schou, J.; Shi, M.; Bahr, D.; Atteberrry, C. Sputtering of water ice. *Nuclear Instruments and Methods in Physics Research Section B: Beam Interactions with Materials and Atoms* **2003**, *209*, 294–303.

(215) Baragiola, R.; Atteberry, C.; Dukes, C.; Famá, M.; Teolis, B. Atomic collisions in solids: Astronomical applications. *Nuclear Instruments and Methods in Physics Research Section B: Beam Interactions with Materials and Atoms* **2002**, *193*, 720–726.

(216) Russo, M. F. J.; Szakal, C.; Kozole, J.; Winograd, N.; Garrison, B. J. Sputtering Yields for C_{60} and Au_3 Bombardment of Water Ice as a Function of Incident Kinetic Energy. *Analytical Chemistry* **2007**, *79*, 4493–4498.

(217) Palumbo, M. E.; Baratta, G. A.; Rangel, C.; Da Cruz, N. C.; Fulvio, D.; Garozzo, M.; Gomis, O.; Leto, G.; Spinella, F.; Strazzulla, G. Ion irradiation of astrophysical ices. *Journal of Physics Conference Series* **2008**, *101*, 1–8.

(218) Dartois, E.; Ding, J. J.; de Barros, A. L.; Boduch, P.; Brunetto, R.; Chabot, M.; Domaracka, A.; Godard, M.; Lv, X. Y.; Mejía Guamán, C. F.; Pino, T.; Rothard, H.; da Silveira, E. F.; Thomas, J. C. Swift heavy ion irradiation of water ice from MeV to GeV energies. *Astronomy & Astrophysics* **2013**, *557*, 1–8.

(219) Mejía, C.; de Barros, A.; Seperuelo Duarte, E.; da Silveira, E.; Dartois, E.; Domaracka, A.; Rothard, H.; Boduch, P. Compaction of porous ices rich in water by swift heavy ions. *Icarus* **2015**, *250*, 222–229.

(220) Kimmel, G. A.; Dohnálek, Z.; Stevenson, K. P.; Smith, R. S.; Kay, B. D. Control of amorphous solid water morphology using molecular beams. II. Ballistic deposition simulations. *The Journal of Chemical Physics* **2001**, *114*, 5295–5303.

(221) Manca, C.; Martin, C.; Roubin, P. Spectroscopic and volumetric characterization of a non-microporous amorphous ice. *Chemical Physics Letters* **2002**, *364*, 220–224.

(222) Noble, J. A.; Congiu, E.; Dulieu, F.; Fraser, H. J. Thermal desorption characteristics of CO, O_2 and CO_2 on non-porous water, crystalline water and silicate surfaces at submonolayer and multilayer coverages. *Monthly Notices of the Royal Astronomical Society* **2012**, *421*, 768–779.

(223) Fillion, J.-H.; Amiaud, L.; Congiu, E.; Dulieu, F.; Momeni, A.; Lemaire, J.-L. D_2 desorption kinetics on amorphous solid water: from compact to porous ice films. *Physical Chemistry Chemical Physics* **2009**, *11*, 4396–4402.

(224) Hornekaer, L.; Baurichter, A.; Petrunin, V. V.; Luntz, A. C.; Kay, B. D.; Al-Halabi, A. Influence of surface morphology on D_2 desorption kinetics from amorphous solid water. *The Journal of Chemical Physics* **2005**, *122*, 124701\1–11.

(225) Al-Halabi, A.; Kleyn, A. W.; Kroes, G. J. Sticking of HCl to ice at hyperthermal energies: Dependence on incidence energy, incidence angle, and surface temperature. *The Journal of Chemical Physics* **2001**, *115*, 482–491.

(226) Paldor, A.; Toker, G.; Lilach, Y.; Asscher, M. Xe interacting with porous silicon. *Physical Chemistry Chemical Physics* **2010**, *12*, 6774–6781.

(227) Villalba, S.; Failache, H.; Lezama, A. Light-induced atomic desorption and diffusion of Rb from porous alumina. *Physical Review A* **2010**, *81*, 032901\1–8.

(228) Vidali, G.; Roser, J. E.; Ling, L.; Congiu, E.; Manic, G.; Pirronello, V. The formation of interstellar molecules via reactions on dust grain surfaces. *Faraday Discussions* **2006**, *133*, 125–135.

(229) Hornekaer, L.; Baurichter, A.; Petrunin, V. V.; Field, D.; Luntz, A. C. Importance of surface morphology in interstellar H_2 formation. *Science* **2003**, *302*, 1943–1946.

(230) Ratnasamy, C.; Wagner, J. P. Water Gas Shift Catalysis. *Catalysis Reviews* **2009**, *51*, 325–440.

(231) Smith, R.; Loganathan, M.; Shantha, M. A review of the water gas shift reaction kinetics. *International Journal of Chemical Reactor Engineering* **2010**, *8*, 1–32.

(232) Bustamante, F.; Enick, R.; Rothenberger, K. Kinetic study of the reverse water gas shift reaction in high-temperature, high pressure homogeneous systems. *Fuel Chem. Div.* **2002**, *47*, 663–664.

(233) Newsome, D. The water-gas shift reaction. *Catalysis Reviews Science and Engineering* **1980**, *21*, 275–318.

(234) Pettigrew, D.; Trimm, D.; Cant, N. The effects of rare earth oxides on the reverse water-gas shift reaction on palladium/alumina. *Catalysis letters* **1994**, *28*, 313–319.

(235) Tingey, G. Kinetics of water-gas equilibrium reaction. *The Journal of Physical Chemistry* **1966**, *70*, 1406–1412.

(236) Ginés, M. M.; Marchi, A. A.; Apesteguía, C.; Apesteguia, C. Kinetic study of the reverse water-gas shift reaction over $CuO/ZnO/Al_2O_3$ catalysts. *Applied Catalysis A: General* **1997**, *154*, 155–171.

(237) Weatherbee, G.; Bartholomew, C. Hydrogenation of CO_2 on group VIII metals: IV. Specific activities and selectivities of silica-supported Co, Fe, and Ru. *Journal of Catalysis* **1984**, *87*, 352–362.

(238) Rofer-DePoorter, C. Comprehensive mechanism for the Fischer-Tropsch synthesis. *Chemical Reviews* **1981**, *81*, 446–474.

(239) Bradford, B. The water-gas reaction in low-pressure explosions. *Journal of the Chemical Society* **1933**, 1557–1563.

(240) Chinchen, G.; Spencer, M.; Waugh, K. Promotion of methanol synthesis and the water-gas shift reactions by adsorbed oxygen on supported copper catalysts. *Journal of the Chemical Society* **1987**, *83*, 2193–2212.

(241) Spencer, M. S. M. On the activation energies of the forward and reverse water-gas shift reaction. *Catalysis Letters* **1995**, *32*, 9–13.

(242) Koeppel, R.; Baiker, A.; Wokaun, A. Copper/zirconia catalysts for the synthesis of methanol from carbon dioxide: influence of preparation variables on structural and catalytic properties of catalysts. *Applied Catalysis A: General* **1992**, *84*, 77–102.

(243) Kohn, D. W.; Clauberg, H.; Chen, P. Flash pyrolysis nozzle for generation of radicals in a supersonic jet expansion. *Review of Scientific Instruments* **1992**, *63*, 4003–4005.

(244) Zhang, X.; Friderichsen, A. V.; Nandi, S.; Ellison, G. B.; David, D. E.; McKinnon, J. T.; Lindeman, T. G.; Dayton, D. C.; Nimlos, M. R. Intense, hyperthermal source of organic radicals for matrix-isolation spectroscopy. *Review of Scientific Instruments* **2003**, *74*, 3077–3086.

(245) Shebaro, L.; Abbott, B.; Hong, T.; Slenczka, A. Facile production of higher hydrocarbons from ethane in a catalytic supersonic nozzle. *Chemical Physics Letters* **1997**, *271*, 73–78.

(246) Shebaro, L.; Bhalotra, S. Molecular beam chemistry: Formation of benzene and other higher hydrocarbons from small alkanes and alkenes in a catalytic supersonic nozzle. *The Journal of Physical Chemistry A* **1997**, *101*, 6775–6780.

(247) Romm, L.; Kim, Y.; Somorjai, G. Methane chemistry in the hot supersonic nozzle. *The Journal of Physical Chemistry A* **2001**, *105*, 7025–7030.

(248) Romm, L.; Somorjai, G. High-temperature short-contact-time supersonic nozzle chemistry of light aliphatic hydrocarbons. *Topics in Catalysis* **2002**, *30*, 53–62.

(249) Colonell, J. I.; Gibson, K. D.; Sibener, S. J. Carbon monoxide oxidation on Rh(111): Velocity and angular distributions of the CO_2 product. *The Journal of Chemical Physics* **1995**, *103*, 6677–6690.

(250) Gibson, K. D.; Colonell, J. I.; Sibener, S. J. Oxidation of H on Rh(111): H_2O product velocity and angular distributions. *The Journal of Chemical Physics* **1995**, *103*, 6735–6739.

(251) Brown, L. S.; Sibener, S. J. A molecular beam scattering investigation of the oxidation of CO on Rh(111). I. Kinetics and mechanism. *The Journal of Chemical Physics* **1988**, *89*, 1163–1169.

(252) Brown, L. S.; Sibener, S. J. A molecular beam scattering investigation of the oxidation of CO on Rh(111). II. Angular and velocity distributions of the CO_2 product. *The Journal of Chemical Physics* **1989**, *90*, 2807–2815.

(253) Itikawa, Y. Cross Sections for Electron Collisions With Carbon Dioxide. *Journal of Physical and Chemical Reference Data* **2002**, *31*, 749–767.

(254) Tian, C.; Vidal, C. R. Cross Sections of the Electron Impact Dissociative Ionization of CO, CH_4 and C_2H_2. *Journal of Physics B: Atomic, Molecular and Optical Physics* **1998**, *31*, 895–909.

(255) Ponec, V. Some Aspects of the Mechanism of Methanation and Fischer-Tropsch Synthesis. *Catalysis Reviews* **1978**, *18*, 151–171.

(256) Wang, W.; Wang, S.; Ma, X.; Gong, J. Recent advances in catalytic hydrogenation of carbon dioxide. *Chemical Society Reviews* **2011**, *40*, 3703–3722.

(257) Yang, J.; Ma, W.; Chen, D.; Holmen, A.; Davis, B. H. Fischer-Tropsch synthesis: A review of the effect of CO conversion on methane selectivity. *Applied Catalysis A: General* **2014**, *470*, 250–260.

(258) Ma, W.; Shafer, W. D.; Jacobs, G.; Yang, J.; Sparks, D. E.; Hamdeh, H. H.; Davis, B. H. Fischer-Tropsch synthesis: Effect of CO conversion on CH_4 and oxygenate selectivities over precipitated Fe-K catalysts. *Applied Catalysis A: General* **2018**, *560*, 144–152.

(259) Matsumoto, H.; Bennett, C. O. The transient method applied to the methanation and Fischer-Tropsch reactions over a fused iron catalyst. *Journal of Catalysis* **1978**, *53*, 331–344.

(260) Mills, G. A.; Steffgen, F. W. Catalytic methanation. *Catalysis Reviews* **1974**, *8*, 159–210.

(261) Niemantsverdriet, J. W.; van der Kraan, A. M. On the time-dependent behavior of iron catalysts in Fischer-Tropsch synthesis. *Journal of Catalysis* **1981**, *72*, 385–388.

(262) Miguel, C. V.; Soria, M. A.; Mendes, A.; Madeira, L. M. Direct CO_2 hydrogenation to methane or methanol from post-combustion exhaust streams - A thermodynamic study. *Journal of Natural Gas Science and Engineering* **2015**, *22*, 1–8.

(263) Adams, R. O. A review of the stainless steel surface. *Journal of Vacuum Science & Technology A: Vacuum, Surfaces, and Films* **1983**, *1*, 12–18.

(264) Bombara, G.; Alderisio, A.; Bernabai, U.; Cavallini, M. The effects of heating in a vacuum on the surface properties of a low chromium stainless steel. *Surface Technology* **1981**, *14*, 17–23.

(265) Wild, R. Vacuum annealing of stainless steel at temperatures between 770 and 1470K. *Corrosion Science* **1974**, *14*, 575–586.

(266) Park, R.; Houston, J.; Schreiner, D. Chromium depletion of vacuum annealed stainless steel surfaces. *Journal of Vacuum Science* **1972**, *9*, 1023–1027.

(267) Hultquist, G.; Leygraf, C. Highly protective films on stainless steels. *Materials Science and Engineering* **1980**, *42*, 199–206.

(268) Lei, Y.; Cant, N. W.; Trimm, D. L. Kinetics of the water–gas shift reaction over a rhodium-promoted iron–chromium oxide catalyst. *Chemical Engineering Journal* **2005**, *114*, 81–85.

(269) Daza, Y. A.; Kuhn, J. N. CO_2 conversion by reverse water gas shift catalysis: comparison of catalysts, mechanisms and their consequences for CO_2 conversion to liquid fuels. *RSC Advances* **2016**, *6*, 49675–49691.

(270) Keturakis, C. J.; Zhu, M.; Gibson, E. K.; Daturi, M.; Tao, F.; Frenkel, A. I.; Wachs, I. E. Dynamics of CrO_3–Fe_2O_3 Catalysts during the High-Temperature Water-Gas Shift Reaction: Molecular Structures and Reactivity. *ACS Catalysis* **2016**, *6*, 4786–4798.

(271) Lee, D.-W.; Lee, M. S.; Lee, J. Y.; Kim, S.; Eom, H.-J.; Moon, D. J.; Lee, K.-Y. The review of Cr-free Fe-based catalysts for high-temperature water-gas shift reactions. *Catalysis Today* **2013**, *210*, 2–9.

(272) Marrow, T.; Cotterill, P.; King, J. Temperature effects on the mechanism of time independent hydrogen assisted fatigue crack propagation in steels. *Acta Metallurgica et Materialia* **1992**, *40*, 2059–2068.

(273) Pasco, R.; Ficalora, P. The adsorption of hydrogen on iron; A surface orbital modified occupancy — bond energy bond order calculation. *Surface Science* **1983**, *134*, 476–498.

(274) Zou, C.; van Duin, A. C. T.; Sorescu, D. C. Theoretical Investigation of Hydrogen Adsorption and Dissociation on Iron and Iron Carbide Surfaces Using the ReaxFF Reactive Force Field Method. *Topics in Catalysis* **2012**, *55*, 391–401.

(275) Oriani, R. A. Hydrogen Embrittlement of Steels. *Annual Review of Materials Science* **1978**, *8*, 327–357.

(276) Yoshida, K.; Somorjai, G. A. The chemisorption of CO, CO_2, C_2H_2, C_2H_4, H_2 and NH_3 on the clean Fe(100) and (111) crystal surfaces. *Surface Science* **1978**, *75*, 46–60.

(277) Moon, D. W.; Dwyer, D. J.; Bernasek, S. L. Adsorption of CO on the clean and sulfur modified Fe(100) surface. *Surface Science* **1985**, *163*, 215–229.

(278) Moon, D. W.; Bernasek, S. L.; Dwyer, D. J.; Gland, J. L. Observation of an Unusually Low CO Stretching Frequency on Fe(100). *Journal of the American Chemical Society* **1985**, *107*, 4363–4364.

(279) Freund, H. J.; Roberts, M. W. Surface chemistry of carbon dioxide. *Surface Science Reports* **1996**, *25*, 225–273.

(280) Lobb, R.; Evans, H. An evaluation of the effect of surface chromium concentration on the oxidation of a stainless steel. *Corrosion Science* **1983**, *23*, 55–73.

(281) Killeen, J.; Smith, A.; Wild, R. Chromium depletion profiles after preferential removal of chromium from alloys. *Corrosion Science* **1976**, *16*, 551–559.

(282) Musket, R. G.; Bauer, W. Surface Characterization of Stainless Steel Using Proton-Induced X Rays. *Applied Physics Letters* **1972**, *20*, 411–413.

(283) Bustamante, F.; Enick, R. M.; Cugini, A.; Killmeyer, R. P.; Howard, B. H.; Rothenberger, K. S.; Ciocco, M. V.; Morreale, B. D.; Chattopadhyay, S.; Shi, S. High-temperature kinetics of the homogeneous reverse water-gas shift reaction. *AIChE Journal* **2004**, *50*, 1028–1041.

(284) Loiland, J. A.; Wulfers, M. J.; Marinkovic, N. S.; Lobo, R. F. Fe/γ-Al_2O_3 and Fe–K/γ-Al_2O_3 as reverse water-gas shift catalysts. *Catalysis Science & Technology* **2016**, *6*, 5267–5279.

(285) Zhu, M.; Wachs, I. E. Iron-Based Catalysts for the High-Temperature Water–Gas Shift (HT-WGS) Reaction: A Review. *ACS Catalysis* **2016**, *6*, 722–732.

(286) Lissianski, V. V.; Zamansky, V. M.; Gardiner, W. C. In *Gas-phase combustion chemistry*, Gardiner, W. C., Ed.; Springer: 2000, pp 1–123.

(287) Nguyen, T. L.; Peeters, J.; Vereecken, L. Quantum Chemical and Statistical Rate Study of the Reaction of O(^{3}P) with Allene: O-Addition and H-Abstraction Channels. *Journal of Physical Chemistry A* **2006**, *110*, 12166–12176.

(288) Lambert, R. M.; Williams, F. J.; Cropley, R. L.; Palermo, A. Heterogeneous alkene epoxidation: past, present and future. *Journal of Molecular Catalysis A: Chemical* **2005**, *228*, 27–33.

(289) Kahlich, D.; Wiechern, U.; Linder, J. In *Ullmann's Encyclopedia of Industrial Chemistry*; Wiley: 2012; Vol. 30, pp 313–335.

(290) Kirschner, E. M. Production of Top 50 Chemicals Increased Substantially in 1994. *Chemical & Engineering News* **1995**, *73*, 16–20.

(291) Manz, T. A.; Yang, B. Selective oxidation passing through $\eta 3$ -ozone intermediates: applications to direct propene epoxidation using molecular oxygen oxidant. *RSC Advances* **2014**, *4*, 27755–27774.

(292) Cavani, F. Catalytic selective oxidation: The forefront in the challenge for a more sustainable chemical industry. *Catalysis Today* **2010**, *157*, 8–15.

(293) Lee, H.-J.; Shi, T.-P.; Busch, D. H.; Subramaniam, B. A greener, pressure intensified propylene epoxidation process with facile product separation. *Chemical Engineering Science* **2007**, *62*, 7282–7289.

(294) Koda, S.; Endo, Y.; Tsuchiya, S.; Hirota, E. *Branching Ratios in 0(^{3}P) Reactions of Terminal Olefins Studied by Kinetic Microwave Absorption Spectroscopy*; tech. rep.; 1991, pp 1241–1244.

(295) Quandt, R.; Min, Z.; Wang, X.; Bersohn, R. Reactions of O(^{3}P) with Alkenes: H, CH_2CHO, CO, and OH Channels. *The Journal of Physical Chemistry A* **1998**, *102*, 60–64.

(296) Savee, J. D.; Welz, O.; Taatjes, C. A.; Osborn, D. L. New mechanistic insights to the O(^{3}P) + propene reaction from multiplexed photoionization mass spectrometry. *Physical Chemistry Chemical Physics* **2012**, *14*, 10410–10423.

(297) Cvetanović, R. J. In *Advances in Photochemistry*; John Wiley & Sons, Ltd: 1963, pp 115–182.

(298) Morin, J.; Bedjanian, Y.; Romanias, M. N. Rate Constants of the Reactions of O(^{3}P) Atoms with Ethene and Propene over the Temperature Range 230-900 K. *International Journal of Chemical Kinetics* **2017**, *49*, 53–60.

(299) Leonori, F.; Balucani, N.; Nevrly, V.; Bergeat, A.; Falcinelli, S.; Vanuzzo, G.; Casavecchia, P.; Cavallotti, C. Experimental and Theoretical Studies on the Dynamics of the O(^{3}P) + Propene Reaction: Primary Products, Branching Ratios, and Role of Intersystem Crossing. *The Journal of Physical Chemistry C* **2015**, *119*, 14632–14652.

(300) Cavallotti, C.; Leonori, F.; Balucani, N.; Nevrly, V.; Bergeat, A.; Falcinelli, S.; Vanuzzo, G.; Casavecchia, P. Relevance of the Channel Leading to Formaldehyde + Triplet Ethylidene in the O(^{3}P) + Propene Reaction under Combustion Conditions. *The Journal of Physical Chemistry Letters* **2014**, *5*, 4213–4218.

(301) Hughes, A. N.; Scheer, M. D.; Klein, R. The Reaction between O(^{3}P) and Condensed Olefins below 100 K. *The Journal of Physical Chemistry* **1966**, *70*, 798–805.

(302) Klein, R.; Scheer, M. D. Mechanism of O(^{3}P) Addition to Condensed Films. II. Propene, 1-Butene, and Their Mixtures. *The Journal of Physical Chemistry* **1968**, *72*, 617–622.

(303) Cvetanović, R. J. Mechanism of the Interaction of Oxygen Atoms with Olefins. *The Journal of Chemical Physics* **1956**, *25*, 376–377.

(304) Atkinson, R.; Cvetanović, R. J. Activation Energies of the Addition of O(^{3}P) Atoms to Olefins. *The Journal of Chemical Physics* **1972**, *56*, 432–437.

(305) Ward, M. D.; Price, S. D. Thermal Reactions of Oxygen Atoms with Alkenes at Low Temperatures on Interstellar Dust. *The Astrophysical Journal* **2011**, *741*, 121–1–9.

(306) Herbst, E. Chemistry in the Interstellar Medium. *Annual Review of Physical Chemistry* **1995**, *46*, 27–54.

(307) Hickson, K. M.; Wakelam, V.; Loison, J.-C. Methylacetylene (CH_3CCH) and propene (C_3H_6) formation in cold dense clouds: A case of dust grain chemistry. *Molecular Astrophysics* **2016**, *3-4*, 1–9.

(308) Marcelino, N.; Cernicharo, J.; Agúndez, M.; Roueff, E.; Gerin, M.; Martín-Pintado, J.; Mauersberger, R.; Thum, C. Discovery of Interstellar Propylene (CH_2CHCH_3): Missing Links in Interstellar Gas-Phase Chemistry. *The Astrophysical Journal* **2007**, *665*, L127–L130.

(309) Nixon, C. A.; Jennings, D. E.; Bézard, B.; Vinatier, S.; Teanby, N. A.; Sung, K.; Ansty, T. M.; Irwin, P. G. J.; Gorius, N.; Cottini, V.; Coustenis, A.; Flasar, F. M. Detection of Propene in Titan's Stratosphere. *The Astrophysical Journal* **2013**, *776*, L14\1–6.

(310) Rawlings, J. M. C.; Williams, D. A.; Viti, S.; Cecchi-Pestellini, C. A radical route to interstellar propylene formation. *Monthly Notices of the Royal Astronomical Society: Letters* **2013**, *436*, L59–L63.

(311) Garrod, R. T.; Wakelam, V.; Herbst, E. Non-thermal desorption from interstellar dust grains via exothermic surface reactions. *Astronomy & Astrophysics* **2007**, *467*, 1103–1115.

(312) McGuire, B. A.; Carroll, P. B.; Loomis, R. A.; Finneran, I. A.; Jewell, P. R.; Remijan, A. J.; Blake, G. A. Discovery of the interstellar chiral molecule propylene oxide (CH_3CHCH_2O). *Science* **2016**, *352*, 1449–52.

(313) Bergantini, A.; Abplanalp, M. J.; Pokhilko, P.; Krylov, A. I.; Shingledecker, C. N.; Herbst, E.; Kaiser, R. I. A Combined Experimental and Theoretical Study on the Formation of Interstellar Propylene Oxide (CH_3CHCH_2O)—A Chiral Molecule. *The Astrophysical Journal* **2018**, *860*, 108\1–15.

(314) Bergner, J. B.; Öberg, K. I.; Rajappan, M. Methanol Formation via Oxygen Insertion Chemistry in Ices. *The Astrophysical Journal* **2017**, *845*, 29\1–13.

(315) Bergner, J. B.; Öberg, K. I.; Rajappan, M. Oxygen Atom Reactions with C_2H_6, C_2H_4, and C_2H_2 in Ices. *The Astrophysical Journal* **2019**, *874*, 115\1–16.

(316) Sharpe, S. W.; Johnson, T. J.; Sams, R. L.; Chu, P. M.; Rhoderick, G. C.; Johnson, P. A. Gas-Phase Databases for Quantitative Infrared Spectroscopy. *Applied Spectroscopy* **2004**, *58*, 1452–1461.

(317) Sung, K.; Toon, G. C.; Drouin, B. J.; Mantz, A. W.; Smith, M. A. H. FT-IR measurements of cold propene (C_3H_6) cross-sections at temperatures between 150 and 299 K. *Journal of Quantitative Spectroscopy and Radiative Transfer* **2018**, *213*, 119–132.

(318) Huang, W.; White, J. Propene adsorption on Ag(111): a TPD and RAIRS study. *Surface Science* **2002**, *513*, 399–404.

(319) Chesters, M. A.; De La Cruz, C.; Gardner, P.; McCash, E. M.; Prentice, J. D.; Sheppard, N. Infrared spectroscopic comparison of the chemisorbed species from ethene, propene, but-1-ene and cis- and trans-but-2-ene on Pt(111) and on a platinum/silica catalyst. *Journal of the Chemical Society, Faraday Transactions* **1990**, *86*, 2757–2763.

(320) Radziszewski, J. G.; Downing, J. W.; Gudipati, M. S.; Balaji, V.; Thulstrup, E. W.; Michl, J. How predictable are IR transition momemt directions? Vibrational transitions in propene and deuterated propenes. *Journal of the American Chemical Society* **1996**, *118*, 10275–10284.

(321) Huang, W.; White, J. Propene Oxidation on Ag(111): Spectroscopic Evidence of Facile Abstraction of Methyl Hydrogen. *Catalysis Letters* **2002**, *84*, 143–146.

(322) Barnes, A. J.; Howells, J. D. R. Infra-red cryogenic studies. Part 12.—Alkenes in argon matrices. *Journal of the Chemical Society, Faraday Transactions* **1973**, *69*, 532–539.

(323) Davis, K. A.; Goodman, D. W. Propene Adsorption on Clean and Oxygen-Covered Au(111) and Au(100) Surfaces. *The Journal of Physical Chemistry B* **2000**, *104*, 8557–8562.

(324) McKean, D. CH stretching frequencies, bond lengths and strengths in acetone, acetaldehyde, propene and isobutene. *Spectrochimica Acta Part A: Molecular Spectroscopy* **1975**, *31*, 861–870.

(325) Tobin, M. The infrared spectrum of propylene oxide. *Spectrochimica Acta* **1960**, *16*, 1108–1110.

(326) Brown, N. F.; Barteau, M. A. Epoxides as probes of oxametallacycle chemistry on Rh(111). *Surface Science* **1993**, *298*, 6–17.

(327) Stacchiola, D.; Burkholder, L.; Tysoe, W. T. Enantioselective Chemisorption on a Chirally Modified Surface in Ultrahigh Vacuum: Adsorption of Propylene Oxide on 2-Butoxide-Covered Palladium(111). *J. Am. Chem. Soc.* **2002**, *124*, 8984–8989.

(328) Dinger, A.; Lutterloh, C.; Biener, J.; Küppers, J. Adsorption of propylene oxide on Pt(111) surfaces and its reactions with gaseous and adsorbed H atoms. *Surface Science* **2000**, *449*, 1–18.

(329) Davis, J. L.; Barteau, M. A. Polymerization and decarbonylation reactions of aldehydes on the Pd(111) surface. *Journal of the American Chemical Society* **1989**, *111*, 1782–1792.

(330) Brown, N. F.; Barteau, M. A. Reactions of unsaturated oxygenates on rhodium(111) as probes of multiple coordination of adsorbates. *Journal of the American Chemical Society* **1992**, *114*, 4258–4265.

(331) Esan, D. A.; Trenary, M. Surface chemistry of propanal, 2-propenol, and 1-propanol on Ru(001). *Physical Chemistry Chemical Physics* **2017**, *19*, 10870–10877.

(332) Vannice, M.; Erley, W.; Ibach, H. A RAIRS and HREELS study of acetone on Pt(111). *Surface Science* **1991**, *254*, 1–11.

(333) Syomin, D.; Koel, B. E. IRAS studies of the orientation of acetone molecules in monolayer and multilayer films on Au(111) surfaces. *Surface Science* **2002**, *498*, 53–60.

(334) Stacchiola, D.; Burkholder, L.; Tysoe, W. Structure and reactivity of propylene on clean and hydrogen-covered Pd(111). *Surface Science* **2003**, *542*, 129–141.

(335) Hudson, R.; Gerakines, P.; Moore, M. Infrared spectra and optical constants of astronomical ices: II. Ethane and ethylene. *Icarus* **2014**, *243*, 148–157.

(336) Mitlin, S.; Leung, K. T. Film Growth of Ice by Vapor Deposition at 128-185 K Studied by Fourier Transform Infrared Reflection-Absorption Spectroscopy: Evolution of the OH Stretch and the Dangling Bond with Film Thickness. *The Journal of Physical Chemistry B* **2002**, *106*, 6234–6247.

(337) Dostert, K.-H.; O'Brien, C. P.; Mirabella, F.; Ivars-Barceló, F.; Schauermann, S. Adsorption of acrolein, propanal, and allyl alcohol on Pd(111): a combined infrared reflection–absorption spectroscopy and temperature programmed desorption study. *Physical Chemistry Chemical Physics* **2016**, *18*, 13960–13973.

(338) Browarzik, R.; Stuhl, F. Temperature Dependence of the Rate Constants for the Reactions of Oxygen Atoms with Ethene, Propene, and 1-Butene. *The Journal of Physical Chemistry* **1984**, *88*, 6004–6009.

(339) Atkinson, R.; Pitts, J. N. Absolute rate constants for the reaction of $O(^3P)$ atoms with a series of olefins over the temperature range 298–439 K. *The Journal of Chemical Physics* **1977**, *67*, 38–43.

(340) Ashford, R. D.; Ogryzlo, E. A. Temperature dependence of some reactions of singlet oxygen with olefins in the gas phase. *Journal of the American Chemical Society* **1975**, *97*, 3604–3607.

(341) Cvetanovic, R. J.; Singleton, D. L. Reaction of oxygen atoms with olefins. *Reviews of Chemical Intermediates* **1984**, *5*, 183–226.

(342) Cvetanović, R. J. The biradical intermediate in the addition of the ground state oxygen atoms, $O(^3P)$, to olefins. *The Journal of Physical Chemistry* **1970**, *74*, 2730–2732.

(343) Leonori, F.; Occhiogrosso, A.; Balucani, N.; Bucci, A.; Petrucci, R.; Casavecchia, P. Crossed Molecular Beam Dynamics Studies of the O(3 P) + Allene Reaction: Primary Products, Branching Ratios, and Dominant Role of Intersystem Crossing. *The Journal of Physical Chemistry Letters* **2012**, *3*, 75–80.

(344) Rajak, K.; Maiti, B. Trajectory surface hopping study of the O(^{3}P) + C_2H_2 reaction dynamics: Effect of collision energy on the extent of intersystem crossing. *J. Chem. Phys* **2014**, *140*, 44314.

(345) Audouin, L.; Langlois, V.; Verdu, J.; de Bruijn, J. C. M. Role of oxygen diffusion in polymer ageing: kinetic and mechanical aspects. *Journal of Materials Science* **1994**, *29*, 569–583.

(346) Fairgrieve, S. P.; MacCallum, J. R. Diffusion-controlled oxidation of polymers: A mathematical model. *Polymer Degradation and Stability* **1985**, *11*, 251–265.

(347) Yousif, E., *Photostabilization of PVC: principles and applications*; Elsevier Applied Science: 2012, p 595.

(348) Pawela-Crew, J.; Madix, R. J. Anomalous effects of weak chemisorption on desorption kinetics of alkenes: The desorption of propylene and propane from Ag(110). *The Journal of Chemical Physics* **1996**, *104*, 1699–1708.

(349) Baker, T. A.; Xu, B.; Jensen, S. C.; Friend, C. M.; Kaxiras, E. Role of defects in propene adsorption and reaction on a partially O-covered Au(111) surface. *Catalysis Science & Technology* **2011**, *1*, 1166–1174.

(350) Nart, F. C.; Kelling, S.; Friend, C. M. Oxygen Lability on Thin Oxide Films on Mo(110). *The Journal of Physical Chemistry B* **2000**, *104*, 3212–3218.

(351) Kay, B. D.; Lykke, K. R.; Creighton, J. R.; Ward, S. J. The influence of adsorbate-absorbate hydrogen bonding in molecular chemisorption: NH_3, HF, and H_2O on Au(111)., 1989.

(352) Giussani, E.; Fazzi, D.; Brambilla, L.; Caironi, M.; Castiglioni, C. Molecular Level Investigation of the Film Structure of a High Electron Mobility Copolymer via Vibrational Spectroscopy. *Macromolecules* **2013**, *46*, 2658–2670.

(353) Yates, J. T.; Madey, T. E., *Vibrational spectroscopy of molecules on surfaces*; Plenum Press: 1987, p 468.

(354) Thompson, R. S.; Brann, M. R.; Sibener, S. J. Sticking Probability of High-Energy Methane on Crystalline, Amorphous, and Porous Amorphous Ice Films. *The Journal of Physical Chemistry C* **2019**, *123*, 17855–17863.

(355) Hudson, R.; Ferrante, R.; Moore, M. Infrared spectra and optical constants of astronomical ices: I. Amorphous and crystalline acetylene. *Icarus* **2014**, *228*, 276–287.

(356) Paz, Y.; Trakhtenberg, S.; Naaman, R. Phase transitions in organized organic thin films as detected by their reactivity. *The Journal of Physical Chemistry* **1993**, *97*, 9075–9077.

(357) Paz, Y.; Trakhtenberg, S.; Naaman, R. Destruction of organized organic monolayers by oxygen atoms. *The Journal of Physical Chemistry* **1992**, *96*, 10964–10967.

(358) Gerakines, P. A.; Hudson, R. L. Infrared Spectra and Optical Constnats of Elusive Amorphous Methane. *The Astrophysical Journal* **2015**, *805*, L20\1–5.

(359) Alentiev, A.; Drioli, E.; Gokzhaev, M.; Golemme, G.; Ilinich, O.; Lapkin, A.; Volkov, V.; Yampolskii, Y. Gas permeation properties of phenylene oxide polymers. *Journal of Membrane Science* **1998**, *138*, 99–107.

(360) Tian Zhao, C.; Do Rosário Ribeiro, M.; De Pinho, M. N.; Subrahmanyam, V. S.; Gil, C. L.; De Lima, A. P. Structural characteristics and gas permeation properties of polynorbornenes with retained bicyclic structure. *Polymer* **2001**, *42*, 2455–2462.

(361) Kilburn, D.; Townrow, S.; Meunier, V.; Richardson, R.; Alam, A.; Ubbink, J. Organization and mobility of water in amorphous and crystalline trehalose. *Nature Materials* **2006**, *5*, 632–635.

(362) Smith, R. S.; Matthiesen, J.; Knox, J.; Kay, B. D. Crystallization Kinetics and Excess Free Energy of H_2O and D_2O Nanoscale Films of Amorphous Solid Water. *The Journal of Physical Chemistry A* **2011**, *115*, 5908–5917.

(363) Avrami, M. Kinetics of Phase Change. I General Theory. *The Journal of Chemical Physics* **1939**, *7*, 1103–1112.

(364) Rao, C. N. R.; Rao, K. J., *Phase transitions in solids : an approach to the study of the chemistry and physics of solids*; McGraw-Hill: 1978, p 330.

(365) Doremus, R. H., *Rates of phase transformations*; Academic Press: 1985, p 176.

(366) Pradell, T.; Crespo, D.; Clavaguera, N.; Clavaguera-Mora, M. T. Diffusion controlled grain growth in primary crystallization: Avrami exponents revisited. *Journal of Physics: Condensed Matter* **1998**, *10*, 3833–3844.

(367) Tait, S. L.; Dohnálek, Z.; Campbell, C. T.; Kay, B. D. n-alkanes on MgO(100). II. Chain length dependence of kinetic desorption parameters for small n-alkanes. *The Journal of Chemical Physics* **2005**, *122*, 164708\1–13.

(368) Dounce, S. M.; Mundy, J.; Dai, H.-L. Crystallization at the glass transition in supercooled thin films of methanol. *The Journal of Chemical Physics* **2007**, *126*, 191111\1–4.

(369) Safarik, D. J.; Meyer, R. J.; Mullins, C. B. Thickness dependent crystallization kinetics of sub-micron amorphous solid water films. *The Journal of Chemical Physics* **2003**, *118*, 4660–4671.

(370) Thompson, R. S.; Langlois, G. G.; Sibener, S. J. Oxidative Destruction of Multilayer Diisopropyl Methylphosphonate Films by $O(^3P)$ Atomic Oxygen. *The Journal of Physical Chemistry B* **2017**, *122*, 455–463.

(371) Thompson, R. S.; Brann, M. R.; Purdy, E. H.; Graham, J. D.; McMillan, A. A.; Sibener, S. J. Rapid Laser-Induced Temperature Jump Decomposition of the Nerve Agent Simulant Diisopropyl Methylphosphonate under Atmospheric Conditions. *The Journal of Physical Chemistry C* **2019**, *123*, 21564–21570.